CO_2 Saline Storage Demonstration in Colorado Sedimentary Basins: Applied Studies in Reservoir Assessment and Dynamic Processes Affecting Industrial Operations

Dag Nummedal, Alexis Sitchler, John McCray, Katherine Mouzakis,
John McCray, Andy Glossner, Kevin Mandernack, Marte Gutierrez,
Kevin Doran, Matthew Pranter and Chris Rybowiak

Final Report for DOE Award Number DE-FE0000730

Reporting period (start/stop dates): January 10, 2009 - December 12, 2014

Type of Report: Final Technical
Frequency of Report: FINAL REPORT
Reporting Period: FINAL REPORT
DOE Award Number: Submitting Organization: The Colorado School of Mines
1500 Illinois Street
Golden, CO 80401-1887

Submitted to: U.S. Department of Energy
National Energy Technology Laboratory
DOE Project Manager, Dawn Deel

DOE Award Number: DE-FE0000730, Colorado School of Mines
USGS Project Number: DE-FE0000432

Date Submitted: Dec. 12, 2014

DISCLAIMER

CO_2 Saline Storage Demonstration in Colorado Sedimentary Basins: Applied Studies in Reservoir Assessment and Dynamic Processes Affecting Industrial Operations

Type of Report: Final Technical

Frequency of Report: FINAL REPORT

Reporting Period: FINAL REPORT

DOE Award Number: DE-FE0000730

Submitting Organization:
The Colorado School of Mines
1500 Illinois Street
Golden, CO 80401-1887

Preparers:
Dag Nummedal
Phone: 303 384-2506
E-mail: nummedal@mines.edu,
and
Kevin L. Doran
Phone: 303 492-5127
Email: dorank@colorado.edu

Submitted to:
U.S. Department of Energy
National Energy Technology Laboratory

DOE Project Manager, Dawn Deel

DOE Award Number: DE-FE0000730, Colorado School of Mines
USGS Project Number: DE-FE0000432

Authors: Dag Nummedal, Alexis Sitchler, John McCray, Katherine Mouzakis, John McCray, Andy Glossner, Kevin Mandernack, Marte Gutierrez, Kevin Doran, Matthew Pranter, Chris Rybowiak

Date Submitted: Dec. 12, 2014

Abstract

This multitask research project was conducted in anticipation of a possible future increase in industrial efforts at CO_2 storage in Colorado sedimentary basins. Colorado is already the home to the oldest Rocky Mountain CO_2 storage site, the Rangely Oil Field, where CO_2-EOR has been underway since the 1980s. The Colorado Geological Survey has evaluated storage options statewide, and as part of the SW Carbon Sequestration Partnership the Survey, is deeply engaged in and committed to suitable underground CO_2 storage.

As a more sustainable energy industry is becoming a global priority, it is imperative to explore the range of technical options available to reduce emissions from fossil fuels. One such option is to store at least some emitted CO_2 underground. In this NETL-sponsored CO_2 sequestration project, the Colorado School of Mines and our partners at the University of Colorado have focused on a set of the major fundamental science and engineering issues surrounding geomechanics, mineralogy, geochemistry and reservoir architecture of possible CO_2 storage sites (not limited to Colorado). Those are the central themes of this final report and reported below in Tasks 2, 3, 4, and 6. Closely related to these reservoir geoscience issues are also legal, environmental and public acceptance concerns about pore space accessibility—as a precondition for CO_2 storage. These are addressed in Tasks 1, 5 and 7.

Some debates about the future course of the energy industry can become acrimonius. It is true that the physics of combustion of hydrocarbons makes it impossible for fossil energy to attain a carbon footprint anywhere nearly as low as that of renewables. However, there are many offsetting benefits, not the least that fossil energy is still plentiful, it has a global and highly advanced distribution system in place, and the footprint that the fossil energy infrastructure occupies is orders of magnitude smaller than renewable energy facilities with equivalent energy capacity. Finally, inexpensive natural gas here in North America is pushing coal for electricity generation off the market, thus reducing US CO_2 emissions faster than any other large industrialized nation. These two big factors argue for renewed efforts to find technology solutions to reduce the carbon footprint (carbon dioxide as well as methane and trace gases) of conventional and unconventional oil and gas. One major such technology component is likely to be carbon capture, utilization and storage.

Task 1. Project management. Management of this multitask project was established in accordance with a few principles that seem to serve scientific inquiry well. The most fundamental one is to ensure that development of new theory, testing and observation is incrementally additive to prior research. Each investigator, therefore, built these studies on a comprehensive background of prior published research work, a fact that is reflected well in the many citations in each chapter. To ensure close communication between investigative teams and exchange of ideas and results, we held many formal and informal workshops between the parties during the project. At least once a year, we held a formal review attended by NETL staff.

Also, the graduate students engaged in this project not only performed the majority of the laboratory

work, but they were also instrumental in organizing oral and poster technical seminars and meetings with other students, faculty and external industrial and governmental visitors. The number of people exposed to—and therefore also indirectly contributing to the project success over these several years—easily measure more than 50.

Task 2. Geomechanics. The geomechanical laboratory at the Colorado School of Mines has recently built a new high pressure and high temperature triaxial core testing system. This facility was 'inaugurated' in this project with detailed studies of how the elastic wave velocity in fractured rocks depend on fracture normal—and shear—oriented stiffness. The new facility is able to test for temperatures up to 150°C and pressures that range up to 70 MPa.

Task 3. Pore scale network structure. The pore network in rocks of any kind is critical to the understanding of the effects of CO_2 being injected into reservoirs because this network carries the fluids to sites where mineralogical reactions take place. This particular study utilized a combination of three different instrumental approaches to characterize the pore structure of fine-grained rocks ("mudstones") that could form caprocks at future subsurface CO_2 sequestration sites. These were: 1) small angle neutron scattering, 2) electron imaging, and 3) gas adsorption and mercury porosimetry.

Task 4. Geomicrobiological influence. Saline aquifers, depleted oil reservoirs, basalt aquifers and deep, unmineable coal seams are all considered potential targets for CO_2 utilization and sequestration. Therefore we have investigated the impacts of CO_2 injections on subsurface microbial communities. To this end, we have analyzed bacterial cell membrane phospholipids, which target living microorganisms, in ground waters from two field sites where CO_2 injections have either occurred or were targeted for injection as well as from laboratory microcosm experiments.

Task 5. Making fossil energy more sustainable. The original proposed Task 5, which was focused on the subsurface characterization of the Dakota Group in the Denver basin, was redirected to Task 5 as described here, with emphasis on making fossil energy more sustainable. This change was a necessary adjustment, because the scientist assigned to that task had to return to France for family reasons. The project PI (DN) redirected a small amount of funds into overall project management (for which his responsibility grew) and also into an evaluation of the broader techno-socio-economic issues surrounding GHG emissions more broadly. This shift allowed the further development of Colorado School of Mines research expertize in greenhouse gas emissions, a shift that was rewarded with a new methane emissions project in 2014.

Task 6. Pore-Volume and Permeability for Geologic Storage of CO_2. Detailed core-based measurements of sandstone permeability and its distribution is one first step in evaluating the storage capacity for CO_2 in sandstone reservoirs. What the study in this task documents, however, is that access to this permeability—whether the goal is to extract gas or oil at an optimal rate, or inject

CO_2 for storage—is critically dependent of how the pores are actually connected. Connectivity is dependent on facies as well as reservoir architecture. This detailed study of sandstone cores from the Hygiene field in the northern reaches of the Denver basin has developed permeability and connectivity models that are crucial for the optimal design of CO_2 storage in such sandstone reservoirs. The findings are applicable both to modeling of storage following potential enhanced oil recovery, or injection in saline reservoirs in similar lithofacies outside the oil field. This task also covers much of the research that was originally envisioned as being part of Task 5, prior to its redirection (see above).

Task 7. Regulatory Regimes and Enforcement Structures. The last task of this comprehensive study of CO_2 storage in Colorado sedimentary basins reached two profound conclusions of great significance to the further growth of this industry in the state. One is that legal precedent seems to imply that the Federal Government holds title to perhaps as much as 70 million acres of land across the West that is potentially suitable for CO_2 storage. One might conclude that federal ownership of the pore space in large swaths of Western lands would serve to drastically reduce the transaction costs associated with a pooling and unitization scheme for CCUS. The investigator notes, however, that federal ownership of pore space does not necessarily result in the effortless deployment of CCUS projects because the government tends to be risk-adverse, particularly for novel projects that are plagued with scientific and social acceptance uncertainty.

Introduction

This project was undertaken with the primary purpose of advancing the understanding of a series of interrelated geoscience, bioscience and engineering questions that are fundamental to the continued advancement of subsurface storage of CO_2. Close collaboration between several research teams essentially co-located between the Colorado School of Mines in Golden, CO, the University of Colorado in Boulder, CO and the US Geological Survey in Lakewood, CO created a very healthy and creative atmosphere during the 4-year performance period of this contract.

The scientists involved in the project, together with NETL management, also strongly supported the establishment of broad scientific ties with relevant research and demonstration centers elsewhere, both within the United States and internationally. Consequently, the Colorado CCUS research community has built very strong ties with many other US academic centers (including such centers as UT Austin; Stanford University; the Joint Institute for Strategic Energy Analysis at the National Renewable Energy Laboratory in Golden, CO; the National Oceanic and Atmospheric Administration in Boulder, CO; and the Los Alamos National Laboratory. Strong links have also been established with international centers—particularly the Norwegian carbon sequestration research center SUCCESS (where Dr. Nummedal now serves on the board) and the Norwegian Gassnova company (where Dr. Nummedal was past advisory board member) and the CCUS capture demonstration facility at Mongstad.

In addition to the scientific research results presented in detail in this final report, this NETL project has also been instrumental in establishing the foundation for a new Carbon Management Center here in Colorado: the CMC (www.carbonmanagementcenter.org). The CMC has already organized several industry workshops, including student-led symposia and poster sessions, all of which have been very well received by the research community. These workshops have also been effective in reaching out to a broad industrial community. The management team of this NETL project is currently building on these contacts to establish broad industrial and private funding for growth of the Carbon Management Center. There is now widespread acceptance in industry that fundamental research on many issues in pore-scale science supported over many years by NETL's CCUS program has opened new doors for industrial progress on enhanced oil recovery, unconventional oil and gas extraction, and novel geothermal energy extraction methods.

When evaluated against all these broad measures of lasting industrial impact, this NETL-sponsored research program has been successful. As a team here in Colorado, we are emerging from these years of NETL funding with a stronger focus on the fundamental geomechanical properties of CO_2 storage reservoirs, mineral dissolution and related permeability and porosity changes in CO_2 storage reservoirs, geomicrobiologial consequences of CO_2 storage, permeability changes in sandstone storage reservoirs, and the regulatory regimes and public attitudes related to uses of subsurface pore space. The results have been widely distributed both in oral presentations, theses and publications.

CCUS is a technology in its infancy. It was initially conceived as basic research for the purpose of capturing CO_2 from large emitters such as coal burning power plants and storing this safely for a long time in underground storage reservoirs. Development of all such technologies is continuing. Over the years, the CCUS research program has evolved to also explore the many components of the “U” – utilization – in the program title. Because of the rapid growth in shale-hosted oil in the U.S., the application of CO_2 to enhance production of this unconventional resource is now becoming a focus. Overall, this drives a gradual change in industry’s perspectives on the future market demand for CO_2 as well as the desirable research focus for NETL’s CCUS research program during the coming years.

We hope that the extensive research projects reported here will provide some new insights, perspectives and data to accelerate the national effort to develop new and growing market demand for CO_2 in the next generation, more sustainable, low-emission fossil fuel industry.

Table of Contents

Individual Task Reports

Task 1. Project Management and Planning

1.1. Goals/Objectives

Management of this multitask project was established in accordance with principles that seem to serve scientific inquiry well. The most fundamental one is to ensure that development of new theory, testing and observation is incrementally adding new insights to prior research. Each investigator, therefore, built these studies on a comprehensive background of prior published research work, a fact that is reflected well in the many citations in each chapter.

To ensure close communication between investigative teams and exchange of ideas and results, many formal and informal workshops between the parties were conducted during the project. At least once a year, we held a formal review attended by staff from the Pittsburgh NETL Laboratory, colleagues at the Colorado School of Mines and invited industry participants. Also, the graduate students engaged in this project not only performed the majority of the laboratory work, but they were also instrumental in organizing oral and poster technical seminars and meetings with other students, faculty and external industrial and governmental visitors. The number of people exposed to—therefore also indirectly contributing to the project success over these several years—easily measure at least one hundred. Abstract booklets for the student-organized workshops are available on request.

1.2. Background

Flow of CO_2, gas, oil and water in sandstone reservoirs occurs in a complex interplay of flow from rock matrix to wellbore via connected pores as well as natural and artificially induced fractures. In sandstones, however, the natural architecture of porosity and permeability, the structural and stratigraphic paths for fast flow alternating with seals, and connectivity between sand bodies of different size, shape, packing and orientation in the subsurface gas fields all control flow rates and ultimate paths to CO_2 storage.

Because of the complexity of CO_2, and associated gas, oil and water flow in reservoirs, no single technology or scientific discipline can alone tell the story. Instead, only an integrated workflow combining the clues from the various disciplines: geomechanics, pore scale science issues, geomicrobiology and pore volume connectivity can stand a chance of realistically capturing the complexity of flow in such systems. For that very reason, we assembled this broad team of experts with experiences in theory, lab experiments and field work, and practical oil and gas field applications to help develop new scientific principles to guide injection and long-term storage of CO_2 in the subsurface. For the CCUS industry to grow in the marketplace and public acceptance, it is equally critical to also understand and be able to communicate the socio-economic risks, public perception, and subsurface pore space ownership issues; all of which are also explicitly addressed in this report.

1.3. Methods/Approach

All research tasks explicitly included assessments of the technology status prior to commencement of new analysis, modeling and experimental work. This is ‘normal operating procedure’ in most academic research, but it is taking on added significance in today’s highly diverse and dispersed global research culture.

In addition to explicit review or assessment of prior technology, what has been equally important to the success of this project is the culture of open exchange of data and insights between scientists and engineers in several universities, other research organizations and consulting companies. Regular meetings of project PIs and their students during annual reviews at NETL in Pittsburgh have been equally important.

1.4. Task Results

For the public at large, as taxpayers and beneficiaries of new technologies that reduce the rate of global warming, it is essential that expensive studies like this one clearly articulate the need for action and that CCUS be one among several essential technologies that have the potential to move the globe towards reduced rates of warming.

There is a strong convergence in forward-looking climate models: our planet is warming and will continue to do so for decades—probably much longer because of the greenhouse gases already emitted. Based on the current trajectory of emissions, a warming of as much as 4 degrees Celsius for most of the world’s continents is plausible by the late 21st century (Romps et al., 2014) This should hardly surprise us; there is abundant evidence in the geological record to reconstruct, and thereby calibrate, the relationship between atmospheric CO_2 concentrations and temperatures. Most such data come from the detailed and precise records of the Antarctic and Greenland ice sheets and make it abundantly clear that past doubling of atmospheric CO_2 generated a temperature increase of about 5 to 6 degrees centigrade. Those past (ice-age to inter-glacials) CO_2 concentrations ranged from a low (ice age) of about 180 ppm to a high (interglacials, like now) of about 280 ppm (parts per million). We are now at 400 ppm of CO_2 in our atmosphere. Thus, human’s “industrious” activities have already added more than twice as much CO_2 to our atmosphere as nature did in the past when our planet moved from an ice age to an interglacial stage. That past natural variation was triggered by changes in our planet’s orbit around the sun, a factor that still is with us – but is now greatly augmented by humanity's global warming drivers.

Earth systems are very complex, and we do not understand all of them well enough to make any kinds of precise predictions, but a conservative conclusion from the data presented above is that the amount of human-made GHG emissions already in our atmosphere have “built in” a significant warming that will continue to make itself felt, even if we were to stop additional emissions soon. Therefore, the Coupled Model Intercomparison Project's estimated warming predicted to occur by the end of the 21st century is eminently reasonable in light of the geological record.

Today's warming is not due to changes in the Earth's orbit or other astronomical variables—they are superimposed on those and generally operate at faster time scales. A recent historical reconstruction by the Berkeley Earth Surface Temperature Project demonstrated there is a very clear differentiation of short-term astronomical and anthropogenic signals. Their record starts in 1750, as the Earth was emerging out of the "Little Ice Age", and continues by recording high-frequency land surface temperature variations on about 40 year time scales. Starting in 1870, the temperature takes a more continuous upward climb, moving from a mean global temperature of 8.5°C to 9.0°C by about 1930. This was the first phase of massive industrialization on our planet, mostly taking place in Europe and North America and made possible by coal and other fossil fuels. From the 1930s to the 1960s there was a stabilization of global land temperatures because of the Depression followed by World War II. From the 1960s to the present, global land surface temperatures have risen rapidly again to 9.8°C, this time in response to fossil-fuel driven industrialization across the entire world.

1.5. Significance and Discussion

The conclusion is inescapable that fossil fuel combustion is warming the planet. This is hardly a surprise; we have understood the physics of this process ever since Tyndall's experiments in the 1840s and Gustav Arrhenius' calculations in the 1890s. All that was needed at those times was experimental verification. Now, unfortunately, we have run the 'experiment' and verified the physics models.

Faced with this new reality, what are the responsibilities and capabilities of different sectors of our society to deal with the problem we have created? Because the authors of this report represent the university research and education community, let me start there. Our mission is to do discovery-based scientific research and technology development and to educate mostly, but not exclusively, the new generations. With global warming being such a dominant driver behind new technology (and policy) developments, our research and teaching should (and does) address the many science, engineering, economic and policy questions generated by the total transformation of the global energy system, already taking shape around us. Industry has parallel responsibilities—which translate into opportunities—to develop technologies and strategies to reduce greenhouse gas emissions while providing low-cost fuels and power, delivering reliable quantities of high-quality feed stocks for chemical industries and other sectors; all this while reducing the emissions and lowering the cost. Industrial financial engineering must be a major part of this because we have already seen how challenging it has proven for governments alone to create effective means of regulating, taxing or trading emissions "permits" or creating an effective market.

Clearly, government must, and does, play a big role in linking to incentives like Federal loan guarantees to requirements for emissions reductions, promulgate rules and regulations based on sound science and economics, and incentivize creativity and risk taking.

Task 2. Geomechanics of CO_2 Storage Reservoirs Applied to Saline Storage

2.1. Goals/Objectives

In the quest to better understand the geomechanics of CO_2 storage reservoirs, researchers working on Task 2 established three objectives. These were

- the development of a high pressure and high temperature triaxial core testing system simulating geological CO_2 sequestration at reservoir conditions
- the development of a model of stress-dependent wave velocity response of micro- and macro-fractured porous rocks
- the hydro-mechanical characterization of porous reservoir rocks at reservoir conditions

In the first objective, a high pressure and high temperature rock core testing system was developed to simulate CO_2 injection in fractured porous rock samples. The goal was to use the system to study the effects of effective stress and fluid content on ultrasonic wave velocity responses of porous rock samples. Researchers sought to understand the permeability of porous rock samples in the presence of two-phase fluid flow of saline water and supercritical CO_2 as well as the stress dependency of permeability of the porous rock.

In the second objective, researchers sought to develop a model for the stress-dependent elastic wave velocity response of fractured rock mass that would take into account parameters with clear physical meanings. Recognizing that previous models failed to account for these parameters, they developed a model based on experimental evidence of stress-dependent fracture normal and shear stiffnesses.

Finally, in objective three, laboratory studies of CO_2 injection in specimens of fractured reservoir rocks were performed under field conditions to provide input data to numerical models and as small-scale validation models of CO_2 injection in porous/fractured rocks. The laboratory studies focused on the response of micro-fractured porous reservoir rocks under multiphase fluid pressures and flow conditions encountered in CO_2 Geological Sequestration. During testing, changes in the P&S seismic wave velocities of the fractured rock sample were monitored using seismic monitors installed at the ends of the sample. The aim was to determine whether changes in P&S wave velocities can be used to detect movements of CO_2 in fractured rock samples. In addition, the relative permeabilities of porous rock for saline water and CO_2 were determined at reservoir conditions.

2.2. Background

Deep saline aquifers are estimated to have a storage capacity of at least 1000 Gt of carbon dioxide (CO_2) (IPCC, 2005). These aquifers, and potential storage reservoirs, are found in many places in the United States. The cost of geological CO_2 sequestration is highly dependent on site-specific conditions, for example, depth, reservoir temperature, pore pressure, soundness of cap rock layers, and the degree of continuity of reservoir layers. CO_2 leaking from reservoirs can contaminate available water and cause adverse effects on underground biological systems. Distribution of CO_2 injected in storage reservoirs needs to be predicted and monitored at a long time scale. Predicting behavior of CO_2 accumulated in geological sequestration reservoirs requires the solution of coupling problems of hydro-thermo-mechanical behaviors of saline water and CO_2 flowing in fractured porous rock mass.

CO_2 injection is required to be carried out at higher rates for higher displacement and cost efficiencies. Increases in fluid pressure due to CO_2 injection can cause fracture openings, fault movements, seismic activities, and degradation of sealing capacity of cap rock layers. One of the potential monitoring techniques of CO_2 distribution is seismic survey. For accurate CO_2 content detection using a seismic survey, wave velocity responses of fractured porous rocks must be studied, aiming at the effects of effective stress and fluid content changes due to CO_2 injection.

2.3. Methods/Approach

2.3.1. Development of High Pressure and High Temperature Triaxial Core Testing System Simulating Geological CO_2 Sequestration at Reservoir Conditions

A high pressure and high temperature testing system was developed to simulate sequestration of CO_2 in porous rock mass at reservoir conditions of deep saline aquifers (Fig. 2.1). The triaxial core holder is capable of applying overburden pressures and temperatures up to 70 MPa and 150ºC. Two syringe pumps, ISCO 260D and 100DX, can control fluid flow at 0.001-107 ml/min and 0.00001-50 ml/min, respectively. The testing system is enclosed in a constant temperature air bath to insulate the system from temperature disturbance. Figure 2.2 shows the triaxial cell covered with a rubber heater used to control the cell fluid temperature.

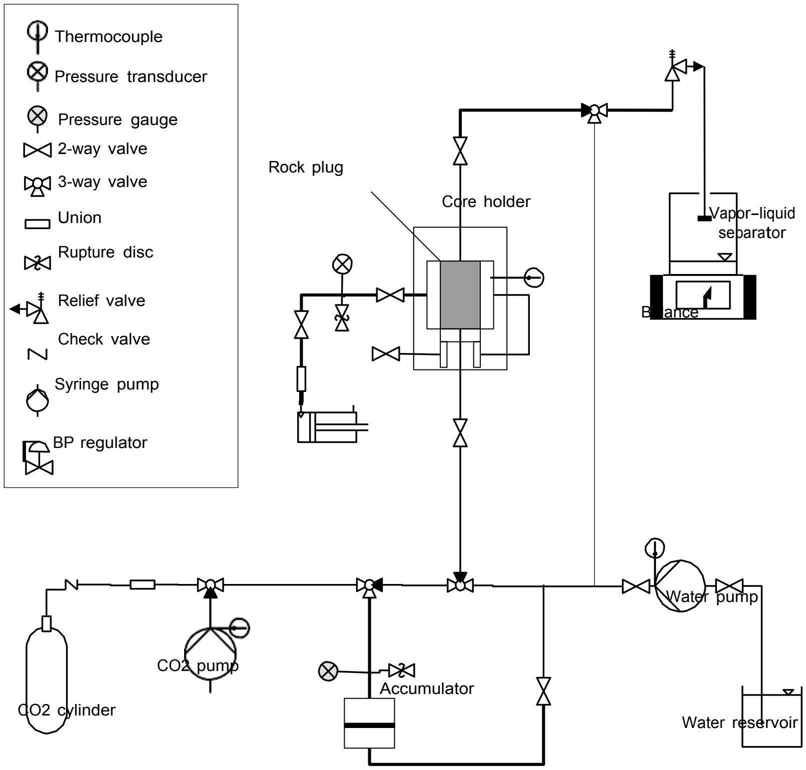

Fig. 2.1. A schematic of high pressure triaxial core testing system for simulating CO_2 injection.

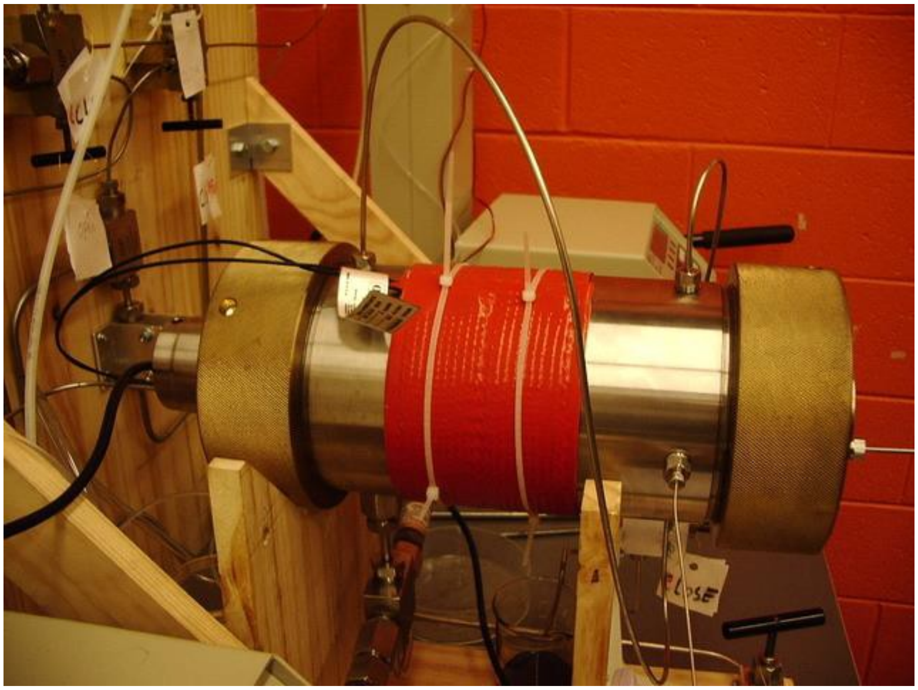

Fig. 2.2. Triaxial core holder covered with rubber heater.

Figure 2.3 shows the triaxial cell testing the hydromechanical response of a macroscopically fractured rock core sample. The normal stress acting on the fracture joint can be controlled through regulating cell pressure with a hydraulic pump. The differential pressure between the inlet and outlet of a core sample is measured with a variable reluctance differential pressure transducer having accuracy of ±0.25% full scale. An electronic balance monitors the mass of saline water produced from the core sample to analyze fluid content of the core sample during CO_2 injection.

Core samples whose diameter is 38.1 mm are enclosed in Viton rubber sleeves. The inlet/outlet faces of core samples are in contact with porous metal filters or grooved aluminum alloy plates to allow pore fluids to flow homogeneously into core samples. Figure 2.4 illustrates the ultrasonic wave velocity measurement system used in the research. The end-caps of the triaxial core holder are equipped with piezoelectric transducers to generate and receive ultrasonic waves propagating along the longitudinal axis of core samples. The pulser sends square pulses to the piezoelectric transducers at 100, 200, 300, and 400 volts. The ultrasonic waves received at the other end of the core sample are received by the receiver and subsequently by digital oscilloscope. A personal computer acquires the ultrasonic waveforms by communicating with the oscilloscope. A single waveform acquired by the personal computer is an average of 16 waveforms.

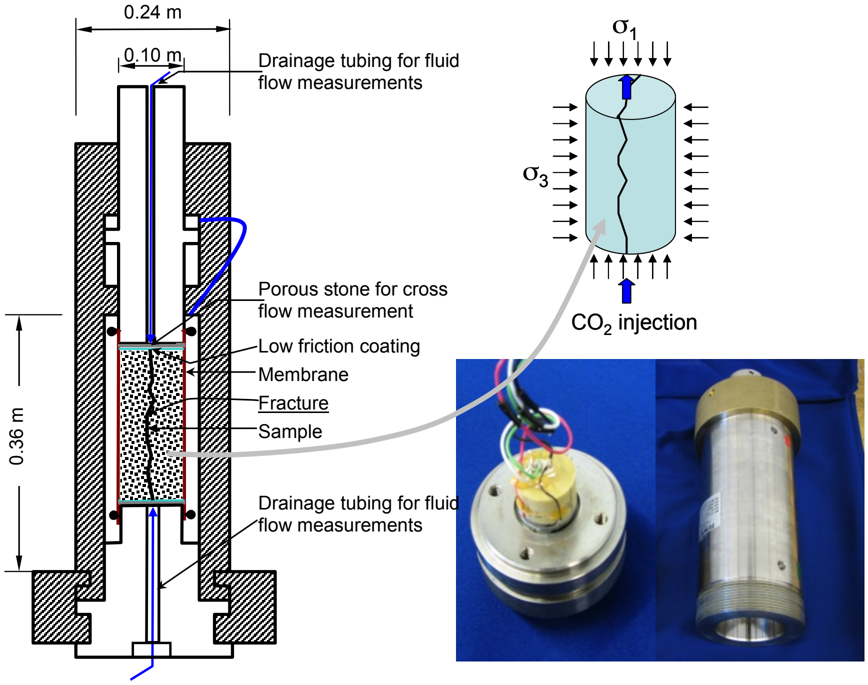

Fig. 2.3. Triaxial cell for testing of the hydro-mechanical behavior of macro-fractured rock specimens.

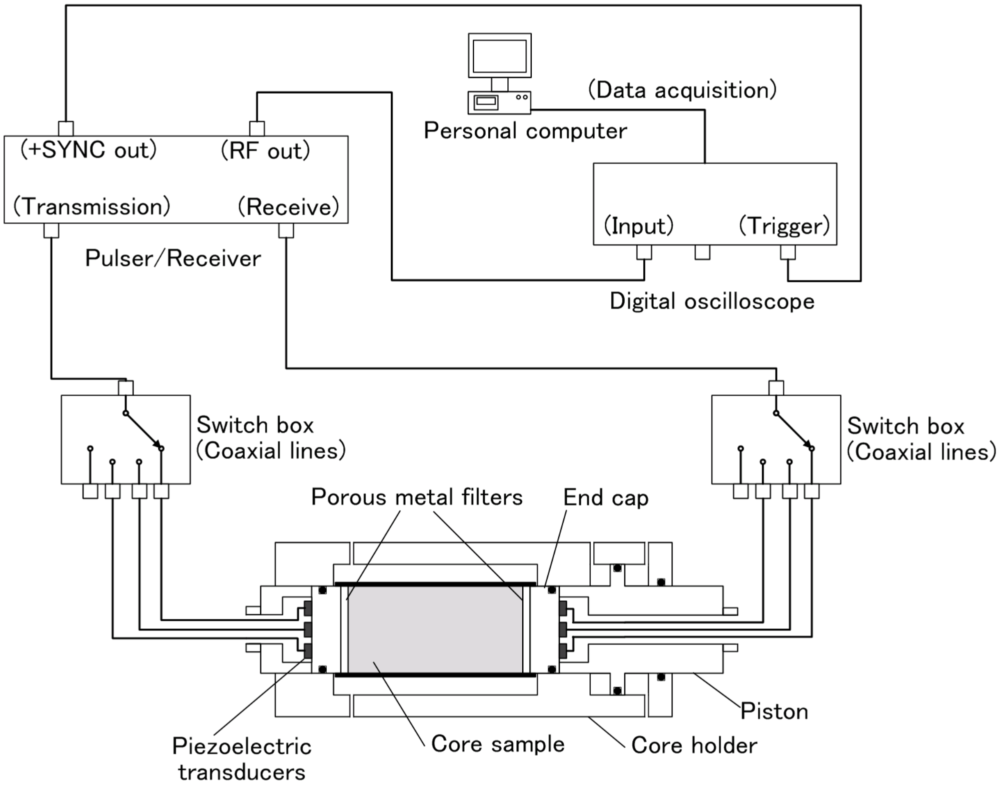

Fig. 2.4. Schematic of the ultrasonic wave velocity measurement system.

Figure 2.5 shows the arrangement of piezoelectric transducers mounted on the end-caps. Three different sets of transducers are prepared to send compressional (P-) and two shear (S-) waves in different oscillation directions. The two shear waves oscillate in orthogonally different directions as shown in the figure. The two different shear waves are used to investigate shear wave splitting of macroscopically fractured core samples. The natural frequencies of piezoelectric transducers range from 0.25 to 1.0 MHz. The minimum time interval of waveform acquisition in the personal computer is 6 seconds.

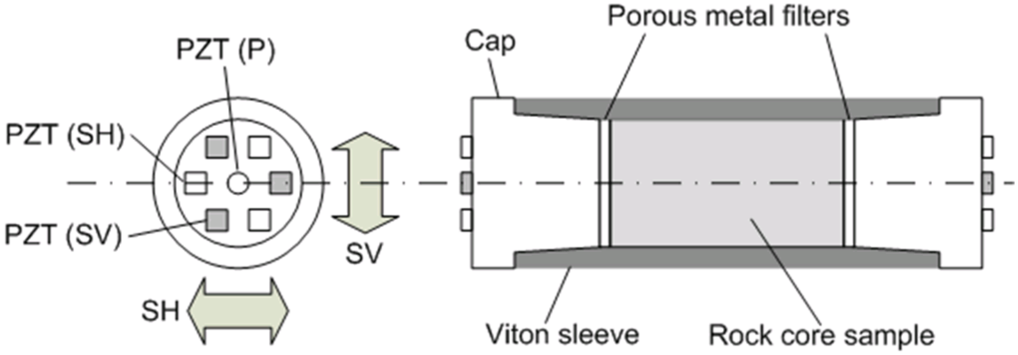

Fig. 2.5. Alignment and oscillation directions shear wave transducers mounted on end-caps.

2.3.2. Development of a model of Stress-Dependent Ultrasonic Wave Velocity Response of Micro- and Macro-fractured Porous Rocks

In this part of the task, a model for the stress-dependent elastic wave velocity response of fractured rock mass is proposed based on experimental evidence of stress-dependent fracture normal and shear stiffnesses. Most of the existing stress-dependent elastic wave velocity models are empirical with model parameters that do not have clear physical meanings. In the new model, the rock mass is assumed to have randomly-oriented microscopic fractures. The macroscopic stress-dependent elastic wave velocity response is attributed to the stress dependency of fracture stiffness. The stress-dependent fracture normal stiffness is defined as a generalized power law function of effective normal stress, which is a modification of the Goodman’s model. On the other hand, the stress dependency of fracture shear stiffness is modeled as a linear function of normal stress based on experimental data.

Ultrasonic wave velocity responses of a dry core sample of Berea sandstone were tested at effective stresses ranging from 2 to 55 MPa. Visual observation of thin sections obtained from the Berea sandstone confirms that the assumptions made for the microstructure of the rock mass model are appropriate. The model can describe the stress-dependent ultrasonic wave velocity responses of dry Berea sandstone with a set of reasonable material parameter values.

The effect of the presence of a macroscopic fracture on ultrasonic wave velocity response has been experimentally studied especially for shear wave velocity splitting. Shear wave splitting is pronounced at lower effective stresses. The proposed model has been demonstrated to be capable of describing the observed shear wave velocity splitting of a macrofractured porous rock sample by adjusting only material parameters characterizing stress dependency of shear fracture stiffness.

2.3.2.1. *Materials tested and testing procedure*

Core samples having 38.1 mm in diameter and approximately 70 mm in length were obtained from a block of Berea sandstone. The dry densities of the core samples were 2.22 g/cm^3. The ultrasonic wave velocities of air-dried core sample were measured at various effective stresses ranging from 2 to 55 MPa. The testing temperature was 40ºC.

A macroscopically fractured dry core sample was created by artificially fracturing a Berea sandstone core sample loaded with wedges shown in figure 2.6. In the core sample, indirect tensile stresses could be generated due to line contacts between the lateral face of the core sample and loading wedges. The artificial fracture was satisfactorily created as shown in figures 2.7 and 2.8.

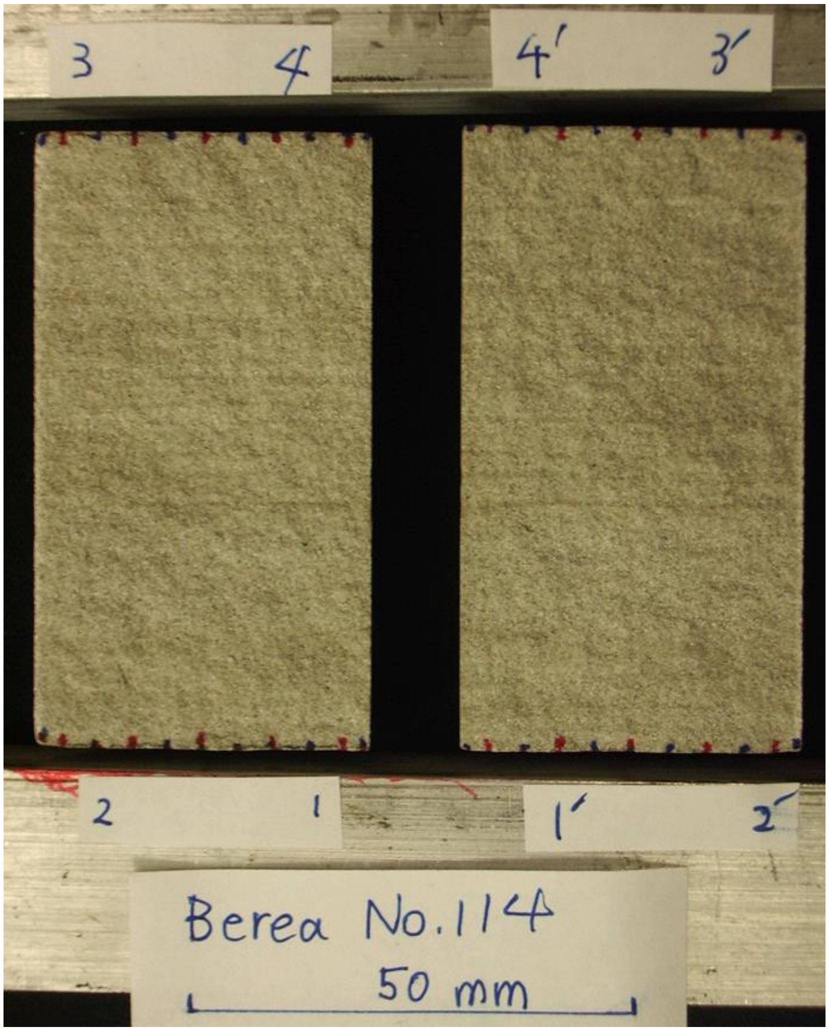

Fig. 2.6. Fracture surface of Berea sandstone core sample created by loading wedges.

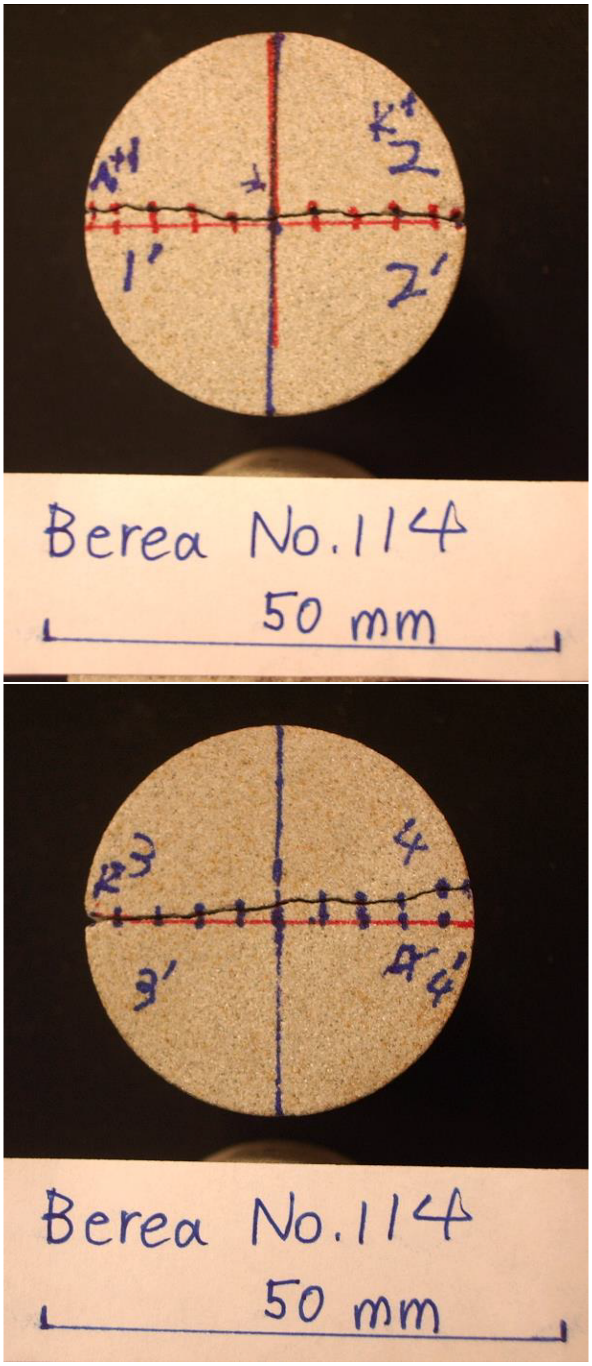

Fig 2.7. Fracture in Berea sandstone core sample observed from both end faces. Fracture is running horizontal direction of pictures.

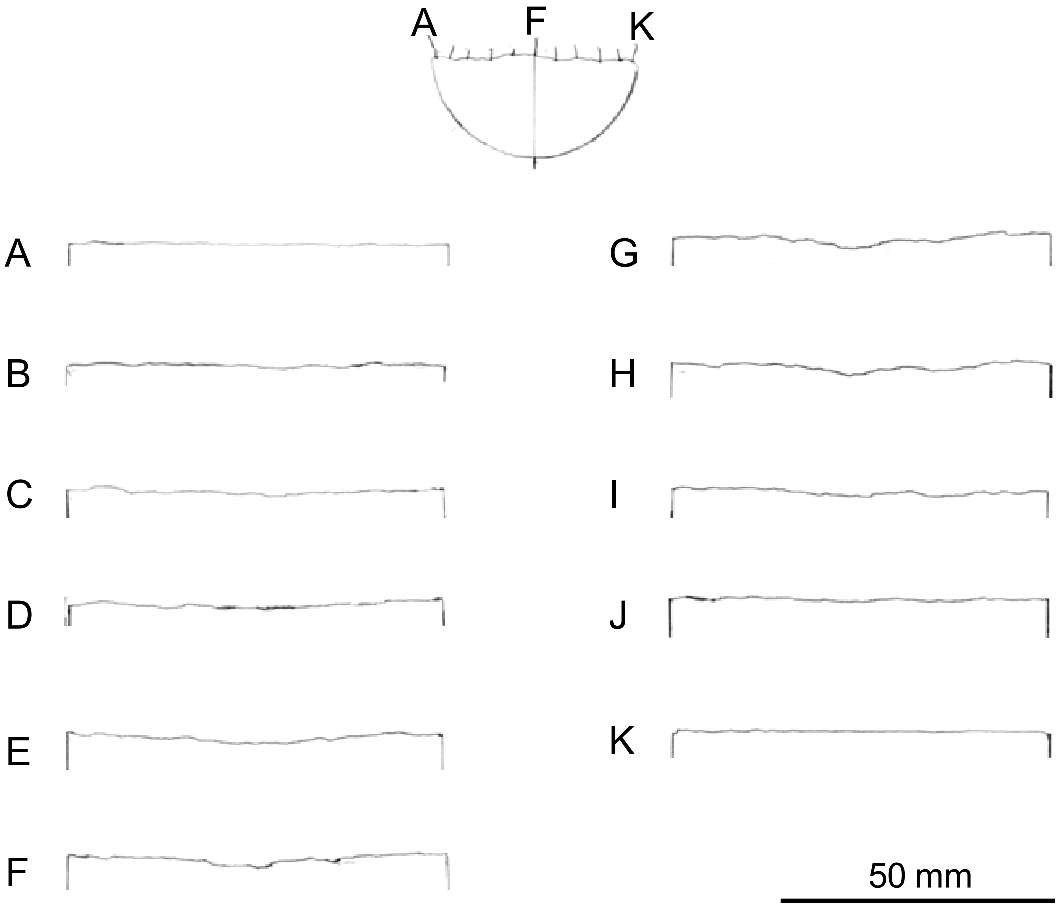

Fig. 2.8. Surface profile of fracture created by using a profilometer. The fracture joint becomes rougher closer to the center of the core sample.

To erase the initial disturbance of fracture core sample induced by the fracturing process, isotropic stresses up to approximately 60% of unconfined compression strength were applied to the fractured core sample in the triaxial core holder used in this study and subsequently unloaded. This cycle was repeated 3 times.

2.3.2.2. Visual observations of thin sections of Berea sandstone

The microscopic structure of a Berea sandstone sample was visually observed by preparing thin sections to propose a realistic model of stress dependent seismic wave velocity response of sandstone based on appropriate assumptions. Figure 2.9a and figure 2.9c are images obtained from the thin sections. Figure 2.9b and figure 2.9d illustrate distribution of microscopic fractures in the sections shown in figure 2.1a and figure 2.1c, respectively. It was observed that the microfractures were randomly oriented without any predominant direction. The lengths of the microfractures were approximately several hundred micrometers or smaller. The microfractures were spaced at micrometers of intervals. The dimensions and spacings of microfractures are much smaller than typical volumes of rock core samples tested in laboratories.

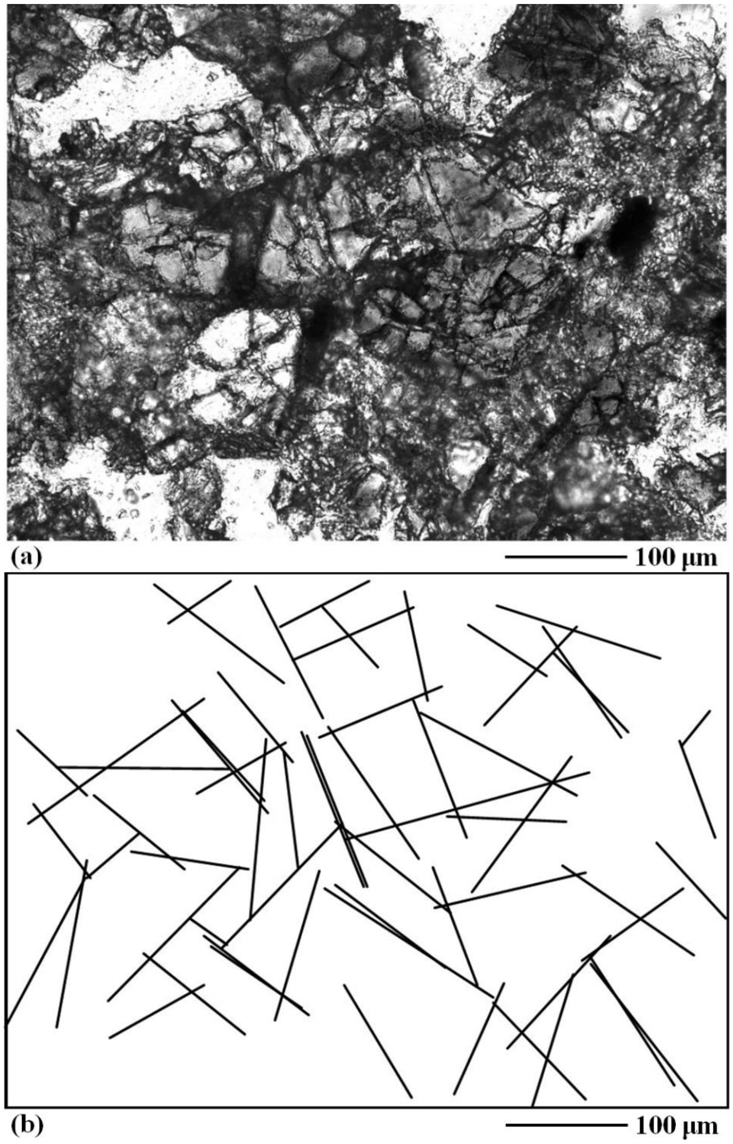

Fig. 2.9. Visual observation result of thin section of Berea sandstone: (a) thin section image and (b) sketch of distribution of main micro-fractures observed in (a).

2.3.2.3. Development of ultrasonic wave velocity response model for fractured porous rocks

Based on the visual observations of microstructure of Berea sandstone sample, the microstructure of sandstone is idealized as shown in figure 2.10. The rock mass is considered to have micro-fractures randomly oriented. The following assumptions are made: (1) The principal stresses σ_1 and σ_3 are parallel to the reference axes x_V and x_H, respectively; (2) The intact rock matrix indicated as the shaded area is isotropic; and (3) The fracture lengths and spacings are much smaller than the volume of the rock mass being considered.

The volumetric strain increment of the fractured rock mass is presumably subdivided into two components arising from compression of intact rock matrix and closure of micro-fractures:

$$dv = dv_{\mathrm{m}} + dv_{\mathrm{f}} \tag{2.1}$$

where dv_{m} and dv_{f} are the volumetric strain increments attributed to the compression of intact rock matrix and closure of fractures, respectively. The latter component can be given by

$$dv_{\mathrm{f}} \approx \frac{d\sigma'_{\mathrm{v}}}{s \cdot k_{\mathrm{n}}} \tag{2.2}$$

where s is the spacing between fractures, $d\sigma'_{\mathrm{v}}$ is the increment of vertical effective stress, and k_{n} is the fracture normal stiffness. Assuming negligible shear stress acting on the fractured rock mass, equation (2.1) can be rewritten as:

$$\frac{dp'}{M} = \frac{dp'}{M_{\mathrm{m}}} + \frac{dp'}{s \cdot k_{\mathrm{n}}} \tag{2.3}$$

where M and M_{m} are the longitudinal moduli of fractured rock mass and intact rock matrix. The following expression of longitudinal modulus of fractured rock mass is derived from equation (2.3):

$$M = \frac{s \cdot k_{\mathrm{n}} M_{\mathrm{m}}}{M_{\mathrm{m}} + s \cdot k_{\mathrm{n}}}. \tag{2.4}$$

Also for the shear modulus of fractured rock mass, the same form is derived, that is,

$$G = \frac{s \cdot k_{\mathrm{s}} G_{\mathrm{m}}}{G_{\mathrm{m}} + s \cdot k_{\mathrm{s}}} \tag{2.5}$$

where k_{s} is the fracture shear stiffness.
The following model is proposed for stress-dependent fracture normal stiffness:

$$k_{\mathrm{n}} = k_{\mathrm{ni}} \left(\frac{\sigma'_{\mathrm{n}}}{\sigma'_{\mathrm{ni}}} \right)^{n} \tag{2.6}$$

where k_{ni}, σ'_{ni}, and n are material parameters, and σ'_{n} is the effective normal stress acting over fracture. Equation (2.6) is a generalized form of the Goodman's (1974) model. As a model of fracture shear stiffness, the following linear function is likely to be appropriate based on the experimental data carried out on macroscopic fractures:

$$k_{\mathrm{s}} = k_{\mathrm{si}} + k_{\mathrm{sn}} \left(\frac{\sigma'_{\mathrm{n}}}{\sigma'_{\mathrm{ni}}} - 1 \right) \tag{2.7}$$

where k_{si} and k_{sn} are material parameters. The P- and S-wave velocities of dry rock mass, V_{p} and V_{s}, can be expressed as:

$$V_{\mathrm{p}} = \sqrt{\frac{M}{\rho}}, \; V_{\mathrm{s}} = \sqrt{\frac{G}{\rho}} \tag{2.8}$$

where ρ is the density. Assuming $\sigma'_{\mathrm{n}} = p'$ and combining equations (2.4), (2.5), (2.6), (2.7) and (2.8), the following expressions are obtained for V_{p} and V_{s}:

$$V_{\mathrm{p}} = V_{\mathrm{pm}} \sqrt{\frac{f_{\mathrm{n}}(p'_{\mathrm{nor}})}{1 + f_{\mathrm{n}}(p'_{\mathrm{nor}})}}, \; V_{\mathrm{s}} = V_{\mathrm{sm}} \sqrt{\frac{f_{\mathrm{s}}(p'_{\mathrm{nor}})}{1 + f_{\mathrm{s}}(p'_{\mathrm{nor}})}} \tag{2.9}$$

where V_{pm} and V_{sm} are the P- and S-wave velocities of intact rock matrix, p'_{nor} is the normalized mean effective stress by $p'_{\mathrm{i}} (= \sigma'_{\mathrm{ni}})$. $f_{\mathrm{n}}(p'_{\mathrm{nor}})$ and $f_{\mathrm{s}}(p'_{\mathrm{nor}})$ are termed fracture-matrix normal and fracture-matrix shear stiffness ratios, respectively, and written as:

$$\begin{aligned} f_{\mathrm{n}}(p'_{\mathrm{nor}}) &= \frac{s \cdot k_{\mathrm{n}}}{M_{\mathrm{m}}} = \frac{s \cdot k_{\mathrm{ni}} {p'_{\mathrm{nor}}}^{n}}{M_{\mathrm{m}}} \\ f_{\mathrm{s}}(p'_{\mathrm{nor}}) &= \frac{s \cdot k_{\mathrm{s}}}{G_{\mathrm{m}}} = \frac{s\left[k_{\mathrm{si}} + k_{\mathrm{sn}}(p'_{\mathrm{nor}} - 1)\right]}{G_{\mathrm{m}}} \end{aligned} \tag{2.10}$$

where M_{m} and G_{m} are the longitudinal and shear moduli of intact rock matrix. The material parameter values can be determined by curve fitting to experimental data of stress dependent elastic wave velocity.

Figure 2.11 indicates the best fitting curve of the fracture normal stiffness model Equation (2.6) to the experimental data obtained from macroscopic fractures of granodiorite (Malama and Kulatilake, 2003). It can be seen that the proposed model is capable of describing the observed stress dependency of normal stiffness. On the other hand, the Goodman's model indicated as 'Hyperbolic model' is not sufficient, because the value of compliance drastically decreases to almost zero values even when the effective stress is 2 MPa.

Fitting results of the fracture shear stiffness model equation (2.7) to experimental data obtained from oolitic limestone (Pyrak-Nolte et al., 1996) is shown in figure 2.12. In the experimental run performed on the fracture inclined, there exists shear stress on the fracture plane. Even for the inclined fracture, the model works well to describe the stress dependency of fracture shear stiffness.

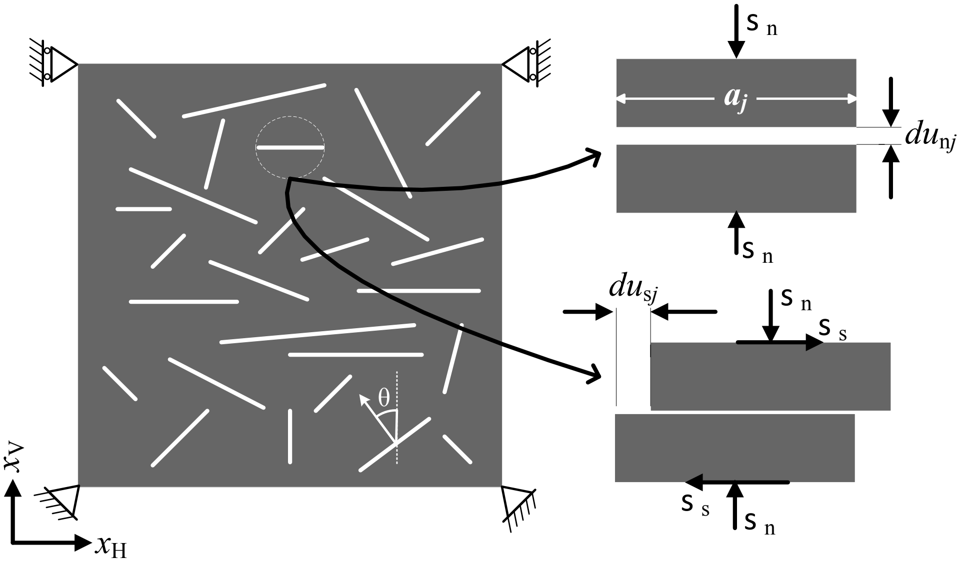

Fig. 2.10. Stress level dependency of ultrasonic wave velocities of dry and saline water-saturated core samples of Berea sandstone.

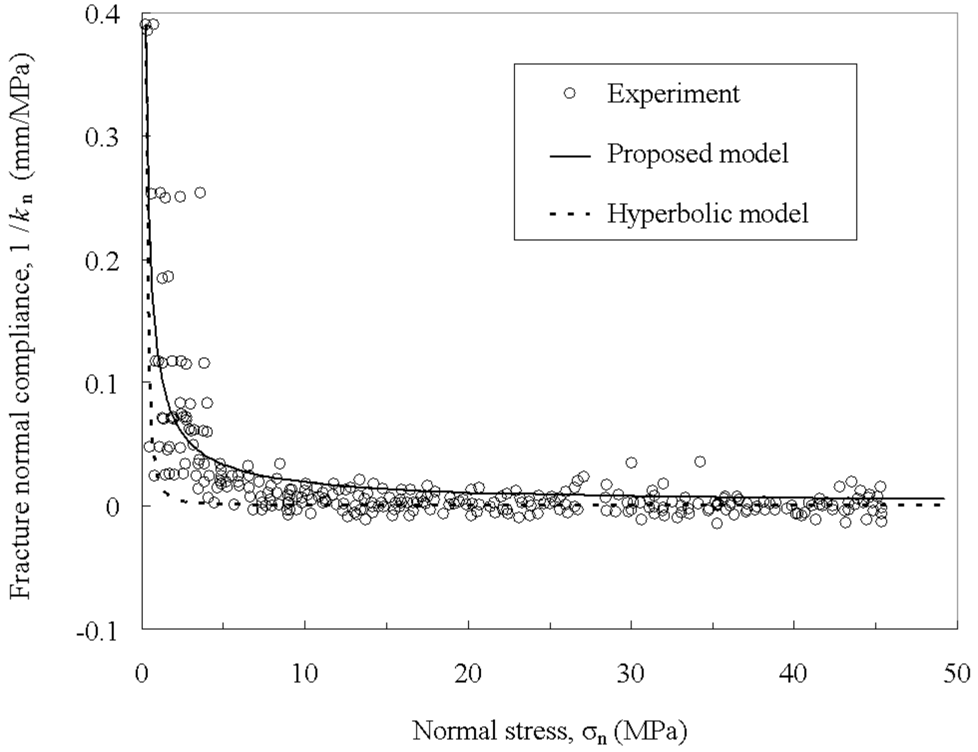

Fig. 2.11. Normal stress dependency of normal compliance of macroscopic fractures of granodiorite.

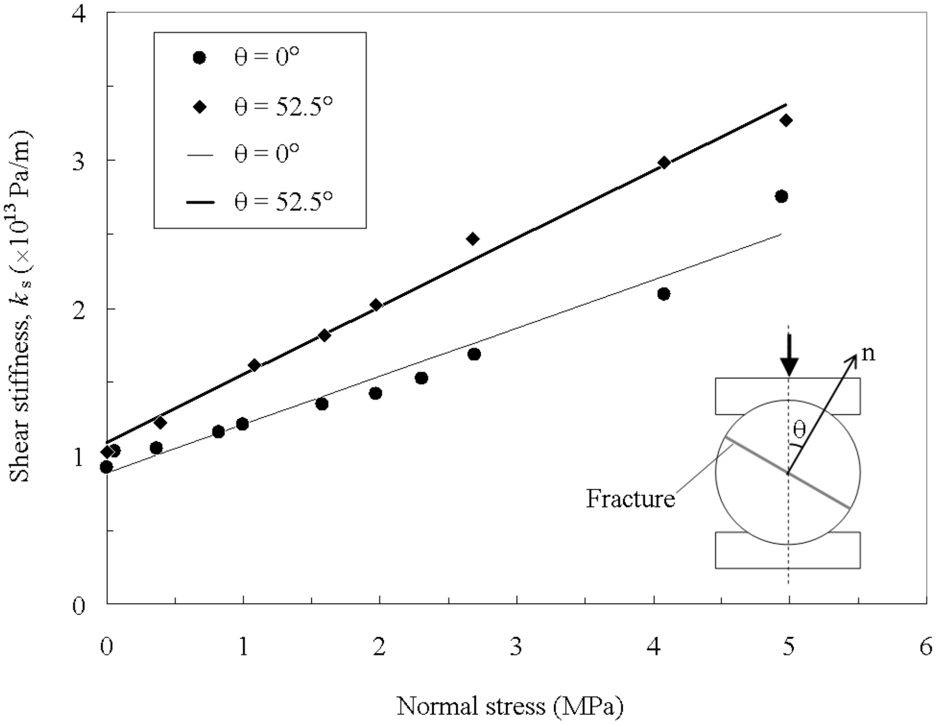

Fig. 2.12. Normal stress dependency of shear stiffness of macroscopic fractures of oolitic limestone.

2.3.2.4. Ultrasonic wave velocity measurement and model validation for micro- and macro-fractured dry Berea sandstone cores

Figure 2.13 shows the experimental data of ultrasonic wave velocities and the best fitting curves of the proposed model. The material parameter values determined by fitting are indicated in Table 2.1. The R^2-values for the curve-fitted V_p and V_s functions are 0.991 and 0.996, respectively. The model proposed sufficiently describes the observed stress dependencies of both P- and S-wave velocities at the wide-ranging stress levels.

Table 2.1. Material parameter values of proposed model determined for the tested dry Berea sandstone core.

ρ (kg/m^3)	M_m (Pa)	G_m (Pa)	p_i' (Pa)	$s \cdot k_{ni}$ (Pa)	$s \cdot k_{si}$ (Pa)	$s \cdot k_{sn}$ (Pa)	n
2.215×10^3	5.00×10^{10}	1.75×10^{10}	1.0×10^6	1.30×10^{10}	9.24×10^9	2.66×10^9	0.618

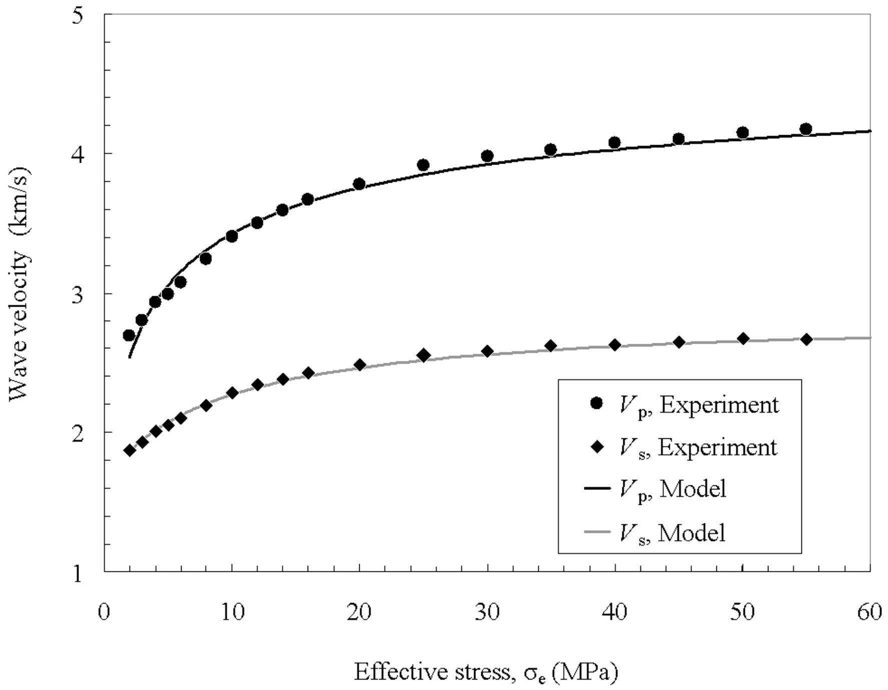

Fig. 2.13. Comparison of proposed model with experimental data of stress dependent P- and S- wave velocities.

Figure 2.14 compares the velocity ratio of P- to S-waves V_p/V_s observed by using the dry Berea sandstone core sample and that given by the proposed model. The expression is given by:

$$\frac{V_p}{V_s} = \frac{V_{pm}}{V_{sm}} \sqrt{\frac{1 + f_s^{-1}}{1 + f_n^{-1}}} \tag{2.11}$$

The observed value of V_p/V_s increases as the effective stress increase. As can be seen, the model can reproduce the observed stress dependency of V_p/V_s.

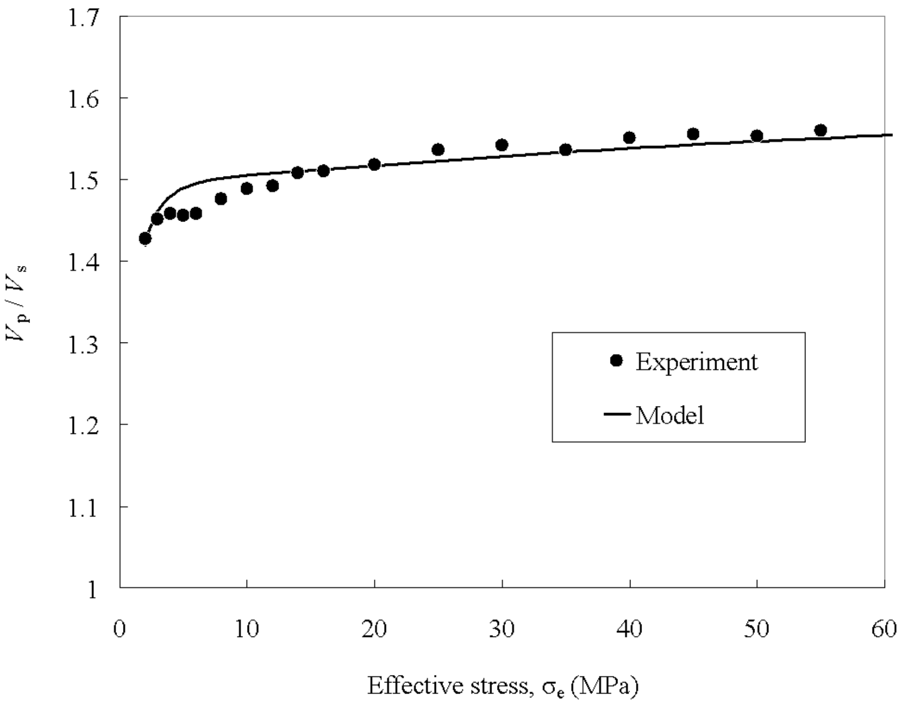

Fig. 2.14. Effective stress dependency of velocity ratio of P- to S-waves for Berea sandstone.

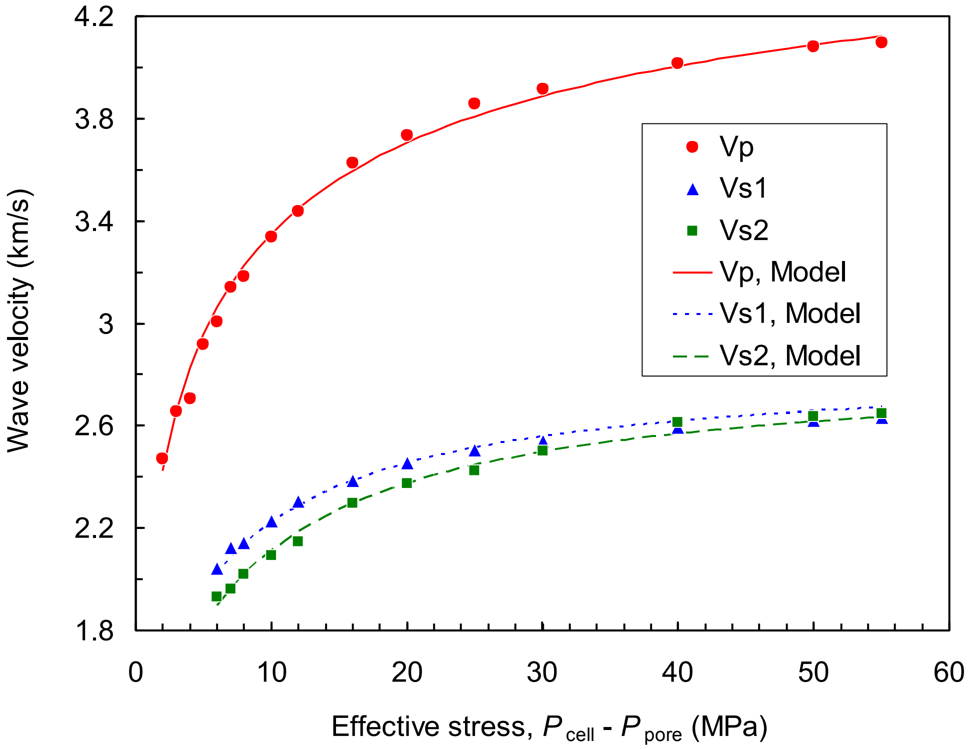

Fig. 2.15. Validity of proposed model for stress-dependent ultrasonic wave velocity response of fractured Berea sandstone core sample. V_{s1} and V_{s2} are velocities of shear waves oscillating in parallel and vertical directions of fracture surface.

The wave velocity responses of macro-fractured dry Berea sandstone sample are shown in figure 2.15. The S1-wave velocity response (V_{S1}) of macro-fractured sample is obtained by using the S-wave oscillating in the parallel direction of fracture joint surface. The P- and S1-wave velocities of fractured sample are slightly lower than those of macroscopically intact sample shown in figure 2.13 when the effective stress is lower than 12 MPa. The effects of fracture on P- and S1-wave velocities become negligible as the effective stress increases. Even at the low stress levels, the effects of fracture presence on P- and S1-wave velocities are not significant. The V_{S2} is the velocity of shear wave (S2) oscillating in the vertical direction of fracture joint surface. At effective stresses less than 40 MPa, the S2-wave velocity is smaller than that of S1-wave. The V_{S2} is approximately 94% of V_{S1} at 6 MPa of effective stress. When the effective stress is higher than 40 MPa, the presence of macroscopic fracture hardly affects the shear wave velocity response. Tables 2.2 and 2.3 show the material parameter values determined for P-, S1-, and S2-wave velocities and compare with those values determined for the macroscopically intact rock sample.

Table 2.2. Material parameter values of proposed P-wave velocity model determined for macroscopically intact and artificially-fractured dry Berea sandstone core.

	ρ (kg/m^3)	M_m (Pa)	p_i' (Pa)	$s \cdot k_{ni}$ (Pa)	n

Macro-intact	2.215×10^3	5.00×10^{10}	1.0×10^6	1.30×10^{10}	0.618
Fractured	2.17×10^3	5.00×10^{10}	1.0×10^6	1.10×10^{10}	0.635

Table 2.3. Material parameter values of proposed S-wave velocity model determined for intact and artificially-fractured dry Berea sandstone core. S1 and S2 denote the shear waves oscillating into parallel and vertical directions of fracture plane, respectively.

	ρ (kg/m^3)	G_m (Pa)	p_i' (Pa)	$s\cdot k_{si}$ (Pa)	$s\cdot k_{sn}$ (Pa)
Macro-intact	2.215×10^3	1.75×10^{10}	1.0×10^6	9.24×10^9	2.66×10^9
Fractured (S1)	2.17×10^3	1.75×10^{10}	1.0×10^6	6.04×10^9	2.40×10^9
Fractured (S2)	2.17×10^3	1.75×10^{10}	1.0×10^6	4.49×10^9	1.91×10^9

When determining the material parameter values, the macroscopically fractured rock sample is assumed to be the same with the macroscopically intact rock in terms of the longitudinal and shear moduli of no-fracture rock matrix, M_m and G_m. The other parameters characterizing the stress dependency of fracture stiffnesses were determined by curve fitting of the model.

Figure 2.15 compares the model curves with the experimentally-observed stress-dependent wave velocity responses of macroscopically fractured sample. The proposed model is demonstrated to be capable of describing the observed stress dependency of wave velocity response of macroscopically fractured rock. As shown in Table 2.2, the material parameter values characterizing stress dependency of P-wave velocity response, $s\cdot k_{ni}$ and n, are hardly dependent on the presence of single macroscopic fracture parallel to the direction of propagation of wave. Table 2.3 indicates that in the S2 direction the initial fracture modulus $s\cdot k_{ni}$ becomes lower compared to S1 direction due to the higher effect of macroscopic fracture. The lower value of $s\cdot k_{sn}$ in the S2 direction that is 1.91×10^9 Pa indicates that the S2-wave velocity more gradually increases with increasing effective stress.

2.3.3. Hydro-mechanical Characterization of Porous Reservoir Rocks at Reservoir Conditions

Laboratory studies of CO_2 injection in specimens of fractured reservoir rocks were performed under field conditions to provide input data to numerical models, and as small-scale validation models of CO_2 injection in porous/fractured rocks. The laboratory studies focused on the response of micro-fractured porous reservoir rocks under multiphase fluid pressures and flow conditions encountered in CO_2 Geological Sequestration. During testing, changes in the P&S seismic wave velocities of the fractured rock sample were monitored using seismic monitors installed at the ends of the sample. The aim was to determine whether changes in P&S wave velocities can be used to detect movements of CO_2 in fractured rock samples. In addition, the relative permeabilities of porous rock for saline water and CO_2 were determined at reservoir conditions

CO_2 injection tests were carried out on Berea sandstone core samples having 21% porosity. Carbon dioxide having 99.9999% purity was used to prepare the supercritical CO_2 ($scCO_2$). Saline water used was a mixture of distilled water and sodium chloride at 3.4% salinity. Stress dependency of the permeability of the Berea sandstone saturated with saline water was investigated at 40ºC and 10 MPa of pore pressure. The relative permeability test was carried out at 40ºC, 10 MPa of pore pressure, and 15 MPa of cell pressure. In this test, the core sample was initially saturated with saline water and subsequently $scCO_2$ was injected into the core sample at a 2.0 cm^3/min. injection rate. The effect of fluid content on ultrasonic wave velocity was tested by simulating $scCO_2$ injection into a Berea sandstone core sample saturated with saline water at 40ºC, 10 MPa of pore pressure, 40 MPa of cell pressure, and a 0.2 cm^3/min. injection rate.

2.3.3.1. Stress dependency of permeability of Berea sandstone

The effective stress tested was elevated from 1 to 10 MPa at which the permeability is supposed to be more sensitive to stress change. Figure 2.16 shows the observed permeability and P-wave velocity at different effective stresses. The P-wave velocity clearly increases as the effective stress increases. On the other hand, the stress dependency of permeability is not obvious, although it slightly decreases. The insignificant stress dependency of permeability supports the assumptions made about the fractured rock mass microstructure shown in Figure 2.9. The closure of micro-fractures due to stress increase is unlikely to have a strong influence on the permeability.

2.3.3.2. Relative permeabilities for saline water and supercritical CO_2

Figure 2.17 shows the volume of saline water produced from the core sample and differential pressure change due to CO_2 injection at 2.0 cm^3/min. The differential pressure ΔP increased from the start of injection and then reached 65 kPa when the pore volume of CO_2 injected, ($N_{CO2,inj}/N_{pore}$), is 0.53. Subsequently, it abruptly dropped to 17 kPa at ($N_{CO2,inj}/N_{pore}$) = 1.21. The production rate of saline water significantly decreased at the same time. After this largest peak in differential pressure was reached, several small peaks were observed in the ΔP−($N_{CO2,inj}/N_{pore}$) relationship.

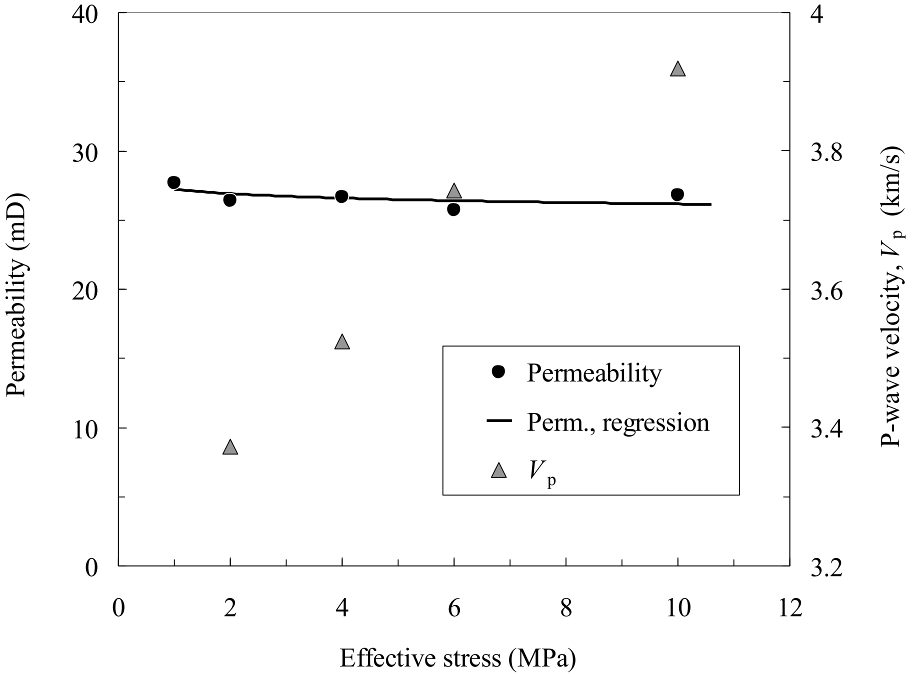

Fig. 2.16. Effective stress dependency of permeability and P-wave velocity of Berea sandstone saturated with saline water.

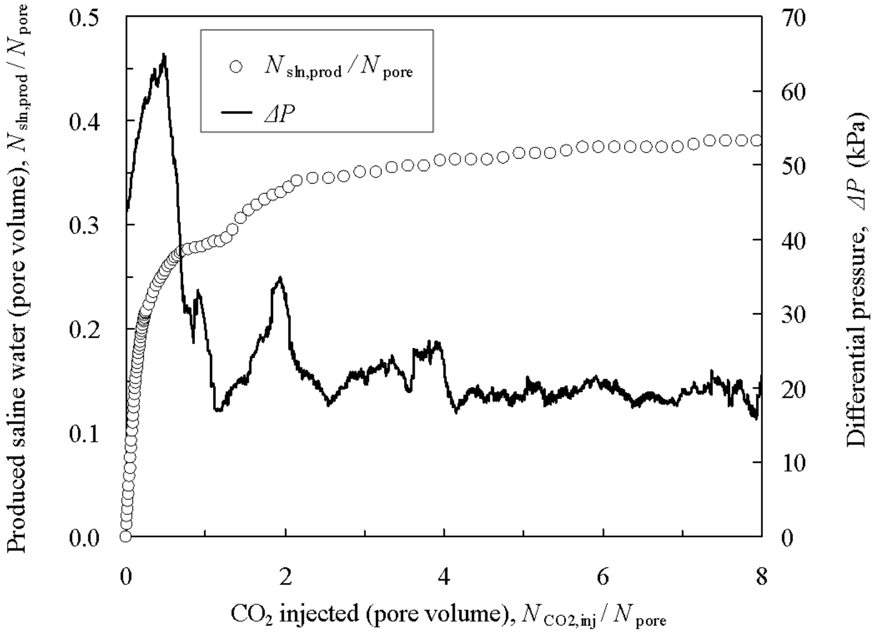

Fig. 2.17. Volume of saline water produced and differential pressure during CO_2 injection.

Figure 2.18 shows the relative permeability curves of Berea sandstone for saline water and CO_2 obtained by analyzing the data shown in figure 2.17. The CO_2 saturation at the outlet face of core sample was calculated based on the Welge's extension of the Buckley-Leverett concept. The

CO_2 saturation at the end point of displacement is 0.37. The relative permeability for CO_2 increased to 0.13 at the end point. It can be seen that dependency of relative permeability for CO_2 on CO_2 saturation is insignificant. The relative permeability for saline water is more sensitive to increase in CO_2 saturation. The relative permeability for saline water decreased to 0.16 when the CO_2 saturation is 0.15. The best fit curves of the Corey (1951)-type model to the observed relative permeabilities for CO_2 and saline water are shown in the figure. The model is defined as:

$$k_{\mathrm{r,sln}} = k^*_{\mathrm{r,sln}} \left(\frac{S_{\mathrm{sln}} - S_{\mathrm{sln,i}}}{1 - S_{\mathrm{sln,i}} - S_{\mathrm{CO2,r}}} \right)^{m_{\mathrm{sln}}} \tag{2.12}$$

$$k_{\mathrm{r,CO2}} = k^*_{\mathrm{r,CO2}} \left(\frac{1 - S_{\mathrm{sln}} - S_{\mathrm{CO2,r}}}{1 - S_{\mathrm{sln,i}} - S_{\mathrm{CO2,r}}} \right)^{m_{\mathrm{CO2}}} \tag{2.13}$$

where $k^*_{\mathrm{r,sln}}$ and $k^*_{\mathrm{r,CO2}}$ are the end-point relative permeability for saline water and CO_2, $S_{\mathrm{sln,i}}$ is the irreducible saline water saturation, $S_{\mathrm{CO2,r}}$ is the residual CO_2 saturation, and m_{sln} and m_{CO2} are empirical parameters. The values of the empirical parameters m_{sln} and m_{CO2} determined by fitting equations (2.12) and (2.13) to the experimental results are 2.5 and 1.1, respectively.

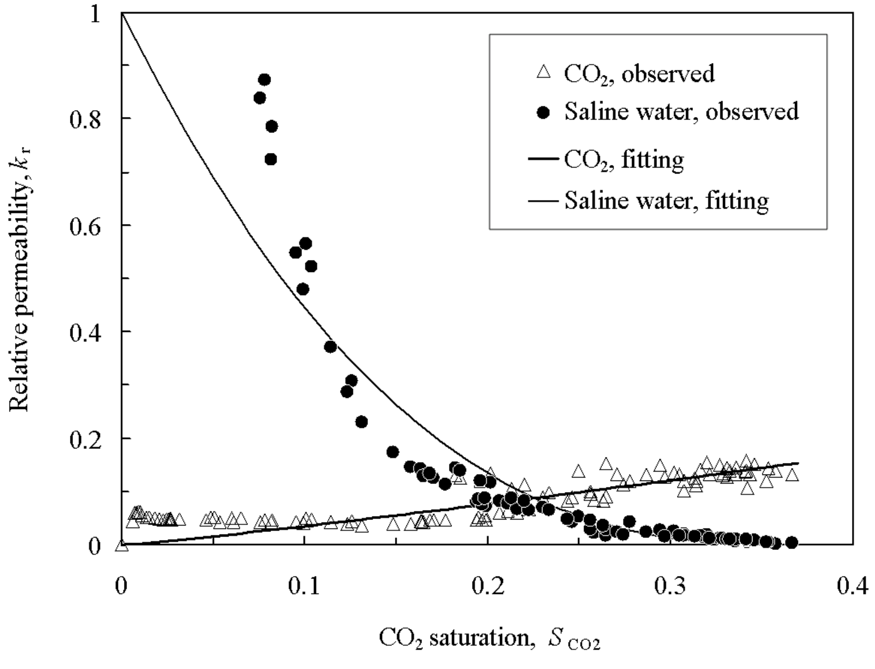

Fig. 2.18. Relative permeabilities of Berea sandstone for saline water and CO_2 at 40°C.

2.3.3.3. Fluid content effect on ultrasonic wave velocity response

Figure 2.19 shows dependency of bulk and shear moduli of Berea sandstone core sample on CO_2 saturation determined by P&S wave velocity measurement during CO_2 injection at 0.2 cm^3/min of injection rate and 40 MPa of cell pressure. It is validated that the bulk modulus of porous rock is highly sensitive to the CO_2 content compared to the shear modulus. The bulk modulus decreased from 17.5 to 13.3 GPa during the displacement of saline water. On the other hand, the shear modulus slightly increased from 12.5 to 12.7 GPa due to the increase in CO_2 saturation from 0 to 0.23.

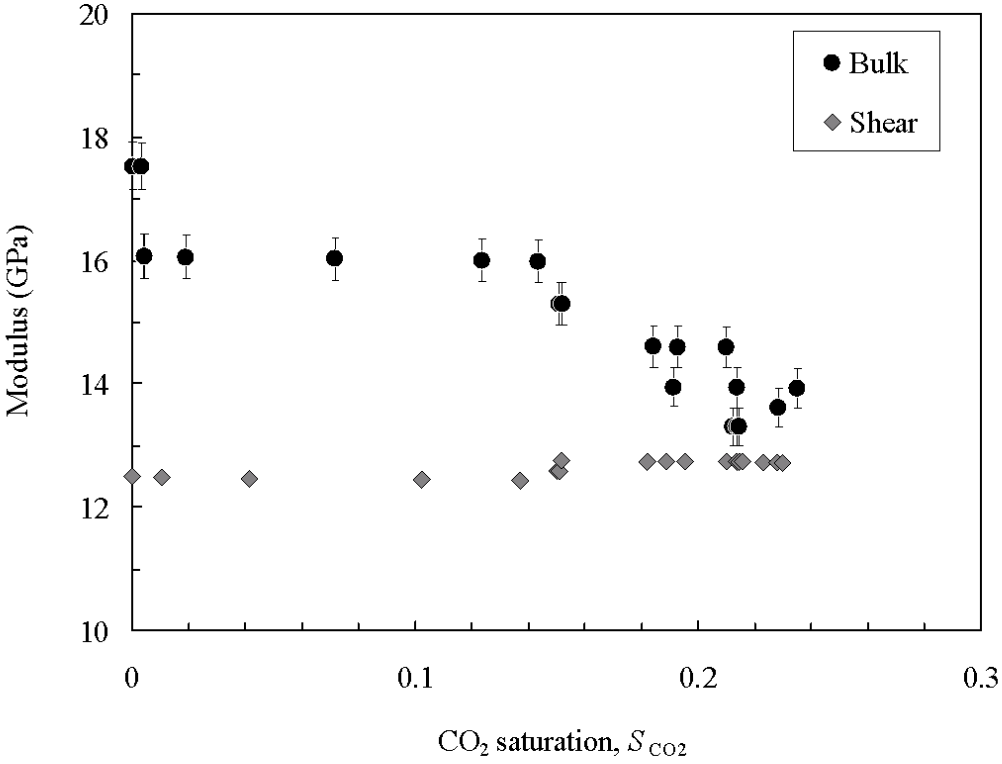

Fig. 2.19. Volume of saline water produced and differential pressure during CO_2 injection.

Figure 2.20 shows the CO_2 content effect on P-wave velocity of Berea sandstone observed during displacement of saline water by $scCO_2$. The P-wave velocity decreases as the CO_2 saturation increases. The curves shown in Figure 2.20 indicate the relationships between V_p and CO_2 saturation given by using the Gassmann's (1951) equation:

$$K_{sat} = K_{dry} + \frac{\left(1 - \frac{K_{dry}}{K_m}\right)^2}{\frac{\phi}{K_{fl}} + \frac{1-\phi}{K_m} - \frac{K_{dry}}{K_m{}^2}} \tag{2.14}$$

where K_{sat} is the saturated and undrained bulk modulus of the rock sample, K_{dry} is the rock frame or drained bulk modulus, K_m is the mineral bulk modulus (bulk modulus of the rock grains), K_{fl} is the pore fluid bulk modulus, and ϕ is the porosity. The second term of the right-hand side of Equation (2.10) represents the effect of pore fluid content on the bulk modulus K_{sat}. Equation (2.14) evaluates the effect of fluid content as the change of fluid bulk modulus, K_{fl}. To properly evaluate the effect of fluid content on P-wave velocity with equation (2.14), appropriate determination of the fluid content dependency of bulk fluid modulus is the key issue. The parallel law and Wood's (1941) law (series law) define theoretical upper and lower bounds of fluid bulk modulus described respectively in the following forms:

$$K_{\mathrm{fl}} = S_{\mathrm{sln}} K_{\mathrm{sln}} + \left(1 - S_{\mathrm{sln}}\right) K_{\mathrm{CO2}} \tag{2.15}$$

$$\frac{1}{K_{\mathrm{fl}}} = \frac{S_{\mathrm{sln}}}{K_{\mathrm{sln}}} + \frac{1 - S_{\mathrm{sln}}}{K_{\mathrm{CO2}}} \tag{2.16}$$

where S_{sln} is saturation of saline water, K_{sln} and K_{CO2} are the bulk moduli of saline water and CO_2. Neither the parallel nor Wood models provides appropriate prediction for CO_2 content effect on P-wave velocity. A much improved empirical equation to estimate the fluid bulk modulus of mixtures multiphase fluid is the following equation proposed by Brie et al. (1995):

$$K_{\mathrm{fl}} = S_{\mathrm{sln}}{}^{n} K_{\mathrm{sln}} + \left(1 - S_{\mathrm{sln}}{}^{n}\right) K_{\mathrm{CO2}} \tag{2.17}$$

where n is an empirical exponential parameter. The effect of the lower bulk modulus of $scCO_2$ phase becomes predominant at lower CO_2 saturations as the value of n increases. The best fitting curve based on Gassmann-Brie et al.'s model to the observed data is given when the value of n equals to 4.19. The value of the coefficient of regression R^2 of this fitting is 0.85.

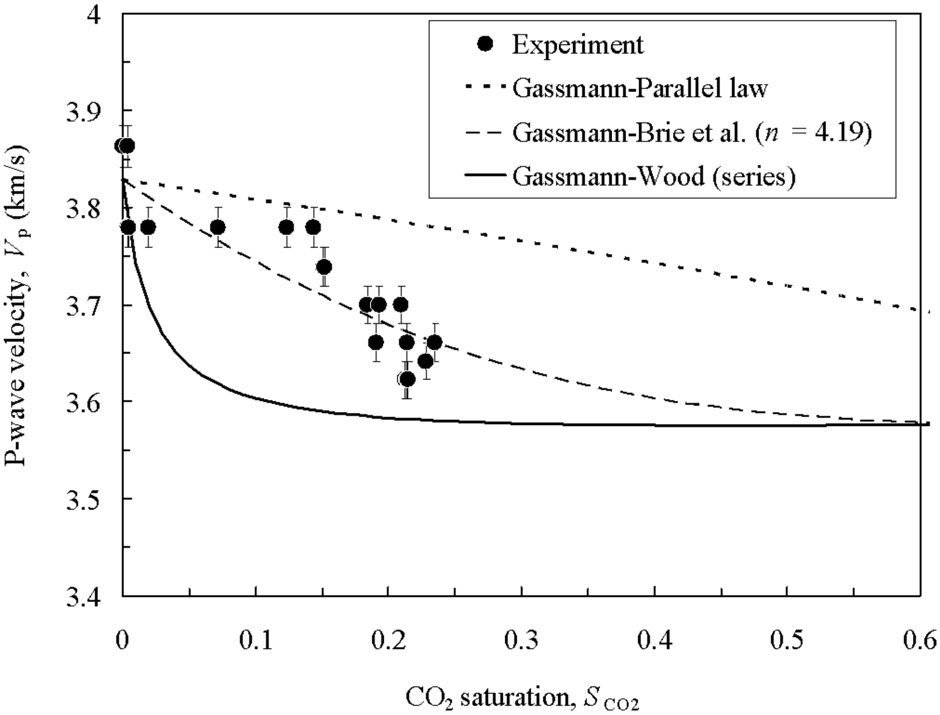

Fig. 2.20. Volume of saline water produced and differential pressure during CO_2 injection.

2.4. Task Results

The newly developed high pressure and high temperature triaxial core testing system is demonstrated to be capable of characterizing micro- and/or macro-fractured porous rock samples in terms of permeability, relative permeability, and ultrasonic wave velocity responses. The triaxial core holder can apply up to 70 MPa of cell pressures at temperatures not exceeding 150ºC. The ultrasonic wave velocity measurement devices built in the system enable us to test the ultrasonic wave response change of rock samples due to changes in CO_2 saturation and effective stress.

A model for the stress-dependent elastic wave velocity response of microscopically fractured rock mass is proposed based on experimental evidence of stress-dependent fracture normal and shear stiffnesses. Based on the visual observation of thin sections of Berea sandstone, the microstructure of rock mass body is idealized as an elastic matrix in which sufficiently small-scale fractures are distributed randomly. The normal stiffness of fractures dependent on effective stress is formulated as a generalized Goodman's model. The stress dependency of fracture shear stiffness is assumed to be given by a linear function.

The performance of proposed model has been validated by applying it to the experimental data of P- and S-wave velocity responses of dry Berea sandstone core sample at different effective stress ranging from 2 to 55 MPa. The model is capable of describing the observed stress dependencies of ultrasonic wave velocities with sufficient accuracy. Furthermore, the observed wave velocity ratio $V_\mathrm{p}/V_\mathrm{s}$ is also described by the proposed model. In addition, the proposed model is demonstrated to have capability of describing the stress dependent shear wave velocity splitting observed in the macroscopically fractured porous rock. Interestingly, the change of stress dependency due to shear wave splitting is describable by adjusting only the model material parameters characterizing stress dependency of shear fracture stiffness.

The relative permeabilities of porous rock sample for saline water and supercritical CO_2 and stress dependency of permeability were characterized at reservoir conditions. The compression wave velocity response of Berea sandstone core sample decreases with increasing CO_2 content. It is demonstrated that the dependency of compression wave velocity on CO_2 content can be evaluated by using the Gassmann's equation combined with the bulk fluid modulus model of Brie et al. (1995).

2.4. Significance and Discussion

The results presented in this report are envisioned to be useful in the use of seismic surveys for monitoring CO_2 distributions and movements in sequestration reservoirs. For accurate CO_2 content detection using a seismic survey, the study showed how seismic wave velocity responses of fractured porous rocks are affected by effective stress and fluid content changes due to CO_2 injection.

Task 3. Nanometer to micrometer scale pore network structure in fine-grained caprocks and geochemical response in high CO_2 environments

3.1. Goals/Objectives

Researchers in Task 3 studied factors related to the long-term performance of CO_2 sequestration sites. In particular, researchers sought to

- identify and characterize the impact that CO_2 injection has on mineral dissolution and porosity and permeability changes
- characterize the pore networks of five fine-grained rock samples using neutron scattering and electron microscopy techniques
- understand the geochemical response to CO_2 injection and the potential impacts on caprock integrity
- investigate the changes to nanoporosity in pore sizes typical of shale and mudstone caprocks resulting from reaction with CO_2 saturated brine under conditions relevant to CCUS in samples of the Gothic Shale and Marine Tuscaloosa Shale formations.

3.2. Background

Rock pore networks carry reactive fluids to surfaces of minerals. The pore network is a dynamic interface between minerals and pores that, through geochemical reactions, changes the physical properties of the rock. As the surface advances or retreats with mineral precipitation or dissolution, the volume of pores (or porosity), connectivity of pores, surface area, and surface roughness may change (Navarre-Sitchler et al., 2008; Navarre-Sitchler et al., 2009). Understanding these changes is important for prediction of pore-scale processes that control transport and mineral-weathering rates, as well as reaction mechanisms. Despite the importance of the pore network on many fundamental transport phenomena, the physical characteristics of pore networks in rocks are poorly understood, in part due to their dynamic nature and features at different length scales.

Characterization of pore networks in fine-grained rocks, such as shales and mudstones that serve as caprocks for Carbon Capture, Use and Storage (CCUS) storage formations, is especially difficult. These flow barriers contain small pore throats and water-wet pores that prevent the upward movement of carbon dioxide (CO_2) due to high capillary pressures and low permeabilities (Baines and Worden, 2004, Al-Bazali et al., 2005). These rocks have numerous pores in the micron to nanometer (nm) length scales that require advanced techniques for quantification and characterization (Heath et al., 2011). Increasingly, these rocks are of interest because they are sources of hydrocarbon energy and play an important role in the containment of waste fluids in the subsurface. Small angle neutron scattering (SANS) provides statistical data on the topology and architecture of pore networks (Mildner et al., 1986; Anovitz et al., 2009; Jin et al., 2011). When SANS is combined with high-resolution imaging, gas sorption, and other techniques, a full characterization of the multi-scale and often irregular pore system is possible. Here we characterize pore networks of five fine-grained rock samples using neutron scattering and electron microscopy techniques. This information is compared to data from Heath et al. (2011) who previously reported on these samples, which represent continental to marine mudstone caprocks at CO_2 sequestration sites.

Over long time scales, the dissolution of CO_2 into pore fluids of caprock formations may create carbonic acid (equations 3.1 through 3.3), reduce pH, and induce a state of geochemical disequilibrium. Resulting mineral dissolution and precipitation may alter the shape and size of small pores and pore throats, thus changing the structure of the pore network and impacting effective porosity, surface area, and pore size distribution. To predict long-term performance of CO_2 sequestration sites we need to not only understand the distribution and connectivity of pores in caprocks but also their geochemical response to CO_2 injection and the potential impacts on caprock integrity.

$$CO_2(aq) + H_2O \leftrightarrow H_2CO_3(aq) \tag{3.1}$$

$$H_2CO_3(aq) \leftrightarrow H^+ + HCO_3^- \tag{3.2}$$

$$HCO_3^- \leftrightarrow H^+ + CO_3^{2-} \tag{3.3}$$

Past research investigated the potential precipitation and dissolution reactions to caprocks under theoretical geologic carbon sequestration conditions with the use of laboratory experiments. Precipitation of different minerals including iron carbonate, illite, and smectites and dissolution of calcite, quartz, illite/smectite, and chlorite have all been observed in these experiments (Andreani et al., 2008, Carroll et al., 2011, Lima et al., 2011, Kaszuba et al., 2005). The specific geochemical response is influenced by chemical parameters such as the ratio of CO_2/H_2O in the reactive fluid of batch experiments (Kohler et al., 2009) or by physical parameters such as the fracture aperture in core experiments (Ellis et al., 2011). This previous work highlights the need to understand controlling processes to be able to evaluate natural systems where temperature/pressure conditions, brine chemistry, caprock mineralogy and pore networks vary.

Geochemical reactions in caprocks may potentially impact porosity and permeability of the formation (DOE, 2007) and recent research has focused on the integration of reaction experiments with porosity/permeability studies. In one study reaction with CO_2 decreased porosity in limestone and dolomite samples but led to contrasting changes in capillary diameter between the two rock types (Tarkowski and Wdowin, 2011). In other research on caprocks, the final porosity after reaction with CO_2 was dependent on the initial porosity (%) and hydraulic conductivity (m/s) of the samples (Labus and Bujok, 2011). Here we investigate changes to nanoporosity, in pore sizes typical of shale and mudstone caprocks, resulting from reaction with CO_2 saturated brine under conditions relevant to CCUS in samples of the Gothic Shale and Marine Tuscaloosa Shale formations.

3.3. Methods/Approach

3.3.1. Sample Selection

Samples were acquired from colleagues at Sandia National Laboratory and come from cores of 3 different CCUS pilot or demonstration site caprocks. These samples were previously studied by Heath et al., (2011) and detailed descriptions of the samples beyond the data provided here can be found in that publication. The five samples studied are from the Upper Kirtland Formation (2050 feet (’) below the surface), the Lower Kirtland Formation (2693’ below the surface), the Lower Tuscaloosa (~ 8590’ below the surface), the Marine Tuscaloosa (7925–7930’ below the surface, and the Gothic Shale (~ 5390’ below the surface). The samples represent a gradient in depositional setting from continental overbank flood deposits of the Upper Kirtland to the marine muds of the Gothic Shale. The total organic carbon (TOC) increases from ~ 0.1 weight % in the Upper Kirtland to 4.4 weight % in the Gothic Shale (Table 3.1).

Table 3.1. Summary of porosity and surface area results

Sample	SANS Porosity, volume % (1-6 nm)	FIB-SEM porosity[§], volume%	SANS Effective porosity, volume % (Hg breakthrough pressure)[+] [§]	MIP porosity[§], volume %	SANS Surface area, $m^2 g^{-1}$	Organic Carbon[§] %
UK 2050	2	6.3 - 9.9	(1)	3.2	8.5	0.06-0.13
LK 2693	3.4	6.5 - 6.7	(~50)	2.8	18.6	0.06-0.27
LT 8590.9		8.5 - 9	(29)	3.2	41.0	1.06-1.23
LT 8590	5.7		(66)	2.0	37.0	
MT 7925		2.2 - 9.9	(56)	1.9	63.8	0.56-0.73
MT 7931	7.3		(66)	2.4	65.6	
GS5390	5.1	2.7 - 4.3[++]	(~105)[++]	3.2	32.9	2.2-4.4
GS5391				0.5	87	

[+] HG breakthrough pressure is supposed to correlate with pore connectivity

[++] Measured at 5390.8’

[§] Reported in Heath et al. (2011)

Clays are a dominant component in the mineralogy of all the samples with up to 10% carbonate minerals and trace amounts of quartz and feldspars. The Gothic Shale (at 5390’ below the surface) from the Desert Creek Aneth Unit Enhanced Oil Recovery (EOR) Sequestration Project (Southwest Regional Partnership) and the Marine Tuscaloosa Shale (at 7925.5’ below the surface) from the Plant Daniel Mississippi Saline Reservoir CO_2 injection project (Southeast Carbon Sequestration Regional Partnership) were chosen for the laboratory reaction experiments.

The Pennsylvanian Gothic Shale (Fig. 3.1A) is a carbonate mudstone containing minor silt-sized quartz, calcite, dolomite and mica in a clay matrix with authigenic pyrite. Porosity of the shale ranges from 2.7 to 4.3%, permeability ranges from 1.3×10^{-19} to 1.4×10^{-19} m^2, and TOC ranges from 2.2 to 4.4 weight percent (Heath et al., 2011). Kerogen present in the shale is of type II and mixed type II-III (Heath et al., 2011). Porosity primarily appears to be located within or adjacent to organic matter with slit-like small pore throats and pore bodies that are not well connected (Heath et al., 2011).

The Cretaceous Marine Tuscaloosa Shale (Fig. 3.1B) is a silica-rich mudstone containing quartz, micas, feldspars and clays of chlorite, kaolinite, and illite with approximately 5 weight percent calcite (Heath et al., 2011). Porosity of this sample is ~2.2%, permeability is ~ 1×10^{-19} m^2, and TOC is 0.73 weight percent. Kerogen in the sample is of low maturity and contains mixed type II-III kerogen. The Marine Tuscaloosa is more porous and less homogeneous than the Gothic shale containing circular/tabular pores and concentrated organics.

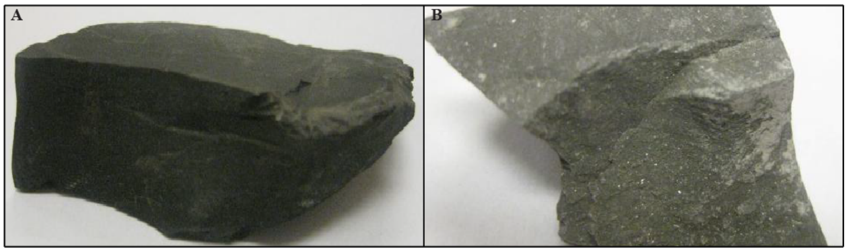

Fig. 3.1. Hand samples of A) Gothic Shale at 5390' and B) Marine Tuscaloosa Shale at 7925.5' obtained from cores.

3.3.2. Neutron Scattering

Neutron scattering has proven useful for analyzing and understanding pore networks in shales at nanometer length scales (Mildner et al., 1986; Jin et al., 2011). Here we compare results from neutron scattering with other traditional methods used to study shale pore networks (high-resolution imaging, mercury porosimetry, and gas-sorption experiments). All of these techniques provide different "views" of the pore network and when combined with detailed chemical and mineralogical studies can be used to explain how the pore structure relates to the lithologic framework of the rock.

Neutrons effectively scatter from interfaces or particles of differing neutron scattering length density(SLD) quantified as ρ^*. The ρ^* ($Å^{-2}$) of a given phase is a function (equation 4) of the chemistry and material density.

$$\rho^* = \prod_{i=1}^{N} b_i \frac{\rho_j N_A}{M_i} \tag{3.4}$$

Here, b_i is the bound coherent scattering length of atom *i*, N is the total number of atoms of mass density, and ρ_j is the mass density. M_i is the molar mass, and $N_A = 6.023 * 10^{23}$ is Avogadro's number. Values of ρ for minerals present in the shales were calculated using the NIST online calculator[1]. In rocks, minerals often have very similar SLD, on the order of 10^{-6} $Å^{-2}$ (Radlinski, 2006), but pores have a SLD of zero. Thus, rocks can be treated as a 2-phase system, minerals + pores, for SANS data analysis (Radlinski, 2006; Anovitz et al., 2009; Jin et al., 2011). Mudrocks often have significant amounts of kerogen (organic matter insoluble in aqueous alkaline or organic solvents (Anders, 1991)), as indicated by total organic carbon up to 20% or more in some formations. Kero-

---

[1] http://www.ncnr.nist.gov/resources/sldcalc.html

gen is separated into 3 types based on the C:H:O ratios. However, rarely is the chemical composition of kerogen measured. In practice, the type of kerogen is determined from the Hydrogen Index (HI) and Oxygen Index (OI). Kerogen types I and II are more hydrogen-rich and oxygen-poor. These kerogens tend to produce oil upon maturation. In contrast, type III kerogens, hydrogen-poor and oxygen-rich, tend to produce gas (Anders, 1991). Plays involving the Gothic Shale, Fruitland Formation and Tuscaloosa Formation all produce gas, suggesting the kerogens in these formations are type III, although the kerogen in the Marine Tuscaloosa has been reported as mixed type II – III (Heath et al., 2011). ρ^* of kerogen decreases with increasing hydrogen concentration and decreasing density. ρ^* for type III kerogens ranges from 3.4x10^{-6} Å $^{-2}$ for kerogen composition of H/C = 0.5 and O/C = 0.3 with density of 1.5 g cm^{-3} to 1.4x10^{-6} Å $^{-2}$ for compositions of H/C = 1 and O/C = 0.1 and density of 1 g cm^{-3}. These kerogen ρ^* values are similar to ρ^* values of the minerals found in shale samples (Table 3.2).

Table 3.2. Scattering Length Densities for Minerals present in Shale Samples

Mineral	Neutron SLD [A-2]
Quartz	4.14e-6
Albite	3.97e-6
Anorthite	3.93e-6
Biotite (Mg rich)	4.01e-6
Biotite (Fe rich)	4.18e-6
Chamosite (Fe rich)	3.22e-6
Chamosite (Mg rich)	3.48e-6
Kaolinite	3.5e-6
KFe2Si4O10 (illite – iron rich)	2.67e-6
Illite- Mg rich	2.82e-6
Calcite	4.69e-6
Montomorillite	2.85e-6
Pyrite	3.81e-6
Dolomite	5.88e-6
Water	-2.23e-5
Empty Pores	0
NaCl	2.95e-6

Thus, neutrons do not scatter significantly from interfaces between kerogen and minerals in the samples studied here and the two-phase approximation was used for data analysis (Radlinski et al., 1996). For a two-phase system, the intensity of scattered neutrons is a function (equation 3.5) of the square of scattering length density contrast between two materials $\left(\Delta\rho^*\right)$ and the volume of scattering particles, or porosity in rocks (ϕ).

$$I(Q) = 4\pi\left(\Delta\rho^*\right)^2 \phi(1-\phi)F(Q) \tag{3.5}$$

Neutron scattering analyses of rocks are often performed on thick sections (150 mm to 1 mm) cut from intact rock (e.g., Anovitz et al., 2009). However, mudstones often exhibit anisotropic scattering of neutrons related to preferential pore orientation, which complicates the data analysis. Therefore, the mudstones were broken into small chips and placed into a 1 mm quartz cuvette to randomize the pore orientation and minimize multiple scattering. Great care was taken to minimize space between the chips after packing of the cuvette. Scattering data were collected from samples dried at ambient temperature and relative humidity and immersed in contrast-matched fluid to investigate the pore connectivity. Neutrons dominantly scatter from unconnected pores in a contrast-matched sample, and connectivity was assessed by comparison of scattering from the dry and fluid immersed samples. The contrast-matched fluid was comprised of a mixture of H_2O and D_2O to produce a fluid scattering length density of 4.3×10^{-6} Å $^{-2}$.

The samples were analyzed on the CG-2 and CG-3 small-angle neutron scattering (SANS) beamlines at the High Flux Ionization Rector (HFIR) at Oak Ridge National Laboratory. On CG-2 the intensity of scattered neutrons was measured at sample to detector distances of 1.2, 8.9, and 18.4 m with a 2-Dimensional (2D) position-sensitive detector with 1 m^2 active area. Variable wavelengths of neutrons were used to obtain a broad Q-range (4.75 Å at detector distances of 1.2 and 8.9 m and 6 Å at detector distance of 18.4 m). On CG-3 the intensity of scatter neutrons was measured at sample to detector distances of 0.3, 6, and 14.5 m with a 2D position-sensitive detector with 1 m^2 active area. Variable wavelengths of neutrons were used to obtain a broad Q-range (l = 6 Å at detector distances of 0.3 and 6 m and l =18 Å at detector distance of 14.5 m) The resulting Q range measured provided information on features ranging from ~ 0.5 to 700 nm $\left(d \approx \frac{2\pi}{Q}\right)$.

3.3.3. SANS Data Reduction

Scattering intensity ($I(Q)$, cm^{-2}) was radially averaged using vycor standards and packing factors for all samples and plotted as a function of Q (scattering vector, Å^{-1}) on a log-log plot. Hydrogen in the sample produced incoherent scattering at all Q values. The $I(Q)$ contribution from incoherent scattering was estimated by fitting a power law (equation 3.6) to the long tale of constant intensity at high Q (c in equation 3.6) and subtracted from the intensity at all Q values.

$$I(Q) = aQ^{-m} + c \tag{3.6}$$

The incoherent corrected scattering data were fit to a hard sphere model using the histogram routine in the software program PRINSAS (Hinde, 2004). The specific surface area, porosity, and pore size distribution were calculated from the pore size distribution resulting from the model fit.

The incoherent corrected scattering data were plotted on Porod plots (log $I(Q)*Q^4$ vs. log Q) to enhance differences in the power law dependence of $I(Q)$ on Q (the apparent slope of the data on a scattering diagram). Scattering data from linear regions over > 1 order of magnitude in Q identified on the Porod diagrams were fit with a power law (equation 3.7).

$$I(Q) = aQ^{-m} \tag{3.7}$$

The resulting power (or apparent slope, m) was used to calculate the fractal dimension (equations 3.8a and 3.8b). Where $2 < m < 3$ corresponds to a mass fractal dimension, D_m, and $3 < m < 4$ corresponds to a surface fractal dimension, D_s, and:

$$D_m = m \qquad (3.8a)$$

$$D_s = 6 - m \qquad (3.8b)$$

3.3.4. Imaging and Gas Adsorption

Images of the shale were collected on a JEOL Ltd. JSM-7000F field emission scanning electron microscope (FESEM) with an EDAX Genesis Energy Dispersive X-Ray (EDAX) Spectrometer at the Colorado School of Mines. The shale chips were mounted on JEOL Ltd. JSM-840 12.5 mm diameter, 10 mm tall aluminum stubs with liquid carbon dag and vacuum sputter gold coated to reduce charging of the surface. Electron backscatter images were collected using a TSL Electron Backscatter Diffraction Detector. Over 400 images (magnifications from 10 to 50,000x) were collected during 43 hours of FESEM time under an accelerating voltage of 5 to 10 kilovolts (kV). FESEM allowed for imaging of the pore network and identification of the precipitation and dissolution reactions with EDAX point and plot maps.

N_2-adsorption experiments were performed on de-gassed samples at -197.26°C on the Micromeritics ASAP 2020 surface area analyzer. Using ISO 9277:2010 procedures, samples were degassed at 110°C for 12 hours under a 10 μm Hg vacuum. The surface area of connected pores is calculated by applying Brunauer, Emmett, and Teller (BET) theory to the gas adsorption data. A modification of the BET method was used on the Gothic shale sample due to the high component of pores < 2 nm detected in the isotherms (Rouquerol et al., 2007). The connected pore volume and median pore size was also determined from this data.

3.3.5. Laboratory Experiments

The characteristics of reservoir brine are difficult to reproduce in a laboratory. Previous CO_2-fluid-rock experiments designed to study potential reactions have used water (Busch et al., 2009), NaCl brines (Lima et al., 2011), or synthetic brines attempting brine-rock equilibrium conditions (Ellis et al., 2011; Andreani et al., 2008; Kaszuba et al, 2005). The use of synthetic brines, especially water and NaCl, may produce artificial reactions as the fluid equilibrates with the rock. These reactions may skew results; therefore, a brine composition in equilibrium with the rock was created for each experiment using the React program of Geochemists Workbench ® (GWB) Standard 8.0 (Bethke, 2007). For the Marine Tuscaloosa brine model, the major brine components initial concentrations were approximated using well brine chemistry data from 3 locations (API wells 2303500226, 2303500228, 2310900002) near the Plant Daniel Site (30°31’48”N, 88°33’22”W) taken from the National Technology Energy Laboratory (NETL) National Brine Database (Carr et al., 2009). Gothic Shale experiments were started prior to investigating the available data in the NETL brine database. Therefore, dilute concentrations were used for the initial concentrations for the Gothic Shale brine composition models. Next, React was used to determine the conditions where the minerals pyrite, calcite, dolomite and quartz in the Gothic Shale and k-feldspar, albite, and pyrite in the Marine Tuscaloosa Shale were at equilibrium with the brine model. The resulting synthetic brines were a Ca-Na-Cl brine for the Gothic Shale and a Na-Cl brine for the Marine Tuscaloosa Shale (Table 3.3).

Table 3.3. Synthetic Brine Chemistries used in High Pressure High Temperature Experiments

Sample	SiO_2	Mg	Mn	Ca	Na	K	Ni	Cl	SO_4^{2-}	F	CO_2	pH[a]
<u>*Gothic Shale*</u>												
brine	DL	723	DL	5E4	4E3	156	54	10E4	5	DL	3.52	6.14
CO_2	56	708	1.8	5E4	4E3	191	42	11E4	77	0.7	32	6.14
<u>*Marine Tuscaloosa*</u>												
brine	46	146	0.1	1E4	6E4	2650	0.3	12E4	242	0.19	12	5.5
CO_2	49	173	DL	1E4	7E4	2950	.5	14E4	249	1.3	3	5.5

[a] value at experimental temperature of 160˚C

Laboratory grade salts were mixed with de-ionized, argon deoxygenated water to create the modeled anoxic brine used in each experiment. Additionally, GWB was used to determine an appropriate experimental temperature that would accelerate reaction and ensure physical changes at laboratory time scales, without altering the expected reactions at in situ temperatures of the two sites. Based on this modeling, an experimental temperature of 160°C was chosen because all of the minerals in the samples are predicted to be in thermodynamic equilibrium with the synthetic brines with the exception of chlorite in the Marine Tuscaloosa. We were unable to find a mineral assemblage that represented the reported mineralogy of the Marine Tuscaloosa where all minerals were in equilibrium at the experimental temperature and pressure. This may be due to the use of end-member clay mineral formulas in the modeling. Additionally, the use of these end-member clay mineral formulas introduces some uncertainty in the equilibrium state of the experimental system.

CO_2-brine-shale experiments (referred to as CO_2-reacted) (45 days) and brine-shale experiments (referred to as brine-reacted) (35 days) experiments at 150 bars and 160°C were conducted in an Autoclave Engineers 300 milliliter (mL) EZE-seal stirred Hastelloy C-276 reactor (Fig. 3.2). The temperature was controlled with a thermal sleeve and pressure was controlled through injection of CO_2 or argon, a nonreactive gas used in brine-shale experiments, into the reaction vessel. Experimental temperature varied $^{+}/_{-}$ 1.9°C in both experiments and experimental pressure varied $^{+}/_{-}$ 7 bars in the CO_2 –reacted experiments and $^{+}/_{-}$ 19 bars in the brine-reacted experiments. Pressure variations were greater in the brine-reacted experiment due to the higher solubility of argon into brine.

Five grams (g) of shale (4 g chips/1 g ground) resulted in an initial brine/shale ratio of 54 in the CO_2-reacted and 58.8 in the brine-reacted experiments. The final CO_2/shale ratio was 3.4 in the Gothic experiment and 1.9 in the Marine Tuscaloosa experiment, the variation is due to more dissolution of CO_2 into the brine in the Gothic Shale experiment. Brine samples were extracted from the reactor after the first 24 hours and every 7 days subsequently to determine pH, concentrations of major and trace cations and anions, and concentrations of CO_2 and SO_2 gas in the brine. The measured pH of the extracted samples was corrected to in situ reactor pH using Geochemist's Workbench and the b-dot ion association model (Kaszuba et al., 2005). Unreacted and reacted whole-rock samples underwent digestion (Farrell et al., 1980) and were analyzed for major cation and anion concentration by inductively coupled plasma optical emission spectrometry (ICP-OES). Cations including SiO_2, Mg^{2+}, Fe^{2+}, Mn^{4+}, Ca^{2+}, Al^{3+}, Na^{+}, K^{+}, Ni^{3+} and anions including Cl^{-}, SO_4^{2-}, and F^{-} were analyzed using typical analytical tools further described in a separate article focused on the comprehensive evaluation of the analytical changes during these high temperature and pressure experiments[2].

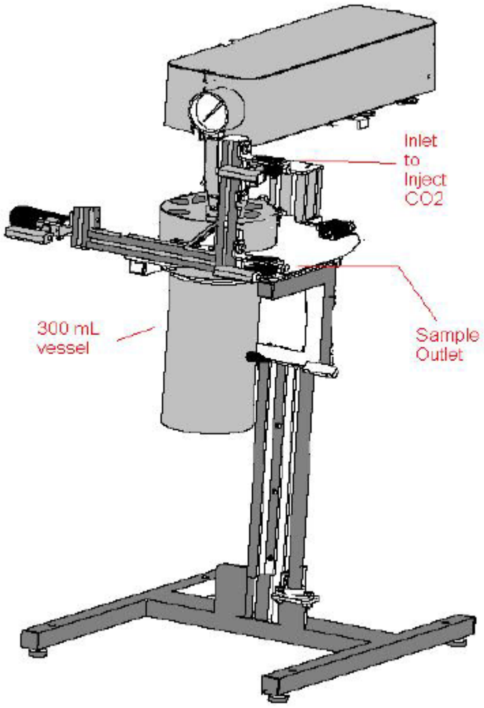

Fig. 3.2. Schematic of Autoclave Engineers 300 mL ESE-seal stirred reactor (modified from manufacturer schematics).

3.4. Task Results

3.4.1 Nanoscale Pore Structure in Mudstones

Pores were observed in the SEM images of all samples at length scales from mms to < 100 nm (Fig. 3.3). Larger pores typically exist at silt-like grain boundaries or between sheets of clay

---

[2] Wang et al. (in prep) – a paper in preparation by collaborators at University of Wyoming reporting the analysis of brine chemistry of the experiments. For information beyond the pH and whole rock chemistry, refer to this separate article.

particles. Smaller pores (< 100nm) exist at grain boundaries and within mineral grains.

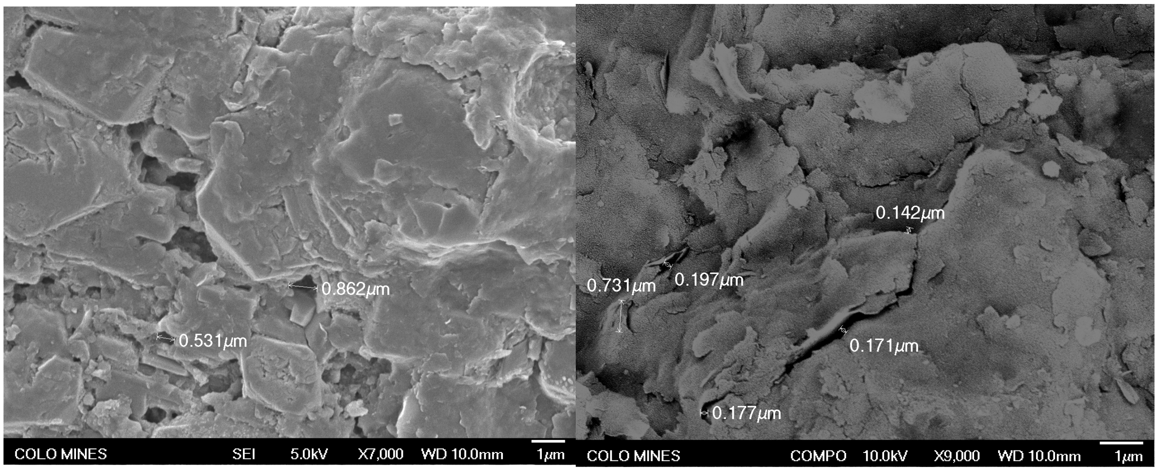

Fig. 3.3. Field emission scanning electron microscope images of the unreacted Gothic Shale (left) and Marine Tuscaloosa (right) showing pores in the hundreds of nm size range.

Much of the nm scale structure is related to surface roughness of the pore-mineral interfaces that gives rise to a fractal distribution observed in the scattering data as a power-law relationship between intensity and scattering vector (Table 3.4). A power-law relationship is observed for features > 100 nm in all samples analysed both dry and saturated with contrast-matched fluid (Figs. 3.4–3.7). In samples with low TOC (Kirtland Formation samples) a distinct population of scatters at ~ 2 nm diameter is observed that creates an intensity peak in the dry samples (Figs. 3.4, 3.5 white squares). This peak may be a structural peak related to the repeating pattern created by clay floccules or the interlayer spacing of expandable clay minerals (e.g., smectites). This hypothesis will be tested in on-going work. This peak is not apparent in the contrast-matched data for the same samples (Figs. 3.4, 3.5 black squares) suggesting that if pores between clays or interlayer spacing is the source of this scattering, the pores or interlayers are accessible to fluid diffusion. In samples of Tuscaloosa Formation and Gothic Shale (Figs. 3.5, 3.6 and 3.7) the peak at high intensity is not present. In the Gothic Shale many of the small pores appear to be associated with organic carbon (Fig. 3.7), which leads us to hypothesize that the organic carbon influences the structure of the pore network at the nm scale.

Pore size and surface area distributions determined from the scattering data illustrate the importance of small pores in the pore network (Fig. 3.8). Pores < 10 nm radius contribute 20–50% of the total porosity and > 80% of the total surface area of these mudstones (Fig. 3.8). For all samples, the pore size distribution for total and connected porosity calculated from SANS data is compared to the pore size distribution determined from mercury porosimetry provided by Heath et al. (2011) (Figs. 3.9 through 3.12). While pore size distributions from SANS provide information about the total volume of pores at a given radius, the pore size distributions from mercury porosimetry provide information about the volume of porosity accessible through a given pore throat size. However, the high pressures necessary to force the Hg through pore throats < 1 nm diameter may break the sample, introducing artifacts of the analysis into the data (Bustin et al., 2008). Therefore, the pressures are limited and Hg porosimetry only interrogates pore volume accessible through pore throats

> 1 nm diameter. While the two types of data are very different, careful comparisons of the pore size distributions from SANS and Hg porosimetry can provide information about the relative volume and accessibility of pores.

Table 3.4. Summary of Neutron Scattering Results on the CO_2-reacted and Unreacted Samples

Caprock Formation	Incoherent[b] Scattering	Fractal Behavior		% Porosity[c] (Fit Histogram)[a]	SLD (cm^{-2})	Specific Surface Area[b] (m^2/g)
Gothic Shale						
CO2-reacted	0.0868	$D_m = 2.53 \pm .016$ $D_s = 2.89 \pm .010$ $D_s = 2.68 \pm .005$	*6 to 13 nm* *15 to 30 nm* *50 to 170 nm*	5.53	$4.39e^{10}$	63.66
CO2-reacted Dup	0.0877	$D_m = 2.54 \pm .017$ $D_s = 2.90 \pm .014$ $D_s = 2.69 \pm .005$	*6 to 13 nm* *15 to 35 nm* *50 to 170 nm*	4.75	$4.39e^{10}$	60.29
Unreacted	0.10836	$D_m = 2.55 \pm .033$ $D_m = 2.98 \pm .010$ $D_s = 2.70 \pm .007$	*6 to 13 nm* *20 to 50 nm* *60 to 260 nm*	ND	$4.38e^{10}$	ND
Unreacted Dup	0.08586	$D_m = 2.59 \pm .014$ $D_s = 2.92 \pm .031$ $D_s = 2.75 \pm .006$	*7 to 13 nm* *20 to 40 nm* *90 to 260 nm*	4.47	$4.38e^{10}$	52.42
MarineTuscaloosa						
CO2-reacted	0.117025	$D_m = 2.84 \pm .004$	*7 to 230 nm*	3.36	$4.53e^{10}$	47.73
CO2-reacted Dup	0.120289	$D_m = 2.83 \pm .004$	*7 to 230 nm*	3.12	$4.53e^{10}$	43.43
Unreacted	0.12519	$D_m = 2.98 \pm .011$	*15 to 160 nm*	ND	$4.57e^{10}$	ND
Unreacted Dup	0.10873	$D_m = 2.94 \pm .003$	*15 to 240 nm*	3.26	$4.57e^{10}$	41.94

[a] determined using PRINSAS
[b] using Packing Fraction 1.6%
ND Not Determined

In all samples, we attribute differences between the SANS-measured porosities and MIP to low pore connectivity, or the inability of MIP to fully access the pore network due to pressure limitations of the method. In the Upper Kirtland Formation (Fig. 3.9), porosity from the Hg porosimetry distribution is higher than from either the total or connected SANS distributions. High porosity at the small pore radii does not equate to pores with radius < 10 nm but rather pore volume accessible through pore throats < 10 nm radii. We attribute this pore volume to pores > 1 mm in radius observed in SEM images but not interrogated in the SANS experiments (Fig. 3.9 SEM image). The Hg porosimetry and connected SANS porosity are similar for the Lower Kirtland Formation sample suggesting that nearly all of the porosity is accessible through pore throats > 1 nm diameter (Fig. 3.10). In the Tuscaloosa samples, there is a lot of pore volume in pores < 5 nm radius that appear not to be accessible through pore throats > 1 nm (Fig. 3.11). In both of the Tuscaloosa samples, the porosity accessible through pore throats > 1 nm is ~ 50% of the connected pore volume determined by SANS. In the Gothic Shale sample, the connected porosity from SANS and Hg porosimetry porosity is approximately the same (Fig. 3.12). Unlike the Lower Kirtland Formation, where the two measures of connected porosity were similar but the shapes of the curves were very different, the two curves have similar shape in the Gothic Shale, suggesting that the pore network is not limited by small pore throats like in the Lower Kirtland Formation. Total porosity determined by SANS generally increases with TOC while pore volume decreases with TOC (Fig. 3.13).

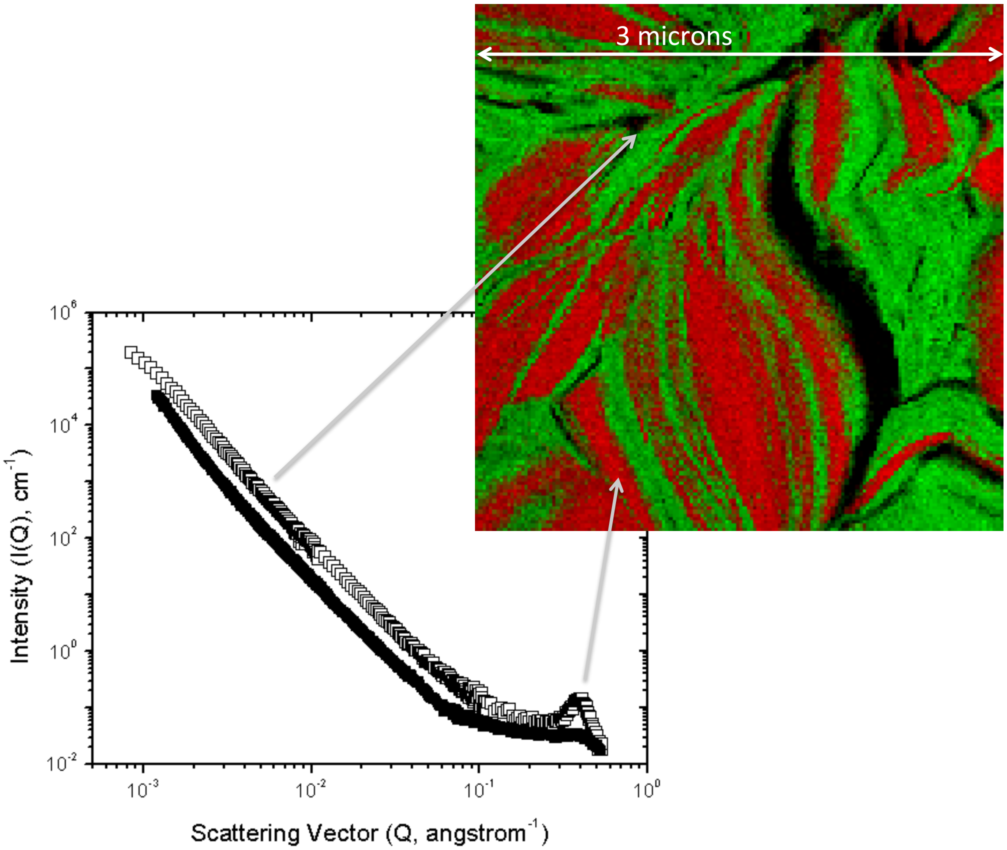

Fig. 3.4. Scattering diagram and SEM-EDS image of Upper Kirtland Formation. Power law behavior on scattering diagram indicates fractal behavior of the pore network. Red in the EDS image shows the location of iron rich clay and green shows the location of iron poor clays. These are likely interlayered smectite and illite minerals. Black shows the pore space that neutron scattering data provides information on.

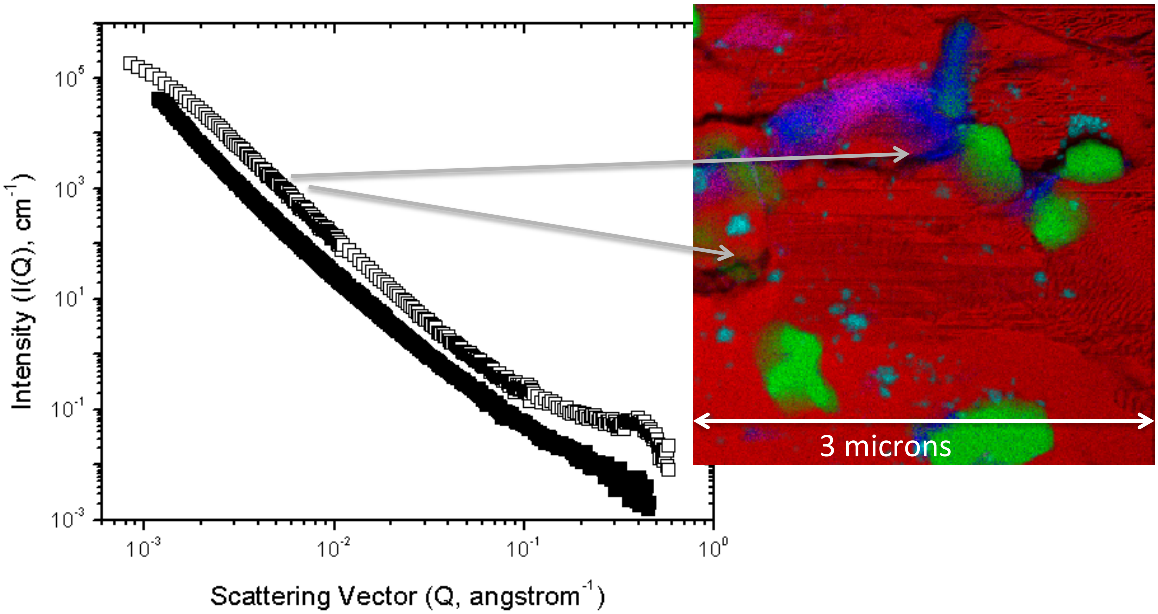

Fig. 3.5. Scattering data and SEM-EDS image for the Lower Tuscaloosa sample. Red in the EDS image indicates the location of calcite, green is Si rich phases, magenta is organic carbon and blue is Al rich phases. Arrows point to pores in the image that at the length scale that neutrons scatter from in the SANS experiments.

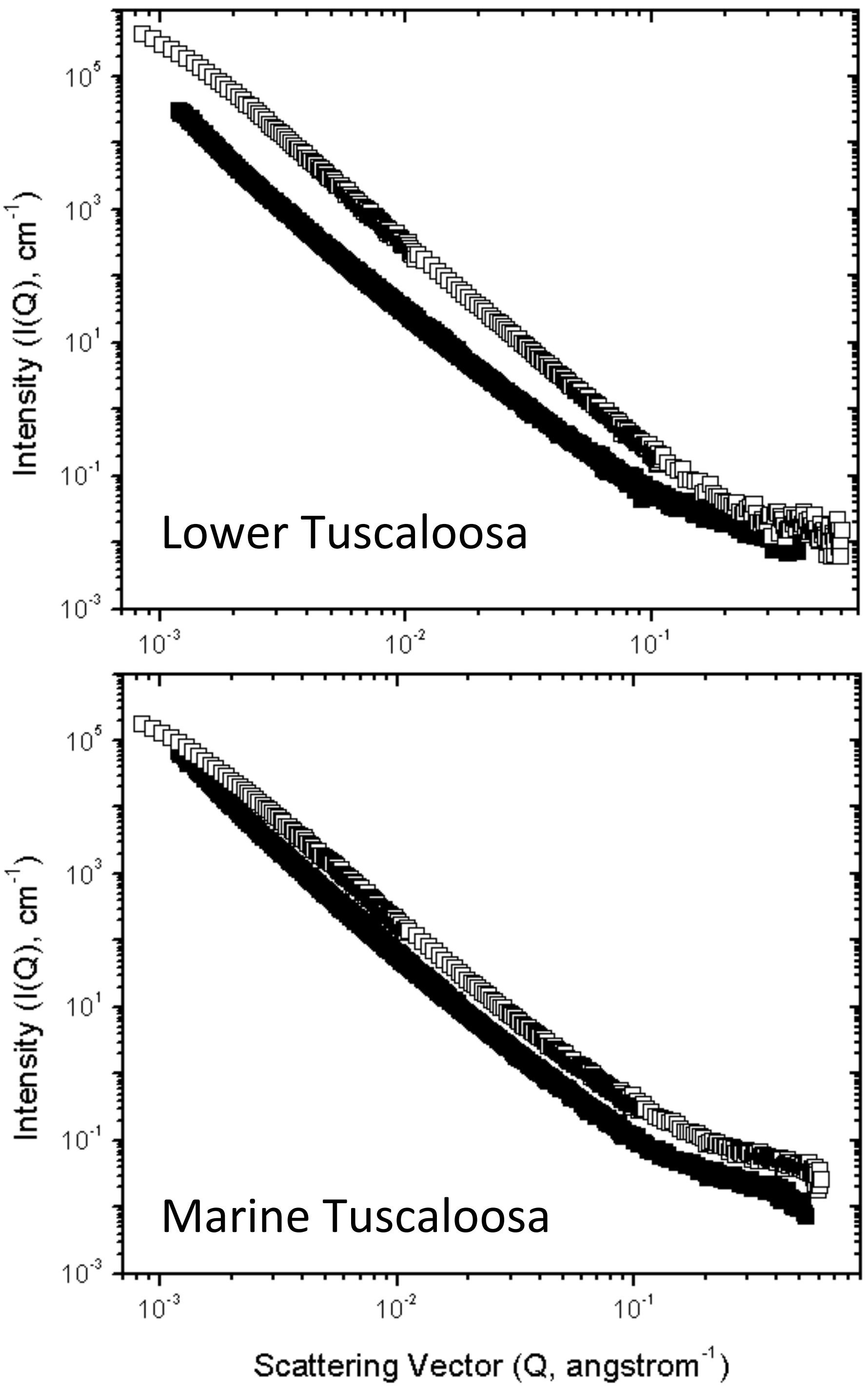

Fig. 3.6. Scattering diagrams for the Lower and Marine Tuscaloosa samples. The distinct population of scatters is not evident in these samples.

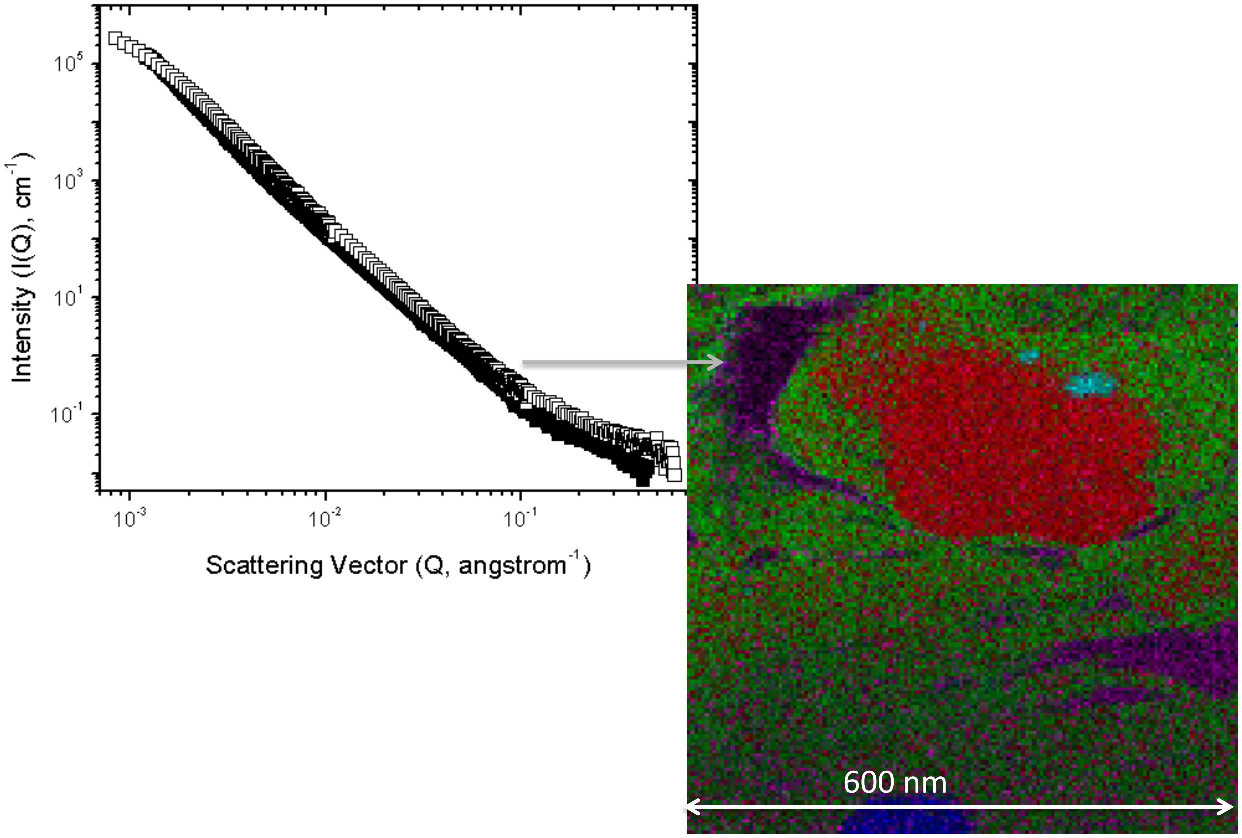

Fig. 3.7. Scattering diagram and SEM-EDS image of the Gothic Shale sample. Green is Si rich phases, red indicates Calcite and magenta is organic carbon. In the Gothic Shale many of the small pores are associated with organic carbon.

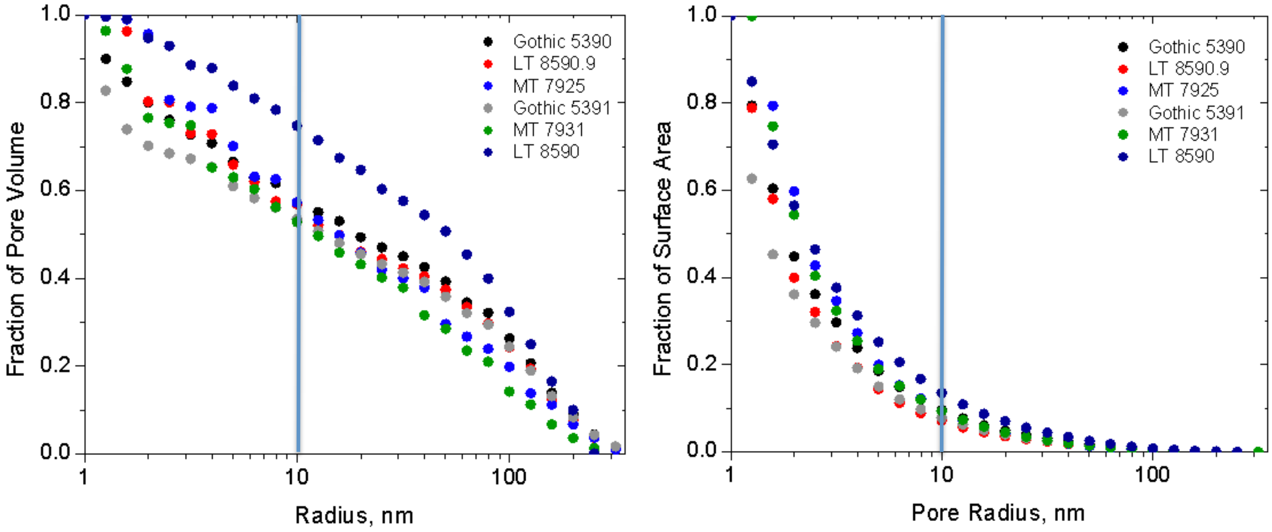

Fig. 3.8. Pore size (left) and surface are (right) distributions calculated from SANS data.

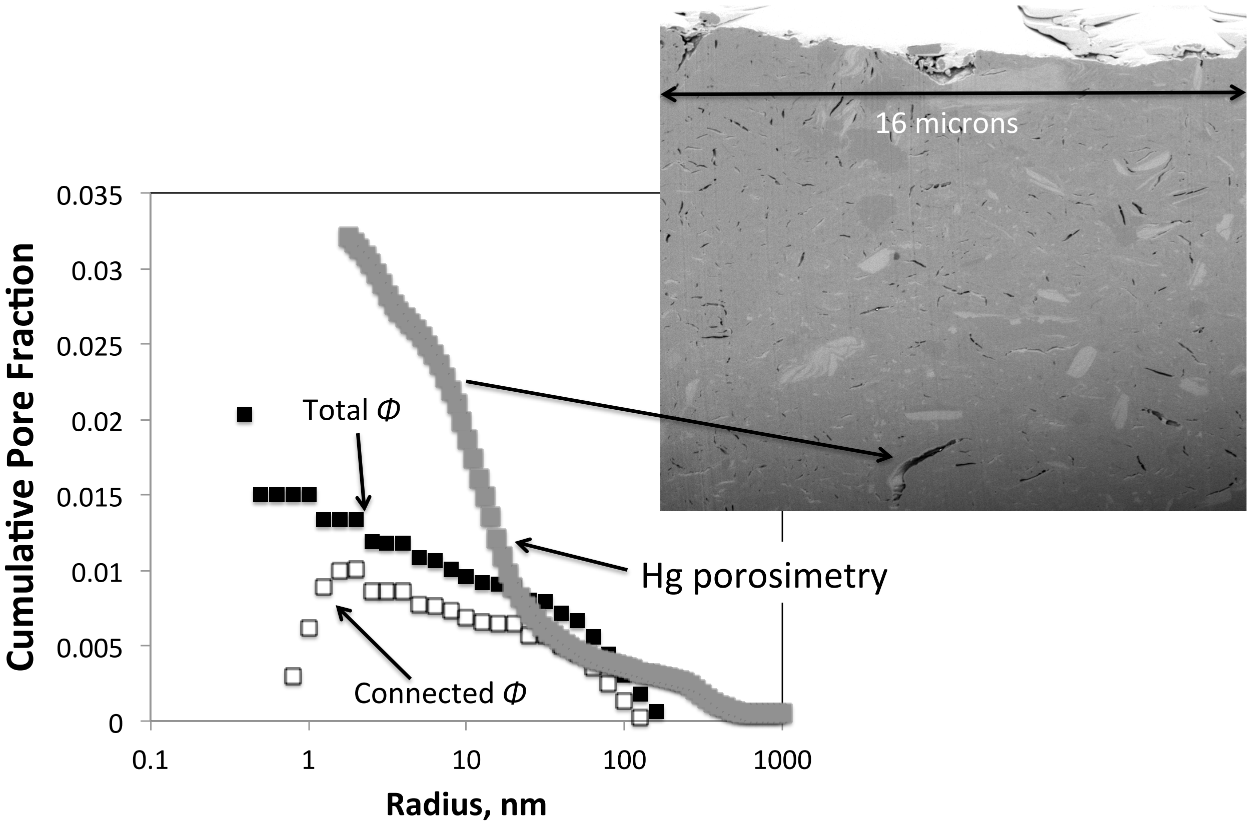

Fig. 3.9. Pore size distributions calculated from dry SANS (black squares), contrast matched SANS (white squares) and mercury porosimetry (grey squares) for the Upper Kirtland formation. The discrepancy in the total porosity calculated from porosimetry and SANS is likely related to the presence of pores larger than the length scale interrogated by SANS (black arrow).

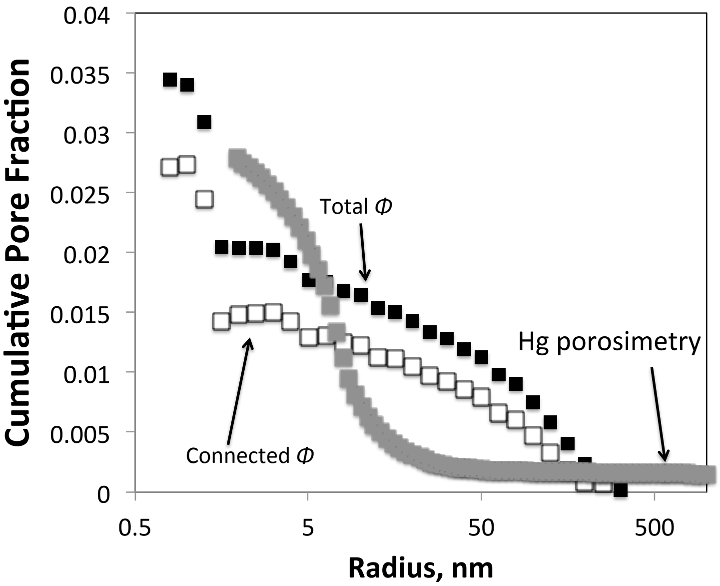

Fig. 3.10. Pore size distributions calculated from dry SANS (black squares), contrast matched SANS (white squares) and mercury porosimetry (grey squares) for the Lower Kirtland Formation.

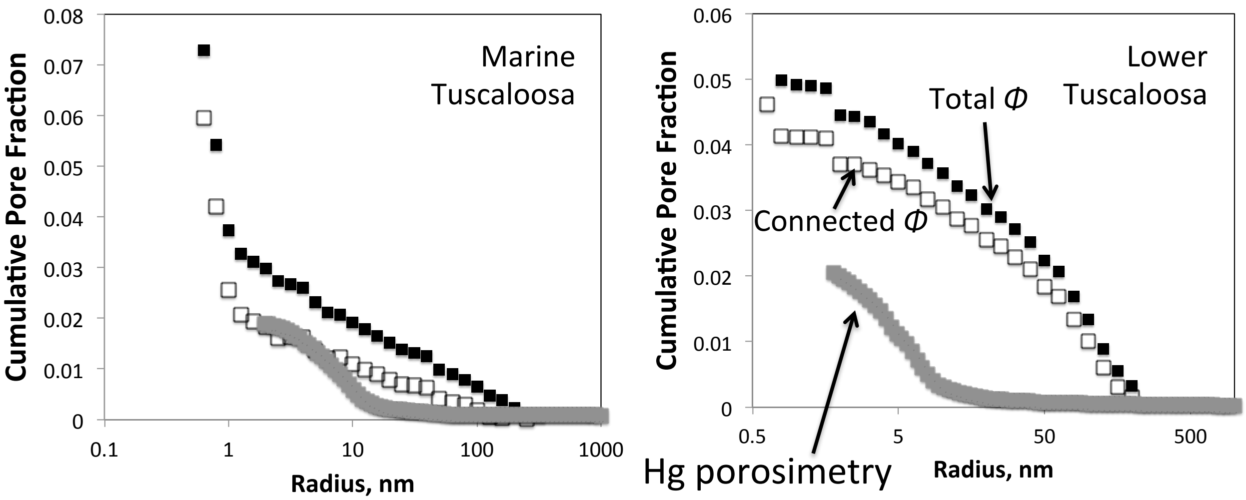

Fig. 3.11. Pore size distributions calculated from dry SANS (black squares), contrast matched SANS (white squares) and mercury porosimetry (grey squares) for the Marine (left) and Lower (right) Tuscaloosa formations. In both of these samples the mercury porosimetry analysis gives a lower estimate of the total porosity than the SANS data. This is likely due to the presence of < 1 nm pore throats that restrict the intrusion of the mercury at the pressure conditions of the analysis.

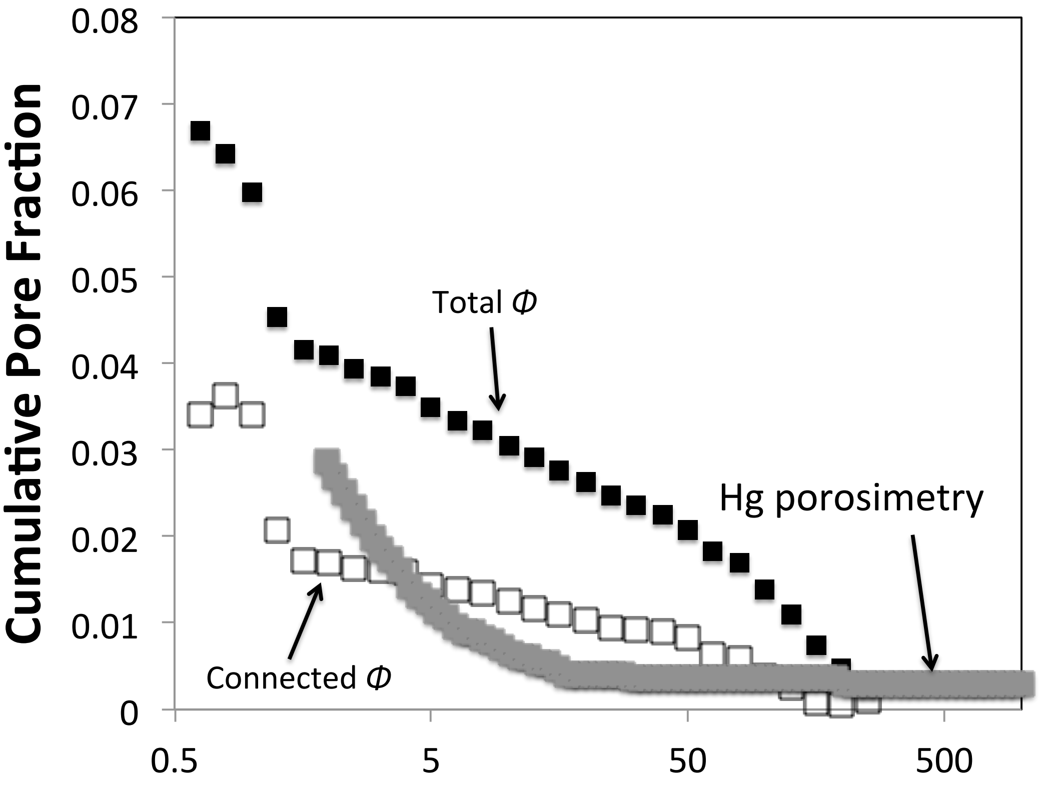

Fig. 3.12. Pore size distributions calculated from total SANS (black squares), connected SANS (white squares) and mercury porosimetry (grey squares) for the Gothic Shale. In this sample the connected porosity estimated from SANS data and mercury porosimetry is similar.

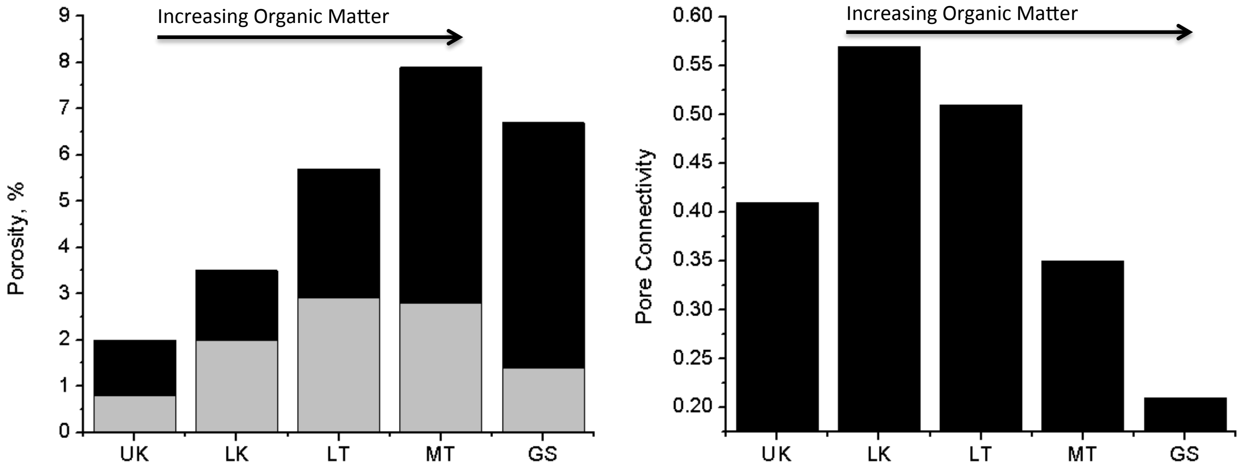

Fig. 3.13. Connected (grey) and unconnected (black) porosity in the five mudstone samples (left) and pore connectivity in the five mudstone samples (right) plotted in order of organic matter content. In the samples analyzed for this study total porosity appears to increase with the organic matter content but connectivity appears to decrease.

3.4.2. Observational Evidence of Reaction between Brine, CO_2, and Shale Minerals

Monitoring the pH variation during experiments allowed for a quantitative approach to determining reaction between brine, CO_2, and shale. Initial *in-situ* pH in the Gothic and Marine Tuscaloosa experiments was 6.1 and 5.5, respectively (Fig. 3.14). The pH decreased in the brine-reacted experiments with the Gothic stabilizing at 5.3 and the Marine Tuscaloosa stabilizing at 5.5. In the CO_2-reacted experiment, the pH reached steady state values of 3.6 and 4 for the Gothic Shale and Marine Tuscaloosa, respectively. Initially pH dropped to 3 in the Gothic Shale experiments but increased to 4 over the first ~ 600 hours of the experiment, indicating potential dissolution of carbonate minerals and buffering of the pH.

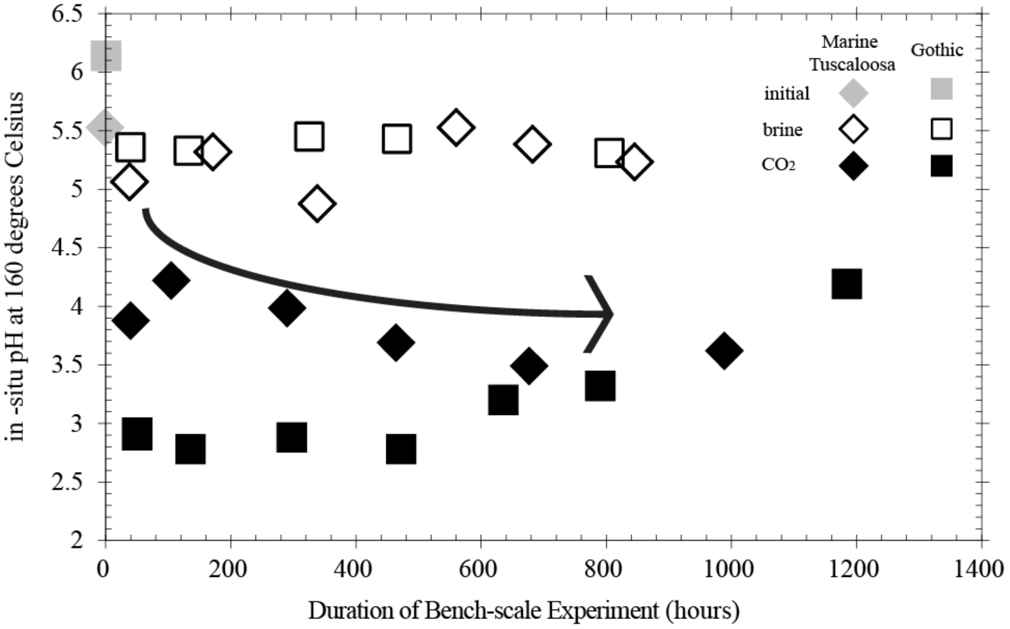

Fig. 3.14. Gothic Shale experiments started at a pH of 6.1 and Marine Tuscaloosa experiments started at a pH of 5.5. The reactions with CO_2 show an initial pH decrease of 2 in the Marine Tuscaloosa shales and an initial decrease of 3 in the Gothic Shales. The Gothic Shales show an increase in pH due to buffering in the system at ~600 hours while the Marine Tuscaloosa Shales do not show a significant amount of buffering.

Images of the unreacted Gothic Shale show slit-like and irregular inter-granular nanopores (Fig. 3.15A) and less porosity than the unreacted Marine Tuscaloosa. Unreacted Marine Tuscaloosa exhibited rougher surfaces with more nanopores and fractures (Fig. 3.15B) under the SEM. Framboidal pyrites were observed in both shales however the clusters in the Gothic samples were all ≤ 5 µm in diameter while the clusters in the Marine Tuscaloosa samples range from 5 to 10 µm in diameter. The unreacted samples contained no additional crystalline precipitates or obvious physical characteristics.

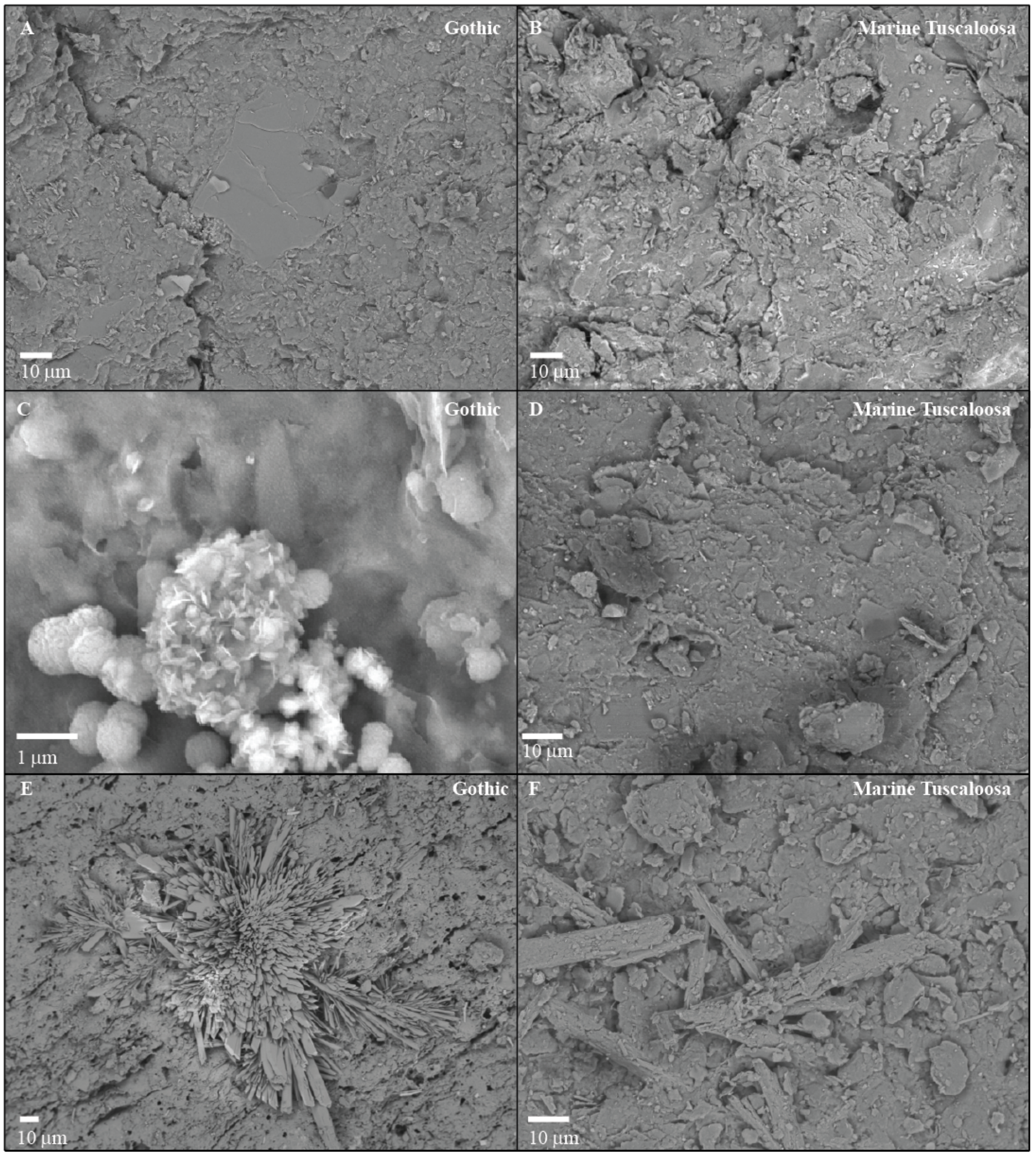

Fig. 3.15. FESEM images of unreacted, brine-reacted and CO_2-reacted samples of Gothic Shale and Marine Tuscaloosa. A) Gothic Shale consists of rough sheet surfaces that lack pores > 10 µm. B) Marine Tuscaloosa Shale has a rougher sheet surface with more pores along edges and surfaces compared to the Gothic samples. C) Gothic brine-reacted shale sample at a magnification of 14,000 illustrates the plated silicas (potentially analcime) that were observed on both Gothic and Marine Tuscaloosa samples. D) Illustration of silica precipitate size compared to CO_2-reacted precipitates in 2.F. E) Largest precipitates are bladed $CaSO_4$ rosettes found only in Gothic CO_2-reacted samples. F) Marine Tuscaloosa CO_2-reacted $CaSO_4$ blades at smaller sizes than the rosettes.

Following the CO_2-shale-brine experiments, dissolution features and crystalline precipitates were observed in SEM images of both reacted samples. In the Gothic Shale CO_2-reacted system, FE-SEM images showed dissolution features such as etching on mineral surfaces (Fig. 3.16A) and secondary precipitates of crystalline calcium sulfate rosettes and blades (Fig. 3.15E) as large as 80,000 nm (80 µm). An increase in the number and size of pores, as well as a new morphology of pores that was more circular and intra-granular, (Fig. 3.15E) was observed. Small precipitates of Fe and Ni sulfides were observed in spheres, blades, or octahedrons (Fig. 3.16C).

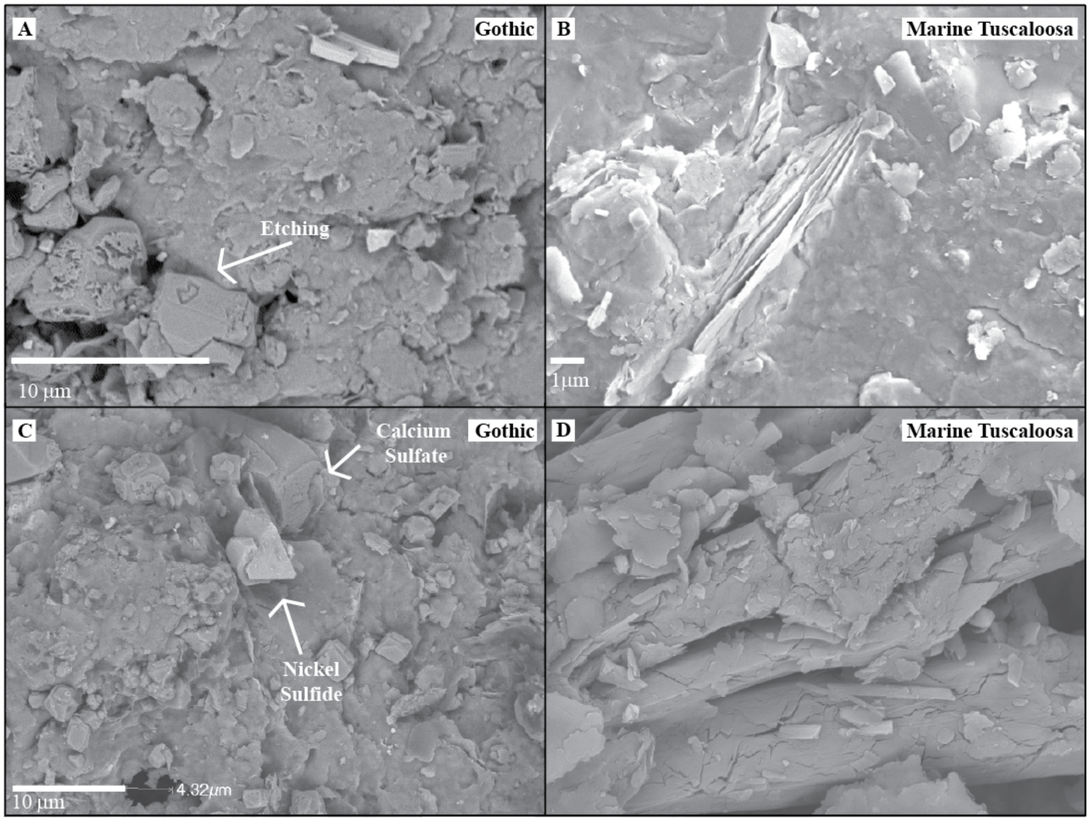

Fig. 3.16. FESEM images of A) Dissolution features of etching in Gothic Shale. B) Dissolution features include visible dissolution in between silicate sheets in Marine Tuscaloosa Shale. C) $CaSO_4$ and Nickel sulfide precipitate in the Gothic Shale CO_2-reacted sample. Pore present in lower left corner with a diameter of 4.32 µm. D) Microfractures present on $CaSO_4$ blades.

Dissolution features, typically separation of silicate sheets in the clays, were observed in SEM images of the Marine Tuscaloosa. These dissolution features tended to be smaller than those observed in the Gothic Shale samples (Fig. 3.16B). Precipitates of calcium sulfate and Fe and Ni sulfides were also observed in the Marine Tuscaloosa Shale CO_2-reacted sample. The calcium sulfate minerals were only observed as blades, no rosette morphology, and were smaller in size than in the Gothic Shale (Fig. 3.15F). Microfractures were observed on the surfaces of secondary calcium sulfate precipitates (Fig. 3.16D), potentially indicating a complex precipitation and dissolution history during the experiment as the calcium sulfate mineral saturation state changed. Although experiments were conducted in a nonreactive reactor, a nickel-bearing lubricant (LOCTITE ™) was used for the bolts of the experimental apparatus. The precipitation of Ni sulfide in both experiments, therefore, cannot be unequivocally attributed to Ni sourced from the shale and synthetic brine. High concentrations of nickel in the whole rock (Table 3.5) and brine chemistry (Wang et al, in prep) provide additional evidence of contamination of the experimental apparatus by the LOCTITE ™ lubricant.

Table 3.5. Whole Rock Chemistry

	P_2O_5	MnO	Fe_2O_3	MgO	SiO_2	Al_2O_3	CaO	TiO_2	Na_2O	K_2O	Ni[a]
Gothic Shale											
unreacted	0.58	0.03	4.15	4.24	42.4	11.4	14.4	0.51	0.68	2.49	123
Brine	0.45	0.02	4.03	2.97	40.8	7.95	12.2	0.49	0.38	2.45	1229
CO_2	0.44	0.02	3.95	3.42	44.2	11.7	14.5	0.46	0.38	2.70	369
Marine Tuscaloosa											
unreacted	0.09	0.05	5.98	1.53	56.3	24.4	0.66	1.04	0.99	3.33	42.3
Brine	0.10	0.01	5.46	1.52	53.5	22.5	0.65	1.01	0.58	2.95	1544
CO_2	0.16	0.01	4.90	1.40	60.9	23.5	0.65	0.98	0.75	3.30	1064

[a] concentration in ppm, all others in weight %

Both dissolution and precipitation features were observed on mineral surfaces in brine-reacted experiments indicating some degree of undersaturation of the synthetic brine with respect to the minerals in the shale samples. However, overall there was less evidence of reaction observed when compared to the CO_2-reacted experiments. Precipitates on brine-reacted surfaces only consisted of plated silicates (Fig. 3.15C) that were unique to these samples. The sizes of these silicate precipitates are orders of magnitude smaller than the precipitates seen in the CO_2-reacted samples (Fig. 3.15D). Observed changes in the brine-reacted samples in an experimental design where great care was taken to limit the degree of chemical disequilibrium due to synthetic brine highlight the difficulty of simulating reservoir geochemical conditions in laboratory experiments.

In summary, FE-SEM images combined with EDAX plot and point maps provide evidence of dissolution and precipitation reactions in all experiments, with more evidence of reaction in CO_2-reacted experiments, especially the Gothic Shale, than brine-reacted experiments. The increased evidence of reactivity in the Gothic shale experiment may be attributed to a period of initial intense reaction (pH ~ 3, Fig. 3.14) followed by carbonate dissolution and buffering of pH creating rapidly changing geochemical conditions that induce both dissolution and precipitation simultaneously. Given the observational evidence of less reaction in the brine-reacted samples, we conclude that reaction between CO_2, brine, and minerals in the shale samples under sequestration-like conditions does produce visible alterations to the pore network that may impact the way brine and CO_2 flow through the caprock. Neutron scattering and gas adsorption experiments provide a means of quantifying changes to the pore networks of these samples.

3.4.3. Nanoporosity, Surface Area and Pore Volume

Total and connected nanoporosity, as determined by small-angle neutron scattering, increased in the Gothic Shale CO_2-reacted experiment from 4.5 to 5.2% and from 2.6 to 3%, respectively (Fig. 3.17, Table 3.4). The increase in total nanoporosity is attributed largely to an increase in connected porosity (Table 3.6). As expected, in the Gothic system, the increase in porosity was accompanied by an increase in specific surface area from 52.42 m^2g^{-1} (85.18% connected) in unreacted samples to 61.98 m^2g^{-1} (85.24% connected) in CO_2-reacted samples (Fig. 3.18). Most of the surface area increase is attributed to pores in the 14 to 200 nm diameter size range. Median pore size increased from 1.58 nm in unreacted to 2 nm in the CO_2-reacted sample. In contrast, CO_2-reacted connected surface area of 4.05 m^2g^{-1} and median pore size of 15.72 nm was estimated by N_2 gas adsorption techniques. The discrepancy between SANS and BET surface area data highlight the difficulty of using BET on samples with a large volume of angstrom sized nanopores, such as the Gothic Shale (Sing et al, 1982). The increase in median pore size suggests that porosity is either created by increasing the size of existing pores or through the creation of entirely new pores that are larger than the existing pores. The analysis of unreacted Gothic Shale concluded the pore network is not limited by small pore throats (<1 nm). This combined with the information from CO_2-reacted SANS and SEM data supports a theory of larger pore throats (> 1nm) between small nanopores which results in an increase in the surface area for reactive fluids and increased dissolution reactions.

Table 3.6. Summary of Neutron Scattering Results on the Contrast Match Samples of CO_2-reacted and Unreacted Shale

Caprock Formation	Incoherent Scattering[b]	Fractal Behavior		% Porosity (Fit Histogram)[a]	SLD (cm^{-2})	Specific Surface Area (m^2/g)[b]
Gothic Shale						
CO2-reacted	0.98408	$D_s = 2.88 \pm .008$ $D_s = 2.72 \pm .007$	*17 to 45 nm* *70 to 200 nm*	1.99	$4.39e^{10}$	9.22
CO2-reacted-Dup	0.74579	$D_s = 2.94 \pm .011$ $D_s = 2.73 \pm .007$	*18 to 45 nm* *70 to 200 nm*	2.24	$4.39e^{10}$	9.07
Unreacted Dup	0.66166	$D_m = 2.94 \pm .012$ $D_s = 2.74 \pm .010$	*15 to 40 nm* *70 to 200 nm*	1.88	$4.38e^{10}$	7.77
Marine Tuscaloosa						
CO2-reacted	0.53708	$D_m = 2.82 \pm .005$	*15 to 260 nm*	2.69	$4.53e^{10}$	16.49
CO2-reacted-Dup	0.60849	$D_m = 2.82 \pm .005$	*15 to 250 nm*	2.32	$4.53e^{10}$	14.11
Unreacted Dup	0.75841	$D_m = 2.85 \pm .006$	*15 to 165 nm*	1.85	$4.57e^{10}$	8.63

[a] determined using PRINSAS

[b] using Packing Fraction 1.6%

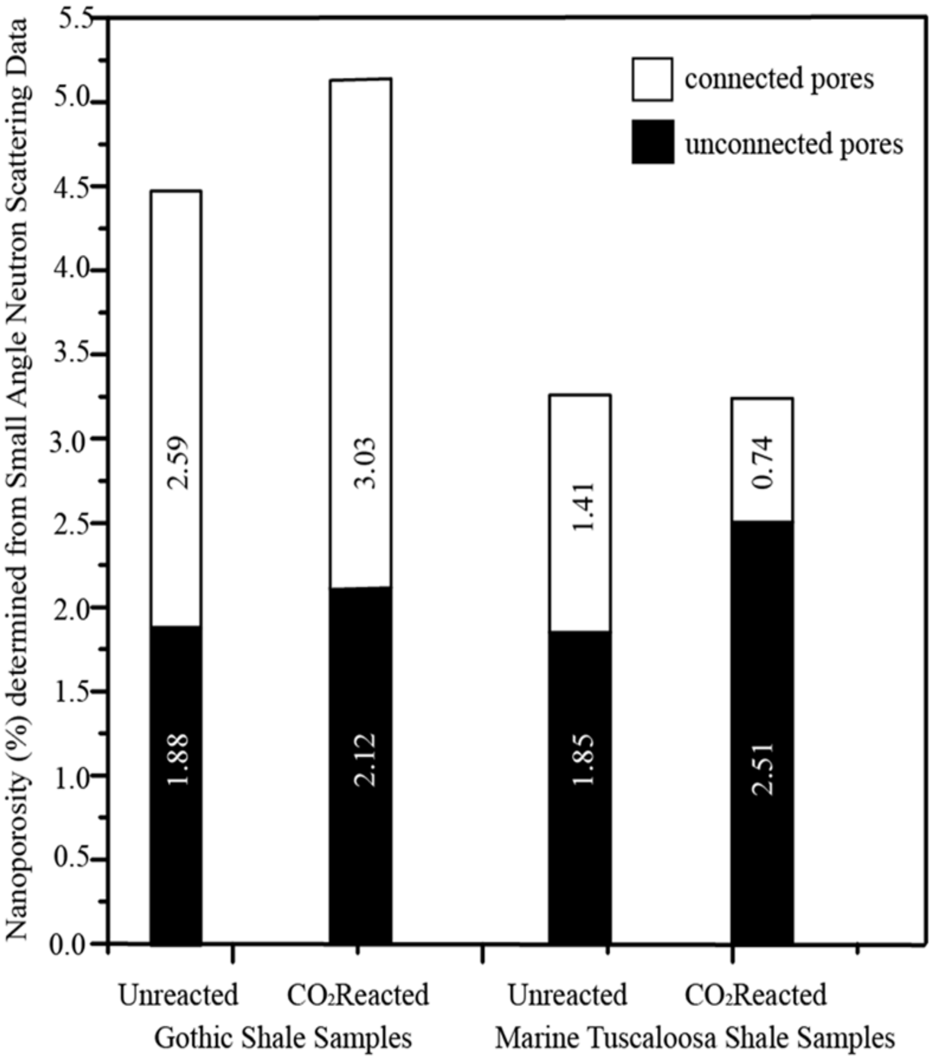

Fig. 3.17. Changes to nanoporosity in connected and unconnected pores of Unreacted and CO_2-reacted Gothic and Marine Tuscaloosa Shale Samples. Increases in porosity due to an increase in connectivity occurs in the Gothic Shale, while a decrease in connectivity in the Marine Tuscaloosa shale results in the same total porosity.

The unreacted nanoporosity of 3.26% and CO_2-reacted nanoporosity of 3.24% show no significant change in total porosity in the Marine Tuscaloosa system with reaction (Fig. 3.17, Table 3.4). However, there is a decrease in the connected porosity (Table 3.6). Analysis of the unreacted Marine Tuscaloosa indicates that much of the pore volume may be connected by small pore throats (<1 nm). We hypothesize that the decrease in pore connectivity is due to precipitation of minerals that block these small pore throats and converts connected porosity to unconnected porosity. In the Marine Tuscaloosa system, the unreacted total surface area of 41.94 m^2g^{-1} (79.4% connected) increased to 45.58 m^2g^{-1} (66.4% connected) in CO_2-reacted samples (Fig. 3.18). The median pore size (2 nm as determined by SANS and 4.93 nm as determined by BET) was not altered by reaction with CO_2 in Marine Tuscaloosa sample. The SANS and BET connected porosity (30.28 and 34.13 m^2g^{-1}, respectively) and median pore size are in closer agreement for the Marine Tuscaloosa sample than for the Gothic Shale sample, likely due to the lower number of angstrom sized pores in the Marine Tuscaloosa.

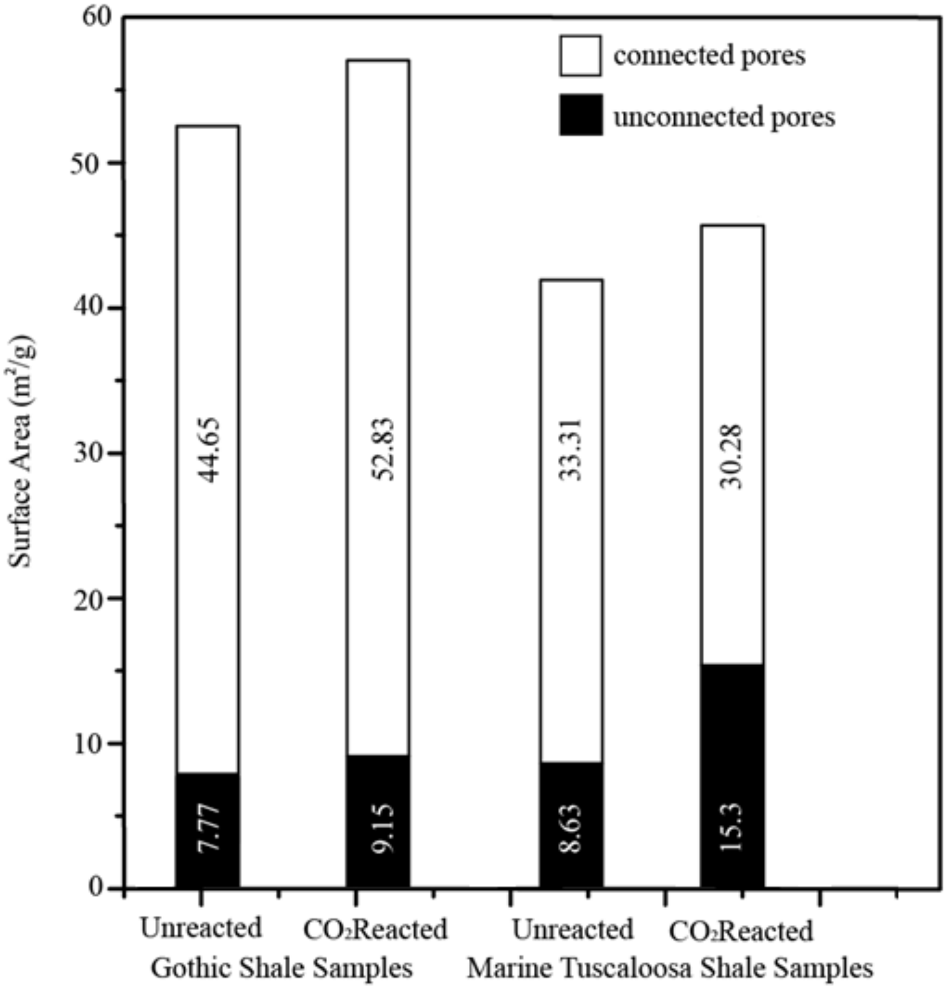

Fig. 3.18. Total Surface Area from connected and unconnected pores for the Gothic Shale and Marine Tuscaloosa Shale Unreacted and CO_2-reacted samples from SANS measurements.

3.5. Significance and Discussion

Small angle neutron scattering, electron imaging, gas adsorption and mercury porosimetry were used to investigate the structure of five fine-grained caprocks of CCUS projects. Two of these caprocks were reacted with CO_2 saturated brine in laboratory experiments at conditions relevant to CCUS to evaluate how geochemical reactions in CCUS conditions change the pore network structure. Based on the data collected we conclude:

1. Nanometer scale pores contribute 20–50% of the pore volume and > 80% of the surface area in the samples analyzed.

2. The connectivity and accessibility of the pore network through pore throats > 1 nm varies with sample and appears to decrease with TOC even through total pore volume increases with TOC.
3. Geochemical reactions between CO_2 saturated brine and the Gothic and Marine Tuscaloosa samples resulted in mineral dissolution and precipitation that altered the pore network.

This work demonstrates the importance of nanopores, especially pores < 10 nm radius, in the pore networks of fine-grained rocks with a median pore radius $\leq$ 2 nm radius in both samples. Additionally, data show that geochemical reactions take place in these very small pores. The fact that the majority of pores occur at these small scales and that alteration does occur at these small nanoscales shows the importance of including these pore size when determining the effects in a carbon sequestration experiment to porosity, surface area and pore size distribution. The significant fraction of nanopores in shales stresses the need to use appropriate modeling and analytical techniques such as small angle neutron scattering that can realistically portray the complex nanoscale pore environment to fully evaluate changes to a system.

The differences observed between a carbonate-rich and silicate-rich shale support a theory that geochemical response of a system is dependent on physical parameters such as mineralogy and initial pore networks. Larger initial pores, smaller pore throats and a silicate-rich shale resulted in decreased pore connectivity while smaller initial pores, bigger pore throats and a carbonate-rich shale resulted in increased pore connectivity. The mineralogy plays a part during geochemical reactions and can contribute to the pH level of the system. Further the size of the initial pore network may play a role, such as precipitates forming on the nonporous surface (Gothic) or forming inside the µm-sized pores in the more porous shale (Marine Tuscaloosa). Other researchers have also noted the importance of initial pore network characteristics when determining the geochemical response of caprocks in CO_2 rich environments, such as initial fracture size (Ellis et al., 2011).

We attempted to determine if the integrity of a caprock is affected by reaction with CO_2. This research has shown that basic changes to the pore network does occur at laboratory time scales; however, this knowledge needs to be extrapolated with modeling techniques to determine if these increases and decreases to connectivity will be detrimental or beneficial to the seal of the caprock. Additionally, the role of physical parameters on the geochemical response supports the need for site-specific work during characterization, experimental studies and models to evaluate pore network effects in future carbon sequestration projects.

3.6 Next Steps

We are currently in the process of reducing and analyzing neutron scattering data collected in December 2011 on CG-2. These samples consist of contrast matched samples of all of the unreacted caprocks to investigate pore connectivity and dry and contrast matched samples of the brine reacted Gothic Shale and Marine Tuscaloosa to quantify the amount of reaction in the experiments related to the rock and brine establishing geochemical equilibrium. Once these data are reduced, two journal articles that are currently in preparation will be submitted for peer-review, listed below.

Mouzakis, K. Navarre-Sitchler, A. Rother, G., Wang, X, Kaszuba, J., McCray, J. Reaction induced porosity changes to mudrocks in CO_2 sequestration relevant conditions: a laboratory investigation, in preparation for Chemical Geology.

Navarre-Sitchler, A., Mouzakis, K., Rother, G., Heath, J., Dewers, T., McCray, J. Nanometer to micron scale pore network structure in mudrocks, in preparation for Geofluids.

Task 4. Geomicrobiological Influence on Carbon Storage and Conversion Applied to Saline Reservoir Storage

4.1. Goals/Objectives

Saline aquifers, depleted oil reservoirs, basalt aquifers and deep, unmineable coal seams are all considered potential targets for carbon capture, utilization, and sequestration (CCUS) (U.S. Department of Energy, 2010). Since many such subsurface reservoirs also harbor diverse and active microbial communities, understanding the potential impacts of CO_2 injection on these microbes will be critical in predicting the long-term fate of the injected carbon. Researchers in Task 4 sought to build on our limited understanding of the impacts of CO_2 injections on subsurface microbial communities. To this end, they analyzed bacterial cell membrane phospholipids, which target living microorganisms, in ground waters from two field sites where CO_2 injections have either occurred or were targeted for injection, as well as from laboratory microcosm experiments. The field sampling was designed to sample ground water wells before and after CO_2 injection in order to assess the effects of CO_2 injection on the native microbial communities. Logistically, this was far more challenging to complete than originally thought. The lab experiments utilized a coal-degrading microbial consortium under varying pCO_2 conditions.

4.2. Background

4.2.1. Microbial Methanogenesis from Coal

Deeply buried coal seams can harbor complex microbial communities with the ability to produce economically significant quantities of methane. Several highly-productive basins in the continental United States are known to produce gas of biogenic origin, including the Powder River Basin, WY (Flores et al., 2008; Rice and Flores, 1991), the San Juan Basin, CO (Scott et al., 1994), and the Black Warrior Basin, AL (Pashin, 2007). Previous studies have demonstrated the potential for either native microbes or coal samples inoculated with specialized consortia to produce methane under laboratory conditions (Harris et al., 2008; Jones, 2010 #816; Jones et al., 2010; Shumkov et al., 1999). Under anaerobic conditions, the process of coal degradation is believed to begin with fermentative cleavage of the macromolecules within coal to long chain fatty acids. Recent evidence has confirmed the importance of long chain fatty acids as intermediates in the process (Jones et al., 2010). The long chain fatty acids are then degraded to shorter chain organic acids such as lactate, formate, propionate, and acetate, and other products such as hydrogen, methanol, and carbon dioxide by fermentative organisms. The final steps of the conversion of coal to methane require the actions of secondary fermenters, homoacetogenic bacteria, as well as acetoclastic and hydrogenotrophic methanogens (Strapoc et al., 2011). Because CO_2 is both a product and a substrate in this complex process, it is likely that small changes in pCO_2 would have significant impacts on the process of methanogenesis from coal and the microbial community mediating the process.

Modeling studies have shown that increasing pCO_2 to injection-level pressures (~200 bars at reservoir T and P) would have a negative effect on acetoclastic methanogenesis (Onstott, 2005), a potentially important reaction in coal-bearing methanogenic systems. However, since increasing the CO_2 and HCO_3^- concentrations increases the free energy yield of the CO_2-reducing methanogenic and acetogenic pathways, this could instead lead to enhanced acetoclastic-methanogenesis. The situation is further complicated because of the anticipated effect of decreasing the pH due to CO_2 dissolution. While methanogenesis may remain an active microbial pathway even at a very low pH (~pH 3) (Williams and Crawford, 1985), and acid- tolerant methanogens have been found in acidic peat bogs (Bräuer et al., 2004; Chanton et al., 1995; Kotsyurbenko et al., 2004), it is thought that a lower pH (<6) will inhibit H_2-consuming and producing processes (Goodwin et al., 1988). In addition, decreasing the pH in methanogenic systems is thought to inhibit the acetoclastic pathway as acetate then exists in its protonated form (Fukuzaki et al., 1990). Therefore, even modest changes in pCO_2 could have important implications for methanogenesis in coal-bearing strata where both methanogenic pathways are possible.

Understanding the effects of changing pCO_2 on a coal-metabolizing and methanogenic microbial consortia incubated in the laboratory was one of the major objectives of this study.

In addition, we sought to understand what effect urea amendment might have on the methanogenic microbial community, as urea can buffer the effects of decreased pH resulting from CO_2 injections as well as serving as a readily available nutrient for a N-limited microbial community (Nielsen et al., 1998; Swensen and Bakken, 1998).

Urea is a commonly utilized N-fertilizer that is isolated from human waste treatment processes. It is often applied to rice fields, global sources of atmospheric methane, to stimulate plant growth. Urea hydrolysis occurs both abiotically and biotically, with the latter process governed by the urease enzyme whose rate is 1014 times more rapid than the uncatalyzed reaction (Jabri et al., 1995). The first step of urea hydrolysis requires splitting the urea molecule into a primary amino acid and ammonia (equation 4.1). The primary amino acid is then further decomposed to ammonia and carbonic acid (equation 4.2). Equations (4.3) to (4.5) show the pH-dependent reactions of carbonic acid and ammonia. The net result of urea hydrolysis is an increase in pH, NH_3, and $[CO_3^{2-}]_{Total}$, which can lead to calcite precipitation in some systems when sufficient Ca^{2+} is present.

Because urea is a commonly used agricultural fertilizer, its effects on methane flux from agricultural soils, such as found in rice paddies, has been investigated thoroughly. Some studies report stimulation of methane production (Banik et al., 1996; Cicerone and Shetter, 1981; Dan et al., 2001; Lindau, 1994; Singh et al., 1999) while others report inhibition (Bodelier et al., 2000; Bronson et al., 1997). Other studies have suggested the possibility of using urea to stimulate biomineralization in CO_2 storage reservoirs (Ferris et al., 2004; Mitchell et al., 2010). The mechanisms of storage would include both solubility and mineral trapping as a result of the pH increase caused by urea hydrolysis. Mitchell et al. (2010) showed that a pure culture of *Sporosarcina pasteuri* was able to hydrolyze urea and cause calcite precipitation in microcosm experiments. To our knowledge, the effects of urea amendment on a complex consortium of organisms metabolizing coal to methane have not been documented. We hypothesized that any potential pH buffering associated with urea hydrolysis would help maintain the optimal physiological pH for methanogenesis (~7.5) (Boone et al., 1993) in our system, thereby increasing the methanogenic potential from coal.

Urea Hydrolysis

$$CO(NH_2)_2 + H_2O \rightarrow NH_2COOH + NH_3 \qquad (4.1)$$

$$NH_2COOH + H_2O \rightarrow NH_3 + H_2CO_3 \qquad (4.2)$$

$$H_2CO_3 \leftrightarrow HCO_3^- + H^+ \qquad (4.3)$$

$$2NH_3 + 2H_2O \leftrightarrow 2NH_4^+ + 2OH^- \qquad (4.4)$$

$$HCO_3^- + H^+ + 2OH^- \leftrightarrow CO_3^{2-} + 2H_2O \qquad (4.5)$$

Calcite Precipitation

$$Ca^{+2} + 2HCO_{-3} = CaCO_3 + H_2CO_3 \qquad (4.6)$$

4.3. Methods/Approach

4.3.1. Field Sampling

4.3.1.1. Wallula Pilot Site

The Wallula Pilot Site is a CO_2 sequestration pilot project at the Wallula Paper Mill near Richland, WA. The injection well was drilled between January and April 2009 to a total depth of 1253 m in the Columbia River Basalt Formation (McGrail et al., 2011). The Columbia River Basalt Group is a collection of basalt deposits underlying much of eastern Washington, northeastern Oregon, and western Idaho. It has been estimated that this formation may be able to sequester at least 10 to 50 Gt CO_2 (McGrail et al., 2006). The sampling occurred between February 28, 2011 and March 7, 2011 and involved on-site collection for each of the 7 days of a constant rate pumping test designed to test the hydrologic connectivity of the target injection formation. Using a high pressure filter apparatus, our goal for this sampling was to filter sufficient groundwater (0.2 µm filters) from the target injection formation to collect native microbial biomass. At the time of sampling, it appeared that CO_2 injection was imminent; however, as of the writing of this report this injection had not yet taken place. The background data on microbial biomass and community structure will still be useful to compare with post-injection data once that is completed.

4.3.1.2. Rangely Field, Rangely, CO

The Rangely Field is an operational oil reservoir located in northwestern Colorado near Rangely, CO. The Permian-Pennsylvanian Rangely-Weber sandstone reservoir experienced its primary production in the 1940s and 1950s, was waterflooded (surface water injected to increase hydrocarbon production) in 1958, and has seen CO_2 injection-Enhanced Oil Recovery operations (CO_2-EOR) since 1986 (Bowker and Jackson, 1989; Hefner and Barrow, 1992). The CO_2-EOR operations consisted of using a ratio of 1:1 water-alternating-gas in 209 injection wells. The injection of CO_2 occurs at an average depth of 1700 m in the Pennsylvanian-Permian sandstone, for which the Raven Park anticline provides the trap (Bowker and Shuler, 1991). During the mid-2000s the average injection volume of CO_2 was 4.2 million m^3/day and it is estimated that by the time of project completion roughly 25 Mt of CO_2 will have been sequestered (Durie et al., 2001). Roughly 80% of the CO_2 injected at Rangely is recovered, separated, and reinjected, leaving roughly 20% sequestered in the reservoir, mainly dissolved in the formation water (Roedell, 2011).

The Rangely site provides an opportunity to characterize the microbial communities both within and outside of the areas injected with CO_2. There are several important differences in the chemistry of the produced waters as a result of CO_2 injection between the various sites. First, the pH at the injection site was estimated to be ~3.5, increasing to 4.5 near the production wells (Shuler et al., 1989). The pH measured at the surface near the wellhead averages 6.5 due to carbonate scaling within the wellbore and CO_2 off-gassing (Bowker and Shuler, 1991). The pH of produced water outside the injection zone should more readily reflect the pre-injection pH of 7–7.5 (Bowker and Shuler, 1991). Second, the central part of the field has undergone water flooding since the 1960s with water from the White River and Entrada sandstone aquifer. It is believed that this flooding introduced sulfate-reducing bacteria (SRB), producing H_2S, which became problematic for oil and gas production (Shuler, Freitas, & Bowker, 1989). Production wells on the periphery of the basin do not experience these problems. Though introduction of SRB is not a result of CO_2 injection, the microbial community may still be affected by it in other ways. Third, areas which have been impacted by CO_2 injection have significantly higher Ca^{2+}, Ba^{2+}, Fe^{2+}, and HCO_3^- concentrations than what was measured pre-injection (Bowker and Shuler, 1991). The higher Fe^{2+} and HCO_3^- concentrations may promote iron-oxidizing autotrophic microbial communities if other factors remain favorable.

4.3.1.3. Kentucky Field Site

A third site in Kentucky provides a pair-wise comparison between two wells in hydraulic communication that are also part of a CO_2-EOR project, where only one well was impacted by the CO_2 injections. This latter site is being investigated in collaboration with Dr. Marty Parris at the Kentucky Geological Survey, Lexington, KY.

The purpose for sampling the Sugar Creek CO_2-EOR location of Western Kentucky is the same as for the Rangely Field site. The Sugar Creek oil reservoir taps the Mississippian, Jackson Formation sandstone. The EOR wells contain formation waters with a bimodal TDS distribution. The brines of "unadulterated" wells have TDS values of ~50,000 mg/L. However, like the Rangely site, many wells have been waterflooded with more dilute (600–900 mg/L) shallow water to produce TDS values of ~20,000+ mg/L. Wells PH1 and WT4 were specifically chosen because they were not waterflooded. Unlike WT4, the formation waters from PH1 experienced

CO_2 from a nearby injection well, which was "continuously" injected with 20–30 tons of CO_2/day from May 2009 to May 2010. Impacted wells responded with increasing levels aqueous Ca, Sr, and Mg that are likely related to carbonate dissolution from lowering of the pH.

4.3.2. Procedures

4.3.2.1. High pressure manifold sampling (Rangely Field and Wallula Pilot Project)

Filter samples of intact microbial cells were collected via direct filtration of produced water from wells using a stainless steel filtration manifold (142 mm, Millipore, Billerica, MA, USA) with 0.22 µm filters (Millipore # GVWP14250). All filtration equipment was pre-sterilized by autoclaving before going to the field. Individual filters were packaged in foil and autoclaved separately in order to change filters in the field. The stainless steel forceps used to exchange-filters were previously baked at 460°C in a muffle furnace to remove any trace organic contaminants. Prior to filtration, the tubing connecting the well head with the filtration manifold was flushed for at least 15 minutes. The volume of fluid filtered was determined by collecting the filtrate in graduated 20 L containers. At the end of the filtration period, the filter was removed from the manifold and placed in a sterile 50 mL centrifuge tube and frozen on dry ice during return to the lab, where they were stored at -80°C until extraction. Filter blanks were collected in the field by removing a sterile filter from its packaging and placing it in a centrifuge tube and frozen alongside other samples. Samples of produced water were collected in the field for measurement of cations and anions via Inductively Coupled Plasma-Atomic Emission Spectroscopy (ICP-AES) and Ion Chromatography, respectively.

4.3.2.2. Incubation experiments

All experiments were prepared in an anaerobic chamber with 5% H_2, 5% CO_2, and a balance of N_2 atmosphere. Coal was collected in September 2009 by straining drill cuttings from the effluent of working drill rigs. Coal cuttings were immediately rinsed with sterile deionized water to remove drilling fluids and were then sealed in vacuum bags with chemical oxygen scrubbers. Coal cuttings were stored at 4°C until use. Three sampling trips were conducted to collect coal samples in November 2008, April 2009, and again in September 2009.

Experiments were initiated by weighing coal under anaerobic atmosphere and adding it to sterile 200 mL serum bottles. An anaerobic medium (Tanner, 2006) was added at the ratio of 5:1 (vol: wt coal) and all experiments were inoculated with a consortium of organisms enriched from coal cuttings from the Powder River Basin, WY. The consortium was maintained on coal cuttings and the anaerobic medium at 30^{o}C and transferred to fresh coal cuttings approximately every 60 days. The anaerobic medium was modified to exclude sulfate from the medium by replacing $MgSO_4$ with $MgCl_2$. The medium included (g/L) NaCl (0.8), NH_4Cl (1.0), KH_2PO_4 (0.1), KCl (0.1), $MgCl_2{\cdot}6H_2O$ (0.17), $CaCl_2{\cdot}2H_2O$ (0.04), $NaHCO_3$ (1.0), nitrilotriacetic acid (0.02), $MnSO_4{\cdot}H_2O$ (0.01), $Fe(NH_4)2SO_4{\cdot}6H_2O$ (0.008), $CoCl_2{\cdot}6H_2O$ (0.002), $ZnSO_4{\cdot}7H_2O$ (0.002), $CuCl_2{\cdot}2H_2O$ (0.0002), $NiCl_2{\cdot}6H_2O$ (0.0002), $Na_2MoO_4{\cdot}2H_2O$ (0.0002), Na_2SeO_4 (0.0002), Na_2WO_4 (0.0002). The medium was prepared by flash-autoclaving DI water to reduce oxygen saturation, then sparging with 4:1 N_2:CO_2 for 15 minutes before adding 10 mL of Tanner's trace metal solution, 50 mL trace mineral solution, and 1 g/L $NaHCO_3$ just before sealing under N_2:CO_2 and autoclaving. Anaerobic trace vitamin solution was added according to Tanner (2006). Upon sealing with butyl rubber stoppers, the headspace of each bottle was purged with the desired headspace gas (either 4:1 N_2:CO_2 or CO_2) and pressurized to 110 kPa.

Low molecular weight organic acids (acetate, propionate, formate, succinate, oxalic, and citric) were monitored by high performance liquid chromatography (HPLC) on an Agilent 1100 Series with a BioRad HPX-87H column (300 x 7.8 mm) and UV/VIS detector set at 210 nm. The concentrations of CH_4 and CO_2 were measured using a GC-17A gas chromatograph (Shimadzu, Kyoto, Japan). CH_4 was separated using a HayesepQ packed column (2m) and CO_2 was separated using a molecular sieve (5Å pore size, 2m) held at 100^{o}C with a thermal conductivity detector (200^{o}C) and flame ionization detector (200^{o}C) connected in series for quantification. The instrument's calibration was checked periodically with authentic CH_4 and CO_2 standards obtained from Scott Specialty Gases (Plumsteadville, PA).

4.3.2.3. Microbial Community Analysis

Once experiments were completed, samples (1.0 mL) were taken for molecular analysis (DNA, RNA and qPCR) and frozen at –80^{o}C prior to freezing the remainder of the contents of the experiment in the serum bottle at –20^{o}C and lyophilizing the entire sample. Samples were then transferred to glass centrifuge tubes and extracted using a modified Bligh-Dyer extraction (White and Ringelberg, 1998) by shaking on a rotary shaker table at 150 rpm for two hours, followed by centrifugation at 1000 rpm for 30 minutes. The centrifugant was decanted into separatory funnels and the solvent ratios adjusted to 1:1:0.8 by adding chloroform and 0.5 mM phosphate buffer and then allowed to separate overnight. The sample was then re-extracted for Archaeal phosphoether lipids by adding 75 mL methanol, 37.5 mL chloroform, and 30 mL 10% trichloroacetic acid (wt:vol). The centrifugant from this second extraction was phase separated overnight by adding 30 mL water and 37.5 mL chloroform. The volume of both total lipid extracts was reduced under N_2 stream and then separated into neutral, glyco- and polar lipid classes using silica solid phase extraction columns (Alltech 500mg, 209200). SPE columns were prepared by washing with

5 mL methanol followed by 10 mL chloroform. Following loading of the columns with the total lipid extract, neutral lipids were eluted in 10 mL chloroform, glycolipids in 10 mL acetone, and polar lipids in 10 mL methanol. Fatty acid methyl esters (FAMEs) were prepared by mild alkaline methanolysis by treating the polar lipid phase with 1.0 mL 5% KOH:methanol (wt/vol) and 1.0 mL 1:1 methanol:toluene and incubating for 30 min at 37°C. FAMEs were then extracted three times with 4:1 hexane:chloroform and concentrated. All samples and blanks were injected with an internal standard (C13:0, CAS# 1731-88-0) for quantification. Two ubiquitous FAMEs were commonly seen in blanks (C16:0 and C18:0) and were generally on the order of 2 nmol total.

4.3.2.4. Ether lipid protocol

Since it is believed that the mild alkaline methanolysis used to convert PLFAs into FAMEs does not affect the polar head groups of Archaeal phosphoether lipids (PELs) (White and Ringelberg, 1998) they can be analyzed following the methanolysis of bacterial PLFAs. Polar phosphoether lipids containing amino groups in the polar head group are not affected by HCl- methanolysis; therefore, PELs were subjected to acetolysis (Renkonen, 1965) followed by HCl- methanolysis to remove all polar head groups that may be present. Intact phospholipids were heated at 140°C for 18h with 2.0 mL 3:2 acetic acid:acetic anhydride (v/v). The acid mixture was then cooled to room temperature and transferred to screw-top vials where it was then phase- separated using 2.25 mL 4:5 water:methanol (v/v) and 4.0 mL chloroform. The chloroform extraction was repeated 3 times and all organic phases combined and reduced to dryness under N_2 in glass ampules. The remaining polar head groups (glycosidic groups) and acetylated core lipids from amino-containing lipids were liberated using 2.0 mL 5% HCl-methanol (wt/vol) at 110°C for 2h (Nishihara and Koga, 1987). The remaining core lipids were extracted three times after adding 2.0 mL water with 4:1 hexane:chloroform (v/v), and the volume of organic solvent reduced under N_2 stream before adding 30 μL pyridine followed by 30 μL 1% trimethylchlorosilane in N,O-bis(trimethylsilyl) trifluoroacetamide (BSTFA) and heating at 70°C for 2h. Samples were then analyzed by GC-MS within 24h of silylation.

4.3.2.5. GC-MS procedures

FAMEs were analyzed in the laboratory of Dr. Christopher Mills at the U.S. Geologic Survey on an Agilent 7890A Gas chromatograph with a DB-1MS column (60m x 0.25 mm I.D.), and quantified using a Flame Ionization Detector (FID) coupled to an Agilent 5975C Inert XL mass spectrometer for FAME identification. The injector temperature was 280°C, the FID set to 200°C, and the ion source temperature set to 250°C. The oven temperature program began at 50°C, then increased to 150°C at 20°C min^{-1}, then increased to 210°C at 1.5°C min^{-1}, then increased to 280°C at 10°C min^{-1} and held for a final 8 min at 280°C. Silylated ether lipids were separated on a DB-1MS column (60m x 0.25 mm I.D.) with an injector temperature of 300°C and source temperature of 250°C. The oven temperature was held at 70°C for 2 min, increased to 130°C at 25°C min^{-1}, then to 190°C at 6°C min^{-1}, then increased to 320°C at 25 C° min^{-1}.

δ^{13}C analysis of FAMEs

Compound specific gas chromatography combustion isotope ratio mass spectrometry (GC-C-IRMS) was conducted in the laboratory of Dr. Robert Dias at the U.S. Geologic Survey in Lakewood, CO. Two Fatty Acid Methyl Esters (FAMEs) were added to each sample as internal standards (12:0 and 20:0) and each $^{13}C/^{12}C$ ratio was compared to these working standards and internal reference CO_2. Each reported PLFA was corrected for the influence of methylation carbon using equation (4.7).

$$\delta^{13}C_{corrected} = [[\delta^{13}C_{measured}X(\#C+1)] - \delta^{13}C_{MeOH}]/\#C \qquad (4.7)$$

4.4. Task Results

4.4.1. Microcosm Experiments

Figure 4.1 shows the results of the microbial incubation experiments under varying pCO_2 levels and urea concentrations.

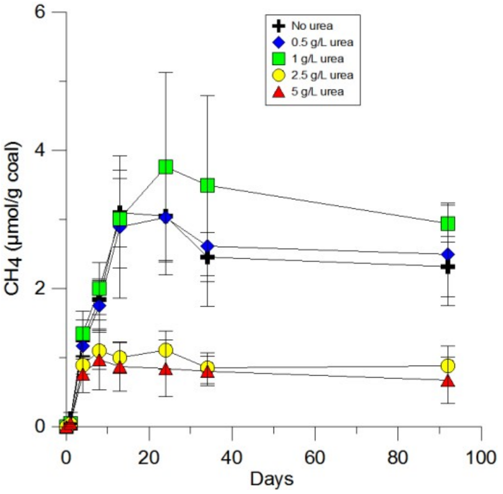

Fig. 4.1. CH_4 production in experiments with 0.2 atm CO_2 and 0.5, 1, 2.5, and 5 g/L urea

The results reveal no significant difference in methane production between the two lowest urea concentrations tested (0.5 g/L and 1 g/L) and the unamended control experiment. In contrast, the experiments amended with 2.5 g/L and 5 g/L urea showed ~ 65% reduction in methane production (~1 µmol $g^{-1}coal^{-1}$ versus ~2.5 µmol $g^{-1}coal^{-1}$). Initially, acetate concentrations produced by fermentation were similar under the various experimental conditions as shown in figure 4.2.

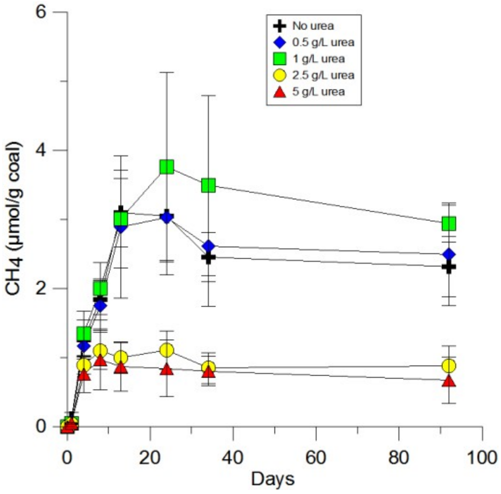

Fig. 4.2. Acetate concentration in experiments with 0.2 atm CO_2 and 0.5, 1, 2.5, and 5 g/L urea

However, after urea hydrolysis commenced between days 7 and 12, as observed by the change in pH and shown in figure 4.3, the remaining acetate was not consumed in experiments with 2.5 and 5 g/L urea.

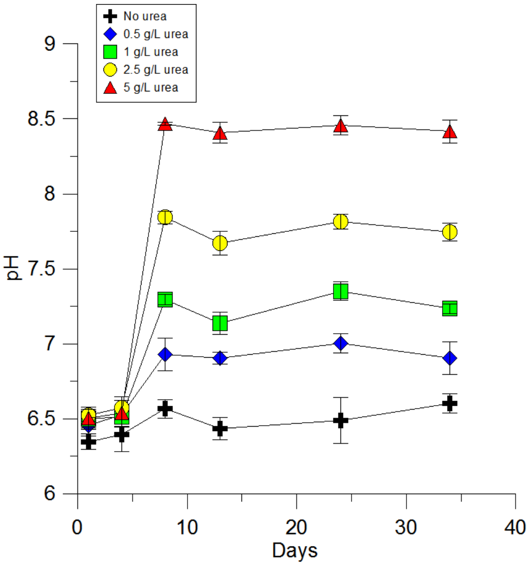

Fig. 4.3. ΔpH in experiments with 0.2 atm CO_2 and 0.5, 1, 2.5, and 5 g/L urea

In addition, as shown in figure 4.4, the headspace CO_2 pressures were greatly reduced in the experiments amended with urea, presumably due to greater CO_2 solubility resulting from the increase in pH (Stumm and Morgan, 1996).

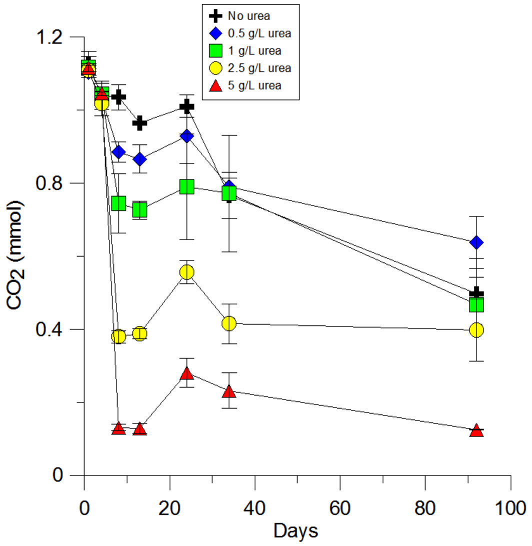

Fig. 4.4. ΔCO_2 in experiments with 0.2 atm CO_2 and 0.5, 1, 2.5, and 5 g/L urea

Because of the dramatic increase in pH during urea hydrolysis under a 0.2 atm CO_2 head-space, it was hypothesized that increasing both the pCO_2 and urea levels would result in no major change in pH and perhaps stimulate methanogenesis. Total methane production reached ~30 µmol g^{-1}coal^{-1} after 10 days in experiments with 0.2 atm CO_2 while those with higher *p*CO$_2$took almost 20 days to reach methane production values >20 µmol g^{-1}coal^{-1}. Figure 4.5 and figure 4.6 show that urea amendment did not enhance methanogenesis relative to the control experiments at similar *p*CO$_2$ levels.

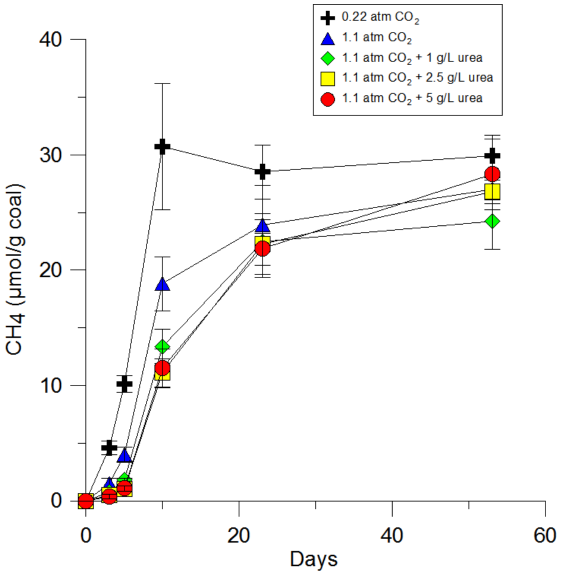

Fig. 4.5. CH_4 in experiments with 0.2 and1.1 atm CO_2 and 1, 2.5, and 5 g/L urea

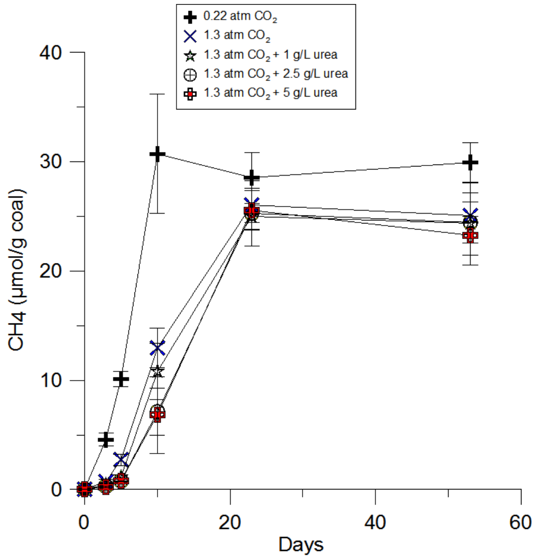

Fig. 4.6. CH_4 production in experiments with 1.3 atm CO_2 and 1, 2.5, and 5 g/L urea

However, the highest urea concentrations (2.5 and 5 g/L) did not inhibit methanogenesis, most likely due to the buffering effect of increased pH and its effect on CO_2 dissolution. The pH remained between 6.3 and 6.5 in these experiments (data not shown). Although each experiment had similar maximum acetate concentrations (~4 mM; Fig. 4.7 and Fig. 4.8), the rate of acetate consumption in each varied and depended on the CO_2 pressure and the urea concentration. Acetate was completely consumed by day 10 in experiments with 0.2 atm CO_2, whereas at 1.1 atm CO_2 the acetate concentrations ranged from 1 to 2.5 mM at day 10 as shown in figure 4.7.

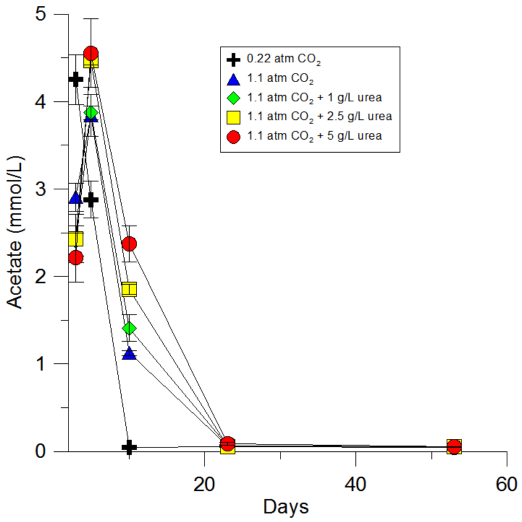

Fig. 4.7. Acetate concentrations in experiments with 0.2 and 1.1 atm CO_2 and 1, 2.5, and 5 g/L urea

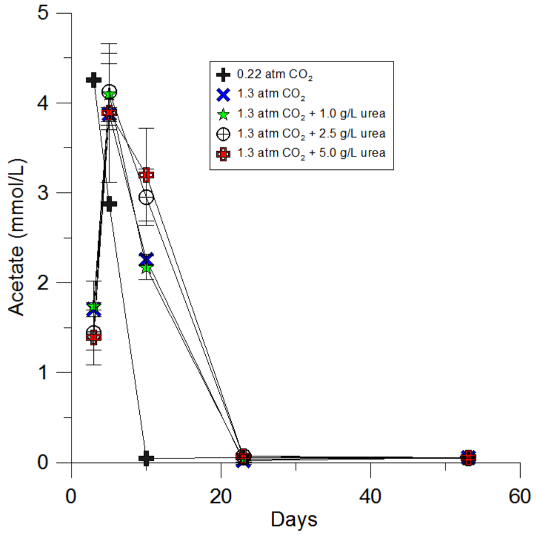

Fig. 4.8. Acetate concentrations in experiments with 1.3 atm CO2 and 1, 2.5, and 5 g/L urea

In order to assess the response of the microbial community to a greater $\Delta p\mathrm{CO}_2$, a third set of experiments was initiated with $p\mathrm{CO}_2$ ranging from 0.2 atm to 2.5 atm. A pCO_2 level of 2.5 atm was the practical upper limit for these experiments due to difficulties with liquid and gas sampling at higher pressures. The cumulative methane production can be seen in figure 4.9 and figure 4.10, which reached only ~0.4 µmol g^{-1} $coal^{-1}$. This is lower than in either of the previous two sets of experiments by as much as 2 orders of magnitude. The acetate measured was also lower by at least 10x as shown in figure 4.11.

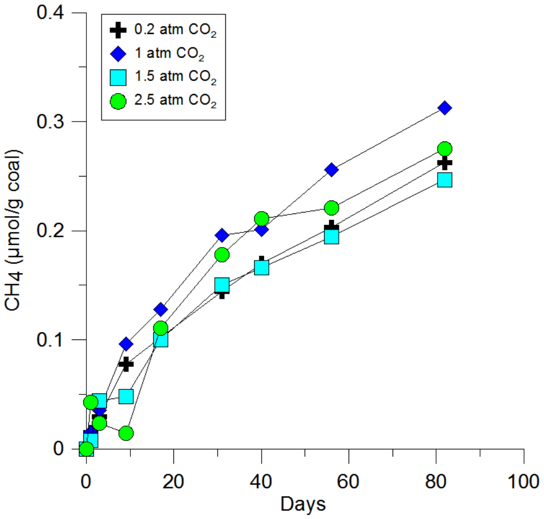

Fig. 4.9. CH4 production in experiments with 0.2, 1.0, 1.5, and 2.5 atm CO2 (error bars not shown for clarity)

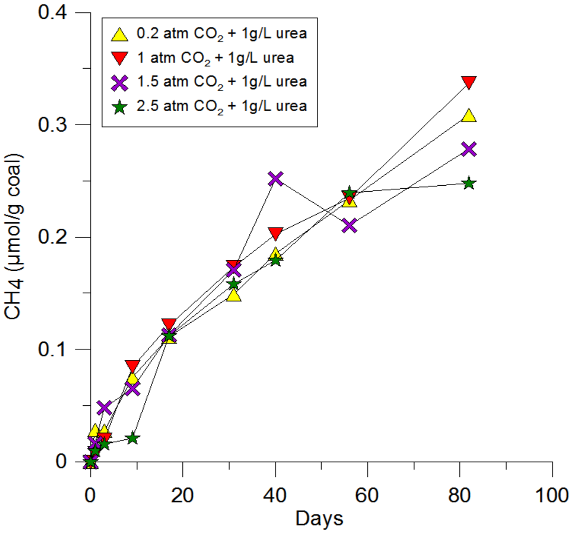

Fig. 4.10. CH_4 production in experiments with 0.2, 1.0, 1.5, and 2.5 atm CO_2 and 1 g/L urea (error bars not shown for clarity)

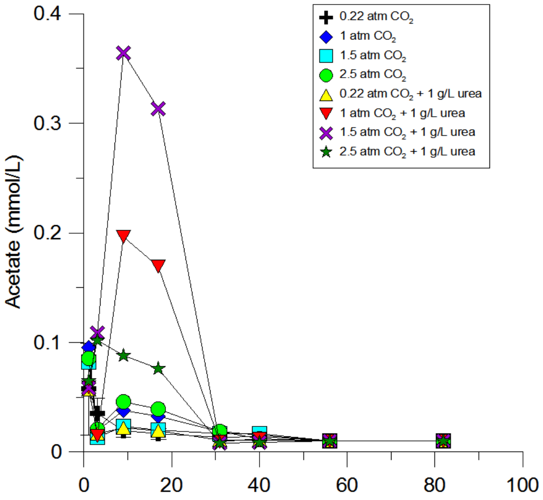

Fig. 4.11. Acetate concentrations in experiments with 0.2 to 2.5 atm CO2 and 1 g/L urea

Neither methane production nor acetate production/consumption showed any correlation with pCO_2 or any relationship with urea amendment. The pCO_2 in each experiment remained constant over the time course of the experiments (Fig. 4.12). This result is in contrast with the results shown in figure 4.4 wherein the increase in pH associated with urea hydrolysis caused a significant decrease in headspace CO_2 pressure as a result of increased CO_2 solubility. The results shown in figure 4.12 suggest that urea hydrolysis did not occur in these experiments, which is also consistent with constant pH values measured at each time point (data not shown).

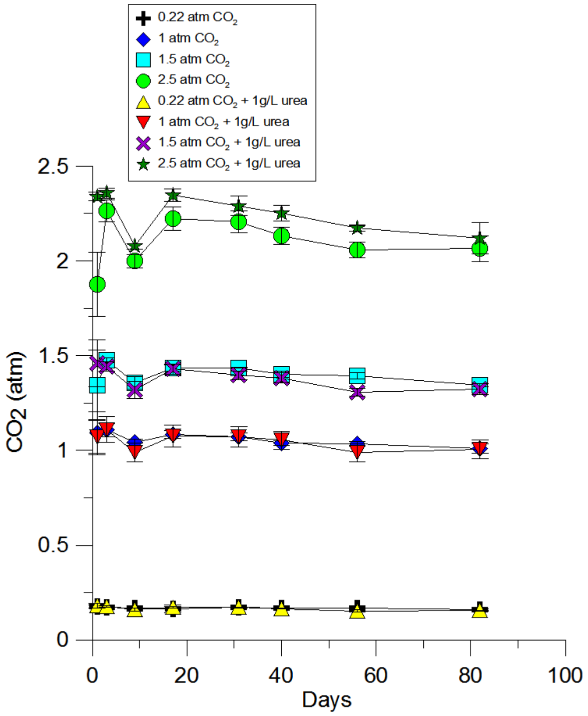

Fig. 4.12. $\Delta p\mathrm{CO}_2$ in experiments with $p\mathrm{CO}_2$ from 0.2 to 2.5 atm

4.4.2. Microbial Community Analysis

Phospholipid-derived fatty acids (PLFA) analysis confirmed the presence of a diverse bacterial community in experiments with 0.2 atm CO_2 and variable concentrations of urea. Figure 4.13 shows the resulting average PLFA profiles (error bars represent 1σ of triplicate incubations).

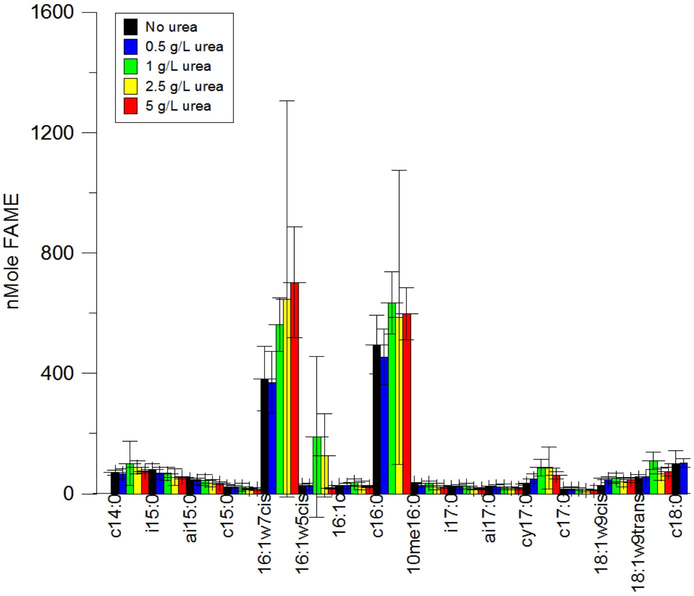

Fig. 4.13. FAMEs extracted from experiments with 0.2 atm CO_2 and variable urea concentrations

Most PLFAs observed in these incubations were ubiquitous (therefore non-diagnostic) indicators of living biomass. These include the unbranched, saturated PLFAs 14:0, 15:0, 16:0, 17:0, and 18:0, as well as the monoenoic PLFAs such as 16:1ω5, and 18:1ω9. The dominant PLFAs observed in these incubations were 16:1ω7 and 16:0, comprising roughly 60% of total PLFAs detected. We also observed PLFAs indicative of sulfate reducing bacteria (SRB) including i15:0, ai15:0, i17:0, and cyclic17:0 (Dowling et al., 1986; Kohring et al., 1994). The total mass of PLFA extracted corresponds to the total bacterial biomass extracted from each microcosm. Using the conversion factor of Balkwill et al. (1988) of 2.4 x 10^4 cells/pmole $PLFA^{-1}$ an average bacterial density was calculated for each experimental condition as shown in figure 4.14.

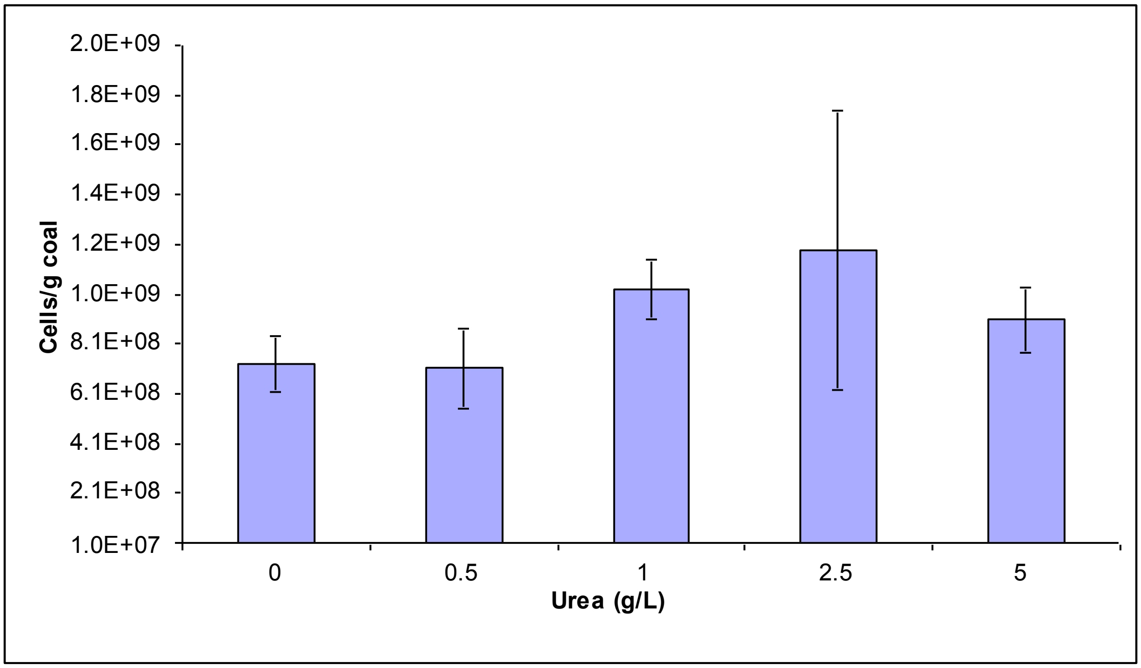

Fig. 4.14. Total bacterial biomass measured in experiments with 0.2 atm CO_2 and vairable urea concentrations. Error bars represent 1σ of triplicate incubations, except for 2.5 g/L urea experiment due to sample loss.

Experiments amended with 1 g/L urea showed a significantly greater bacterial biomass than the unamended control experiments, suggesting stimulation of the bacterial community with urea amendment. This difference can also be seen in figure 13 wherein the PLFA 16:1ω7 is present at slightly greater values (562 ± 88 nmole in 1g/L experiments versus 382 ± 107 nmole in the unamended controls). However, experiments amended with 0.5, 2.5, and 5 g/L urea did not show significantly greater bacterial biomass than the non-amended control experiments.

4.4.3. Field Sampling Results

4.4.3.1. Rangely Field

Using the conversion factor of 2.4 x 10^4 cells/pmole $PLFA^{-1}$ (Balkwill et al., 1988), the total bacterial biomass was calculated for filtered samples collected from the Rangely field site (Table 4.1).

Table 4.1. Total PLFAs and biomass estimates from filters collected at Rangely Field

Sample	**Volume filtered (L)**	**Total mole PLFA**	**Cells/L**
CO_2 flood #1	20	6.86 x10^{-6}	2.2 x10^{10}
CO_2 flood #2	10	3.05 x10^{-6}	1.8 x10^{10}
Non-flooded #1	38	8.85 x10^{-7}	1.4 x10^{9}
Non-flooded #2	55	1.01 x10^{-6}	1.1 x10^{9}

Figures 4.15 and 4.16 illustrate the average PLFA profiles for samples collected in areas within and outside the CO_2 flooding, respectively. The PLFA profile (Fig. 4.15) for the CO_2 flooded area is dominated by biomarkers that are highly suggestive of SRB, including i15:0, ai15:0, 10me16:0, and cy17:0 (Taylor and Parkes, 1983). This finding is consistent with the H_2S known to contaminate the gas stream from wells in this area. These same PLFAs were also identified at station #47, but also included i17:1w7 and 18:1w9 as the dominant PLFAs, which are ubiquitous among bacteria.

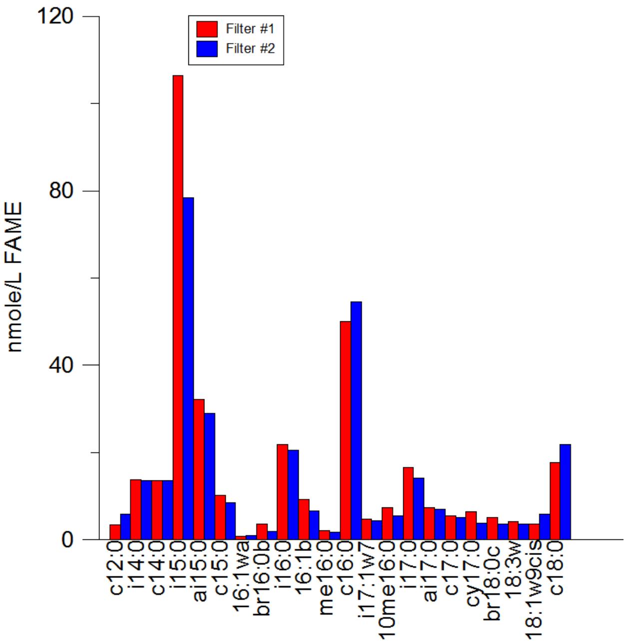

Fig. 4.15. Average PLFA profile for 2 filters collected from area under CO_2 flood at Rangely Field, CO

4.4.3.2. $\delta^{13}C$ values of select PLFAs

Obtaining stable carbon isotopic values for PLFAs ($\delta^{13}C_{PLFA}$) from relatively dilute samples was difficult due to insufficient sample size. The $\delta^{13}C_{PLFA}$ values obtained for the most abundant

FAMEs in collection #5 are presented in Table 4.2. These values are similar to average values for C-3 plant material and consistent with a heterotrophic metabolism with crude oil as the primary carbon source, as would be expected in this environment.

Table 4.2. δ^{13}C values of select PLFAs from Collection #5 Filter #1 sample

PLFA	**Average $\delta^{13}C_{PLFA}$**	**Standard deviation**
i15:0	-24.3	1.5
ai15:0	-26.9	3.0
16:0	-27.1	0.8

4.4.3.3. Wallula Pilot Project results

Figure 4.16 shows a comparison of the PLFA profiles for two of the replicate filters collected at the Wallula site. Difficulties with sample collection prevented us from filtering large volumes (>20 L/filter) necessary for $\delta^{13}C_{PLFA}$ analysis.

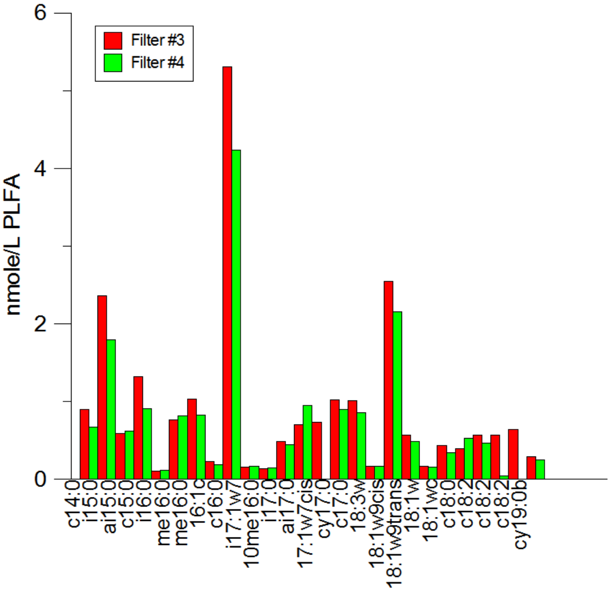

Fig. 4.16. Average PLFA profile for 2 filters collected from area outside of CO_2 flood from Rangely Field, CO

Figure 4.17 shows PLFA profiles for combined filter samples. Due to the small volumes filtered at this site, groups of 3 filtered samples were combined for a single analysis. Using the conversion factor of Balkwill et al. (1988) of 2.4 x 10^4 cells/pmole PLFA^{-1} yields an average bacterial cell density of 1.2 x10^8 cells/L when corrected for contamination in the extraction blank (Balkwill et al., 1988). The sample blank contained 2 nmol of 16:0 and 18:0 FAMEs combined.

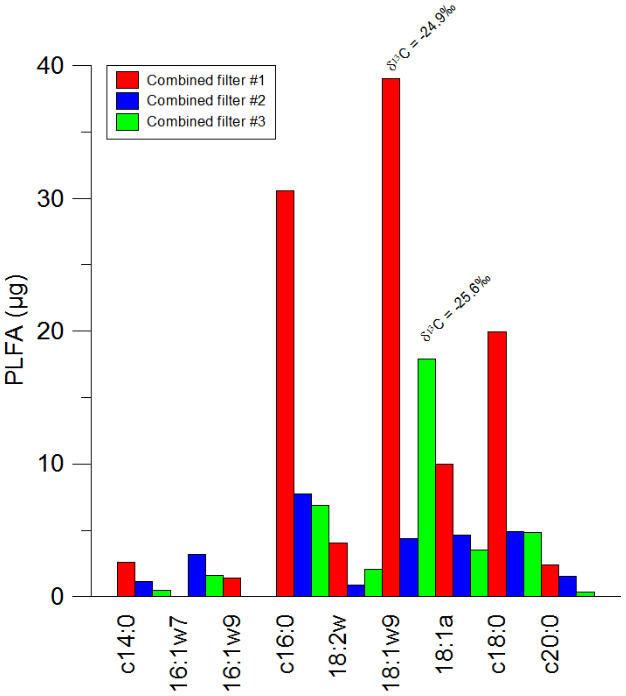

Fig. 4.17. PLFA profiles for combined filter samples from Wallula Pilot Project (3/7/11- 3/14/11). Two samples had sufficient mass to analyze $\delta^{13}C_{PLFA}$ for 18:1ω9.

4.4.3.4. Kentucky Field site results

For the Sugar Creek site, sampling of the PH-1 well was completed in early June, 2011, and the TH4 "control" (non CO_2-injected) well in October, 2011, in collaboration with Dr. Marty Parrish at the Kentucky Geological Survey. Five samples were collected on the 0.22μm filter. However, the volume of water filtered from these samples only totaled 3.2 L. This was due to clogging of the prefilter and manifold filter by oil fowling and from an Fe-carbonate that rapidly precipitated out of solution due to either redox or pH changes during passage of the anoxic water through the filtration system. Filtered samples were sent to Dr. Chris Mills at the U.S. Geological Survey for GC-MS analysis.

All five filtered samples from the June, 2011 sampling were combined to improve the chances of PLFA detection. The filters were extracted three times and extraction solvents combined. Approximately 180 mg of total lipid was recovered. This very large amount of lipid is primarily a result of the oil on the filters. Separation of phospholipids from more neutral lipids was performed by splitting the sample into multiple aliquots and using ten solid phase extraction cartridges (0.5 g silica each) to prevent overloading of silica. The use of one cartridge per sample is typical. The fractions containing phospholipids were recombined prior to methanolysis. Unfortunately, the PLFA concentrations were below detection. Isolation of Archaeal glycolipids was also attempted but none were recovered.

PLFAs were detected, however, from the TH4 "control" site during sampling in October 2011. The current results are, if anything, an underestimation of PLFAs in the sample (Table 4.3). These results indicate bacterial cell densities in Sugar Creek WT4 are similar to those reported in the KNA-6 LTL groundwater collected from the sedimentary formation of a uranium mine (Mills et al., 2010). Mills et al. (2010) determined that ground waters with the cell densities measured at Sugar Creek require a few hundred liters to yield enough PLFAs for carbon isotope measurements. No archaebacterial lipids were detected from the TH4 well.

Table 4.3. Concentration of PLFAs in Sugar Creek WT4

PLFA	integral (mass 74 only)	mole %
12:0	3410946	13.4
14:0	4720162	18.6
i15:0	1293150	5.1
a15:0	632648	2.5
15:0	890800	3.5
i16:0	470995	1.9
16:1	248689	1.0
16:0	9691631	38.1
17:0	323740	1.3
18:0	3758095	14.8
19:0 IS	47726948	
integral sum	25440856	
ratio of sum to IS	0.53	
total nmoles PLFA in sample	18.4	
picomoles PLFA per liter	992	
Calculated cells per ml	60,000	

Although, with considerable effort, we successfully measured bacterial PLFAs in the TH4 well, it was unfortunate that fresh groundwater began seeping into the PH-1 well in fall of 2011. This was apparent from water chemistry measurements made at that time. This intrusion of fresh water precluded a direct comparison of the effects of CO_2 injection alone on the microbial communities of the PH-1 and TH4 wells. For this reason, we abandoned further sampling at these sites.

4.5. Significance and Discussion

In this study, a series of microcosm experiments was conducted to understand what effect increasing pCO_2 would have on a complex microbial consortium metabolizing coal to form methane. One obvious limitation of this type of work is that the pCO_2 levels achievable in laboratory microcosm experiments are much lower than those experienced by microbes under actual reservoir conditions expected at the CO_2 injection site. However, one would expect that a gradient of pCO_2 values would result between the injection site and more distal regions. Our microcosm experiments might mimic conditions in these more distal areas and also permit us to make some general observations of how changes in pCO_2 affects the microbial community, and in coal systems, microbial methanogenesis.

4.5.1. Effect of Increasing pCO_2 on Methanogenesis

In all experiments, pCO_2 was observed to have no discernable effect on rates of methanogenesis. This observation is consistent with recent modeling work wherein it was found that CO_2 injection would only have a moderate impact on methanogenesis if H_2 concentrations are very low (<1µM) (Onstott, 2005). Since H_2 has not been observed to be a significant byproduct of coal fermentation under laboratory conditions (Harris et al., 2008; Jones et al., 2010), it holds that increasing pCO_2 would have little effect on total methanogenesis. Our work here has demonstrated that acetate is the dominant byproduct and precursor for methanogenesis from coal under the conditions tested. Onstott (2005) also found that the free energy available for acetoclastic methanogenesis would remain relatively constant at a variety of temperatures and pressures associated with a deep subsurface CO_2 injection reservoir. Therefore, if acetate availability remains constant, methanogenesis could remain unaffected by CO_2 injection in coal seams.

In the 2.5 and 5 g/L urea amended experiments, the pH increased by roughly 1.5 and 2 pH units, respectively. This change resulted in the inhibition of acetoclastic methanogenesis (Fig. 4.2). This is consistent with the findings of Hunik et al. (1990), though the substrate in their study was poultry manure, and the concentrations of acetate and ammonia used were much higher than in the present work. Ammonia, a byproduct of urea hydrolysis, has also been shown to inhibit methanogenesis in pure cultures at concentrations >400 mM (Sprott and Patel, 1986), which is more than 2X higher than the maximum possible concentration in these experiments, making this an unlikely reason for the observed inhibition. The most likely reason for the inhibition then appears to be the dramatic increase in pH. There are relatively few known species of alkaliniphilic methanogens, including *Methanobacterium thermoalcaliphilicum* (Blotovogel et al., 1985) and *Methanohalophilus zhilinae* (Mathrani et al., 1988) which have pH optima > 8, but these species tend to be found in hypersaline, alkaline lakes.

Comparing each set of experiments is somewhat difficult due to the complex nature of the coal substrate used to support microbial growth. Each experiment was initiated by adding a sterile, anaerobic medium to coal that had been stored at 4°C for months or even years under anoxic conditions in vacuum sealed bags with O_2-scrubbing packets. Although the coal remained saturated and anoxic during these storage conditions, it also appears to have supported the growth of fermentative organisms that in some cases made significant amounts of acetate, as confirmed by subsequent HPLC analysis. This pre-formed acetate was added to the experimental medium as part of the coal inoculum, and methane production commenced shortly thereafter. This occurred for experiments shown in figures 4.2, 4.7 and 4.8. Each of these experiments had an initial acetate concentration between 1 and 4 mM that was derived from the coal itself and which strongly influenced methane production rates throughout the experiment. In contrast, the experiments shown in figures 4.9–4.11 had <100 µM acetate at the start of the experiment and consequently produced far less methane. In the first two sets of experiments when methane production was greater than 1 µmol/g coal, most of the production occurred within the first 21 days (Fig. 4.1, Fig. 4.5, and Fig. 4.6). In the final set of experiments when methane production only reached ~0.3 µmole/g coal (Fig. 4.9 and Fig. 4.10), the production continued throughout the duration of the experiment, reaching maximum values at the final time point. This trend suggests ongoing acetate production, albeit at very low rates, supporting very low rates of methanogenesis (average 0.035 µmole CH_4 day^{-1}). This situation is probably more akin to what would be expected in the subsurface, where acetate is maintained at near-zero concentrations by methanogens consuming it as rapidly as it is made.

Our data show that the methanogenic potential of the microbial microcosms and their response to a given treatment is largely determined by the amount of acetate present at the start of the experiment, which in turn is controlled by the metabolism of fermentative organisms on the coal. Since coal is an inherently recalcitrant, complex, organic substrate, the availability of acetate may be controlled by the access these fermentative organisms have to the substrate. Kolak and Burruss (2006) recently showed that a number of polycyclic aromatic hydrocarbons (PAHs) and high molecular weight *n*-alkanes were mobilized from coal by extraction with supercritical CO_2. These molecules could become a potential feedstock for fermenters if they diffuse into the formation water away from the injection site, potentially increasing the rate of acetate production and enhancing methanogenesis *in situ*.

Work is ongoing to characterize the microbial community in experiments with $pCO_2 > 1.3$ atm and to determine if there is any correlation between microbial biomass and initial acetatecon-centration and methane production. Samples are also being analyzed via 16S rRNA sequencing which may help to elucidate which members of the microbial community were not present in experiments where little methane was produced. We are also preparing samples for quantitative PCR of the mcrA gene, the functional gene associated with methanogens, in order to understand how their numbers are related to pCO_2 and urea amendment.

4.5.1. Field Sampling

Samples collected from the Wallula Pilot site showed that the basalt aquifer slated for CO_2 injection harbors a low-density microbial population that could be impacted by CO_2 injection. Previous studies have shown evidence for microbial life in the Columbia River Basalt (Lin et al., 2012; O'Connell et al., 2003; Stevens and McKinley, 1995). The biodensity measured at this site is commensurate with similar low-energy subsurface sites, including deep granitic groundwater in Japan (Mills et al., 2010), Colorado (Sahl et al., 2008), a deep sandstone aquifer in Montana (Olson et al., 1981), and below the Hanford Site in eastern Washington (Lin et al., 2012). Post- injection analysis of fluid samples will help to determine what impact CO_2 injection and the related changes to groundwater geochemistry have had on this microbial community.

PLFA profiles from the Rangely Field, CO differed with respect to the location of collection. Samples collected from under the CO_2 flooded area (Fig. 4.15) were largely composed of branched, saturated PLFAs including i15:0, ai15:0, i16:0, i17:0 and ai17:0, suggesting a microbial community dominated by gram negative anaerobic bacteria (Lechevalier, 1977). Additionally, the presence of iso- and anteiso PLFAs listed above suggests the presence of SRB (Dowling et al., 1986; Kohring et al., 1994; Taylor and Parkes,

1983), which is consistent with the observation by Chevron employees of significant "souring" problems associated with H_2S production in this area (Roedell, 2011). By contrast, the samples collected from the area outside of CO_2 flooding (Fig. 4.16) were dominated by the branched monoenoic fatty acid i17:1ω7, which has been attributed to hydrogenotrophic SRB belonging to the genera *Desulfovibrio* (Dowling et al., 1988). While it would be difficult to say that the differences between the two sites are due to the CO_2 injection, it is likely playing a role in changing the microbial community structure. The driving factor may be pH, as the pH in the CO_2 flooded area is known to be significantly lower than in the non-flooded area (Klusman, 2003). The dominance of SRB in the wells associated with CO_2 flooding is surprising because the pH in these wells is lower than those outside of the CO_2 impacted area. SRB are generally inhibited by undissociated sulfide that exists at lower pHs (Widdel, 1988). The predominance of SRB may be controlled not by the pH but rather by the injection of groundwater as part of the water-alternating-gas injection process used for CO_2-enhanced oil recovery. It would not be possible with our limited dataset to determine what the controlling factor is.

It is difficult to draw broad conclusions regarding the impact of CO_2 injection on subsurface microbial populations based on this study. However, our work supports the conclusion that CO_2 injection into deeply buried coal seams may not always negatively impact the native microbial community or methanogenesis from coal. This conclusion is supported by the observations that total methanogenesis is determined by the availability of acetate from fermentation of the coal and that acetoclastic methanogenesis generally is less sensitive to the impacts of increasing pCO_2. Our work also shows that the dominant control on methanogenic potential is activity of the fermentative community making acetate to support methanogenesis, and that this activity can be highly variable. Urea amendment may be a viable way to both enhance CO_2 solubility in coal seams and may potentially stimulate growth of the bacterial community, particularly at the lower urea concentrations used in our experiments and $pH < 7.5$. The results from field studies at Rangely, Colorado, Sugar Creek, Kentucky, and the Wallula Pilot site showed the efficacy of using polar lipid techniques to measure low density microbial populations in CO_2 injection zones. Further post-injection analysis will be needed to determine what effects occurred as a results of CO2 injection at these sites.

Task 5. Making Fossil Energy More Sustainable: Technology Pathways and Conflict Reduction

5.1. Goals/Objectives

This task was redirected due to the departure (for family reasons) of the co-investigator that was originally assigned to examine the stratigraphy-specific CO_2 storage options in Colorado's Denver Julesburg Basin.

The understanding of the earth's subsurface and availability of data to document what is there and how it all works has never been greater. Yet, conflicts and acrimonious debate about how we utilize this zone are also greater than ever. Is this because there is more money at stake than before? Is it because of a fear of the unknown or the 'unseen' parts of nature that lie below the ground? Is it because multiple uses of the subsurface always represent a "you win, I lose" scenario—the modern equivalent of the historic conflicts between cattlemen and farmers? These are the reasons why we set out to explore, in a context a bit broader than just CO_2 storage, how technical approaches to dealing with fluids in the subsurface can and should be framed in the context of well-understood scientific and engineering principles. Presenting the public and their elected representatives with such a scientific context will, we believe, prepare all of us better for political acceptance of a range of subsurface engineering activities.

The conflict is most vividly captured in the often acrimonious debate about the oil and gas industry both in its conventional and unconventional incarnations. The physics of combustion of hydrocarbons makes it impossible for fossil energy to attain a carbon footprint anywhere nearly as low as that of renewables. However, there are many offsetting benefits, not the least that fossil energy is still plentiful; it has a global and highly advanced distribution system in place, and the footprint that the fossil energy infrastructure occupies is orders of magnitude smaller than renewable energy facilities with equivalent energy capacity (Fig. 5.1). That factor alone argues for renewed efforts to find technology solutions to reduce the carbon footprint (carbon dioxide, methane, black carbon and trace gases) of conventional and unconventional oil and gas.

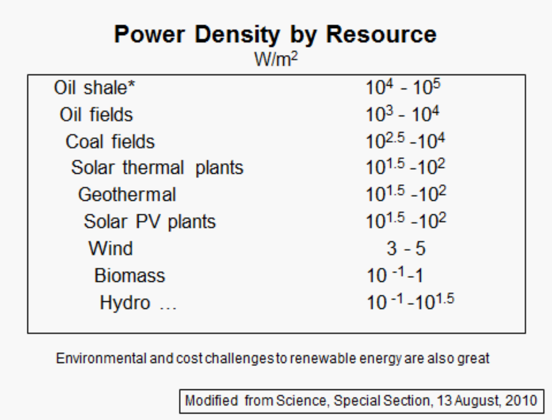

Power Density by Resource

W/m^2

Oil shale*	10^4 - 10^5
Oil fields	10^3 - 10^4
Coal fields	$10^{2.5}$ -10^4
Solar thermal plants	$10^{1.5}$ -10^2
Geothermal	$10^{1.5}$ -10^2
Solar PV plants	$10^{1.5}$ -10^2
Wind	3 - 5
Biomass	10^{-1}-1
Hydro …	10^{-1}-$10^{1.5}$

Environmental and cost challenges to renewable energy are also great

Modified from Science, Special Section, 13 August, 2010

Fig. 5.1. Power density (power per unit area of plant extent) for major energy systems. Calculated from a series of papers in Science, Special Section, August 13, 2010.

5.2. Background

Technology, policy, economics and personal values all can contribute—and have—to the reduction in greenhouse gas emissions from fossil energy currently underway here in the United States. However, current reductions have been mostly due to rapid growth in unconventional natural gas and to the existence of an already developed, but underutilized, power plant capacity that has been able to quickly accommodate this added supply. As documented in figure 5.2, annual CO_2 emissions from the US energy sector have decreased from an all-time high of 6 billion tons/year during 2005–2007 to 5.3 billion tons in 2012.

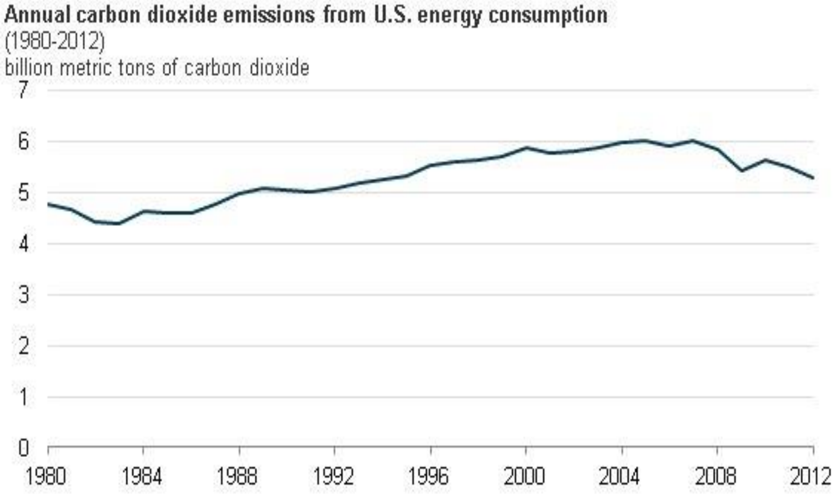

Fig. 5.2. Annual carbon dioxide emissions form U.S. energy consumption. Modified from the US Energy Information Agency Website (U.S. DOE, 2011).

The shift from coal to natural gas, however, is not automatically an unmitigated good. Offsetting the benefits of reduced emissions of CO_2 is the fact that the infrastructure, related to production, transport, storage and consumption of methane, is a pretty leaky system, potentially offsetting many of the gains on the combustion side. This issue is now emerging as a major topic of investigation throughout industry and R&D organizations. For example, ARPA-E has recently issued a call for proposals to address these GHG leakage technology challenges. The great focus now being put on methane emissions suggests that this issue is also moving forward towards a (partial) technology solution.

There are many intertwined policy and economic issues, one of which is that decreasing demand for coal in the domestic market drives US exports of that fuel, shifting some emissions offshore. Also, there are policy and political issues, for example, managed campaigns where some governments use US public opposition to shale fracturing as an argument to try to undermine development of unconventional natural gas, thereby keeping client states dependent on more expensive conventional gas being delivered via existing pipeline systems.

In addition, there are also many issues related to synergy versus conflict between natural gas and renewable energy. Cheap gas does in fact make some renewable energy technologies non-competitive, potentially increasing emissions. Yet, cheap natural gas to 'firm up' intermittent renewable power works the other way. Liquefaction of US natural gas and its export to overseas markets would increase domestic gas prices, a potential boon to the gas industry as well as the renewable energy industry, but an economic drag on many highly energy-dependent manufacturing industries, including industrial chemicals.

Finally, there are a number of challenges (and opportunities) related to economically viable management, treatment and beneficial reuse of co-produced water, protection of surface-water resources, potential infringement of water rights, leakage of drilling fluids or petroleum products into ground water aquifers, and contamination of aquifers due to surface spills and holding ponds for fracturing fluid or co-produced waste.

5.3. Methods/Approach — A Short History

In contrast to some popular recent perceptions, the quest for unconventional fossil energy has a long history going back to World War II. The war pushed syngas research in Germany and unconventional oil and gas here in the United States. In response to the Middle East-related energy price increases in the late 1970s, the US Federal Government invested in R&D for unconventional energy development. The best known projects were the Eastern Gas Shales Project, initiated in 1976 by the US Department of Energy (DOE), followed by the Multiwell Experiment in western Colorado (MWX) also sponsored by the DOE explicitly to increase natural gas production from low-permeability sandstone reservoirs. MWX drilling commenced in 1981; the field program was completed in 1988; and reporting was completed in 1990. In parallel with these research projects, the engagement of driven and creative entrepreneurs led to further advances and the emergence of economically viable technologies to improve unconventional gas production, first from coal beds (1980s), then from fractured tight sandstone (1990s) and then ultimately today's dramatic increase in production both of gas and oil from fractures shale (and other tight lithologies). Nearly 50 years of combined government-funded experiments and industrial R&D and testing lie behind the ultimate emergence of today's global industry in unconventional resources.

In an increasingly resource-hungry world, this development is essential. Now that we have learned how to produce unconventional oil and gas economically, we must ensure that these fuels are used to reduce emissions compared to past practices and to improve management of surface and subsurface water resources. In short, the emerging unconventional fossil energy industry will have to be sustainable.

5.4. Task Results

5.4.1. Emissions Reduction Pathways

The dominant emissions from fossil fuel that drive global warming are carbon dioxide, methane and black carbon (soot), in that order. Carbon dioxide is the biggest concern both because its radiative forcing is the highest, at 1.68 W/m^2, and because it stays in the atmosphere a long time. Methane has the second highest radiative forcing, at 0.97 W/m^2. Methane is often referred to as a 'short-lived' climate pollutant because its half-life in the atmosphere is much less than that of CO_2, so once emissions cease, there will be noticeable reductions on a relatively short time scale. Black carbon is also a big problem, now estimated to account for a radiative forcing of 0.64 W/m^2.

Carbon dioxide emissions could be significantly reduced as a direct consequence of growth in unconventional fossil energy development provided the growth is managed correctly. As mentioned above, over the past 10 years, the rapid growth in unconventional gas in the US market has reduced domestic CO_2 emissions by about 700 million tons annually (Fig. 5.2) because it has replaced coal. This amount corresponds to ~12% of US CO_2 emissions. Unfortunately, the law of unintended consequences has kicked in, and less demand for coal in the United States has made coal more competitive in other markets, including Europe, where both Britain and Germany have experienced an increase in coal use, and therefore, coal-related CO_2 emissions. This state-of-affairs is also aggravated by the very low price of CO_2 emissions permits in the European trading market, which makes it uneconomic to use natural gas for power generation in Germany and, at best, a break-even proposition to do so in Britain (Fig. 5.3).

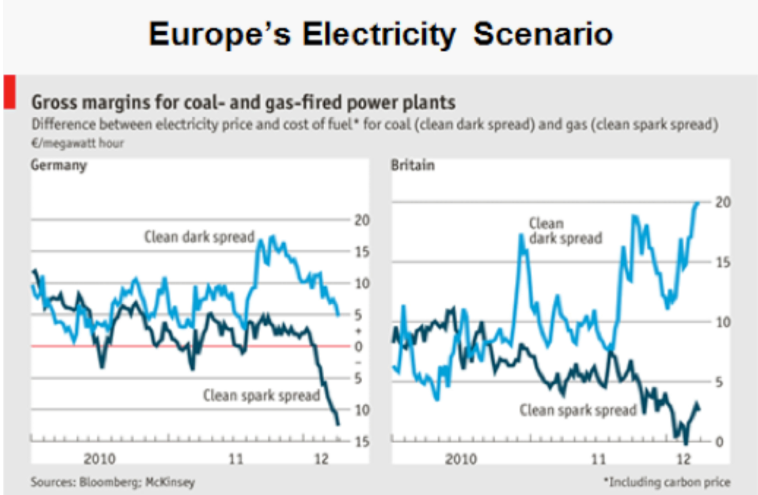

Fig.5.3. Relative cost of power production in Germany and Britain using natural coal (clean dark spread) and natural gas (clean spark spread) (Olivier et al., 2012).

Research and testing on CO_2 capture, utilization and storage (CCUS) is ongoing, but yet at too small a scale to have measurable impacts on US emissions. Utilization of CO_2 for enhanced oil recovery (EOR) in depleted oil fields, however, is a growth industry in the United States, as is also its use in unconventional (tight) oil production, creating a new and promising market.

More than 30 countries, US states, and some Canadian provinces now have enacted CO_2 emissions control policies, economic incentives or taxes. The annual UN COPs, or "Conference Of the Parties", are systematically moving forward with draft agreements to replace the 1992 Kyoto Treaty. Some might argue that the Kyoto Treaty was a failure, yet the fact that its update and replacement is now emerging as a likely outcome of an increasingly growing number of U.N. member nations, would imply the opposite.

The fact that the United States never signed the Kyoto Treaty does not seem to have mattered much because the emergence of natural gas has driven coal off the market for domestic power production at a remarkably fast rate (Fig. 5.4).

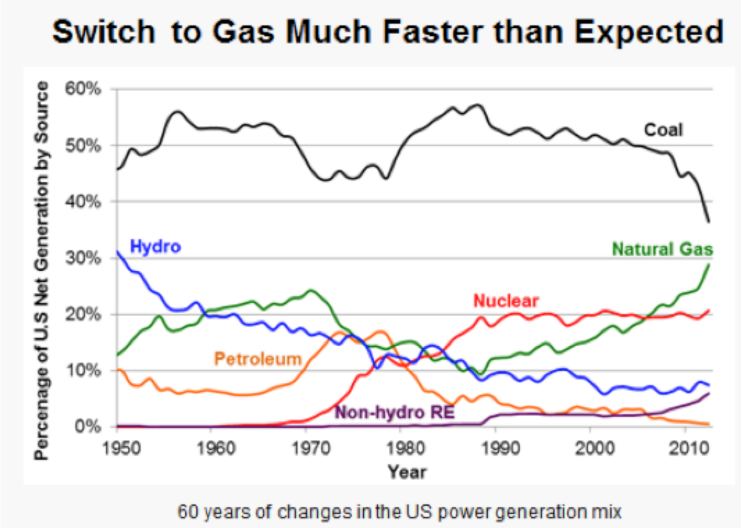

Fig. 5.4. Power generation in the U.S. by resource for the past 60 years. After completion of this report, in early 2012, the curves for coal and natural gas actually did cross, so NG gas (in August 2013) accounts for the largest share of electricity production in the United States (Logan, et al., 2012).

Shortly after the paper that figure 5.4 was taken from was released (fall of 2012), the curves for coal and gas-based power production crossed, such that in 2014 a higher percentage of US electricity is derived from natural gas than from combustion of coal. The data and discussion in the previous paragraphs might lead some to jump to the conclusion that the problem is solved: natural gas is replacing coal and emission concerns are history; thus, as soon as the rest of the world also transitions from coal to unconventional natural gas, the global warming problem will be solved.

Not so fast! Some coal is being replaced by natural gas, and while it is true that CO_2 emissions across the US are down as a consequence, natural gas has other emissions including methane (CH_4) and a smaller amount of other greenhouse gases. Methane concentrations in the atmosphere are measured in parts per billion (currently at about 1800 ppb) rather than parts per million as for CO_2, which now exceed 400 ppm at the Mauna Loa Observatory in Hawaii, where the first observations started in 1957. See Oak Ridge National Laboratory's Carbon Dioxide Information Analysis Center at (see *http://cdiac.ornl.gov/)* for the most up-to-date numbers.

Methane emissions are high and getting higher both because of fossil energy and biological sources of release. These are exceedingly difficult to control, but one release mechanism that is, in principle, controllable is the leakage from the natural gas infrastructure. Most will have seen infrared pictures of plumes of methane from natural gas storage facilities, but actual methane leakage numbers are hard to come by (Alvarez et al., 2012; Petron et al., 2011).

Quite recently, methane emissions have emerged as the number one global warming issue in many peoples' minds. Resources are being made available by the federal government and private industry to establish more facts. As mentioned before, from the perspective of the chemistry of combustion, methane does have lower emission than coal because burning of methane releases the energy of four hydrogen-to-carbon bonds for each CO_2 molecule generated. In contrast, burning coal releases the energy of only one hydrogen-to-carbon bond for each CO_2 molecule. The problem with methane, however, is the part which is not combusted but is released to the atmosphere during production, flow-back, transportation, storage and distribution. Minimizing methane release, therefore, is a complex issue of management of often very long-lived infrastructure and the difficulty in pin-pointing where the leakage occurs. The 'upside', if you wish, with methane emissions mitigation, is that this gas is a highly valued commodity and all producers, transmission companies and consumers would benefit financially from emissions reductions. Also, a tighter emission infrastructure would reduce hazards.

Parts of the current uncertainty surrounding published methane concentration numbers are a result of differences between measurements obtained from aircraft (often referred to as top-down) versus those that are measured from the ground (bottom-up). Reconciliation of methane concentration numbers obtained by such different approaches is currently a big challenge. This issue is about to be addressed in a fairly large study in which some members of this research team will be engaged.

5.4.2. Joint Sustainability of Energy Production and Water Resources

Water resources sustainability is a critical component of oil and gas production, including unconventional sources. McCray and Thyne (2009) outline some critical issues regarding joint sustainability of water resources and petroleum energy production in an editorial in the journal *Ground Water*. Some of the primary issues include economically viable management of co-produced water, protection of surface-water resources, treatment and beneficial re-use of co-produced water, potential infringement of water rights, leakage of drilling fluids or petroleum products into ground water aquifers, and contamination of aquifers due to surface spills and holding ponds for fracturing fluid or co-produced waste. We now understand that a new issue has arisen around water resources: the public perception that unconventional energy production will spoil local water resources. This latter public-perception issue is particularly strong when associated with unconventional energy production, primarily because of the discussion and controversy surrounding fracturing technologies used to increase permeability and porosity of formations to enhance petroleum fluid flow to the well.

First, we will examine the intriguing concept of treating co-produced water for beneficial use. Approximately 21 billion barrels, or 880 gallons of produced water, are generated each year in the United States from nearly a million wells (Clark and Veil 2009). In comparison, the City of Los Angeles used about 215 billion gallons of water in 2007 (about 660 acre-feet of water in public utility terms), and Denver currently uses about 82 billion gallons per year (250 acre feet) supplied by Denver Water[1]. Thus, if we could treat 1/3 of co-produced water each year to water-quality standards for beneficial use (not necessarily as clean as drinking water standards), then we could supply all the public water needs for Denver and Los Angeles! Of course treating co-produced water is not a simple matter because of high salt concentrations and an impressive suite of dissolved chemicals that would be considered contaminants (metals and organic chemicals, primarily) (Hickenbottom et al., 2013; US GAO, 2012). Indeed, treatment of co-produced water is currently in the research arena, and technology that would allow us to treat produced water to drinking water standards is several years away. However, treating this water to standards that are acceptable for discharge to the surface-water environment is rapidly becoming feasible. Then it could be used for local beneficial uses (i.e., agriculture, ground-water recharge, local industries). An additional challenge is that many wells are located in remote locations where the treatment infrastructure does not exist. However, with respect to unconventional oil and gas, wells are now being developed in urban settings, and retrofitting treatment plants in urban areas to treat co-produced water for some beneficial reuse is feasible, particularly in cities such as Los Angeles, Denver, and Houston where water managers are attempting innovative solutions to current and future water-supply problems.

Public perception of the risks of unconventional energy production to water resources, whether based on fact or misinformation, will ultimately control an energy company's "license to operate" in particular states, counties, and even specific cities. Many cities in Colorado have attempted to put laws in place that limit, stop, or delay fracturing. Another interesting example is the significantly different position of politicians in Pennsylvania, which tend toward supporting unconventional energy development, versus New York, which puts forth much more opposition. Both states have similar demographics and geology, but public perceptions (assumed to drive politics) are much different. Thus, it is critical for energy companies to engage the technocrats, bureaucrats, and the public in an honest dialogue with effective communication about public needs, perceptions of risk, and actual risks (which can include hazards to natural resources, as well as economic and social issues). Given the dynamics of human social behavior, developing methods for effective communication of risks related to technology development is also a research area (Schneider and Knaak, 2013; Schneider and Sneider, 2011).

From a technology management standpoint, we need to develop better controls on subsurface engineering to ensure extraction of desired fluids and disposal/re-use/reinjection of the undesired ones with minimal negative effects on geologic formations that are not targeted for either (i.e., freshwater aquifers). For example, the much discussed EPA report regarding shale-gas production near Pavillion, Wyoming convinced much of the public that fracturing fluids were responsible for groundwater contamination (US EPA, 2011). The report suggests that fracturing was conducted near the bottom of a formation that contained an aquifer used by the community. A rigorous hydrologic investigation and risk assessment, prior to development, would prevent most similar problems in the future. Much complex chemistry and hydrology is involved in the full understanding of how fluids and contaminants move in the subsurface during unconventional energy operations, but development of tools and intelligent sensors that allow us to monitor and manage subsurface flows is currently in progress.

---

[1] Denver Water (2014), Denver water key facts, *http://www.denverwater.org/AboutUs/KeyFacts*

From a natural systems standpoint, we need to better understand how water demands for unconventional resources influence the natural water balance in the developed watershed and how multiple current and future uses of water can be sustained. That is, integrated environmental assessments should be conducted that also include impact on air quality. We should understand how produced water releases impact the environment and how the environment may naturally mitigate or buffer water pollution. One example is the impact of spills on subsurface water resources. Spills are inevitable and are a real potential problem. Waxman et al. (2011) identified 29 regulated chemicals of concern (mainly organics and metals) within the hydraulic fracturing fluid. However, some natural settings have an innate ability to mitigate contamination because of favorable soil types, shallow subsurface geology, and sufficient depth to water table. Other sites may be highly susceptible to spills, and thus extra precautions could be taken to mitigate the impact of those that occur. Rigorous hydrogeological risk assessments, and communication of these assessments to the public, would provide confidence that energy production is jointly sustainable with water resources.

Task 6. Assessment of Scale on Pore-volume and Permeability Estimates for Geologic Storage of CO_2 in Saline Aquifers

6.1. Goals/Objectives

Task 6 addresses how reservoir-scale permeability models vary depending on the scale of investigation of the input permeability values. A common practice in reservoir modeling is to directly use permeability measurements from core-plugs or probe permeametry in petrophysical modeling. Three-dimensional permeability model cells are often several orders of magnitude larger than the scale of investigation (volume support) of the permeability measurement. This scale difference can produce unrealistic results in the permeability model, which may not be representative of the reservoir heterogeneity.

This study addresses the relationships between probe permeameter-based measurements and upscaled values of permeability due to the differences in scale of volumes associated with the permeability measurements and reservoir model cells. Researchers created 3-D core lithofacies and permeability models of the Terry Formation in the Denver Basin of Colorado. Permeability values were measured using a mini-probe permeameter. These “original” permeability values were acquired by facies and lamina type, and flow-based upscaling was used to generate effective-permeability values by facies.

Using the original- and effective-permeability values, the significance of fine-scale permeability heterogeneity associated with lithofacies that exist below the resolution of reservoir model cells was investigated through comparative analysis of field-scale, 3-D permeability models and resulting static connectivity of permeability distributions.

6.2. Background

Sandstone reservoirs commonly contain heterogeneities at different scales that are related to the stratigraphic framework, lithofacies, and sedimentary structures. At the bedding and lithofacies scale, it has been shown that sedimentary structures have significant control of porosity and permeability heterogeneity and associated fluid flow (e.g., Weber, 1982; Hurst and Rosvoll, 1991; Corbett and Jensen, 1993; Jackson et al., 2003). Therefore, to model fluid flow through reservoirs, it is essential to model the spatial distribution of permeability that is tied to stratigraphy and lithofacies. For 3-D reservoir permeability modeling, it is common to directly use measurements obtained from core plugs or minipermeametry. The volume of a 3-D reservoir model cell (>6 million in^3 [$\sim 10^8$ cm^3]) is typically several orders of magnitude greater than the volume evaluated through minipermeametry or the volume of a core plug (0.18-1.8 in^3 [3-30 cm^3]) (Jackson et al., 2003). If not properly accounted for, the scale difference can produce unrealistic results in the 3-D permeability model that are not representative of the reservoir heterogeneity.

To create 3-D reservoir permeability models using data that are measured at the lamina scale, permeability values should be upscaled to account for the volume difference between the lamina and the size of a typical geologic-model cell. Similar studies have focused on the integration of small-scale core plug or minipermeameter measurements and wire-line well-log data (Haldorsen, 1986; Worthington, 1994; Nordahl et al., 2005). The scaling of permeability (or any property) in this study is referred to as upscaling, which results in the generation of an effective property. Upscaling refers to the process of transforming a fine-scale grid that contains many data points into a courser grid using averaging techniques, flow-based simulation, or other methods (Wen and Gomez-Hernandez, 1996). Effective permeability, as used in this study, is described as “the permeability of a homogeneous block which, under the same boundary conditions, will give the same average flows as the region the block is representing” (Pickup et al., 1994; p. 230). Some properties, such as porosity, can be upscaled by using an arithmetic average; however, permeability data should not be upscaled using an arithmetic average as it is not an additive property (Tidwell and Wilson, 1997; Renard and de Marsily, 1997; de Marsily et al., 2005; Nordahl and Ringrose, 2008). Common methods to upscale permeability include using a flow-based simulation to generate a property (e.g., flow-based upscaling or flow-based scale averaging), Monte-Carlo analysis, and data inversions related to solving of flow equations through a small-scale (measurement-scale) embedded in the upscaling block (Wen and Gomez-Hernandez, 1996; Tidwell and Wilson, 1997; de Marsily et al., 2005; Nordahl et al., 2005; Ringrose et al., 2005).

A probe-type permeameter was chosen for this study because it is useful for relatively rapid and accurate data acquisition (Tidwell and Wilson, 1997; Ringrose et al., 2005) and for obtaining permeability measurements on lamina (bedding) that are smaller in scale than the dimensions of a core plug. Others have used similar approaches, including Corbett and Jensen (1993), who used a probe-permeameter and upscaling of the fine-scale grid into a coarse grid. While their specific method for upscaling is different, the overall process is similar in that they collected permeability data and used numerical simulations to generate effective properties. Corbett and Jensen (1993) focused on lamina-scale structures for their measurements and have shown that data collected at this scale and upscaled correctly leads to different flow characteristics in the reservoir. Ringrose et al. (2005) detailed a similar approach to the one used in this study for evaluating vertical permeabilities. Permeability data were acquired from laminated Brent Group cores in the North Sea using a probe-permeameter and were upscaled using a similar flow-based upscaling algorithm. They showed that effective permeabilities generated using this approach are better for characterization of oil reservoirs than permeability estimates derived from well logs using numerical calculations. Other previous works that have used processes similar to ones outlined in this study include, for example, Durlofsky (1991), Corbett and Jensen (1993), Ringrose et al. (1993), Tidwell and Wilson (1997), Jackson et al. (2003), and Nordahl et al. (2005). Many of these papers have shown that small-scale sampling of data and upscaling are needed to preserve the permeability anisotropy in the large-scale models.

6.3. Methods/Approach

The study area is located within Spindle field in the Denver Basin of Colorado (Figs. 6.1 and 6.2). Spindle field is one of the oldest producing fields in Colorado, having been discovered and producing since 1971 (Porter and Weimer, 1982; Weimer, 1996). It is the second largest oil and gas field in the basin and has produced over 49.2 million barrels (7.9 billion liters) of oil and over 236 billion ft^3 (6.7 billion m^3) of natural gas (Weimer, 1996). Within Spindle field, the Cretaceous Terry and Hygiene formations are two heterogeneous siliciclastic formations that form petroleum reservoirs and are the focus of the analysis in this study. Spindle field was chosen given the abundance and availability of data (digital well and core data) and data density. The data set includes four cores (263 ft [80.1 m] total length) from Spindle field and the surrounding area (Fig. 6.1), digital and raster well-log data for 9 wells (Fig. 6.2), 832 minipermeameter measurements by lithofacies that were acquired from the cores, and 1539 minipermeameter measurements acquired from core plug standards for calibration as part of this study (ppendix B). Two of the cores penetrate the stratigraphically higher Hygiene Formation and three penetrate all or part of the Terry Formation (the Champlin # 369 well samples both formations; Fig. 6.1). Probe permeametry was conducted on individual lamina of sedimentary structures on the 4 cores to determine average permeability values for sandstone and mudrock lamina. Two of the four cores (one Terry Formation and one Hygiene Formation) were modeled using a near-wellbore modeling program to create fine-scale (inch-scale) model of sedimentary structures in each. These models were populated with permeability data acquired from the probe permeameter and upscaled using a flow-based simulation algorithm to generate an effective property.

The flow-based upscaling procedure creates an effective permeability value for each facies in the fine-scale model. In order to compare how the effective-permeability values compare to the original values, the two are evaluated separately through static connectivity analysis. To do this, facies models along with porosity and both types of permeability models were created using well-log and core data (Fig. 6.2). Pseudo-wells were used with a 10-ac (4-hectacre) spacing (Fig. 6.2) and static connectivity to these wells was determined for a series of porosity and permeability cutoffs to compare the differences in permeability variation and connectivity between models based on probe-permeameter measurements (directly) and upscaled values of permeability.

6.3.1 Geologic Setting

The Denver Basin is a Cretaceous foreland basin that spans most of eastern Colorado and southeastern Wyoming (Fig. 6.1; Moredock and Williams, 1976; Pittman, 1989; Weimer, 1996; Higley et al., 2003). The basin was formed as part of the Laramide Orogeny when the basin was downwarped as a result of uplift and movement along basement Precambrian faults (Raynolds, 2002). The basin is classified as a Laramide perimeter basin with a broad asymmetric bowl shape that stretches onto the mid-continent (Dickinson et al., 1988; Pittman, 1988). The basin is bounded on the east by the Front Range portion of the Rocky Mountains but has no definitive structural boundary in the east (Weimer 1996; Dickinson et al., 1988). In the south, the basin is separated from the Raton Basin by the Apishapa Arch (appendix A). The northern portion of the basin is bounded by the Hartville uplift and Cambridge-Chadron Arch in present day Wyoming. The northern half of the basin is also subdivided by the Greely Arch and creates the Cheyenne sub-basin.

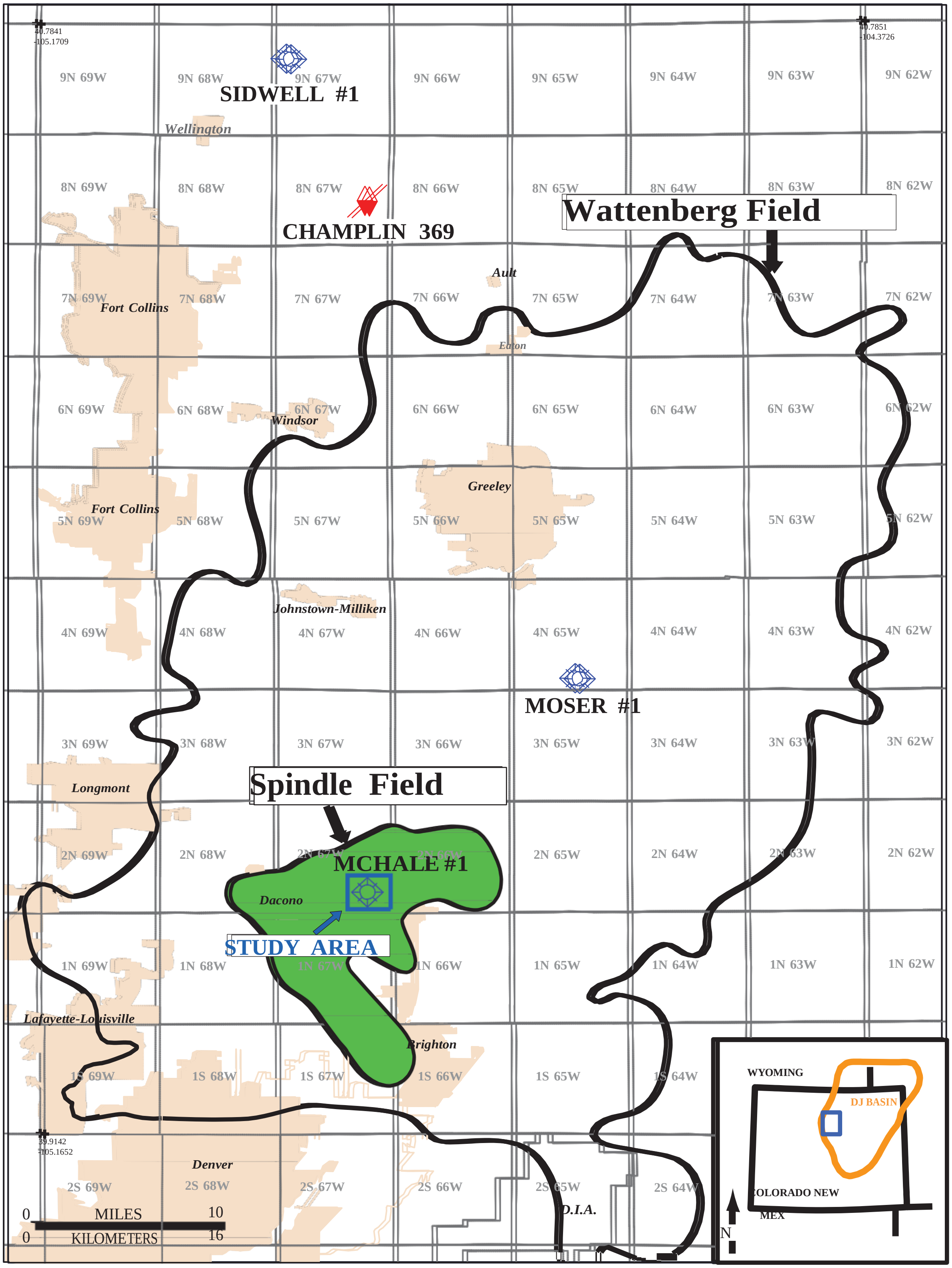

Fig. 6.1. Location map of study area in Spindle Field, Denver Basin, Colorado. Blue box on inset map shows location. Wattenberg field outline from Colorado Oil and Gas Conservation Commission website.

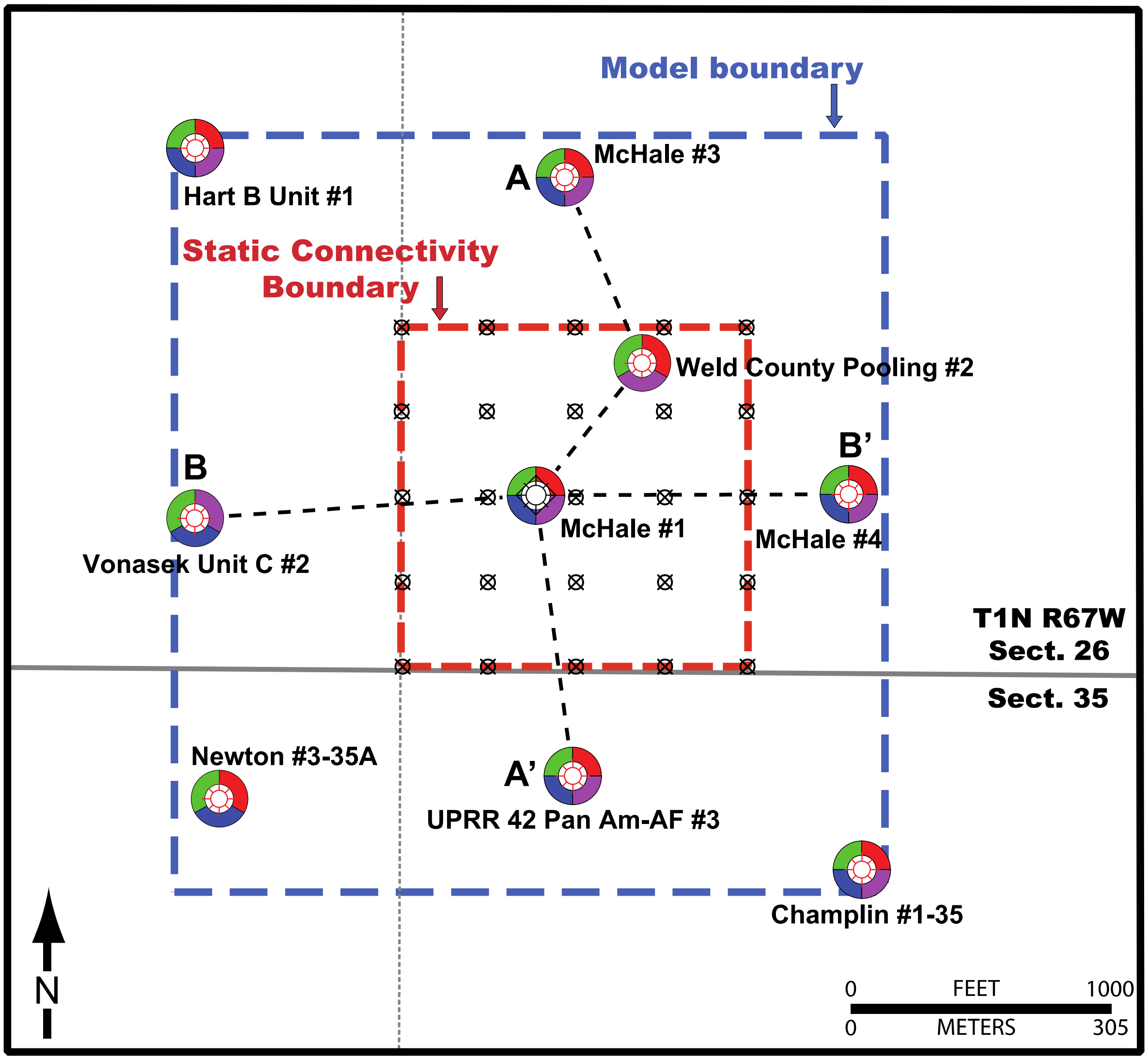

Fig. 6.2. Study area showing well locations with logs present along with static connectivity analysis boundary and pseudowells on a 5-ac (2-hectacre) spacing (⊠). Distance between wells = 330 ft (100.5 m). Color ring around each well corresponds to the logs present in the Terry Formation. Green=gamma-ray, blue=density porosity, purple=resisitivity, red=spontaneous potential. See figure 6.1 for location in Spindle and Wattenberg fields. Cross-sections of figure 6.6 are shown (dashed lines).

Prior to the Laramide Orogeny, the area that is the Denver Basin was a coastal plain that followed the draining of the Cretaceous Western Interior Seaway (Raynolds, 2002). The uplift of the Rocky Mountains disrupted this coastal plain system and separated it into an eastern and western section (Dickinson et al., 1988). As the basin formed, sediments were shed from the newly formed Rocky Mountains and other areas and began filling the basin with continental and marine sediments. The sediments were sourced from as far away as present day Utah and Nevada (Kiteley, 1977; Helsley, 1985; Dickinson et al., 1988).

The Terry and Hygiene formations are both members of the prolific late Cretaceous Pierre Shale located throughout the Denver Basin (Fig. 6.3). The Terry and Hygiene formations have been interpreted as offshore bars (shelf sandstones), beach deposits (shoreface sandstones), and deltaic sediments that were deposited in the Cretaceous Western Interior Seaway (Weimer, 1976; Kiteley, 1977; Porter and Weimer, 1982; Pittman, 1988, 1989; Imam, 1989; Al-Raisi et al., 1996; Weimer, 1996; Slatt et al., 1997; Ladd, 2001; E. R. Gustason, 2012, personal communication). One hypothesis is that both formations are shelf sandstones that were sourced from the Parkman or time equivalent delta in Wyoming (Kiteley, 1977; Imam, 1989; Porter and Weimer, 1982; appendix A). Al-Raisi et al. (1996) suggests the Terry Formation was deposited as discrete sandstone bars near a delta whereas Porter and Weimer (1982) suggest that southerly moving storms would have transported sediments from the delta and moved them the distance of approximately 80 mi (133 km) to where the Terry and Hygiene formations both exist today. There is, however, no direct evidence of storm transportation or any other significant transportation mechanism beyond tidal forces to show how the sediments were moved or that they could have been moved over a great distance.

The Late Cretaceous Terry and Hygiene formations in the Denver Basin are commonly referred to as the Sussex and Shannon formations respectively (Kiteley, 1977; Porter and Weimer, 1982; Helsley, 1985; Pittman, 1988, 1989). However, based on trace-fossil evidence, the Sussex and Shannon formations (of the Powder River Basin) are not time equivalent to the Terry and Hygiene formations of the Denver Basin (appendix B; Kiteley, 1977). The stratigraphic terminology of Kiteley (1975, 1977) is used in this study for the Terry and Hygiene formations of the Pierre Shale in the Denver Basin (appendix B).

6.3.2 Facies and Reservoir Stratigraphy

Four lithofacies are interpreted for the Terry and Hygiene formations: wavy laminated sandstone, planar cross-laminated sandstone, structureless sandstone, and ripple cross-laminated sandstone (Fig. 6.4). The facies are identified based on lithology and sedimentary structures and do not take into consideration the degree of bioturbation. However, bioturbation is prevalent throughout the entire cored interval in both the Terry and Hygiene formations. Among the trace fossils identified in this study and others, the most common are asterosoma, teichichnus, planolites, and paleophycus. Other fossils identified in this area are listed in appendix A and are shown in Helsley (1985).

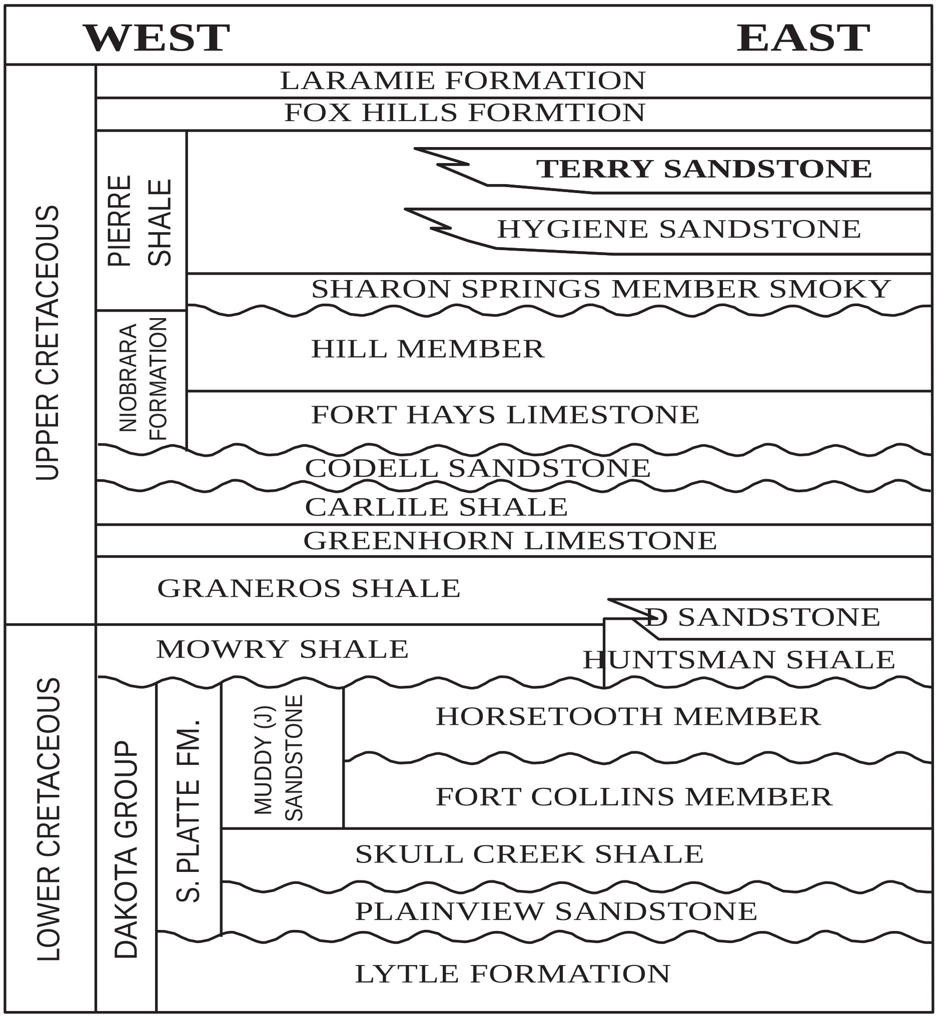

Fig. 6.3. Stratigraphic column for Wattenberg field, Denver Basin, Colorado. Modified from Higley et al., 2003.

For the upscaling portion of this study, the Terry and Hygiene formations are both used to evaluate the upscaling effects on permeability. However, the comparison of the two permeability types through static connectivity is only completed on the Terry Formation. As a result, only detailed information on the Terry Formation including reservoir zonation and log response is discussed. Information on the Hygiene Formation upscaling results is presented later. The Terry Formation in this area is divided into two reservoir and two non-reservoir zones. The top of the Terry Formation was determined based on core observations (appendix A) from the McHale #1 well and exhibits a relative gradational change from interbedded sandstone and mudstone layers to a dominantly sandstone section. The base of the Terry Formation was also determined from the same core and exhibits a fairly sharp contact between the sandstone facies of the Terry Formation and offshore, heavily bioturbated mudstones of the Pierre Shale. Within the Terry Formation, three additional horizons are interpreted based on log responses and core observations that divide the interval into two cleaner, sandstone-rich (reservoir) zones and two mudrock-rich (non-reservoir zones (Fig. 6.5). The non-reservoir, mudrock-rich intervals are sandstone facies but are referred to as non-reservoir, mudrock-rich intervals due to their higher mudrock content as compared to the sandstones in the reservoir intervals. The reservoir zones are characterized primarily by lower gamma-ray (GR) values, a negative spontaneous potential (SP) excursion, and slightly higher porosity (relative to non- reservoir zones) (Fig. 6.5). The non-reservoir mudrock-rich intervals show limited SP response (values near baseline) and relatively higher gamma-ray log values. Deep resistivity (RESD) shows an increase of several ohm-meters in the reservoir zones and a decreased response in non-reservoir zones (Fig. 6.5). Additionally, relatively higher average porosity (range is 9 to 13%) exists within the sandstone-rich units. However, there are zones within the sandstone-rich intervals that contain relatively lower porosity (7.5 to 9.5%). This could be a result of differential cementation, which is observed in the cores.

Porosity is varied across the reservoir zones and shows the same overall trends of higher porosity values compared to non-reservoir zones. Within the reservoir zones, porosity values typically increase upward and have the highest porosities at the top of the reservoir zones (Fig. 6.6). The non-reservoir zones show a smaller amount of pore space than the reservoir zones by several percent depending on location in the study area. A detailed petrographic analysis on a nearby well in Spindle field (Larese, 2008) indicates that the primary control of reservoir porosity is authigenic clay infiltration. Throughout most of the Terry interval, authigenic clay comprises approximately 23% of the total cored volume and is a major pore-filling component. Additionally, a secondary control on porosity is preburial compaction that reduced original porosity by as much as 53% during the time of deposition (Larese, 2008).

While this compaction and loss of porosity is significant, authigenic clay infiltration into the pore network was considered to reduce porosity and reservoir quality more.

Facies Codes and Facies	Description	Depositional Processes	Core Image
A - Wavy Laminated Sandstone	**Texture:** moderately sorted, upper fine-grained sandstone, siltstone **Structures:** Wavy laminations **Average Thickness:** 1.90 in. (4.83 cm) **Mudrock Content:** 10-70% **Comments:** bioturbation likely causing wavy laminations.	Bidirectional flow Bioturbation	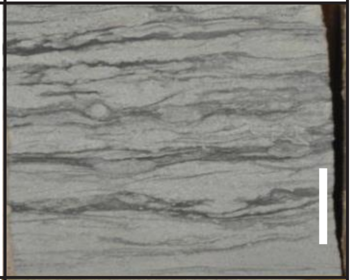
B - Planar Cross- Laminated Sandstone	**Texture:** moderate to well sorted, lower fine- to upper fine-grain sandstone, siltstone. **Structures:** planar laminations **Average Thickness:** 1.42 in. (3.61 cm) **Mudrock Content:** 5-15% **Comments:** low angle dips present (0-15°)	Unidirectional traction currect (upper flow regime)	
C - Structureless Sandstone	**Texture:** moderately sorted, lower fine- to upper medium grained sandstone. **Structures:** none **Average Thickness:** 1.38 in. (3.51 cm) **Mudrock Content:** 0% **Comments:** bioturbation could have homogenized the intervals	Rapid depositions (storm deposit) Bioturbation	
D - Ripple Cross- Laminated Sandstone	**Texture:** moderately to well sorted, upper very fine- to lower medium-grained sandstone, mudrock **Structures:** unidirectional ripple foresets **Average Thickness:** 1.01 in. (2.57 cm) **Mudrock Content:** 0-20% **Comments:** migration direction unknown, bioturbation disturbs nearly all samples	Unidirectional flow	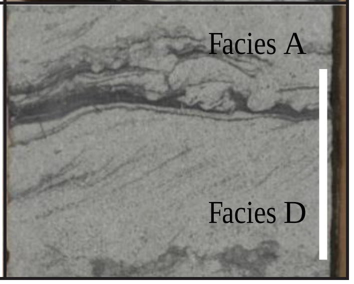

Fig.6.4. Facies codes, facies, and descriptions of the four facies modeled. Scale bars are 1 in (2.54 cm

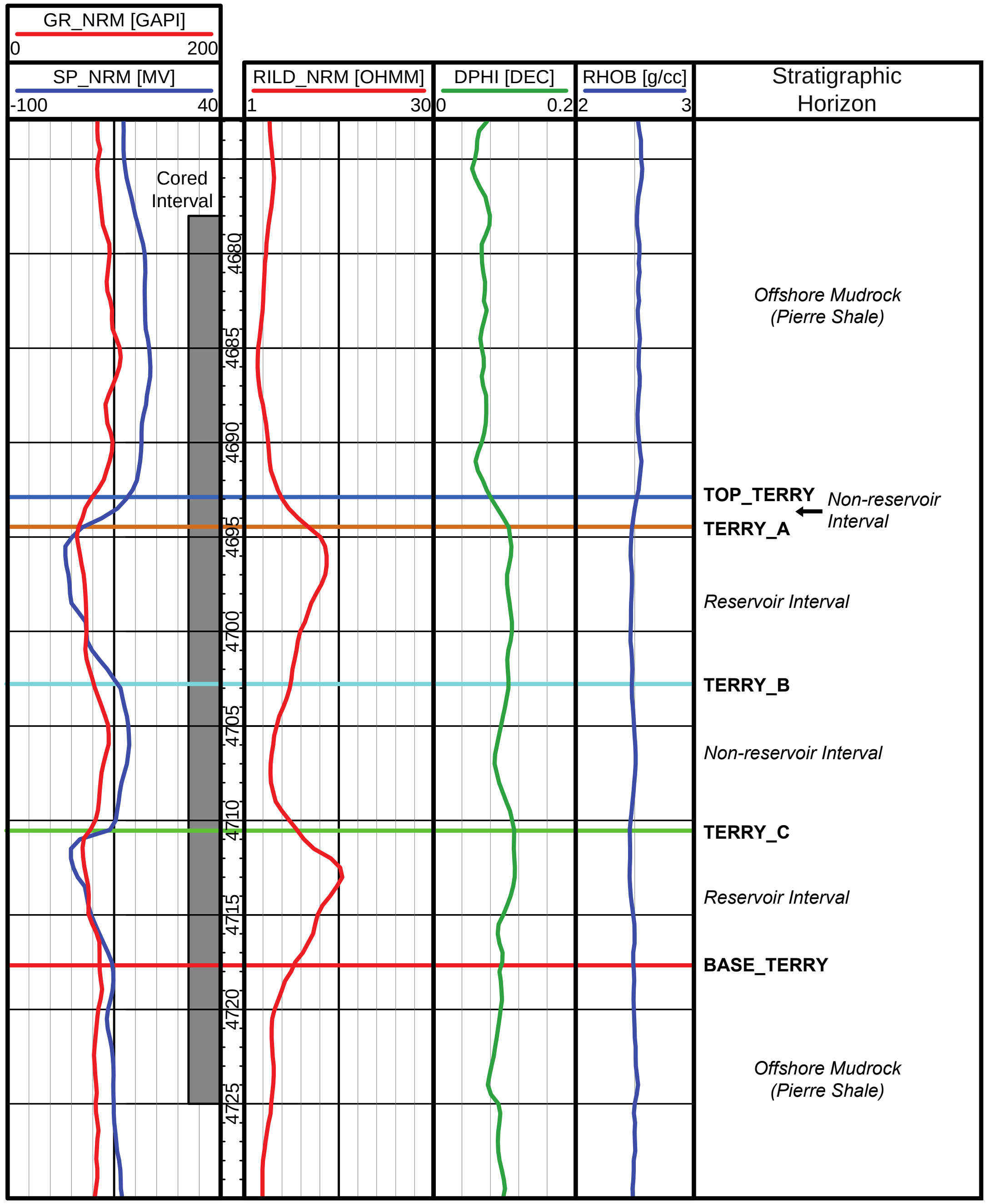

Fig. 6.5. Log suite and cored interval for McHale #1 well (API: 05123076430000) with stratigraphic horizons. Gray bar indicates cored interval. Log response for reservoir intervals includes cleaner GR response, negative SP excursion, and higher porosity. Measured depths in feet. Well location shown in Figure 1.

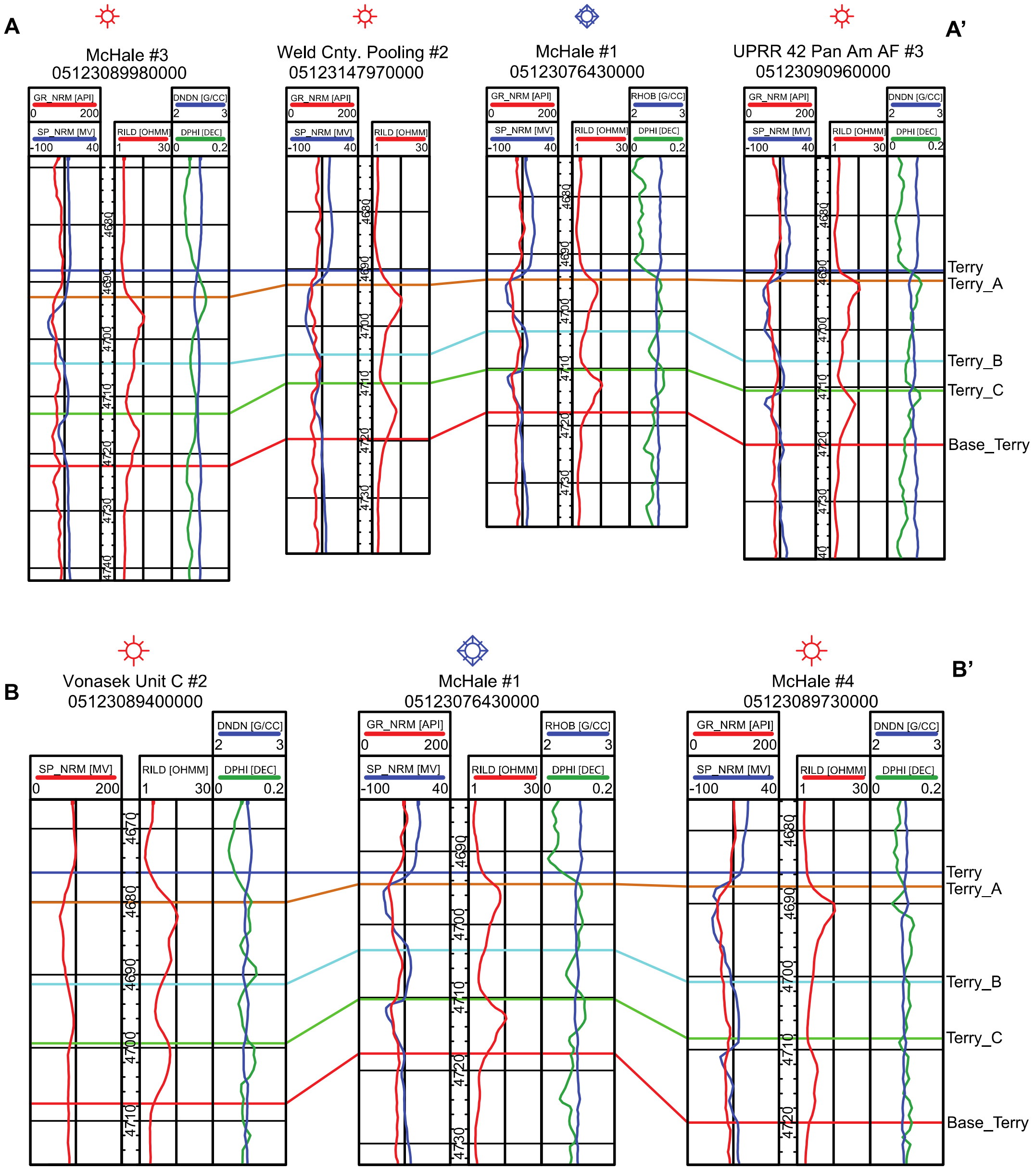

Fig. 6.6. Stratigraphic cross-sections flatten on the top of the Terry Formation showing log suites through the model area. Reservoir intervals are shown with negative SP excursions, higher resistivity, and higher porosity compared to non-reservoir zones. No horizontal scale; distance between wells is uniform. Measured depths are in feet. Locations are shown in figure 6.2.

The fine-scale 3-D core models are then used to generate effective-permeability values by lithofacies using flow-based upscaling.

To create 3-D core models, known as near-wellbore models (NWM), a fine-scale surface-based stochastic modeling software was used that models the core at the lamina scale (Wen et al., 1998). Whereas sedimentary process-based modeling methods simulate the fundamental physics of grain transport and deposition, the modeling method used herein produces a geometrical arrangement of sedimentary lamina sets (bedding) by migrating a set of lamina/bedding surfaces so that the resulting fine-scale model framework mimics observed geometries of sedimentary structures (Wen et al., 1998; Ringrose et al., 2005). This type of lamina-scale modeling is an expansion of the work conducted by Ruben (1987) on 3-D synthetic bedform modeling. A near-wellbore model is defined as a "numerical representation of the sedimentological components and petrophysical properties in a rectangular shaped volume along the wellbore" (Nordahl et al., 2005; pg. 18). The near-wellbore modeling process has been shown to have advantages over other basic statistical methods that are focused on simpler systems (Desbarats, 1987; Deutsch, 1989; Ringrose et al., 2005). These statistical methods are outlined briefly in Ringrose et al. (2005), and a more in-depth review is provided by Renard and Marsily (1997).

Based on detailed core descriptions of sedimentary structures and lithofacies, near-wellbore models were generated for cores of the Terry and Hygiene formations from the McHale #1 and Champlin 369 wells, respectively. The model dimensions are 4 x 4 x 324.48 (10.1 x 10.1 x 824.2 cm; X-, Y-, and Z-directions) for the McHale #1 model (Terry Formation) and 4 x 4 x 564 in (10.1 x 10.1 x 1432.6 cm) for the Champlin 369 model (Hygiene Formation). The models have 40 cells in the X- and Y-directions resulting in lateral cell dimensions of 0.1 x 0.1 in (2.5 x 2.5 mm). Vertically, cell thickness is variable (commonly at the millimeter scale) to represent the curved shapes of cross-stratification and other sedimentary structures. Cell thickness ranges from 0.01 to 1 in (0.25 to 25.4 mm). Given the cell dimensions and length of the cores, 25,988,800 and 21,899,200 cells are present in the McHale #1 and Champlin 369 near-wellbore models, respectively.

As previously discussed, four lithofacies, A) wavy laminated sandstone, B) planar cross-laminated sandstone, C) structureless sandstone, and D) ripple cross-laminated sandstone were interpreted in cores of the Terry and Hygiene formations. The various facies successions that were observed in the cores were reproduced in the near-wellbore models to create numerical representations of the core (Fig. 6.4). Detailed generic models (referred to herein as submodels) of each of the four facies were generated and used as the basis to construct the numerical facies successions (appendix A; Fig. 6.7).

To build the 3-D core models, core photographs are cropped and loaded into the modeling software. Each image is depth registered and displayed along with well log data at the correct depth. The core photographs are then used in conjunction with the core descriptions and actual core to determine what facies is present at what depth. The core photographs allowed for the very detailed placing of facies boundaries and for the fine-tuning of the characteristics for each facies. Each time a facies is seen in the core, there are slight changes in the physical properties observed and they must be accounted for. These variations most often consist of changes in the amount of mudrock present, bedding dip angles, and ripple amplitude among others. All of these variables are controllable and each is manipulated such that the final output of the model matches what the actual core looks like. Each facies is generated in the modeling software by simulating the processes behind each facies including things like bedform migration, deposition, and erosion (SBED Manual). These models are referred to as process-oriented models (Elfenbein et al., 2005).

Following the modeling of the sedimentary structures, the near-wellbore facies models were populated with permeabilities (discussed below). Horizontal permeability values (N=1539); ~500 measurements per core) were measured using a probe-permeameter on the faces of four cores, and the average permeability and standard deviation were calculated for each facies (Table 6.1; appendix B). Because 1-in- (2.54-cm-) diameter core plugs are larger than the thickness of many of the lamina, and measurements could not be directly obtained on the core perpendicular to bedding, vertical permeability measurements were not acquired. Four cores were used to generate a statistically relevant number of permeability values for each facies. The probe-permeameter (TEMCO Mini-Probe Permeameter-410) used in this study, calculates permeability by flowing nitrogen gas through a sample. Using the inner and outer tip diameters, flow rate, flow pressure, and ambient pressure, a modified Darcy's equation is used to calculate the permeability of a sample (appendix B, Goggin et al., 1988). The gas flow rates are converted to permeability based on empirical calibration curves derived from a set of standards (5 core plugs) with known permeabilities (appendix B).

The sample rate and density of the permeability measurements were dependent on the frequency of occurrence and degree of petrophysical change for each facies (appendix B). For each facies, the permeability of sandstone and mudrock lamina was measured separately.
The permeability measurements were sorted by facies and lamina type and average permeability and standard deviation were calculated for each facies (Table 6.1). Each facies was built with its own sandstone and mudrock lamina, which allows for each facies to be assigned permeability values separately. Each facies was assigned a permeability average and standard deviation and the model was populated using these values (Figure 6.7; Table 6.1; appendix C). Each time a facies was observed in the 3-D model, it would be populated with permeability values that were within the minimum and maximum permeability values defined (appendix A) and in such a way that after every cell was modeled in that facies, the average and standard deviation would match what the original inputs were. There are options for variograms and correlations to porosity but due to the nature in which the permeabilities were collected, a variogram could not be calculated. The tip of the probe-permeameter has an inner diameter of 0.125 in (3.175 mm), which allows lamina larger than this diameter to be measured. The lamina were traced laterally in the core and, in most cases, each Target lamina was measured at least three times at different locations. This was not always possible as some lamina were discontinuous or varied in thickness laterally. Additionally, measurements were not acquired near the core edges due to the decreasing core thickness at the edge. The thickness of the sample must be at least five times the inner radius of the measurement tip in order to use the modified Darcy's equation to calculate the permeability (Instrument manual for mini-permeameter Model MP-401).

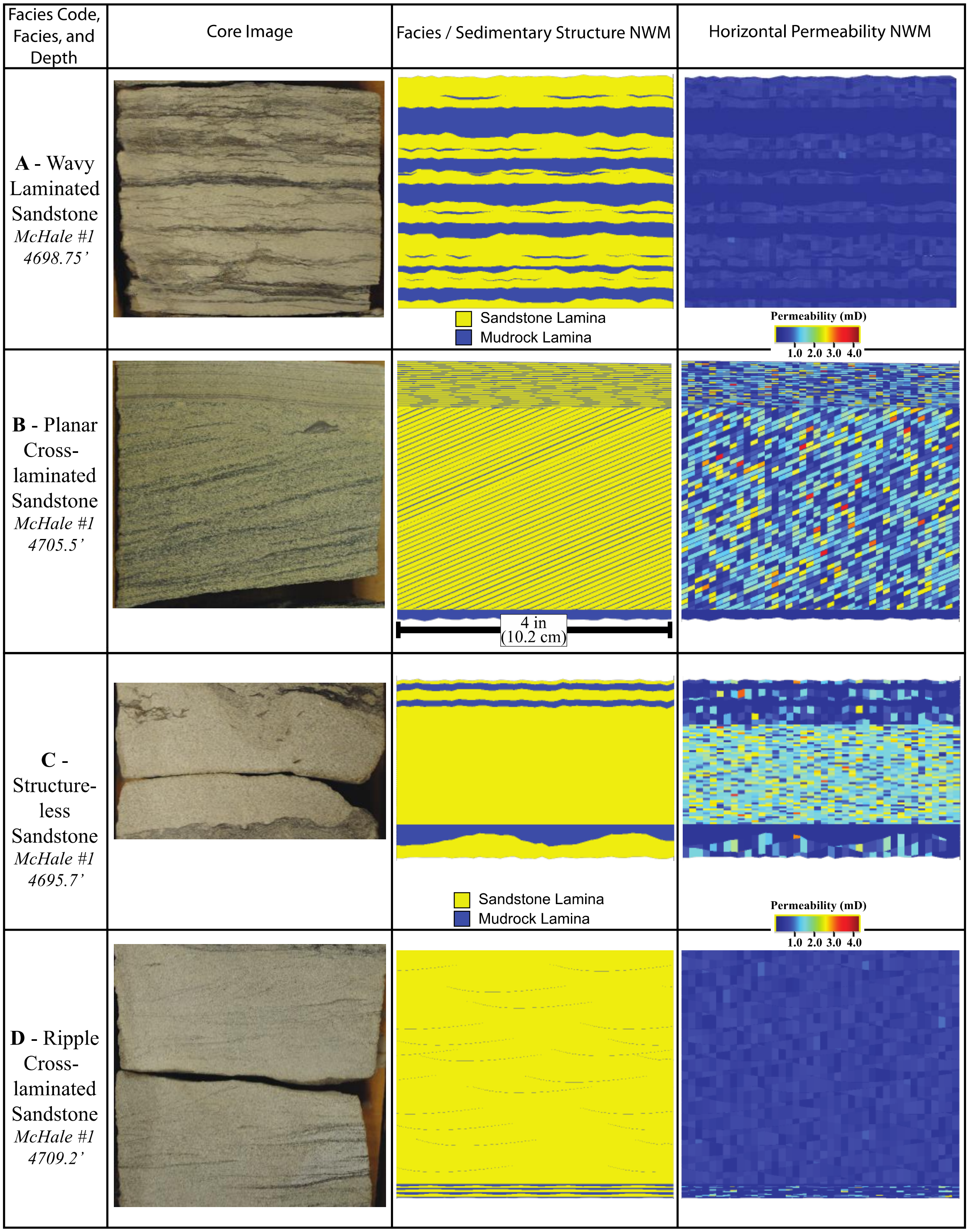

Fig. 6.7. Comparison of facies, near-wellbore models (NWM) of facies, and horizontal permeability. All NWM's and images are 4 in (10.2 cm) wide.

Table 6.1. Permeability statistics for original and effective permeabilities by facies for McHale #1 core. Original-permeability values are divided by facies and lamina type. Effective-permeability values are representative of the entire facies regardless of lamina type. Original-permeability mudrock values are assumed to be 0.004 mD.

Facies	Original Horizontal Permeability			Effective Horizontal Permeability		
	N	Sandstone Lamina Avg. (mD)	Sandstone Lamina Std. Dev. (mD)	N	Effective K Avg.	Effective K Std. Dev. (mD)
A	47	0.332	0.532	32	0.098	0.050
B	73	0.660	0.500	22	0.256	0.071
C	7	0.155	0.187	7	0.081	0.006
D	13	1.561	0.580	16	1.466	0.002

For this research, the minimum core thickness based on the tip size is 0.3125 in (0.79 cm). However, to ensure that the permeability data being acquired was not affected by gas leaking through the base of the core, a minimum core thickness of 0.5 in (1.25 cm) was used. Furthermore, to obtain more accurate measurements, the criterion was used that the calculated permeability from the permeameter could not vary by more than 10% for a minimum of 25 seconds. It was difficult to measure permeability for the mudrock lamina because of the lower permeability of the mudrock, sensitivity of the probe-permeameter, and condition of the mudrock intervals in the core (e.g., microfractures, parting on bedding planes, physical alteration due to exposure and handling, etc.). Therefore, a constant value of 0.004 mD was used for mudrock. The limited permeability data that were obtained suggest qualitatively that the mudrock lamina act as baffles or barriers to fluid flow; however, absolute values could not be acquired.

The fine-scale, near-wellbore permeability models of the Terry and Hygiene formations were upscaled to obtain effective-permeability values by facies. The upscaling procedure used in this study was done by submodel boundary. Through this method, each facies boundary is used as a defining boundary, and an effective-permeability value is generated for each facies. To generate the effective permeability, a single-phase, flow-based upscaling algorithm is used. While several options for flow-based upscaling exist, upscaling by periodic boundary conditions was used. Previous work conducted on similar types of heterogeneous facies has indicated that the periodic boundary condition upscaling method is appropriate (Durlofsky, 1991; Pickup et al., 1994). This type of flow-based simulation imposes a head gradient in three directions and using this, calculates effective permeability by facies. The simulation does not impose any zero-flow boundaries around the model and has the pressure gradients equal on the surfaces in the XY and XZ planes (appendix C). The upscaled permeability values are generated in three directions, one for each direction of simulated flow, but for the purposes of this study, only the values in the x-direction are used for the comparison of original- and effective-permeability (Table 6.1). Typically, an average of permeabilities in the X- and Y-direction is used to estimate horizontal permeability (k_h); however, after a qualitative comparison, the difference between k_x and k_y was negligible throughout the entire stratigraphic interval (difference < 0.15 mD). The differences between original- and effective-permeability values are shown in figure 6.8. Upscaling results for the McHale #1 and Champlin 369 near-wellbore models shows that the effective-permeability data ranges are narrower and average permeabilities for the entire interval are reduced by 49.9% and 77.2%, respectively, as compared to the original-permeability values (Fig.

6.8).

6.3.4. Field-Scale 3-D Facies, Porosity, and Permeability Modeling

The significance of fine-scale permeability heterogeneity associated with lithofacies that exist below the resolution of reservoir model cells was investigated through comparative analysis of 3-D “field-scale” permeability models and associated permeability connectivity. Three-dimensional facies, porosity, and permeability models of the Terry Formation were generated for a 0.28 mi^2 (0.73 km^2) model area within Spindle field (Fig. 6.2). The interpreted lithofacies were modeled first, and porosity was modeled using the resulting lithofacies models as a constraint. Original and upscaled permeability were modeled separately using both lithofacies and porosity models as constraints. The model area contains nine wells with the McHale #1 cored well at the center (Fig. 6.2). All but one well contain gamma-ray (GR), spontaneous potential (SP), deep resistivity (RESD), and density porosity (DPHI) logs; all of which were used in the modeling process. The logs were normalized to the Terry Formation interval in the cored McHale #1 well. This was done to limit the effect of multiple logging tools used over many years. Wells in the model area were logged over a 25-year period. Due to a lack of neutron-porosity logs, only density porosity logs were used. The 3-D model dimensions are 2828 x 2900 x 40 ft (length, width, thickness; 826 x 887 x 12.2 m; Figs. 6.2 and 6.9). Each of the four model zones corresponds to the reservoir and non-reservoir zones previously defined. The zones are based on the core-derived facies, gamma-ray, and spontaneous-potential log responses. Individual cells are 29.8 x 30 ft (9.08 x 9.1 m) in area, and proportional layers (N=46) were used, resulting in 423,890 model cells (average cell/layer thickness is approximately 1 ft [0.3 m]) (Fig. 6.9).

Field-scale facies models were generated to map the distribution of the four main lithofacies within this portion of Spindle field. The 3-D facies models are constrained to the McHale #1 cored well at the center of the model area and in terms of lithofacies percentages based on that cored well. Because distinct relationships do not exist between the lithofacies present in core and the associated well-log responses, facies logs could not be estimated in non-cored wells. However, a general relationship does exist between SP response and lithology (sandstone vs. mudrock). The SP logs exhibit negative SP excursions corresponding to more sandstone-rich facies (structureless, ripple cross-laminated, and planar cross-laminated sandstones), whereas the more mudstone-prone facies and wavy laminated sandstone approximately correspond to near-zero SP values within the Terry Formation. Therefore, to further constrain the facies models, a lithology probability volume was generated based on the SP logs

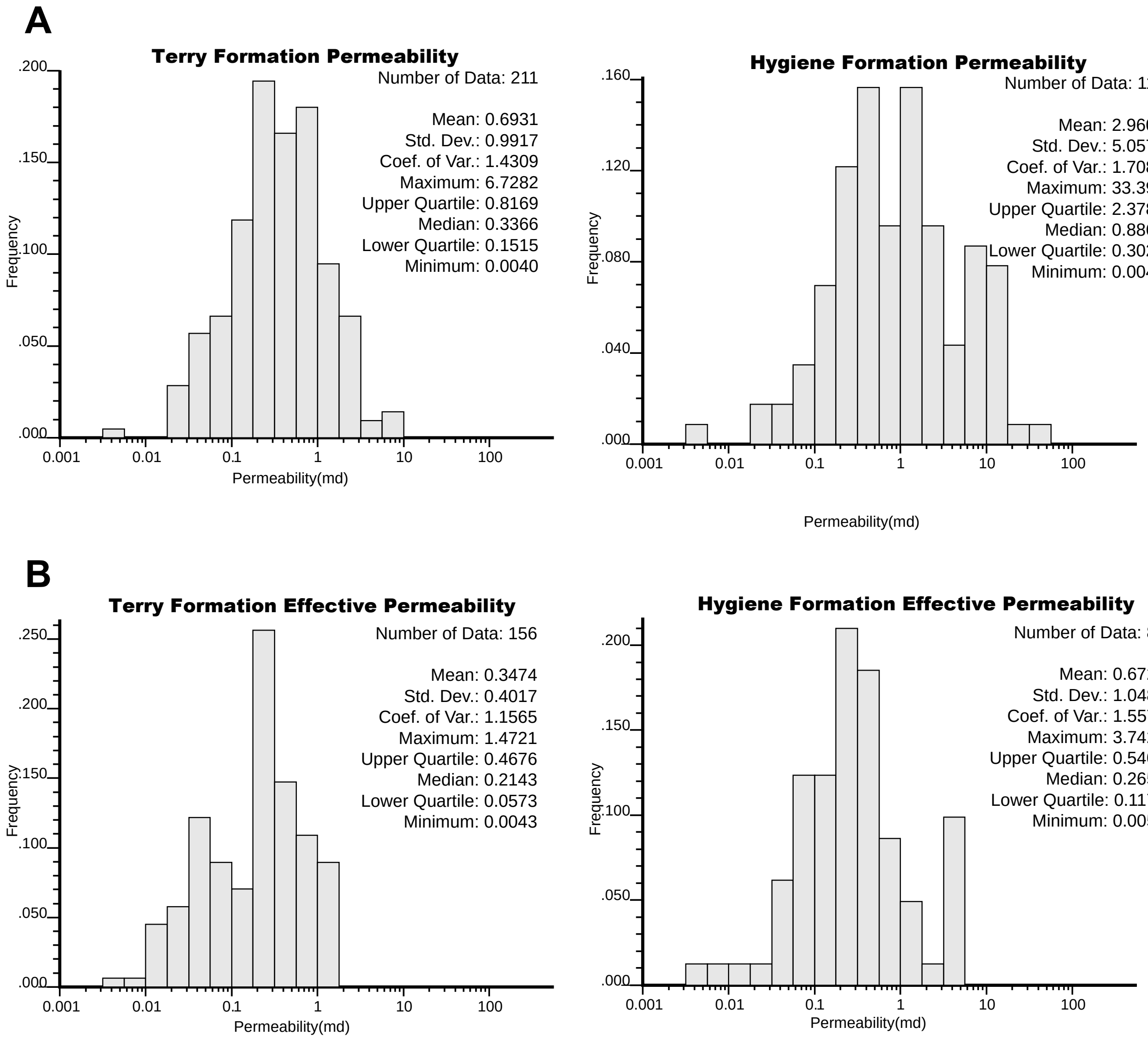

Fig. 6.8. Histograms of A) original and B) effective permeability for the Terry Formation (McHale #1) core and Hygiene Formation (Champlin 369) core.

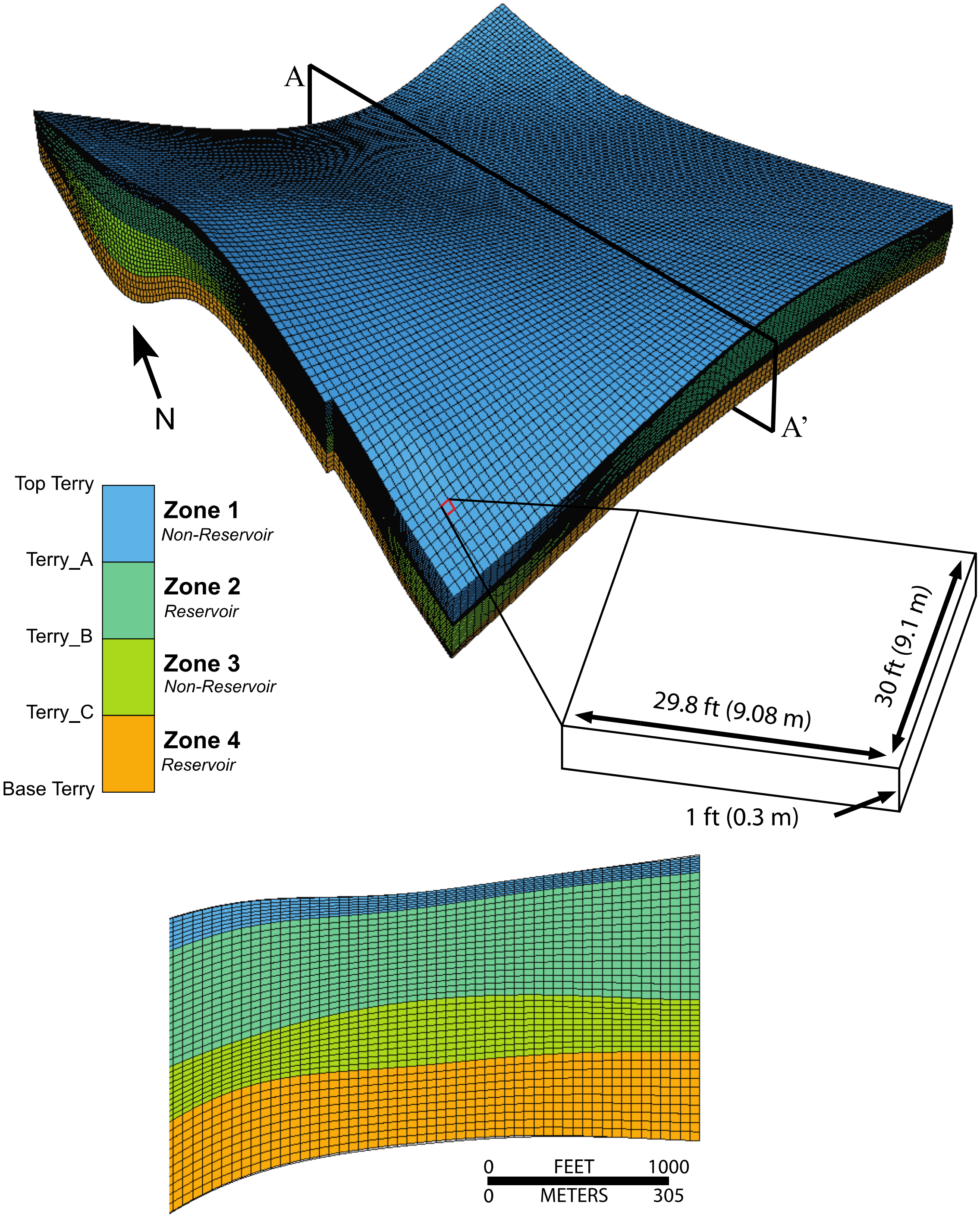

Fig. 6.9. Top: Reservoir model zones and dimensions of a single model cell are shown. Proportional layers (N=46) were used resulting in 423,890 model cells (average cell/layer thickness 1 ft (0.3 m). VE=10x. Bottom: Cross-section A-A' through reservoir model showing zones and cells. VE=30x.

used as a constraint on lithofacies distribution during the modeling process. A 3-D SP model was first generated using the SP logs and sequential-Gaussian simulation (SGS) (Fig. 6.10). The vertical variograms were defined for each zone using the SP logs (appendix D). Spherical variogram models were used with correlation lengths (ranges) between 1 and 4.8 ft (0.3 and 1.52 m). The horizontal variograms were modeled using spherical functions and both major- and minor-direction ranges were arbitrarily set to 1000 ft (305 m) or approximately one-quarter the diagonal distance across the model domain. The SP model was converted to a lithology probability volume (model) by nonlinear rescaling of the SP model such that 0 and 1.0 correspond to the most positive (mudrock-prone) and negative (sandstone-rich) SP values, respectively. The lithology probability volume (model) was also used as a constraint on the sandstone-rich and mudrock-prone lithofacies during the facies modeling process.

Thirty realizations of the facies models were generated using sequential-indicator simulation (SIS). The vertical variograms were defined for each zone using the facies log from the McHale #1 well (appendix D). Spherical variogram models were used with correlation lengths between 1.1 and 8.3 ft (0.34 and 2.53 m). The horizontal variograms were modeled using spherical models and the ranges for major- and minor-directions were arbitrarily set to 1000 ft (305 m). The nugget was set to zero for facies modeling. For subsequent modeling and analysis, an average facies model based on the 30 realizations was computed (referred to herein as average facies model: AFM) (Fig. 36.11). The AFM was generated from the thirty facies realizations, and the most common facies to occur in a given cell of the thirty realizations was assigned to that cell in the AFM. As expected, the AFM exhibits a smooth facies distribution, as compared to a single facies realization, and is similar to a facies model generated using indicator kriging (Fig. 6.11). This smoother distribution is likely to be more realistic than the discontinuous model. This was determined based on limited outcrop observations and the interpreted depositional environment (appendix D).

Porosity models were generated based on normalized density-porosity (DPHI) logs from the nine wells in the model area. Neutron-porosity logs were limited to select wells in the model area and thus were not used in this study. Thirty realizations of the porosity model were generated using sequential-Gaussian simulation constrained to variograms, porosity statistics derived from the DPHI logs, and the AFM (Fig. 6.12). Vertical variograms were defined for each zone and each facies using the normalized DPHI log in the McHale #4 well.

This particular log was chosen because of the quality of the log data. Spherical variogram models were used with correlation lengths between 0.6 and 7.3 ft (0.18 and 2.23 m). The horizontal variograms were modeled using spherical models with ranges for major- and minor-directions arbitrarily set to 250 ft (76.2 m). The nugget was set to zero for porosity modeling. An average porosity model based on the 30 realizations was computed (referred to herein as average porosity model: APM) (Fig. 6.12). The APM was generated using an arithmetic average where, for a given cell, the corresponding porosity values of the thirty realizations were averaged to generate the porosity value in the APM. The APM, like the average facies model, exhibits a smooth distribution of porosity values as compared to a single porosity realization.

Field-scale models were generated to map the distribution of both original and effective permeability in this portion of Spindle field (Fig. 6.13). Thirty permeability realizations were generated using sequential-Gaussian simulation constrained to variograms, permeability statistics derived

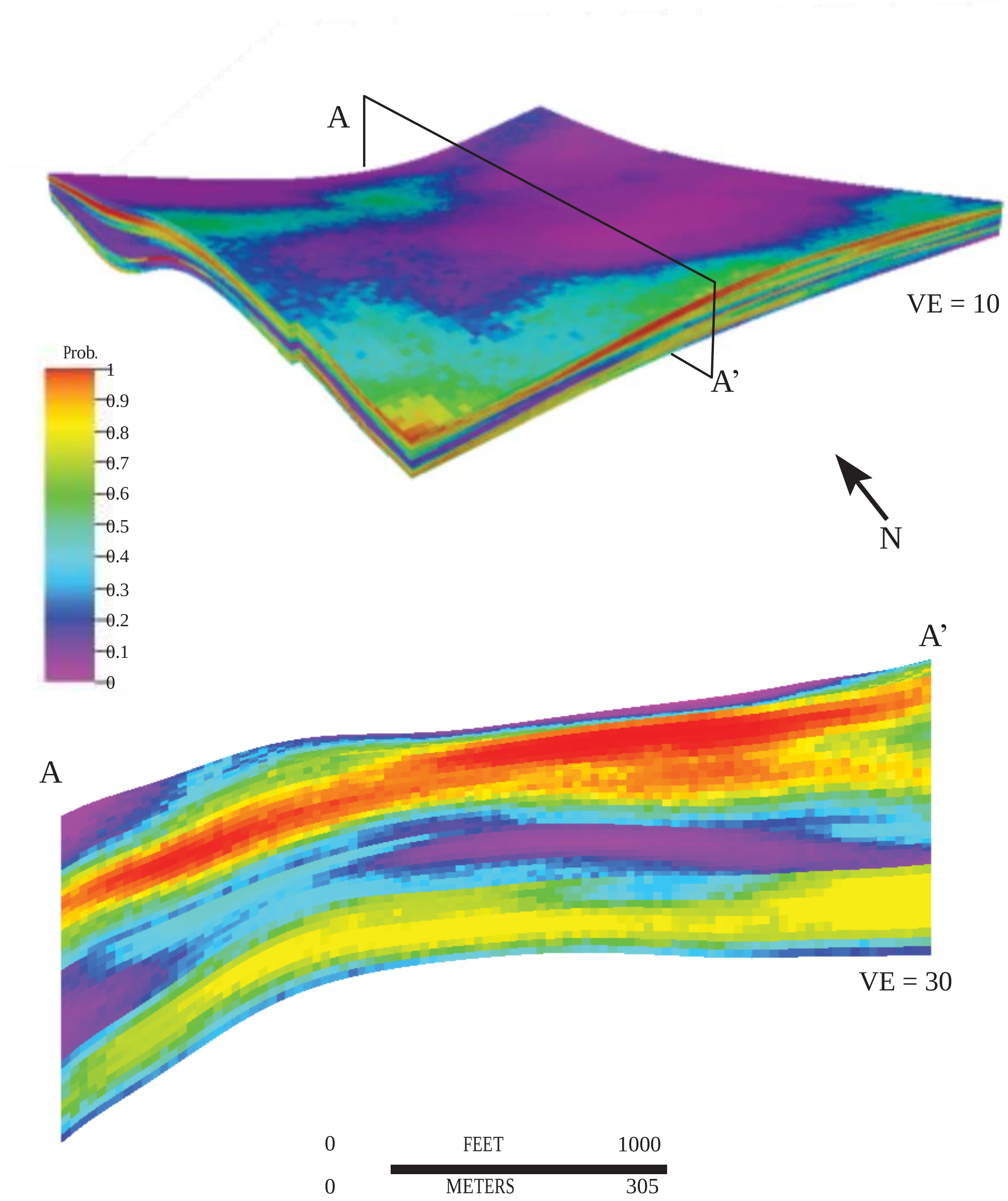

Fig. 6.10. Lithology probability volume (model) used to constrain facies distribution. Higher values indicate a higher probability of sandstone-rich facies. The probability volume is based on the SP response in which negative SP excursions correspond to more sandstone-rich facies and near-zero SP values correspond to more mudstone-prone facies.

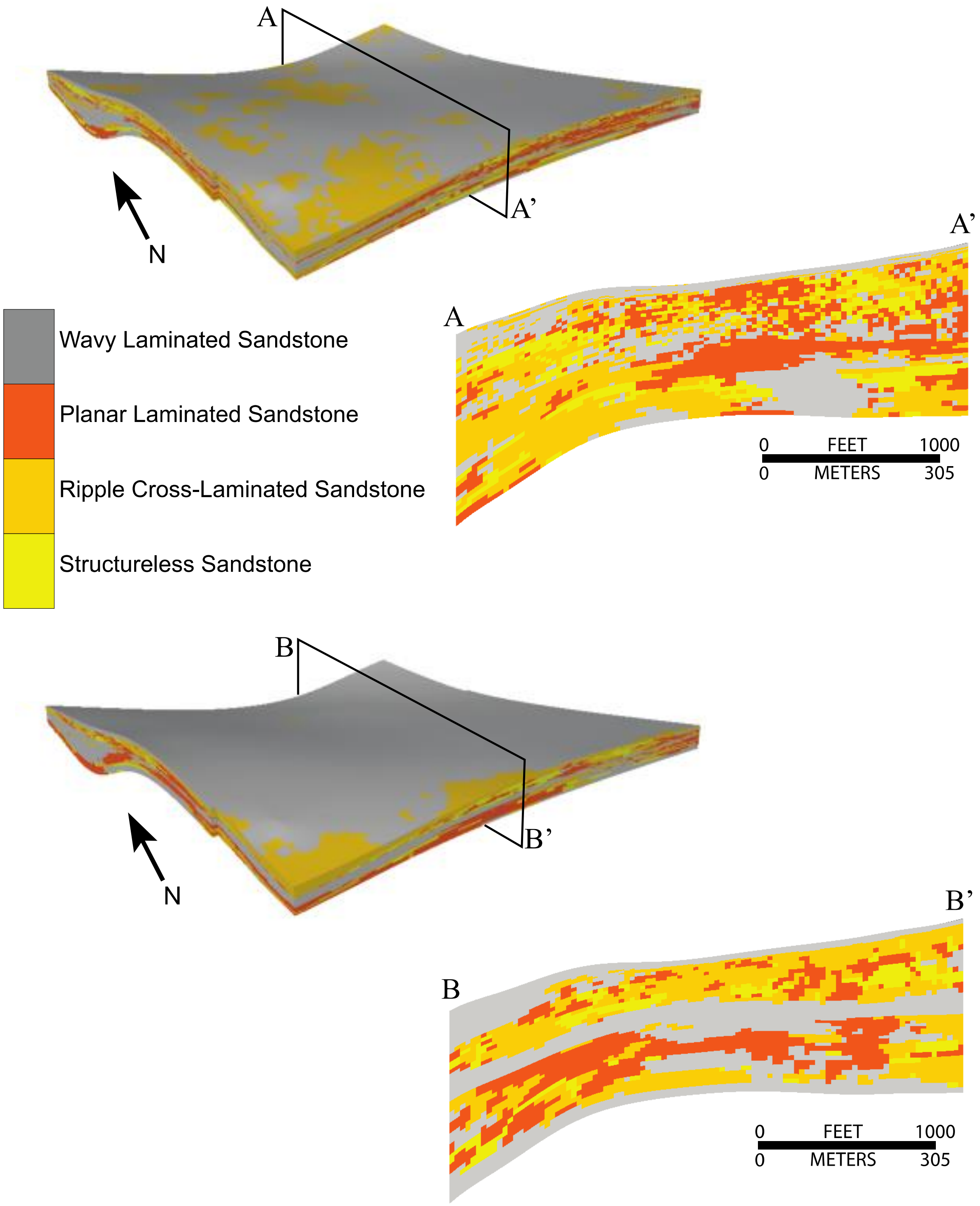

Fig. 6.11. Top: Single facies realization showing a discontinuous distribution of the facies. Bottom: Averaged facies model from 30 realizations (AFM) which shows a more continous and geologically accurate distribution of facies as compared to one realization. 3-D models: VE=10; cross-sections: VE=30.

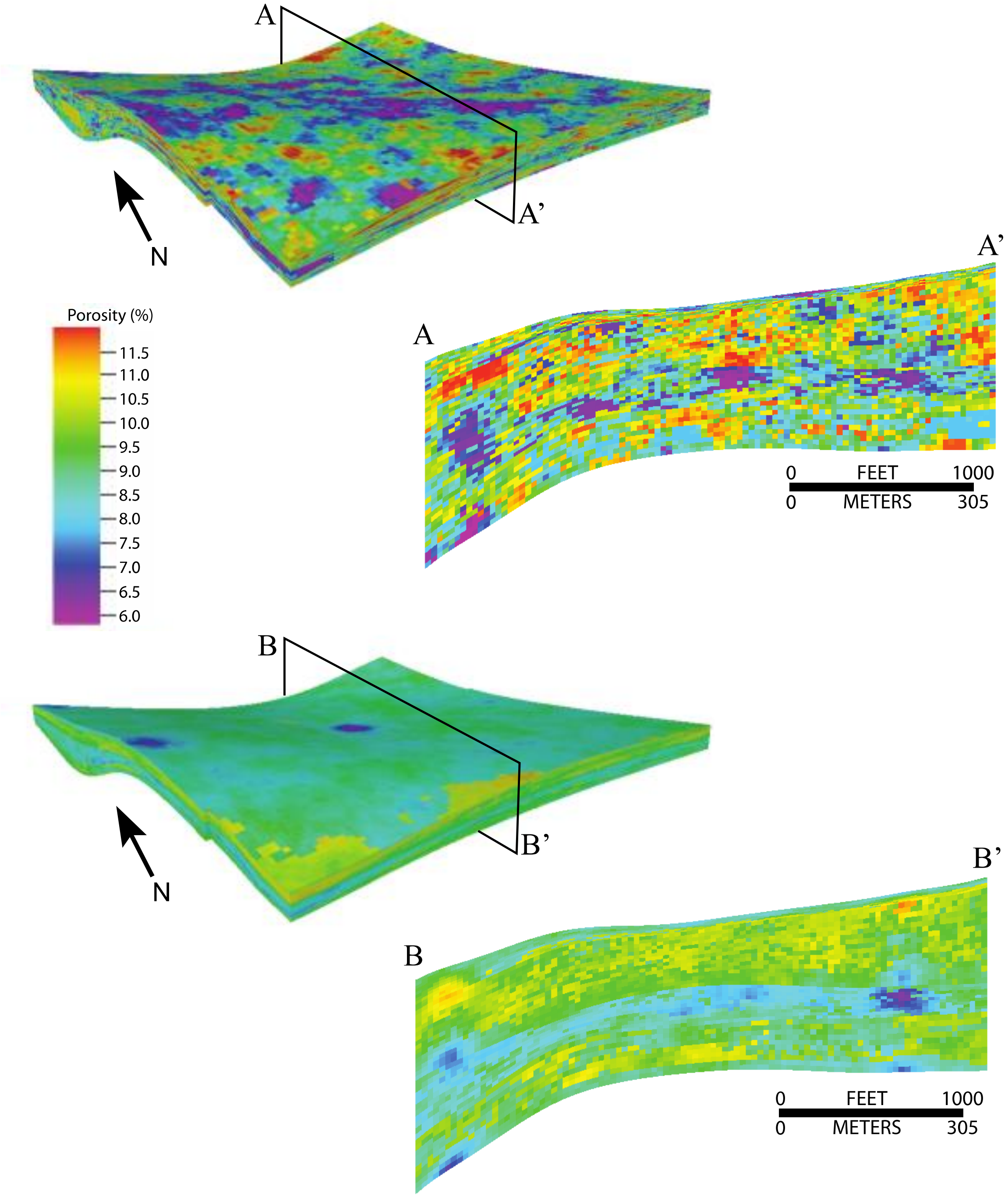

Fig. 6.12. Top: Single porosity realization showing an increasingly discontinuous porosity distribution. Bottom: Average of thirty porosity realizations which shows a more continuous distribution. Porosity models: VE=10x; cross-sectional views VE=30x.

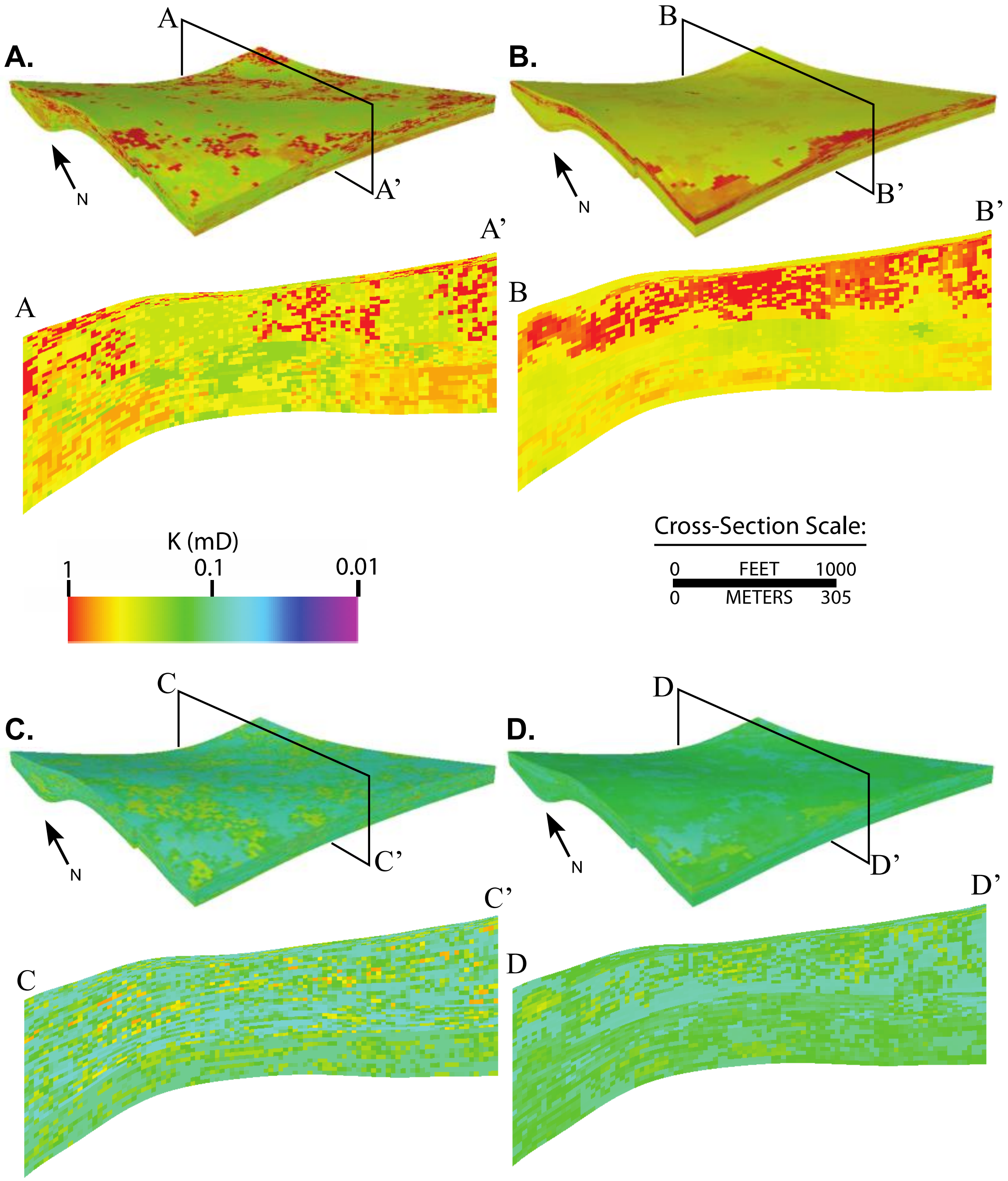

Fig. 6.13. Permeability models using original and effective permeabilities. Models A and B are original (non-upscaled) permeability models. Models C and D are effective (upscaled) permeability models. Models A and C represent a single permeability realization, models B and D represent an average of 30 permeability realizations. 3-D models: VE=10; cross-sections: VE=30. Effective-permeability models show lower permeability values compared to original- permeability models. Average models show smoother distributions compared to a single realization.

from the McHale #1 core and near-wellbore model, the APM, and a bivariate transformation (cloud transformation) between porosity and permeability (appendix D). The cloud transformation was utilized because of the low coefficients of determination (R^2 values) associated with linear regressions between porosity and both original and effective permeability (Sloan, 2012). For the bivariate transformation, a porosity and permeability cross plot was created for both types of permeability. For each cross plot, the porosity scale is divided into ten porosity bins. For a given porosity value within a porosity bin, a range of permeability values is possible because of the low coefficient of determination (data scatter or data cloud). As part of the modeling process, to estimate the permeability values for a model cell, the associated porosity for that cell from the porosity model is considered. Given the porosity value for that cell, the permeability values (from the porosity-permeability cross plot) that fall within the associated porosity bin are used, with other constraints, to define (simulate) the permeability value that is assigned to the model cell.

As expected, because the input original and upscaled (effective) permeability values are honored in the modeling process, the original-permeability models show higher average permeability values (0.52 mD and 0.53 mD for the single and average models, respectively) than the effective-permeability models (0.14 mD and 0.12 mD for the single and average models, respectively). However, the spatial trends of the permeability distributions within the models are similar between the two types of permeability models.

6.3.5 Static Connectivity

Static connectivity is defined and used in this study as the volume sum of reservoir cells connected to a particular pattern of wells (directly or indirectly) divided by the total volume of reservoir cells in the 3-D model and is expressed as a percentage. The static connectivity analysis in this study is primarily a function of permeability and is used to compare the differences in connected volumes between models based on original- and effective-permeability. For each model type, static connectivity was determined using a smaller model area than the field-scale model to avoid edge-effects potentially created during the modeling process (Fig. 6.2). To determine static connectivity, pseudo-wells were used on a 5-ac (2-hectare) spacing (Fig. 6.2). Each model cell was classified as either reservoir or non-reservoir based on a porosity cutoff of > 8.75% and a variable permeability cut-off. The porosity cutoff for this analysis was determined based on the porosity histogram from the porosity models (appendix D). The value was determined so that approximately one third of all the porosity values fall below the cutoff value, the cutoff value is below the average porosity value for the entire model (9.8%), and the cutoff value is greater than that of the average porosity value in the non-reservoir zones (5.1% and 8.4% for both non-reservoir zones). Having this value greater than non-reservoir zones, but less than the overall average porosity, helps ensure that the facies in the previously identified non-reservoir intervals are not included in static connectivity analysis. All of the facies in these zones are not removed as a whole from the static connectivity analysis because it is possible that there are some minor producing facies within these zones and therefore the entire intervals cannot be excluded.

For the permeability portion of the reservoir cell definition, the permeability cut-off is varied by an increment of 0.15 mD starting from 0.0 and going to 1.95 mD. This was done to determine how the static connectivity varied among all the models with multiple reservoir permeability definitions. For the permeability models that are constrained to the single porosity model, the connected volume 62.49% for the 0.0 mD cuts off on both the original- and effective- permeability models (Table 6.2).

Table 6.2. Static connectivity percentages for each of the four permeability models given a porosity cutoff of > 8.75% and a variable permeability defintion for a reservoir cell.

Reservoir K (mD)	**Original Permeabilities**		**Effective Permeabilities**	
	Connectivity		**Connectivity**	
	(Single Φ Model)	**(Avg. Φ Model)**	**(Single Φ Model)**	**(Avg. Φ Model)**
0.00	62.49%	79.55%	62.49%	79.55%
0.15	62.49%	79.55%	18.89%	11.39%
0.30	57.19%	58.70%	4.98%	0.16%
0.45	33.73%	32.90%	0.05%	0.02%
0.60	8.46%	15.79%	0.01%	0.01%
0.75	4.48%	8.81%	0.00%	0.00%
0.90	4.06%	8.11%	0.00%	0.00%
1.05	3.20%	7.23%	0.00%	0.00%
1.20	2.15%	5.95%	0.00%	0.00%
1.35	1.40%	5.39%	0.00%	0.00%
1.50	0.57%	4.88%	0.00%	0.00%
1.65	0.03%	4.23%	0.00%	0.00%
1.80	0.00%	1.39%	0.00%	0.00%
1.95	0.00%	0.00%	0.00%	0.00%

As the permeability reservoir definition was increased to the maximum cutoff of 1.95 mD, the connected percentage decreased to 0% for both model types. As the permeability cutoff increases from 0.0 mD, the differences in connectivity for the two permeability models become evident (Fig. 6.14). For effective-permeability values, static connectivity drops dramatically (42.6%) after the first 0.15 mD increase to 18.89%. As the permeability cutoff increases, static connectivity reaches 0% at 0.75 mD. In contrast, the original permeability values show a different connectivity decay line. After starting at the same connectivity percentage, the percentage of connected cells stays nearly the same through a permeability cutoff of 0.30 mD with only minor changes. A minor drop in connectivity of 5% is observed, but overall, a dramatic decrease like the one seen in the effective-permeability models at the lowest permeability reservoir definitions was not observed. Subsequently, there is a significant decrease in connectivity to 4.48% at the permeability cutoff of 0.75 mD, after which the connected cell percentage decreases at a slower and more consistent rate. For this permeability type and model, the connected percentage reaches 0% at a permeability reservoir definition of 1.95 mD. Fig. 6.15 shows at three strategic permeability cutoffs for this model type how the connected volumes appear in cross-section.

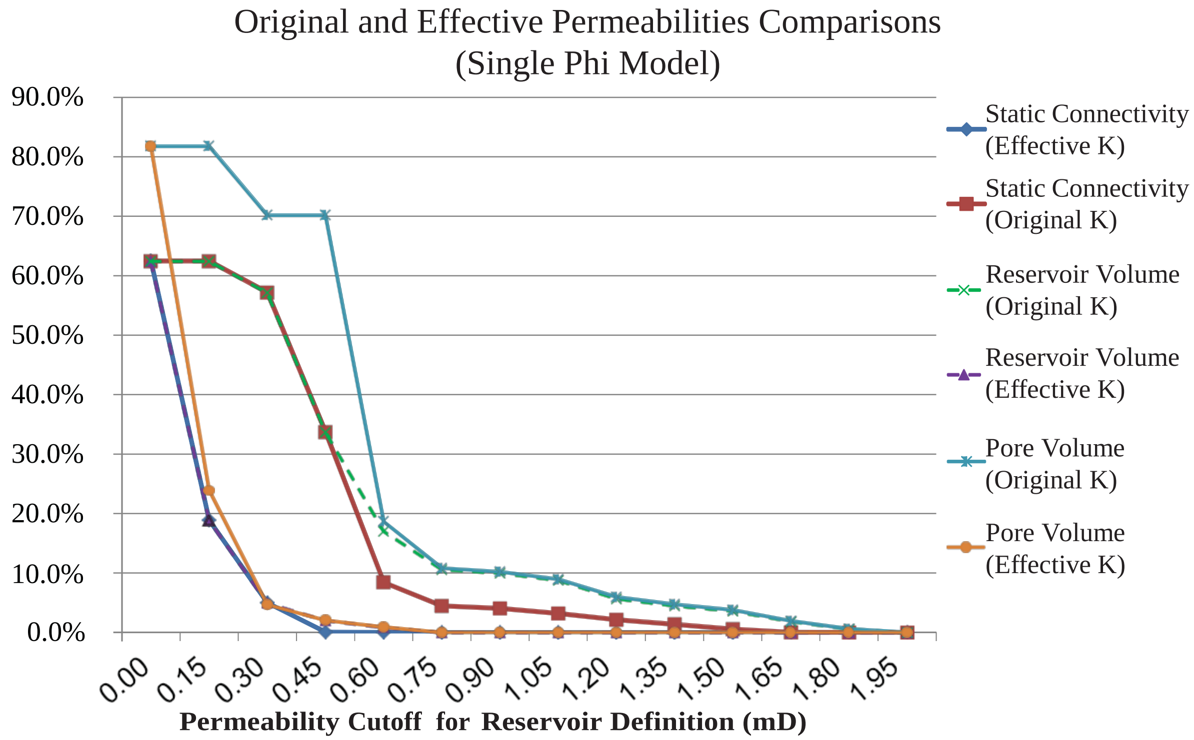

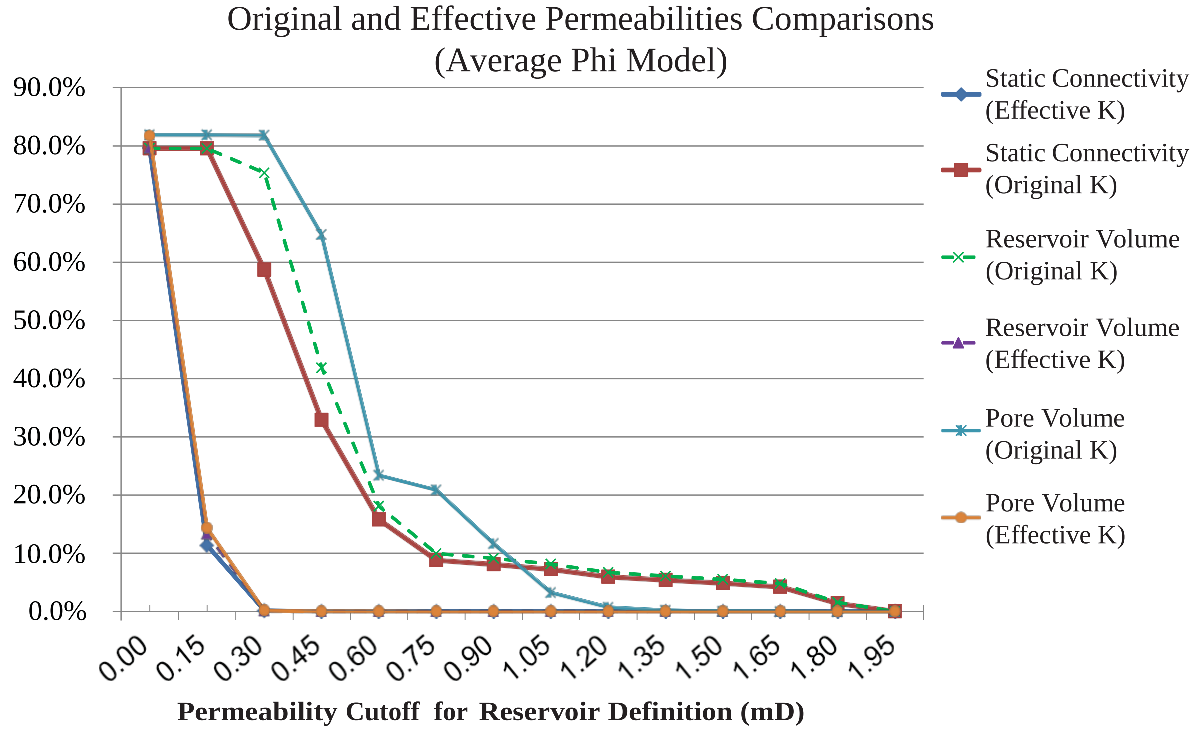

Fig. 6.14. Graphs showing static connectivity, reservoir volume (as percentage of bulk reservoir volume), and pore volume percentage at varying permeability cutoffs. Static connectivity determines how much of the reservoir is connected. Reservoir volume illustrates how much total reservoir volume there at a cutoff. Pore volume illustrates the amount of pore space of cells that meet a reservoir criteria at a given reservoir definition.

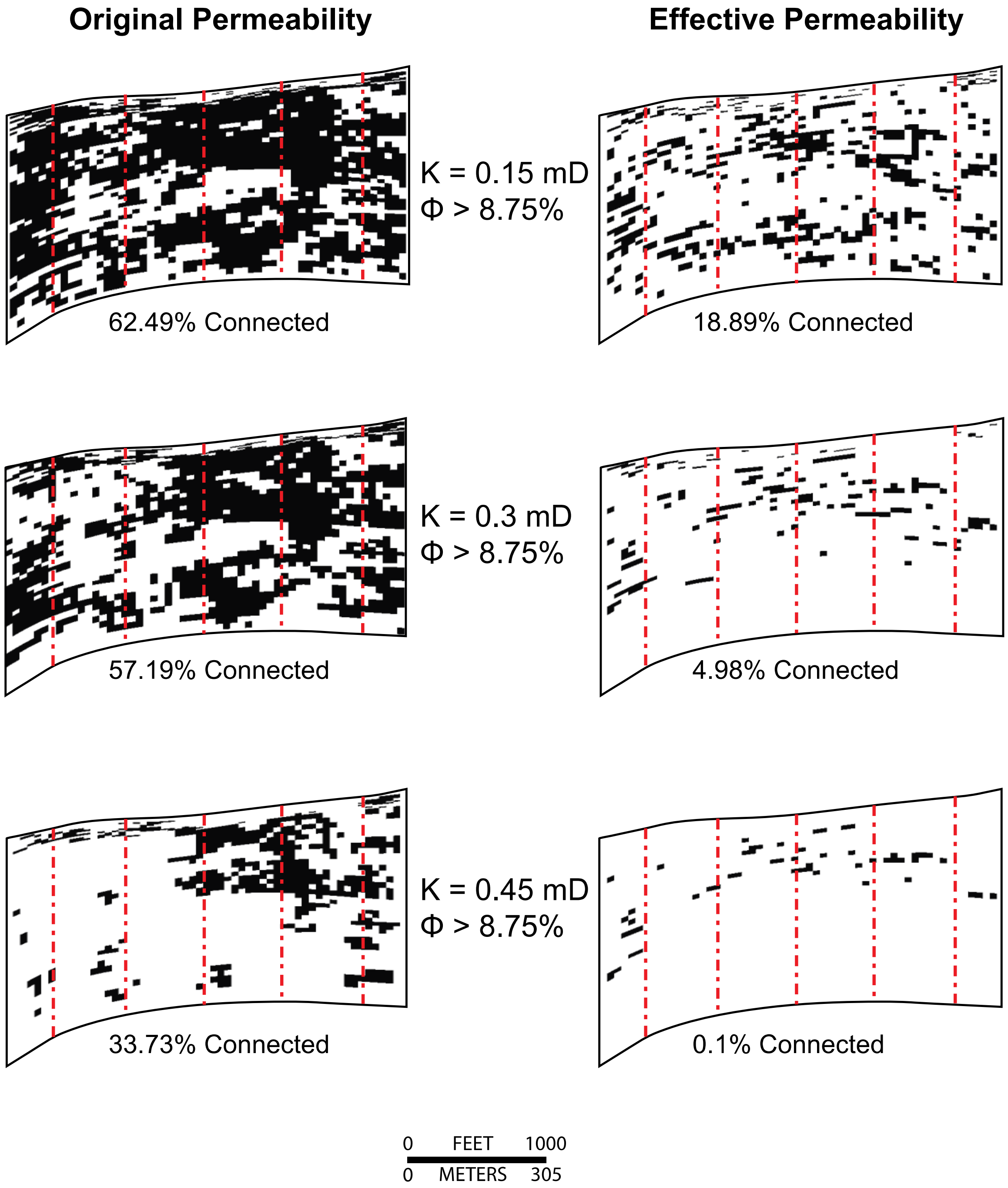

Fig. 6.15. Static connectivity comparison in cross-sectional view (I=54) of single porosity referenced original- and effective-permeability models. This view shows cells in the plane that are connected to a wellbore. Cross-sectional plane is shown in Figure 13 and is consis- tent with all model cross-sections. Red lines indicate wellbores. VE = 30x

The permeability models constrained to average porosity model behave in a slightly different way. For the effective-permeability model, connectivity decreases almost immediately, and the original values remain constant before decreasing at a similar rate (Table 6.2). Both models started with the same static connectivity at the 0.0 mD cutoff, 79.55% for both types of permeability. Like the effective-permeability model that is constrained to the single porosity realization, the effective-permeability values constrained to the average porosity model decrease immediately and reach 0% connectivity by the 0.75 mD cutoff. The original values also show a similar decay pattern to the permeability models that are constrained to the single porosity realization after the 0.15 mD cutoff is reached. The model reaches 0% connectivity when the permeability cutoff value reaches 1.8 mD (Fig. 6.14).

Other comparisons of the permeability models completed in this study include a comparison of bulk reservoir volume and pore volume of the model at given reservoir definitions. Bulk reservoir volume is used in this study as the total volume of all cells in the model that meet the criteria of a reservoir cell at a given permeability and porosity cutoff and is displayed as percentage of bulk model volume. As with static connectivity, bulk reservoir volumes were determined using a porosity cutoff of >8.75% and a variable permeability cutoff. This is useful to compare how much of total reservoir volume in the model area is being utilized in the static connectivity measurements (Fig. 6.14; appendix E). The bulk reservoir volume data indicate that the static connectivities at lower permeability values for all model types utilize all of the available reservoir cells. However, as the permeability cutoff values are increased, the differences between the bulk reservoir volume and the volume of cells connected becomes more apparent before reaching 0%, much like static connectivities (Fig. 6.15). The overall trend of the curve for reservoir volumes follows the same trend as static connectivity. This similar trend is likely due to the 5-acre (2-hectacre) spacing, which causes nearly all reservoir volumes to be connected to a wellbore. Similar to the other two comparison methods, pore volume for a given reservoir definition shows the same curve shape. Pore volume is displayed as a percentage of total model pore volume given no restrictions on porosity or permeability.

As a porosity limit of >8.75% was added and the 0.15mD permeability step was increased, the pore volume decreased at a similar rate to the decline rates of static connectivity and bulk reservoir volume (Fig. 6.14). The decrease shows almost the exact same decrease for the effective-permeability models but has more variability in the original-permeability based models. The difference is likely caused by the original-permeability models having higher permeability values and wider range.

6.4. Task Results

6.4.1. Facies

Four common lithofacies were identified within the Terry and Hygiene formations in this study (Fig. 6.4). These four facies were identified based on sedimentary structures and lithology. All four facies are identified as sandstone with minor amounts of mudrock being present. Three of the four are identified as sandstone-rich, while the fourth is identified in this study as mudrock-rich. Each facies has varying amounts of sandstone and mudrock in it along with variable amounts of each lithology within each facies type as it is repeated throughout the core. Of the three sandstone facies, two (planar laminated and structureless sandstones) would likely be considered reservoir facies based on the higher permeabilities observed (Table 6.1). Similarly, the mudrock-rich facies (wavy laminated) shows permeability values within the sandstones that are near to the other reservoir facies. However, due to the large amount of mudrock in the wavy laminated facies, this facies is not considered a reservoir facies; thus the zones in which this facies occurs are not considered reservoir zones. The large amount of mudrock in this facies would likely limit the connectivity of the small sandstone lamina. These limitations on connectivity would not allow for large scale reservoir communication which would negatively affect the well's performance as either a production well or an injection well.

Based on the four facies described, log analysis, and core observations, the interpreted depositional environment for this study is an offshore bar complex (Porter, 1976; Kiteley, 1977; Pittman, 1988, 1989; Al-Raisi et al., 1996). This interpretation, as previously stated, is one of several hypotheses as to the formation of the Terry Formation. Guided by core interpretation, four distinct zones have been identified in well logs. Each of these zones is interpreted as being as one of two architectural elements, either interbar deposits or sand bar deposits. The mudrock-rich facies indicates a quiet water setting, and this would be representative of the interbar depositional environment. As the sand bar migrates through the area, following each is a zone where more mudrock would be deposited. This would resemble a typical offshore mudrock deposit. Additionally, the bioturbation identified is more prevalent in the wavy laminated facies, indicating this is a quieter setting in which more organisms can live. The ripple laminated facies and planar laminated facies are indicative of the sand bar depositional environment. Both are formed by the water currents, which are also responsible for bringing sand from a nearby delta to the area and depositing it. The structureless sandstone is more ambiguous as it could have been deposited without any internal structure or it may have been extensively bioturbated, making it appear structureless. It is likely that both of these options occurred, however, because they are indistinguishable; an accurate classification of the depositional processes cannot be made for this facies.

6.4.2. Permeability Upscaling

Using the periodic boundary conditions and a flow-based upscaling algorithm, each facies was upscaled and an effective permeability was generated for each (appendix C). This was done for both the McHale #1 and Champlin 369 cores representing the Terry and Hygiene formations respectively. While only the Terry is used for comparison of original to effective properties, the Hygiene Formation core was upscaled as well to compare how a second formation would respond to the upscaling process.

Comparison of the individual facies permeability histograms for each formation indicates that there is a different relationship between the original- and upscaled-permeability values for each (appendix C). For the Terry Formation, the wavy laminated sandstone facies (facies A) shows an average original permeability change from an original, measured permeability of 0.332 mD to 0.098 mD for the upscaled value (Table 6.1). This is a significant change (decrease of 70%) and is likely caused by the large amount of mudrock lamina within the facies. The wavy laminated sandstone facies has a variable mudrock content and ranges from 10–70% mudrock (Fig. 6.4). Due to the mudrock laminas near-zero permeability (0.004 mD), the generation of the effective permeability is adversely affected. During the upscaling process, as flow is simulated through the sample, the mudrock most likely acts as a barrier to flow and limits the permeability of the entire facies despite the sandstone lamina's relatively high permeability (Table 6.1). This example indicates why it is important to consider upscaling of the permeability values to generate an effective permeability value for the entire facies and throughout the core. A core plug or other small scale measurement may be taken in the wavy laminated sandstone facies, and depending on the sandstone lamina thickness, may indicate that the permeability is an order of magnitude or more higher than what the effective permeability of that sample may be. Conversely, the structureless sandstone facies (facies C) is hardly affected by the upscaling process. The structureless sandstone had an average original permeability of 1.561 mD and after upscaling the average permeability decreased only slightly to 1.466 mD, which is a 6.1% decrease. The difference between these two values is smaller than that of the mudrock-rich wavy laminated facies because this facies does not have mudrock incorporated into it. Without permeability-inhibiting mudrock lamina, flow through the structureless sandstone facies is not as affected during the upscaling process as facies that contain mudrock. While this facies is not as affected by the upscaling process due to its lack of mudrock, it is still important to generate an effective-permeability value for it because there is a drop in permeability. That drop may indicate where to place a well and where to not place a well depending on the model and purpose.

The other two remaining facies, the planar cross-laminated and ripple cross-laminated sandstone facies (facies B and D, respectively), show only minor changes in upscaled values compared to the original values (Table 6.1). The ripple cross-laminated sandstone facies show a decrease in permeability from 0.155 mD to 0.081 mD after completing the upscaling processes. This facies, similar to the wavy laminated facies, shows a drop in permeability due to mudrock lamina within the facies. This facies has the smallest mudrock lamina of all the facies with average thicknesses ranging from 0.02–0.125 in (0.51–3.18 mm). While the thickness is less than the other facies, the small mudrock lamina still negatively affect the permeability during the upscaling process by restricting fluid flow in the sample. Facies B showed a permeability decrease as well with the average original permeability decreasing from 0.660 mD to an average effective-permeability value of 0.256 mD. As with the other facies containing mudrock, the permeability is interpreted as being adversely affected by the mudrock. This facies showed a decrease of over 60%. The large drop is likely due to the relatively high number of mudrock lamina throughout the sample in conjunction with relatively thin sandstone lamina (Fig. 6.4).

6.4.3. Static Connectivity

To compare how using effective-permeability values or using original-permeability values affects reservoir modeling, a comparison of four field-scale permeability models was completed. The multiple permeability models were compared through static connectivity analysis, which determines the percentage of cells connected either directly or indirectly to a wellbore. Static connectivity was chosen as the method for comparison because it allows for a direct comparison through reservoir modeling and follows the same process that would be done in the real world. Furthermore, the comparison through reservoir modeling is important because that is where the use of original- or upscaled-permeability values is most likely to be used and where it may make the most difference.

To complete the static connectivity models, a smaller area within the model area was chosen and pseudowells were added to the area (Fig. 6.2). Pseudowells were added to the area due to the somewhat irregular spacing of the regular wells in the model area (Fig. 6.2). The pseudowells were added at a spacing of 5-acre (2-hectacre) so connectivity would be high enough to see how it changed as the reservoir criteria were changed. Additionally, the 5-acre spacing of the pseudowells was chosen as the lateral continuity of some reservoir facies is limited, and this spacing allows for nearly all reservoir geobodies to be penetrated. To determine if all of the reservoir bodies were being penetrated at the lowest reservoir definition, a comparison was made to the total bulk reservoir volume. This bulk reservoir volume is expressed as a percentage of the total model bulk volume and is calculated for every reservoir definition that static connectivity is computed for. For the lowest possible reservoir value, 0.0 mD, the total reservoir bulk volume is the same as the total volume of connected cells, indicating that at this low value, every cell is connected to a well at the 5-ac (2-hectacre) spacing. Additionally, this comparison to bulk reservoir volume allows for insight into how many cells are connected to a wellbore out of the total number of reservoir cells given that reservoir definition (Fig. 6.14, appendix E).

Static connectivity was completed for each of the four model scenarios, two connectivity analyses for original-permeability based models and two for effective-permeability based models. For each permeability type, a model was generated that was linked to the single porosity realization associated with the AFM and to the average porosity model associated with the AFM (Fig. 6.13). This allowed for the comparison of both a thirty realization average model and a single realization and to determine what effects the averaging of the properties might have on connectivity analysis.

For the original-permeability models, the static connectivity of the model associated with the single porosity realization starts at 62.49% connectivity while the average porosity referenced model starts at 79.55% connectivity (Fig. 6.14; Table 6.2; appendix E). The difference in starting connectivity percentages is likely due to the average model having a different porosity distribution due to the averaging of the thirty realizations. The static connectivities for both models are the same as the total percentage of reservoir cells in the modeling, indicating that each model type has all reservoir defined cells connected to a wellbore. This indicates that the porosity values are controlling the number of cells that meet the reservoir definition since the permeability definition is a non-limiting factor at 0.0 mD. However, as the permeability cutoff was increased for both original-permeability models, static connectivity remained relatively flat for the second and third permeability steps before dropping off steeply and leveling off again around the sixth and seventh permeability steps. After this, the static connectivity gradually decreased to 0% connectivity. The dramatic drop in connectivity may indicate that the majority of the permeabilities are in adjoining cells, and as the cutoff for the reservoir cell is changed, the cell clusters are being cut off from a well by other cells. This can be seen by looking at a cross-sectional view through the center of the model area (Fig. 3.14). As the permeability cutoff value is increased, large sections are no longer connected to a wellbore. This is likely the result of two changes : one, some cells no longer meet the definition for reservoir criteria, and two, some cells may lose contact with the wellbore leaving them in a disconnected state and not being included in the static connectivity numbers.

Like the original-permeability models, static connectivity at the 0.0 mD permeability cutoff is 62.49% and 79.55% for the single and average models respectively. These models both show a decrease in connectivity (both greater than 50%) as soon as permeability cutoffs were increased above 0 mD threshold. This indicates that the effective values, as a whole, have been shifted towards the lower permeabilities. This can be seen easily in a histogram of the original- and effective-permeability outputs (Fig. 6.8). The range of permeability values for the effective values have been narrowed considerably compared to the original values. This is manifested in the static connectivity results as the models show more drop-offs in connectivity and happen sooner compared to the original values. Additionally, the connected percentage of cells reaches 0% connectivity much more quickly than the original-permeability connectivity analysis shows. This is because the upper range of permeability values are altered during the upscaling process and brought down closer to the lower values. Furthermore, the initial drop off for the effective-permeability values indicates that the average has shifted towards the lower permeability values due to the upper range of values being negated.

Overall, the comparison shows that as the permeability cutoffs approach the middle of the permeability range; the difference between original- and effective-permeability models becomes increasingly significant. While the two values start at nearly the same connectivity percentage, the two models behave different as the cutoff is increased, with the effective permeability values dropping towards 0% connectivity sooner and more rapidly. These different behaviors indicate why it is important to have the correct permeability value when creating a geologic model. Depending on the type of permeability used, original or effective values, the total volume of reservoir connectivity at this well spacing may be tens of percent different.

6.5. Significance and Discussion

The Terry and Hygiene formations in Spindle field consist of four key lithofacies: 1) wavy laminated sandstone, 2) planar cross-laminated sandstone, 3) ripple cross-laminated sandstone, and 4) structureless sandstone. The facies are stacked in successions that are characterized as either sandstone-rich or sandstone-poor. The sandstone-poor intervals exhibit alternating patterns of dominantly wavy laminated sandstone with minor amounts of structureless sandstone and planar cross-laminated sandstone. The sandstone-poor facies associations are interpreted to have formed in an inter-bar setting as part of an offshore-bar complex, exhibit relatively low permeability values, and are non-reservoir facies. In contrast, the sandstone-rich intervals consist of alternating planar cross-laminated sandstone, ripple cross-laminated sandstone, and structureless sandstone. These deposits are interpreted to represent offshore sand bars and are considered to be the primary reservoir facies given their relatively higher permeability values.

The results suggest that upscaling permeability data is an important step in reservoir analysis, proper definition of reservoir-quality rock at the field scale, and mapping of reservoir-quality lithofacies. The estimation and use of effective properties for reservoir definition and modeling is important as it has a direct impact on the number and type of wells required for reservoir development. The results show that after upscaling, the range of permeability is reduced, and the average permeability is decreased (by more than 50%). The decrease in average permeability varies by facies and is only minimally affected for the structureless sandstone facies. Using the original permeability values from permeametry or core-plug measurements will result in field-scale reservoir maps (models) in which the average permeability values are too high and that exhibit unrealistic distributions of extreme (too high and too low) permeability values. The extreme values of permeability can potentially have a profound effect on fluid-flow simulations and production estimates.

Analysis of the 3-D static connectivity (to producing wells) of reservoir volumes as defined by permeability cutoffs shows that for relatively lower permeability cutoffs, there is a distinct difference in connected volume between original- and effective-permeability models; in some cases, 50% lower connectivity for the effective-permeability model. This is significant because it represents the reservoir volume connected to wells for potential production. Also, for the lower permeability cutoffs, the total volume of potential reservoir rock is essentially the same as the connected volume; all potential reservoir cells are connected to wells. As the permeability cutoff (reservoir definition) increases, static connectivity decreases and the differences between the original- and effective-permeability models is reduced. The differences between original- and effective-permeability values and models indicate why it is important to utilize scale-dependent permeability values for reservoir mapping at the field scale.

Appendix A

Facies and Core Descriptions

Geologic Setting and Information

Prior to the deposition of the Hygiene Formation, the Denver Basin was part of the Cretaceous Western Interior Seaway (Raynolds, 2002; Weimer, 1996). Deep marine shales were deposited by the Western interior seaway, which in the Denver Basin correspond to the Pierre Shale. Correlative deep marine shales are also present in other Rocky Mountain basins as well and are all associated with the seaway. The Cretaceous Western Interior Seaway was partitioned during the Laramide orogenic event and drained when the entire area was uplifted. During this time, the Denver Basin was formed as episodic downwarping of the crust caused structural lows to form just to the west of the rising mountain ranges. The Denver Basin is bounded by structural features in the north, south, and west but has no definitive structural boundary in the east (Fig. A.1) (Weimer, 1996). In the west, the Rocky Mountain Front Range provides the structural boundary for the basin while the basin is bounded in the south by the Apishipa Arch. In the north, the basin is bounded by the Hartville uplift and Cambridge-Chadron Arch. Additionally in the north a small sub-basin within the broader Denver Basin is seen. It contains the same structural boundaries to the north, east, and west but is separated from the deeper Denver Basin by the Greely Arch in the south.

Core and Facies Descriptions

This study utilized four cores located around the Wattenberg and Spindle field areas of the Denver Basin. The cores for this study were identified based on the availability and accessibility of the cores, log data availability for cored wells, and clarity of facies for ease of identification and modeling. Three of the four cores are located at the University of Colorado-Boulder while the fourth is located at the USGS Core Research Center in Golden, Colorado. While two of these cores were used for near-wellbore modeling, the other two cores were only used for permeability acquisition. The McHale #1 and Champlin 369 cores used for the modeling were described in detail (Fig. A.2; Fig. A.3). The Moser #1 and Sidwell cores were used to acquire permeabilities in order to provide enough data for each of the facies. The data collected from the two cores, one from the Terry Formation and one from the Hygiene Formation, were combined with the data collected from the McHale #1 and Champlin 369 cores to provide additional data points for the near-wellbore modeling.

Detailed sedimentary descriptions of the cores lead to the identification of four lithofacies based on sedimentary structures and lithology. These lithofacies were identified in all four cores (Fig. 6.4) and include wavy laminated sandstone, planar cross-laminated sandstone, ripple cross-laminated sandstone, and structureless sandstone. These facies are repeated throughout the entire Terry and Hygiene formations and with varying thicknesses and amounts of each (Figs. A.4; Fig. A.5). Similar facies were identified by previous studies and indicate several potential depositional environments (Kiteley, 1976; Porter, 1976; Al-Raisi et al, 1996; Helsley, 1985; L. Kiteley, personal communication).

Facies A is a wavy laminated sandstone with varying degrees of mud and bioturbation. While

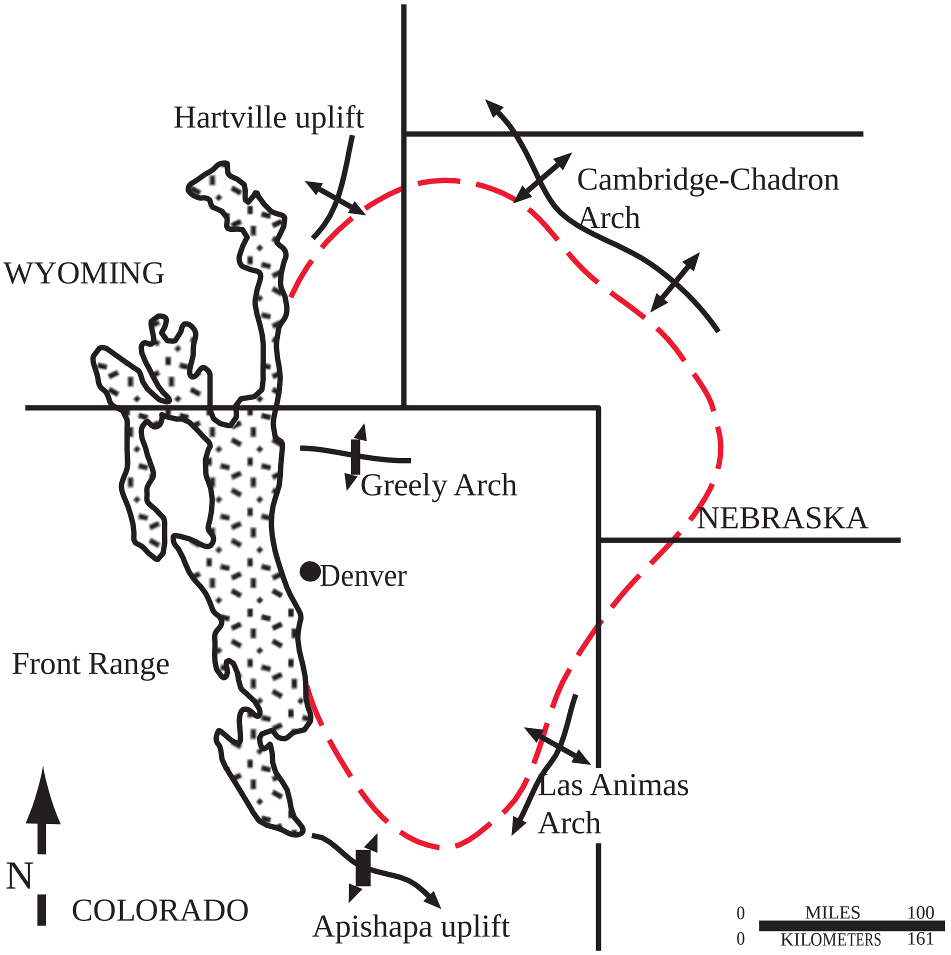

Fig. A.1. Schematic structural map of Denver Basin (outlined in red) showing the structural bondaries in the north, south, and west. There is no defined structural boundary in on the east side of the basin. Modified from Weimer et al. (1986) and Dickinson et al. (1988).

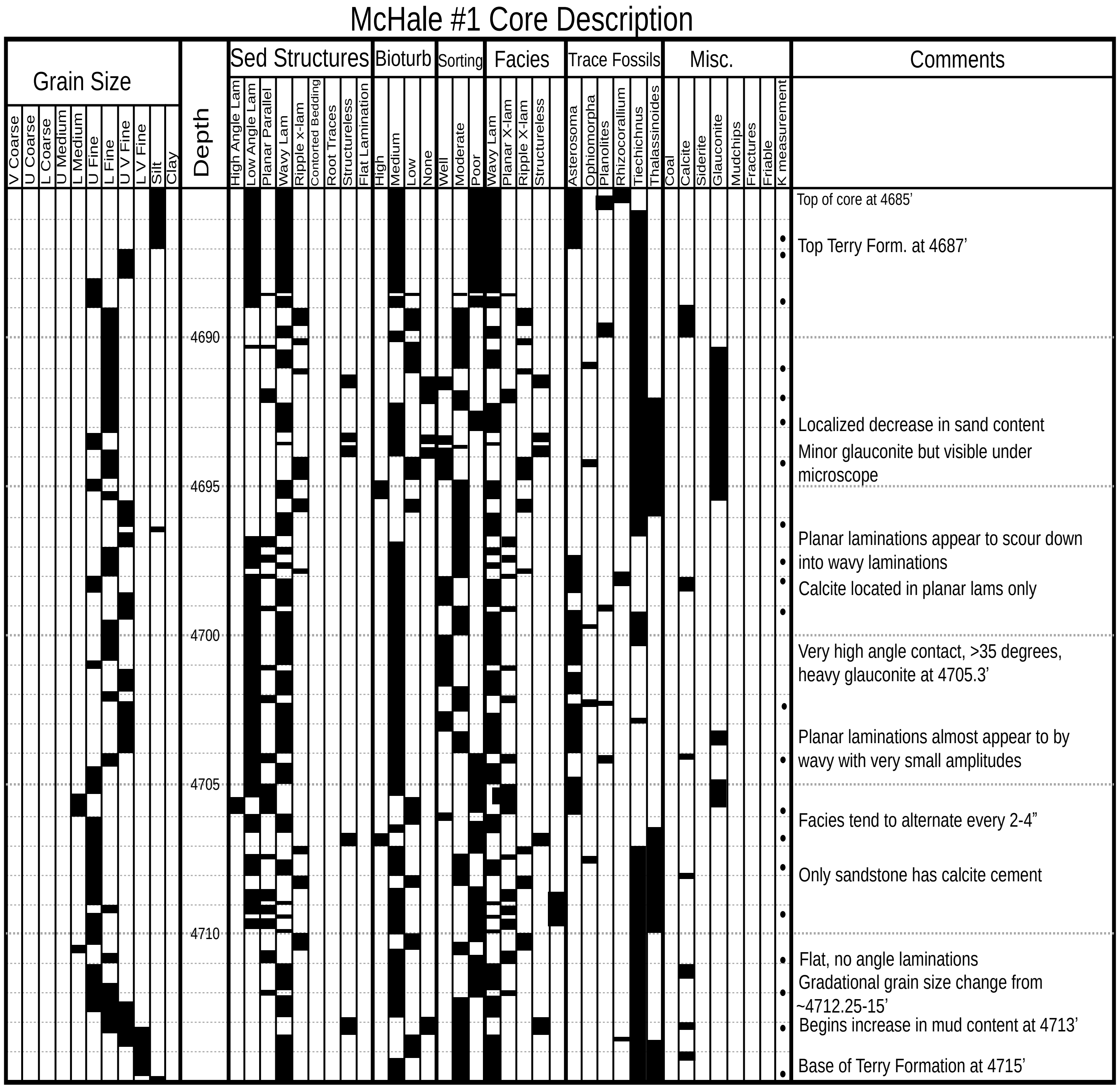

Figure A.2. Core description of McHale #1 core. (API: 05123076430000).

Champlin 369 Core Description

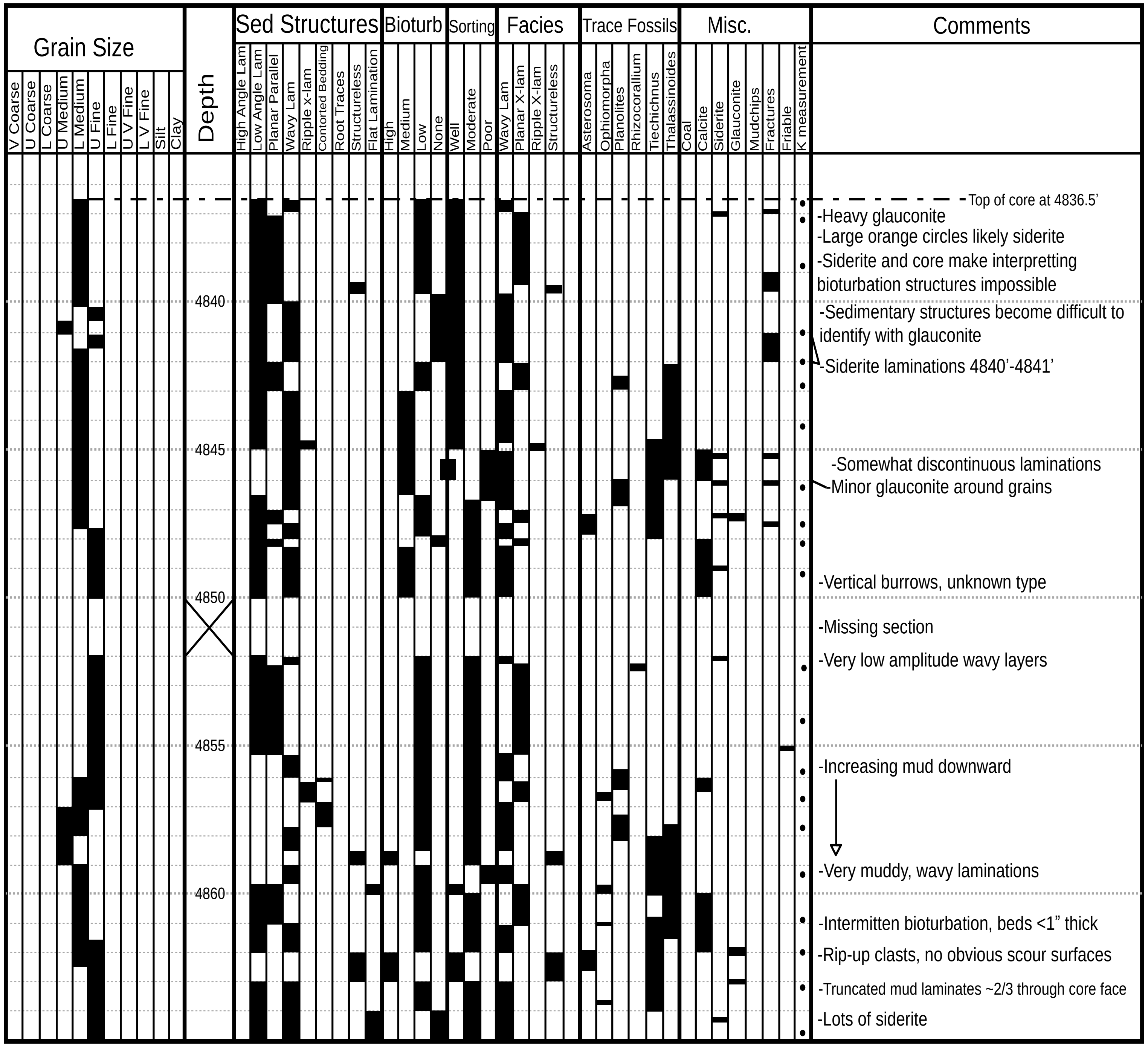

Top of core at 4836.5'

-Heavy glauconite

-Large orange circles likely siderite

-Siderite and core make interpretting bioturbation structures impossible

-Sedimentary structures become difficult to identify with glauconite

-Siderite laminations 4840'-4841'

-Somewhat discontinuous laminations

-Minor glauconite around grains

-Vertical burrows, unknown type

-Missing section

-Very low amplitude wavy layers

-Increasing mud downward

-Very muddy, wavy laminations

-Intermitten bioturbation, beds <1" thick

-Rip-up clasts, no obvious scour surfaces

-Truncated mud laminates ~2/3 through core face

-Lots of siderite

Champlin 369 Core Description

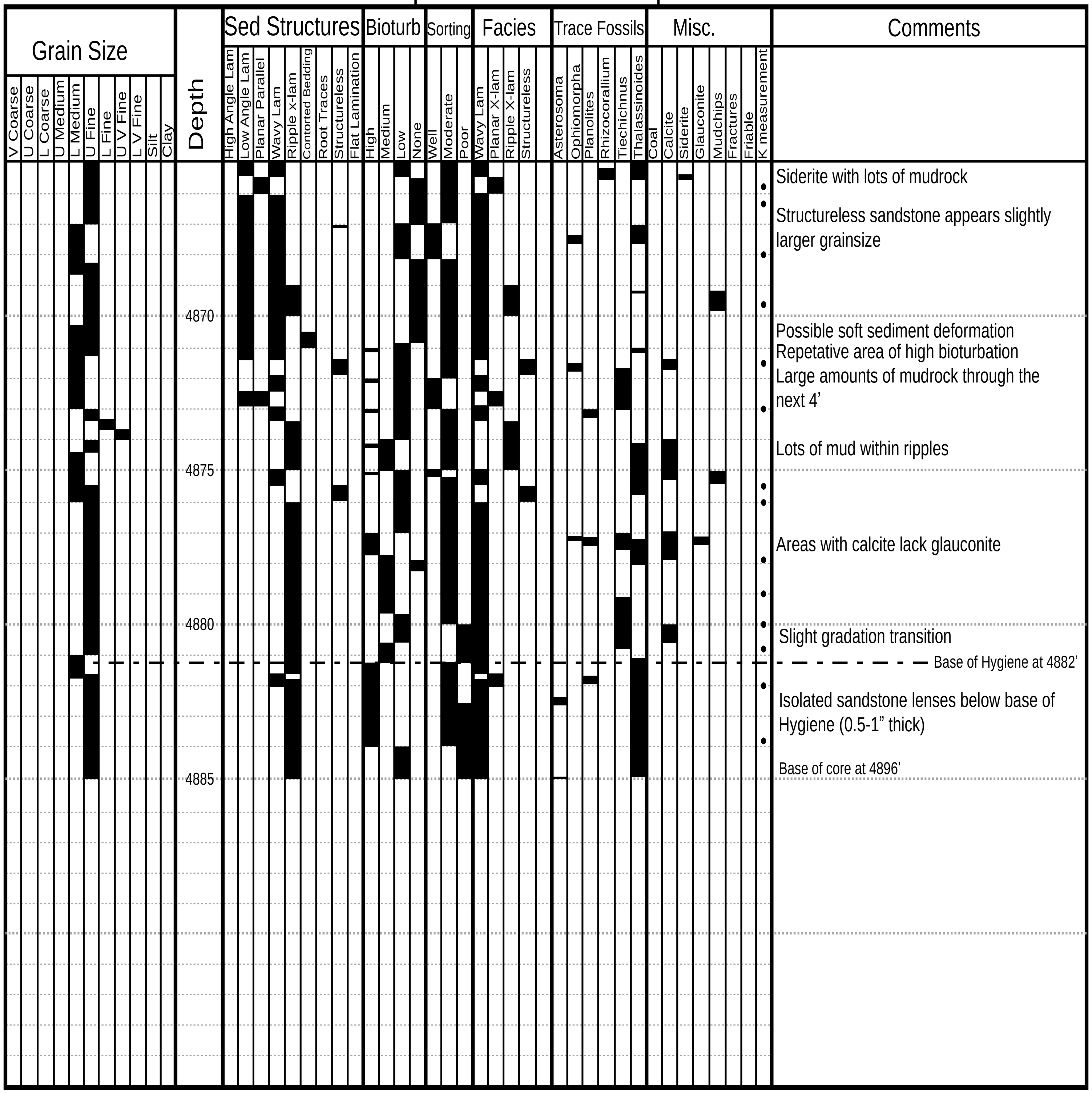

Siderite with lots of mudrock

Structureless sandstone appears slightly larger grainsize

Possible soft sediment deformation

Repetative area of high bioturbation

Large amounts of mudrock through the next 4’

Lots of mud within ripples

Areas with calcite lack glauconite

Slight gradation transition

Base of Hygiene at 4882’

Isolated sandstone lenses below base of Hygiene (0.5-1” thick)

Base of core at 4896’

Fig. A.3 Core description of Champlin 369 core.

Facies Code	Total Footage (ft)	Total %	Arithmetic Average (in)	Geometric Average (in)	Standard Deviation (in)
A	13.27	49.10	2.488	1.901	1.938
B	4.53	16.80	1.754	1.422	1.025
C	1.45	5.40	2.032	1.382	1.628
D	7.79	2.80	1.160	1.006	0.607

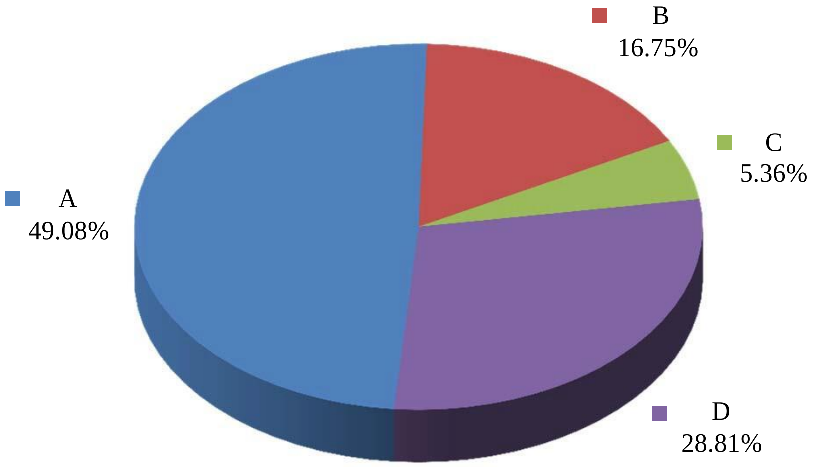

Facies A - Wavy Laminated Sandstone Facies B - Planar Laminated Sandstone Facies C - Ripple Cross-laminated Sandstone Facies D - Structureless Sandstone

Fig. A.4. Facies, facies percentages, and average thicknesses of each facies used in near- wellmore modeling process for the McHale #1 core. Facies A represents the non-reservoir intervals while facies B, C, and D comprise mostly reservoir intervals.

Facies Code	Total Footage (ft)	Total %	Arithmetic Average (in)	Geometric Average (in)	Standard Deviation (in)
A	23.04	49.02%	3.950	2.881	3.411
B	12.34	26.26%	3.365	2.446	2.880
C	6.68	14.21%	2.358	1.851	2.374
D	2.69	5.72%	2.483	2.318	0.937

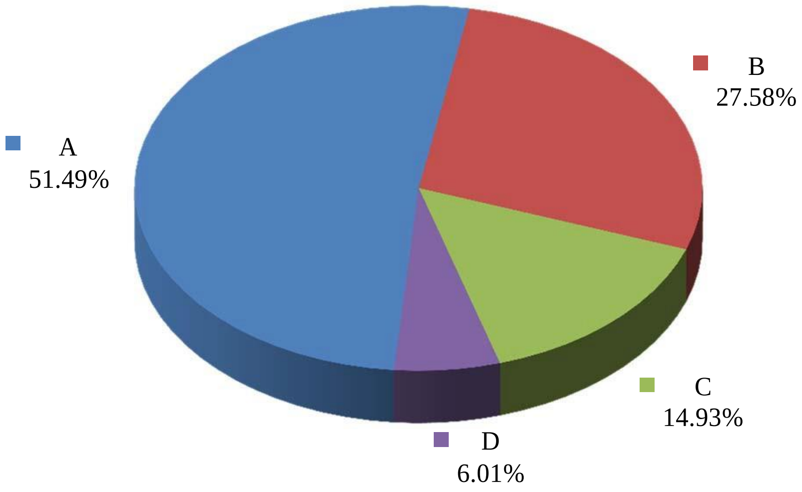

Facies A - Wavy Laminated Sandstone Facies B - Planar Laminated Sandstone Facies C - Ripple Cross-laminated Sandstone Facies D - Structureless Sandstone

Fig. A.5. Facies, facies percentages and average thicknesses for each facies used in the near-wellbore modeling for the Champlin 369 core. Facies A represents mostly non-reservoir intervals and facies B, C, and D represent reservoir intervals.

the bioturbation is the likely cause of some to possibly all of the wavy beds, it is not considered important to differentiate. The bioturbated sandstone and mudrock lamina both have similar petrophysical properties to other non-bioturbation lamina elsewhere in the core. Facies A is commonly seen as containing between 10–50% mud laminations, whereas the wave amplitude and wavelength is only several centimeters. The variation in mud is associated with both the bioturbation, creatures bringing mud in from above or below, as well as with changes in depositional environment. The more mud-dominated wavy laminated facies are likely formed in quiet water settings, indicating that sea level may have dropped locally for a short period of time, causing shelf currents to move further offshore, which did not affect this area.

Facies B, planar laminated sandstone, represents approximately 20% of the facies identified in all of the cores. The planar laminated sandstones have dips ranging from 0–15° with the majority dipping around 5–10°. As this is not an oriented core, dip direction could not be determined; therefore, it was assumed that all lamina dip in the same direction. The general pattern observed in mudrock laminae is densely spaced mudrock layers at the base that decrease in density towards the top. Additionally, of all the facies identified, this one appears to contain the least amount of bioturbation. This is likely caused by the higher energy settings in which planar lamina were deposited.

Facies C is a structureless sandstone that contains very little to no mudrock present. Facies C represents approximately 5% of the total facies observed in the core. The structureless sandstonehas two possible depositional interpretations and both are equally as likely in this setting. The first possible interpretation is that these are storm deposits that are deposited so rapidly that they do not have time to form coherent layers. As this is relatively shallow water (less than 100 ft (30.5 m)), large storms may have swept large volumes of sand out to sea. Additionally, these deposits may be interpreted as being related to bioturbation. The prior sand and mud that was deposited may have been so extensively bioturbated that it was completely homogenized, creating what appears to be a sandstone unit that has no structure. Due to the level of bioturbation in the area and surrounding facies, this is also a quite viable interpretation. As the structureless sandstones tend to show no significant petrophysical differences, it can be assumed that both of these interpretations are correct and the exact nature of its origin is not critical to this study.

Facies D contains ripple foresets and was interpreted to be a ripple cross-laminated sandstone. This facies represented approximately 30% of the facies noted in the described cores and averaged just a few inches thick in most places. The ripple laminated sandstones had amplitudes measured in the tenths of inches with wavelengths of 1–2 in (2.5–5 cm). Similar to the planar laminated sandstone above, migration direction of the ripple laminated sandstone was not able to be determined, so it is assumed the migration direction of all facies is uniform.

Depositional Environment

Over the last 40-plus years, the Terry Formation, and to a lesser extent the Hygiene Formation, have been studied in an attempt to determine what the characteristics of the formations are and what these characteristics mean in terms of the formations' origins (Moredock and Williams, 1976; Porter, 1976; Kitely, 1977, 1978; Porter and Weimer, 1982; Helsley, 1985; Pittman, 1989; Walker and Bergman, 1993; Al-Raisi et al., 1995; Ladd, 2001; E. G. Gustason, 2012, personal communication). Possible depositional environments for the Terry Formation might include: offshore bars, shoreface beach sands, and deltaic sediments. All of these depositional models would have fit the environment at the time of deposition, which consisted of the Cretaceous Western Interior Seaway, a shallow epeiric sea (Fig. A.6) (Kiteley, 1977; Ladd, 1995; Al-Raisi et al., 1996; Slatt et al., 1997; Ladd, 2001). In the same way, the Hygiene Formation is considered to have a similar depositional environment but was more likely a deltaic sandstone deposit (Kiteley, 1977).

Based on the facies observed in this study, an offshore bar complex has been interpreted as the likely depositional environment for the Terry and Hygiene formations. Porter (1976) provided a similar depositional environment for the Terry and provides a good model of the depositional setting (Fig. A.7). The offshore bars (and to a lesser extent offshore sheet sandstones) likely formed as sand was moved away from the shoreline by longshore currents. These currents would have been part of the Cretaceous Western Interior Seaway and would have sourced sediments from a nearby delta. The delta that brought sediments to the seaway is also problematic with some authors indicating that it may have been the large Parkman Delta in present day Wyoming (Porter and Weimer, 1989). The source of these sediments would have likely been shed from the mountains west of the Cretaceous Western Interior Seaway as both formations lie on the western side of the seaway. Using well log analysis, Cant (1992) provides further evidence of an offshore depositional setting. Cant provides evidence for log interpretation based on gamma-ray (GR) and/or spontaneous potential (SP) log shape characteristics (Fig. A.8). Depending on the shape of the log response for a given log, the depositional environment may be determined. While this study focuses primarily on SP logs, GR logs are also displayed in order to present evidence for an offshore setting. Cross-sections of nearly all logs are provided in figure 6.6 and show what Cant (1992) calls a symmetric log shape and a funnel log shape, which indicates a potential offshore bar depositional setting. The symmetric SP (and to a lesser extent GR) log response has been previously shown to represent offshore sandstone bars while the funnel shape log responses may indicate several different environments including shallow marine sheet sandstones. With presence of both of these log shapes in all the logs showing, the depositional environment may be aligned with what the previous works of Kiteley (1977), Porter and Weimer (1989), and Al- Raisi et al. (1996) interpret as being in an offshore setting, potentially an offshore bar complex. As previously discussed, the facies also provide evidence for a potential offshore bar complex with zones of rapid bar build up and zones of slower deposition and quieter water settings being shown.

Nomenclature

Nomenclature of the Terry and Hygiene formations has become muddled between industry and academic use. The Terry Formation is commonly referred to in the petroleum industry as the Sussex Formation, while the Hygiene Formation is known as the Shannon Sandstone (Moredock

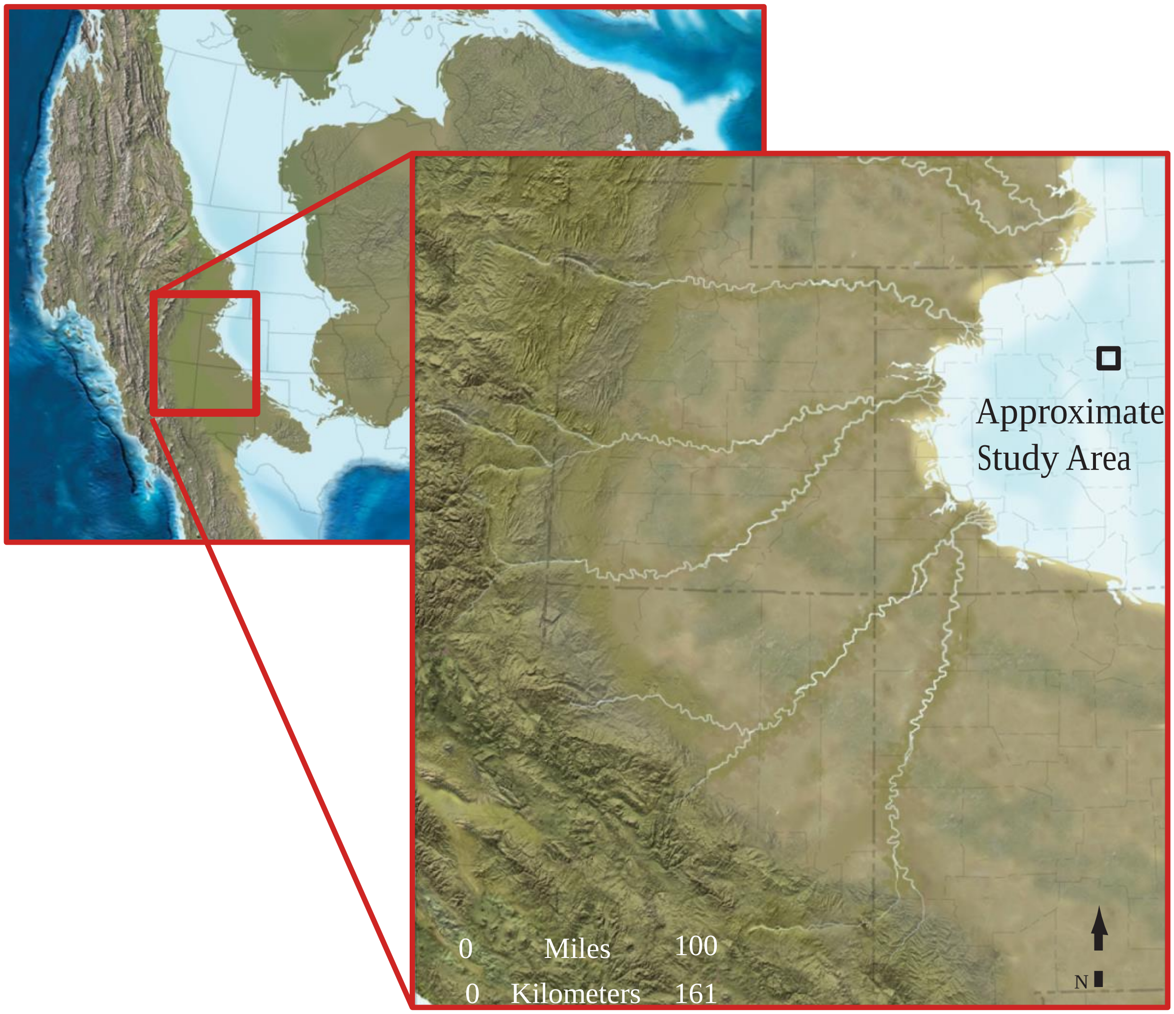

Figure A.6. Paleogeographic map of western United States during the Late Cretaceous Campanian age showing the approximate depositional environment of the Terry and Hygiene formations. The Terry and Hygiene formations were both likely deposited in a shallow marine environment relatively near a delta located to the west. Modified from Blakey (1997).

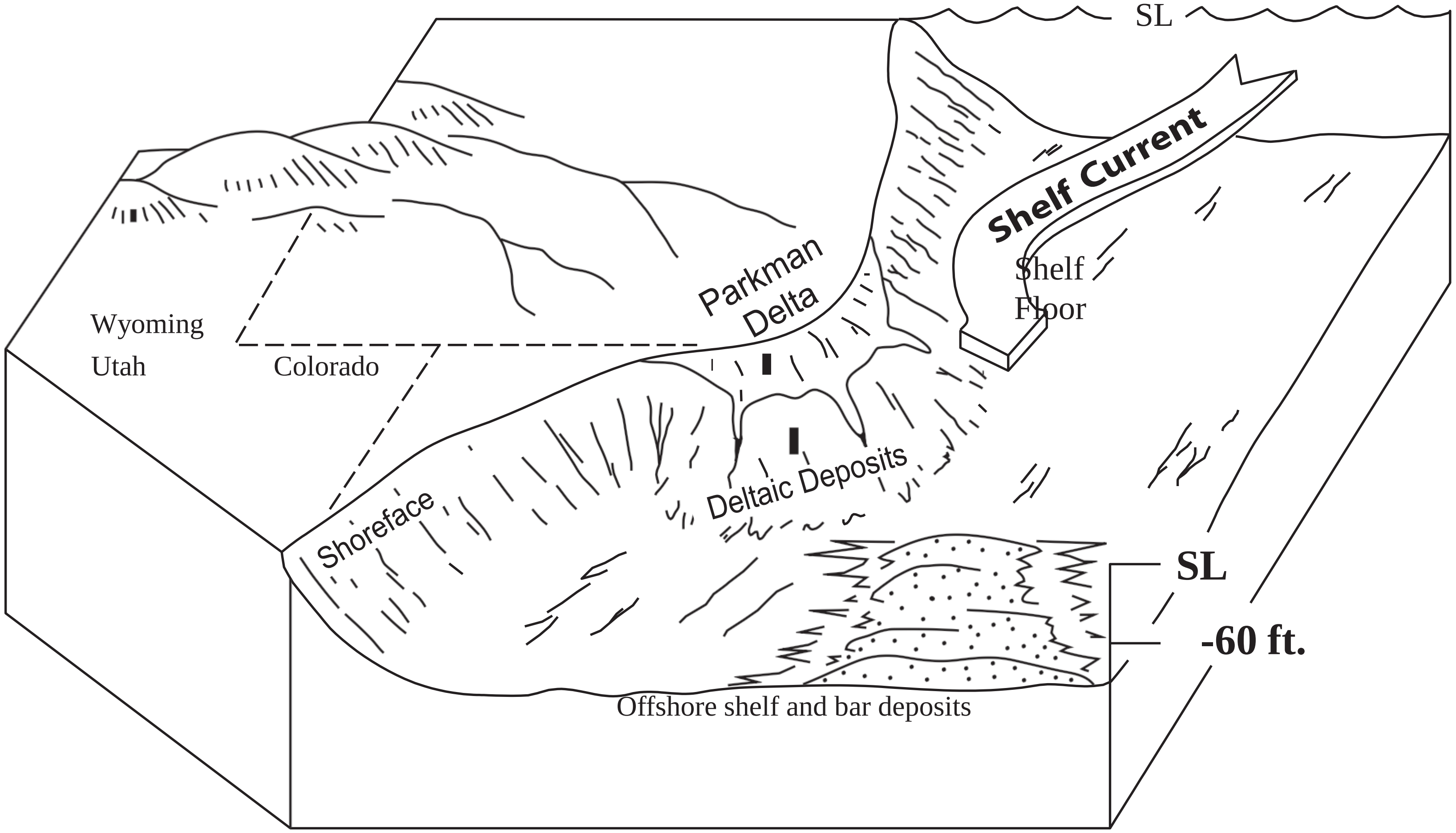

Figure A.7. Block diagram of interpretted depositional environments of the Terry and Hygiene formations. This study inteprets the environment of deposition for both as offshore shelf and bar complex deposits. SL = Sea Level. Modified from Porter (1978).

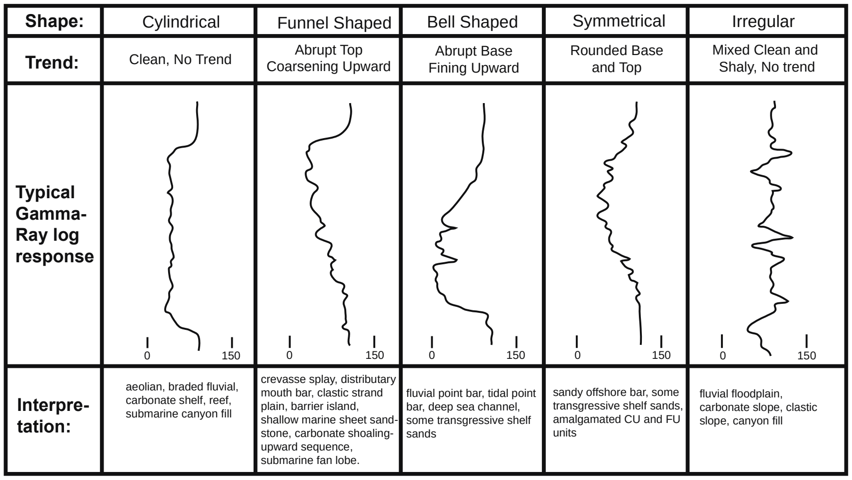

Figure A.8. Typical gamma-ray responce for different depositional environments as determined from log responces. This interpretation method was determined from core-to-log comparisons and can be useful in determining depositional environments. Log interpretation and core descriptions are used to determine depositional environments for the Terry Formation. Modified from Cant (1992) and Sloan (2011).

and Williams, 1976; Kiteley, 1977). These names come from the better known Sussex and Shannon formations of the Powder River Basin. When they were first encountered, it was assumed these formations were time equivalent members of the Pierre and Steele Shale Formation in the Denver and Powder River basins respectively. However, after dating of the formations through ammonite fossil assemblages, the Terry-Sussex formations and the Hygiene-Shannon formations were shown to be of different ages and thus not equivalent (Fig. A.9). However, given the similar nature of the four formations, their depositional environments may be similar with the Sussex and Shannon formations being sourced from the Parkman Delta in Wyoming and being called shelf-ridge complexes (Porter and Weimer, 1982; Walker and Bergman, 1993).

Reservoir Zones

Using digital logs available for the wells in the study area along with core observations and permeability data, four zones were identified (Fig. 6.5; Fig. A.10). These zones are determined to be both reservoir and non-reservoir, based on the facies present and the permeabilities of the facies. Reservoir zones are characterized by the negative SP shifts, higher resistivity, increased porosity, higher permeabilities (depending on facies), and facies consisting of mainly structureless sandstone and planar cross-laminated sandstone with varying amounts of ripple cross-laminated sandstone. Non-reservoir zones are characterized by SP values on or near the baseline (more positive than reservoir zones), resistivities around 1–2 ohm-meters, lower porosity and permeability values, and facies consisting of predominantly wavy laminated sandstone. This facies is more mudrock-rich and it is likely the reason why they are most commonly seen in non-reservoir zones that contain lower porosity and permeability values. These zones can be seen in a cross-sectional view as having varying thicknesses, which is likely associated with varying sand bar sizes (Fig. 6.6). Reservoir zones can be visually identified in core by looking at mudrock content and color. Non-reservoir zones tend to be darker (high mud content), while reservoir zones will appear lighter, due to the sparse amount of mud present (Fig. A.10).

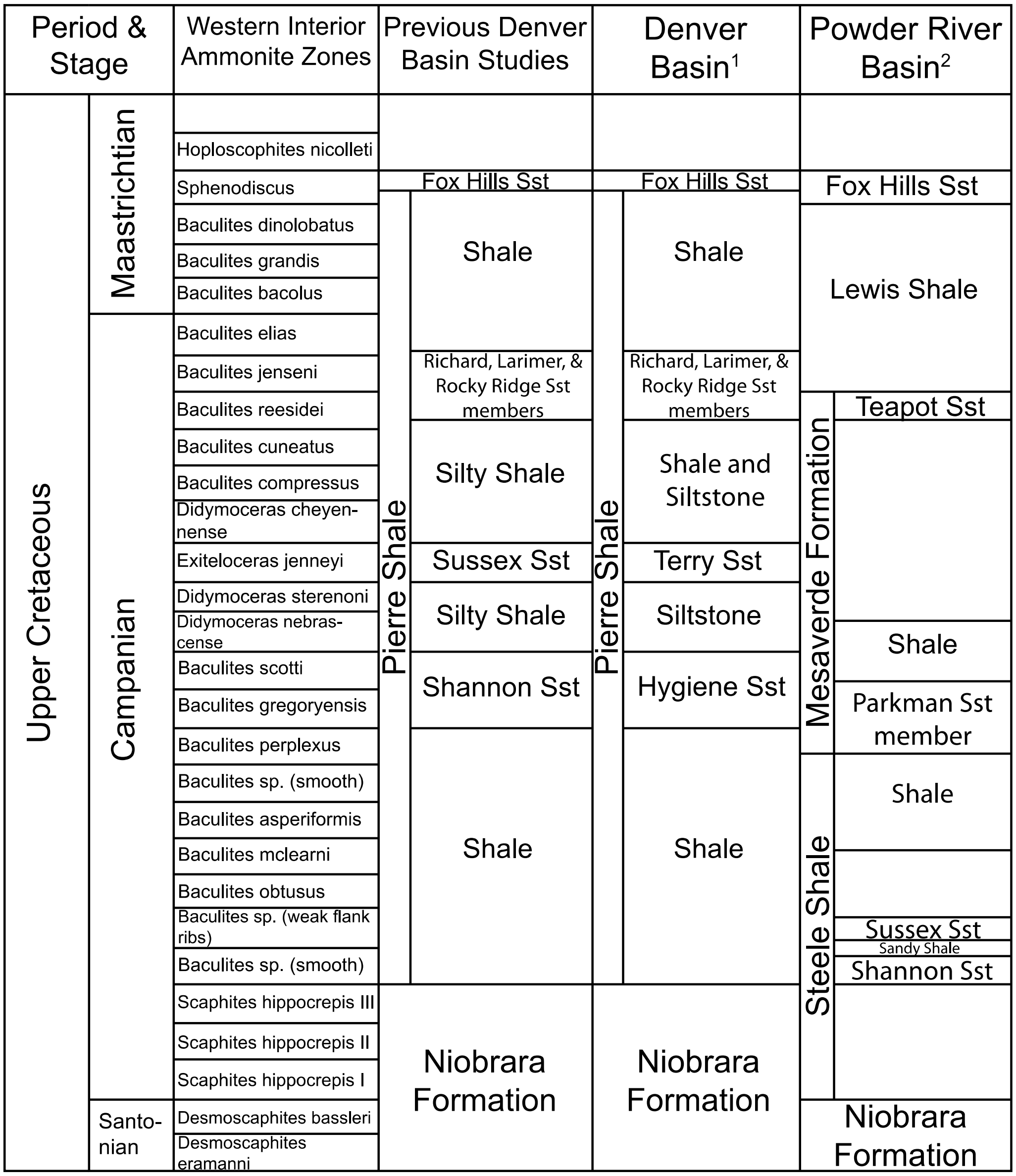

Period & Stage		Western Interior Ammonite Zones	Previous Denver Basin Studies		Denver Basin[1]		Powder River Basin[2]	
Upper Cretaceous	Maastrichtian							
		Hoploscophites nicolleti						
		Sphenodiscus	Fox Hills Sst		Fox Hills Sst		Fox Hills Sst	
		Baculites dinolobatus	Pierre Shale	Shale	Pierre Shale	Shale	Lewis Shale	
		Baculites grandis						
		Baculites bacolus						
	Campanian	Baculites elias						
		Baculites jenseni		Richard, Larimer, & Rocky Ridge Sst members		Richard, Larimer, & Rocky Ridge Sst members		
		Baculites reesidei					Mesaverde Formation	Teapot Sst
		Baculites cuneatus		Silty Shale		Shale and Siltstone		
		Baculites compressus						
		Didymoceras cheyennense						
		Exiteloceras jenneyi		Sussex Sst		Terry Sst		
		Didymoceras sterenoni		Silty Shale		Siltstone		
		Didymoceras nebrascense						Shale
		Baculites scotti		Shannon Sst		Hygiene Sst		
		Baculites gregoryensis						Parkman Sst member
		Baculites perplexus		Shale		Shale	Steele Shale	Shale
		Baculites sp. (smooth)						
		Baculites asperiformis						
		Baculites mclearni						
		Baculites obtusus						
		Baculites sp. (weak flank ribs)						Sussex Sst Sandy Shale
		Baculites sp. (smooth)						Shannon Sst
		Scaphites hippocrepis III	Niobrara Formation		Niobrara Formation			
		Scaphites hippocrepis II						
		Scaphites hippocrepis I						
	Santonian	Desmoscaphites bassleri					Niobrara Formation	
		Desmoscaphites eramanni						

Fig. A.9. Stratigraphic nomenclature chart for the Denver and Powder River Basins. This study follows the Denver Basin nomenclature established by Kiteley (1970). Modified from (1) Kiteley, (1970) and (2) Gill et al., (1970).

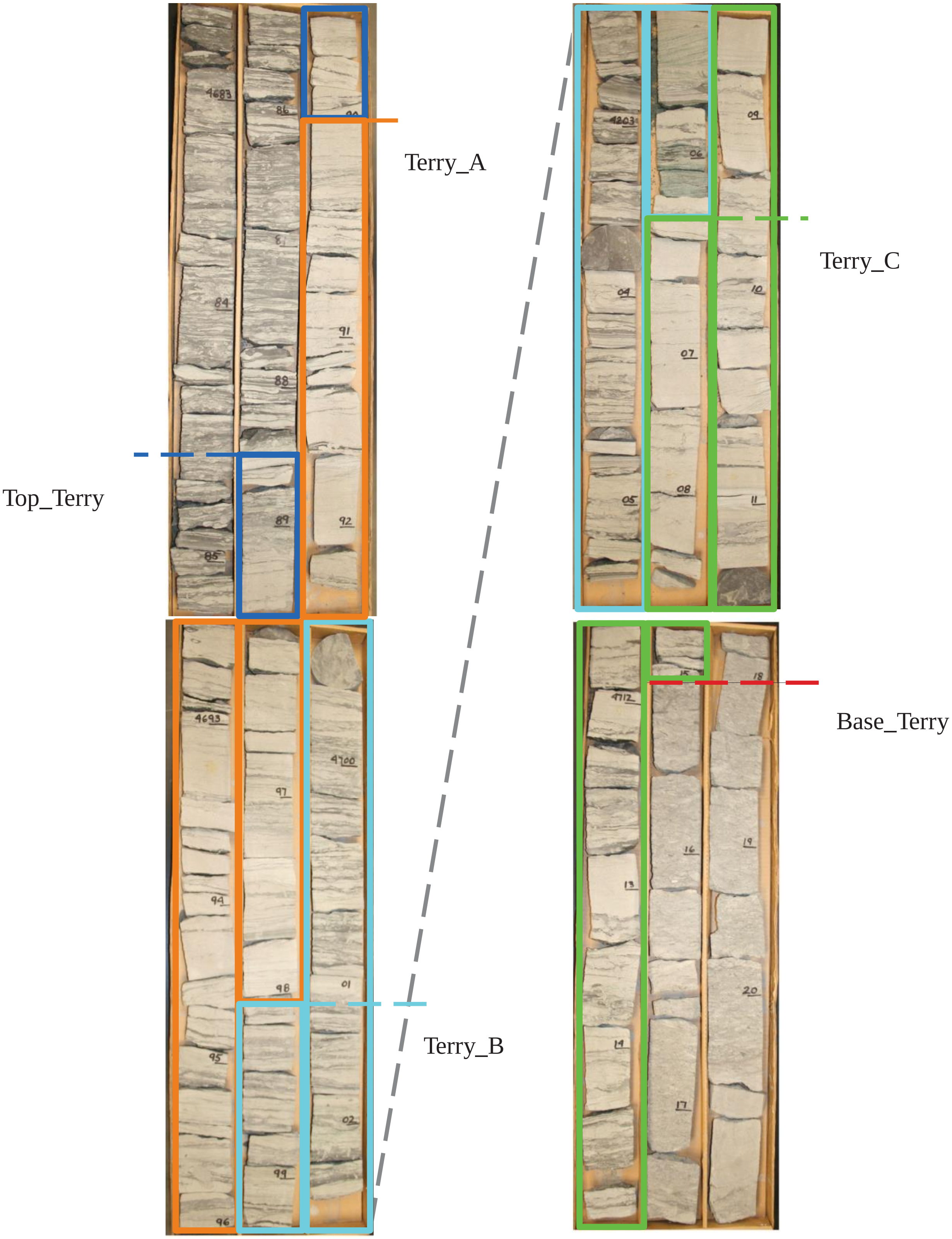

Fig. A.10. McHale #1 core with reservoir zones outlined and zone tops. Colors correspond to zone tops shown in type log (Fig. 6.5). Non-reservoir zones appear a darker color due to the higher mudrock content. This mudrock adversely affects reservoir properties making it a non-reserovir zone. Reservoir zones appear lighter in color and are cleaner sandstones.

Appendix B

Permeability Acquisition and Results

Permeability Acquisition

Permeabilities were acquired on four cores in Spindle field, Denver Basin, Colorado (Fig. 6.1). To acquire these permeabilities, a probe-permeameter at the University of Colorado-Boulder was used. The permeameter was used due to its ability to rapidly capture permeability data, to capture individual lamina permeabilities, and to acquire a large amount of data inexpensively. The permeameter works by flowing nitrogen gas through the core sample and measuring the pressure in the gas line. The flow rate of nitrogen gas is controlled by a valve that affects the flow pressure of nitrogen gas in the gas line leading to the sample. When the pressure in the gas line reaches the same pressure as the atmospheric pressure, the flow rate of nitrogen gas into the sample is consistent with the nitrogen gas flow rate out of the sample. This equilibrium is important as the flow at this point in time is used to calculate the permeability of the sample (equation A.1). All permeability numbers for each core are outlined in this appendix.

$$K_a = \frac{2\mu Q_b P_b T_{act}}{a G_0 (p_1^2 - P_2^2) T_{ref}} * 1000 \tag{A.1}$$

where:

K_a = air or gas permeability (mD)

μ = viscosity of gas flowing through sample (cp)

Q_b = volumetric flow rate standard cc/sec. Used to calculate flow rate where flow rate=Qb / 60

P_b = standard reference pressure for mass flow meters, (atm) P_1 = upstream pressure (pressure at tip). Flow Pressure (psia) P_2 = downstream pressure (atmospheric pressure, psia)

a = Inside radius of tip (cm)

G_0 = Geometrical shale factor

b_d = b / a (used to determine G0, dimensionless)

b = external radius of tip (cm) R_d = Rcore / a (dimensionless) R_{core} =core radius (cm)

L_d = L core / a (dimensionless)

L_{core} = length of core (cm)

T_{ref} = reference temperature of mass flow meters (K) T_{act} = actural flowing temperature of gas (K)

The permeability that is calculated using this equation by the permeameter is known in this study as the Temco permeability. It was determined through permeability comparison with the Temco permeability and standards with known point-permeability measurements that the permeameter could not calculate accurate permeability at high and low values. To counter this issue, a calibration chart was created using core plugs with known permeabilities that are similar to the expected permeabilities of the Terry and Hygiene formations (Fig. B.1). These core plugs were measured at the beginning and end of every day for several reasons. The first was to ensure the machine was performing correctly. Prior to the measuring of any of the permeabilities for this study, the probe permeameter was used to measure the five standards several hundred times. This gave a range of permeability values that the machine would produce when these samples were measured. When collecting the permeabilities on core samples, these core plug standards were measured at the beginning and end of every day, and the values were compared with the measurements defined on the core plugs previously. If the data range was changed, this could indicate a leak in nitrogen gas or other potential problems in the machine. If a potential problem was detected, core data for that day would be resampled to ensure the measurements were correct. Additionally, these standards were used to create the calibration curve used to calibrate the machine permeability to the permeabilities of similar rocks in this study. All Temco permeabilities were calibrated after all data was collected. This allowed for the calibration plot to utilize the maximum amount of data to refine the regression line used for the calibration; a total of 1539 measurements were used.

The calibration curve derived from the core-plug standards was applied to all measures during post-processing. Also during post-processing, each permeability value was evaluated to determine if any incorrect data existed. Due to the nature of the permeameter and the quality of some samples, various bad data points were observed. The bad data points were primarily caused by poor tip seals on the core face. Other bad data points are observed that are related to the nature of some lamina, relatively large fractures or voids were sometimes sampled which caused the permeability to return abnormally high readings which were determined to be false.

Data points were determined to be bad based on observations at the time of the measurement and the evaluation of permeabilities after the data was collected. Some data points were suspect from the beginning and flagged accordingly due to the quality of the core surface. In post-processing, the data was sorted by facies and lamina type and values that were abnormally high or low were excluded. Typically if the data points were larger than one standard deviation from the geometric average of the lamina in that particular facies, the data point was removed. Care was taken at this point to make sure the point was correctly classified as the correct facies. Each suspect data point was compared to the core or core photograph (depending on core availability) at the corresponding depth to determine the facies in which the point was taken.

Mudrock lamina also presented a unique challenge for measuring permeabilities. Data were analyzed as they were collected and after a significant amount of data were collected a problem with the permeabilities collected on the mudrock was observed. The error showed that nearly all of the permeabilities collected on the mudrock lamina were too high; they were almost all higher than that observed in the sandstone lamina. It was determined that the mudrock lamina large enough to be measured were comprised of multiple mudrock layers. Due to the nature of

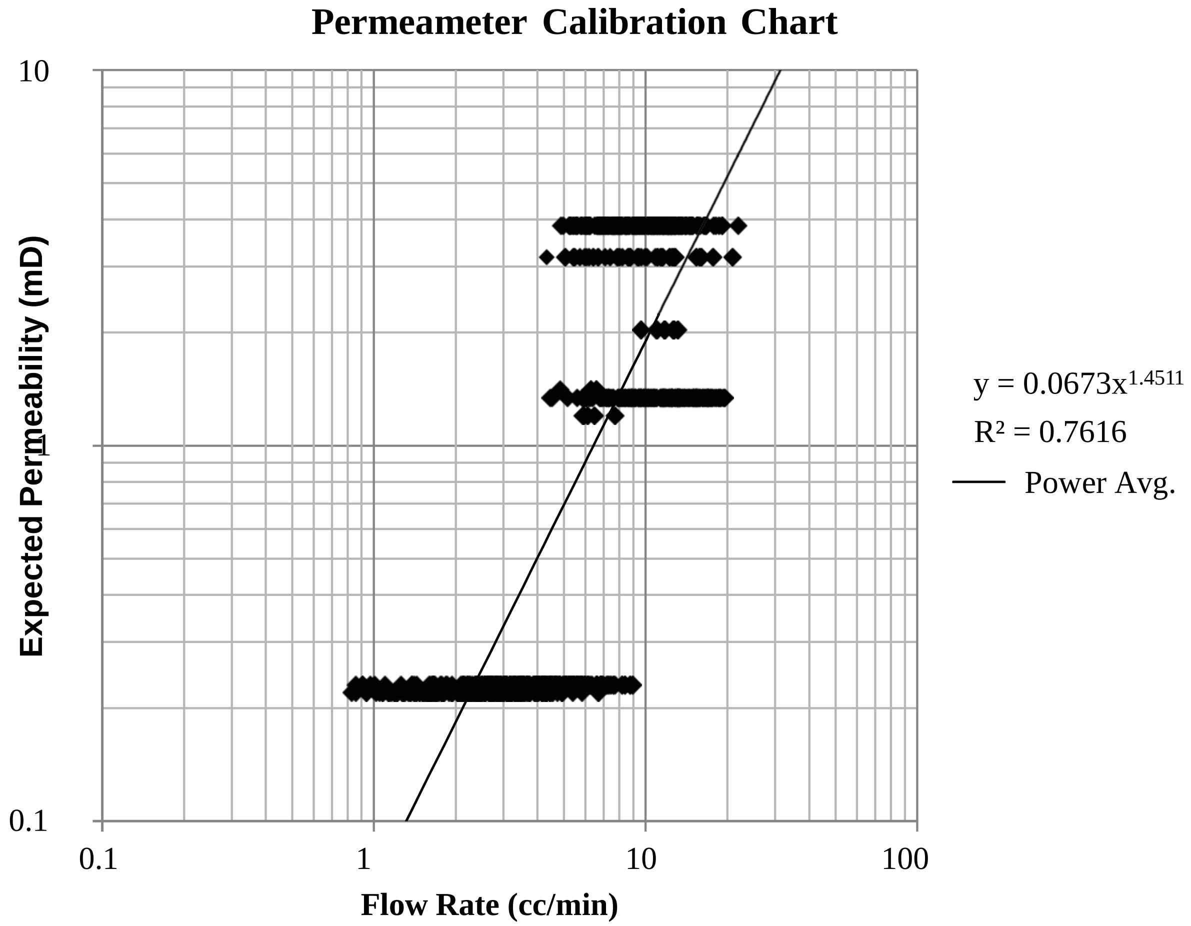

Fig. B.1. Cross-plot used to create calibration curve for TEMCO mini-probe permeamter. Using the flow rate for measurements taken on the core and the equation of the regression line, a calibrated permeability was determined for each data point acquired on the four cores. N=1539.

these lamina, they had begun to part along the bedding planes, causing what amounts to microfractures to form. These microfractures were likely caused or at least exacerbated by the continual wetting and drying of the cores in decades since their removal from the subsurface. As each lamina was sprayed with water during core descriptions, the mud lamina absorbed the water and expanded slightly only to contact again as it dried. With several decades of this, the microfractures would have formed and when measured by the minipermeameter, the permeability would be abnormally high. The higher permeability is due to the gas flowing preferentially through these fractures opposed to the pore network in the core. Attempts were made to measure the mudrock perpendicular to the bedding planes so an accurate permeability could be obtained; however, this proved difficult. The measurements were taken on surfaces where the core had fractured along mudrock layers. These breaks in the core were often sub-parallel to the lamina, so when a measurement was taken, some of the gas was still being flowed through the fractures between bedding planes. Additionally, the nature of the breaks made it difficult to get a good tip seal and to make sure that there was no leaking of nitrogen to the atmosphere. Due to these issues, a definite and accurate mudrock permeability was unable to be obtained for this study, and it was assumed all values would have a near-zero permeability, in this case 0.004 mD was used. What little data was obtained showed qualitatively that the mudrock was a barrier to flow but absolute values could not be acquired.

<u>McHale #1 Core Permeability Data</u>

N2 Flow Press. (psia)	Atm Press. (psia)	Flow Rate (cc/min)	TEMCO Perm (mD)	Calc. Perm (mD)	Core Depth (ft)	Facies
36.29	12.24	4.83	0.663	0.616	4701.00	A
36.26	12.23	10.38	1.426	1.828	4688.33	D
36.28	12.23	8.40	1.153	1.353	4688.33	D
36.28	12.23	9.51	1.305	1.614	4688.33	D
36.23	12.23	17.07	2.350	3.710	4688.33	D
36.22	12.23	13.40	1.846	2.629	4688.33	D
36.22	12.23	17.91	2.468	3.972	4688.33	D
36.25	12.23	14.55	2.001	2.956	4688.33	D
36.25	12.23	5.04	0.693	0.654	4688.33	D
36.30	12.23	8.56	1.174	1.390	4688.33	D
36.26	12.23	2.19	0.301	0.200	4688.33	D
36.16	12.20	6.29	0.871	0.896	4689.58	B
36.22	12.20	1.22	0.168	0.087	4689.58	B
36.21	12.20	3.35	0.463	0.366	4689.58	B
36.20	12.20	0.64	0.088	0.035	4689.58	B
36.18	12.20	1.19	0.165	0.084	4689.58	B
36.18	12.20	4.28	0.592	0.518	4689.58	B
36.23	12.23	5.10	0.703	0.665	4689.58	B
36.21	12.23	5.50	0.759	0.741	4689.58	B
36.21	12.20	4.14	0.572	0.494	4689.58	B
36.22	12.20	0.78	0.108	0.046	4689.58	B
36.21	12.20	3.32	0.459	0.361	4689.58	B
36.19	12.20	5.69	0.787	0.777	4689.58	B
36.22	12.20	2.73	0.377	0.273	4689.58	B
36.16	12.20	5.19	0.719	0.682	4689.58	B
36.19	12.20	15.76	2.179	3.311	4691.08	D
36.23	12.20	6.31	0.870	0.900	4691.08	D
36.24	12.20	4.45	0.613	0.548	4691.08	D
36.19	12.20	12.70	1.756	2.436	4691.08	D
36.25	12.20	9.84	1.355	1.694	4691.08	D
36.18	12.20	13.62	1.884	2.691	4691.08	D
36.19	12.20	9.02	1.247	1.497	4691.08	D
36.24	12.20	8.81	1.214	1.448	4691.08	D
36.16	12.20	9.14	1.265	1.525	4691.08	D
36.21	12.20	9.33	1.288	1.571	4691.08	D
36.21	12.20	5.55	0.766	0.750	4691.92	D
36.23	12.20	8.59	1.183	1.396	4691.92	D
36.20	12.20	7.18	0.992	1.082	4691.92	D
36.18	12.20	10.25	1.417	1.796	4691.92	D
36.25	12.20	13.95	1.920	2.784	4691.92	D
36.25	12.20	11.77	1.620	2.186	4691.92	D
36.23	12.20	10.98	1.513	1.980	4691.92	D
36.24	12.20	10.22	1.408	1.788	4691.92	D
36.24	12.20	11.59	1.597	2.139	4691.92	D
36.20	12.20	5.24	0.724	0.691	4691.92	D
36.23	12.20	7.60	1.048	1.173	4691.92	D
36.22	12.20	7.45	1.028	1.140	4691.92	D
36.19	12.20	5.83	0.806	0.805	4691.92	D
36.21	12.20	6.54	0.903	0.947	4691.92	D
36.23	12.20	6.16	0.849	0.870	4691.92	D
36.22	12.20	6.00	0.828	0.838	4691.92	D
36.23	12.20	7.99	1.101	1.260	4691.92	D
36.19	12.18	5.92	0.813	0.822	4691.92	D
36.14	12.18	6.28	0.865	0.894	4691.92	D
36.21	12.18	8.57	1.177	1.392	4691.92	D
36.22	12.18	5.83	0.800	0.805	4691.92	D
36.18	12.18	4.71	0.648	0.594	4691.92	D
36.21	12.18	6.17	0.848	0.872	4691.92	D

N2 Flow Press. (psia)	Atm Press. (psia)	Flow Rate (cc/min)	TEMCO Perm (mD)	Calc. Perm (mD)	Core Depth (ft)	Facies
36.18	12.18	12.72	1.752	2.441	4693.83	E
36.20	12.18	8.98	1.236	1.488	4693.83	E
36.23	12.18	12.52	1.719	2.387	4693.83	E
36.18	12.18	11.25	1.550	2.050	4693.83	E
36.23	12.18	10.76	1.478	1.924	4693.83	E
36.23	12.18	9.63	1.323	1.643	4693.83	E
36.13	12.18	11.82	1.635	2.199	4693.83	E
36.19	12.18	11.32	1.560	2.068	4693.83	E
36.16	12.18	8.34	1.152	1.339	4693.83	E
36.19	12.18	12.98	1.789	2.512	4693.83	E
36.21	12.18	5.22	0.719	0.687	4694.58	A
36.19	12.18	3.02	0.417	0.316	4694.58	A
36.22	12.18	4.39	0.604	0.537	4694.58	A
36.19	12.18	3.66	0.505	0.415	4694.58	A
36.15	12.18	6.54	0.905	0.947	4694.58	A
36.14	12.18	4.89	0.676	0.626	4694.58	A
36.19	12.18	14.32	1.975	2.889	4694.58	A
36.14	12.18	11.55	1.598	2.128	4694.58	A
36.18	12.18	20.48	2.827	4.807	4694.58	A
36.18	12.18	14.49	2.000	2.938	4694.58	A
36.17	12.18	7.41	1.024	1.132	4694.58	A
36.18	12.18	8.99	1.241	1.490	4694.58	A
36.17	12.18	16.58	2.291	3.559	4694.58	A
36.19	12.21	4.59	0.634	0.573	4695.42	B
36.20	12.21	8.34	1.152	1.339	4695.42	B
36.24	12.21	6.40	0.882	0.919	4695.42	B
36.24	12.21	7.57	1.043	1.167	4695.42	B
36.23	12.21	12.75	1.757	2.449	4695.42	B
36.26	12.21	9.04	1.244	1.502	4695.42	B
36.21	12.21	9.86	1.361	1.699	4695.42	B
36.19	12.21	4.67	0.645	0.587	4695.42	B
36.26	12.21	5.71	0.785	0.781	4695.42	B
36.20	12.21	4.34	0.599	0.529	4695.42	B
36.26	12.21	6.04	0.831	0.846	4695.42	B
36.23	12.21	6.86	0.945	1.014	4695.42	B
36.24	12.21	7.09	0.977	1.063	4695.42	B
36.25	12.21	2.75	0.379	0.276	4695.42	B
36.26	12.21	3.54	0.487	0.396	4695.42	B
36.22	12.21	4.78	0.659	0.607	4695.42	B
36.26	12.21	5.62	0.773	0.764	4695.42	B
36.26	12.21	5.22	0.718	0.687	4695.42	B
35.25	12.21	2.91	0.427	0.299	4695.42	B
36.25	12.21	4.05	0.558	0.479	4696.58	D
36.19	12.21	5.23	0.723	0.689	4696.58	D
36.24	12.21	4.73	0.652	0.598	4696.58	D
36.17	12.21	4.32	0.598	0.525	4696.58	D
36.21	12.21	6.87	0.948	1.016	4696.58	D
36.19	12.21	5.41	0.748	0.723	4696.58	E
36.18	12.21	8.68	1.200	1.417	4696.58	E
36.18	12.21	6.37	0.881	0.913	4696.58	E
36.20	12.21	6.42	0.887	0.923	4696.58	E
36.19	12.21	7.15	0.988	1.076	4696.58	E
36.25	12.21	6.47	0.891	0.933	4697.25	D
36.22	12.21	5.61	0.774	0.762	4697.25	D
36.18	12.21	3.29	0.455	0.356	4697.25	D
36.26	12.21	5.62	0.773	0.764	4697.25	D
36.31	12.27	5.13	0.699	0.671	4697.25	D
35.30	12.27	3.54	0.514	0.396	4697.25	D
36.29	12.27	3.71	0.507	0.423	4697.25	D
36.29	12.27	6.27	0.857	0.892	4697.25	D
36.27	12.27	6.05	0.828	0.848	4697.25	D

N2 Flow Press. (psia)	Atm Press. (psia)	Flow Rate (cc/min)	TEMCO Perm (mD)	Calc. Perm (mD)	Core Depth (ft)	Facies
36.27	12.27	2.68	0.367	0.266	4697.25	D
36.25	12.27	3.90	0.535	0.454	4697.25	D
36.30	12.27	3.65	0.500	0.413	4697.25	D
36.23	12.24	4.25	0.586	0.513	4697.25	D
36.27	12.24	2.82	0.388	0.286	4697.25	D
36.23	12.24	3.45	0.475	0.381	4697.25	D
36.22	12.24	3.27	0.451	0.353	4697.25	D
36.28	12.24	2.84	0.390	0.289	4697.25	D
36.25	12.24	2.37	0.326	0.224	4697.25	D
36.27	12.24	1.57	0.216	0.124	4697.25	D
36.25	12.24	2.74	0.377	0.275	4697.25	D
36.22	12.24	1.47	0.203	0.113	4697.25	D
36.26	12.24	2.39	0.329	0.226	4697.25	D
36.25	12.27	3.30	0.454	0.358	4697.92	D
36.20	12.24	2.47	0.341	0.237	4697.92	D
36.27	12.24	2.97	0.408	0.308	4697.92	D
36.28	12.27	2.39	0.328	0.226	4697.92	D
36.26	12.27	5.63	0.774	0.766	4697.92	D
36.26	12.27	2.34	0.322	0.220	4697.92	D
36.29	12.27	5.24	0.719	0.691	4697.92	D
36.27	12.27	3.21	0.441	0.344	4697.92	D
36.32	12.27	2.92	0.400	0.301	4697.92	D
36.22	12.24	1.65	0.228	0.134	4699.08	C
36.24	12.24	4.44	0.612	0.546	4699.08	C
36.27	12.24	3.72	0.512	0.425	4699.08	C
36.27	12.24	3.11	0.428	0.329	4699.08	C
36.27	12.24	4.27	0.587	0.517	4699.08	C
36.25	12.24	1.07	0.147	0.072	4699.08	D
36.24	12.24	2.48	0.342	0.238	4699.08	D
36.24	12.24	2.79	0.385	0.282	4699.08	D
36.19	12.24	1.92	0.265	0.166	4699.08	D
36.23	12.24	5.66	0.780	0.771	4701.00	D
36.24	12.24	2.29	0.315	0.213	4701.00	D
36.26	12.24	5.81	0.799	0.801	4701.00	D
36.25	12.24	3.72	0.512	0.425	4701.00	D
36.29	12.24	5.67	0.778	0.773	4701.00	D
36.27	12.24	6.69	0.920	0.979	4701.00	D
36.26	12.24	7.64	1.051	1.182	4701.00	D
36.25	12.24	9.28	1.277	1.559	4701.00	D
36.27	12.24	0.95	0.131	0.061	4701.00	D
36.25	12.24	2.09	0.288	0.187	4701.00	D
36.25	12.24	0.70	0.096	0.039	4701.00	D
36.20	12.24	3.19	0.440	0.341	4701.00	D
36.28	12.24	2.92	0.401	0.301	4701.00	D
36.29	12.24	7.67	1.053	1.189	4701.00	D
36.29	12.24	8.60	1.181	1.399	4701.00	D
36.29	12.25	1.77	0.241	0.148	4702.83	A
36.25	12.25	4.26	0.583	0.515	4702.83	A
36.29	12.25	6.13	0.837	0.864	4702.83	A
36.28	12.25	2.10	0.287	0.188	4702.83	A
36.28	12.25	2.00	0.274	0.176	4702.83	A
36.29	12.25	4.26	0.582	0.515	4704.92	C
36.23	12.25	4.96	0.681	0.639	4704.92	C
36.25	12.25	4.77	0.654	0.605	4704.92	C
36.20	12.25	2.73	0.376	0.273	4704.92	C
36.23	12.25	3.81	0.524	0.439	4704.92	C
36.26	12.25	3.42	0.469	0.377	4704.92	C
36.25	12.25	3.79	0.520	0.436	4704.92	C
36.28	12.25	2.24	0.308	0.206	4705.92	D
36.23	12.25	2.89	0.398	0.296	4705.92	D
36.27	12.25	3.07	0.422	0.323	4705.92	D

N2 Flow Press. (psia)	Atm Press. (psia)	Flow Rate (cc/min)	TEMCO Perm (mD)	Calc. Perm (mD)	Core Depth (ft)	Facies
36.29	12.25	1.56	0.214	0.123	4705.92	D
36.27	12.25	3.86	0.530	0.447	4705.92	D
36.29	12.25	6.60	0.905	0.960	4705.92	D
36.26	12.25	4.41	0.606	0.541	4705.92	D
36.29	12.25	4.20	0.576	0.505	4705.92	D
36.29	12.25	2.41	0.331	0.229	4705.92	D
36.28	12.25	4.07	0.559	0.483	4705.92	D
36.21	12.25	2.47	0.341	0.237	4705.92	D
36.24	12.25	2.98	0.411	0.310	4705.92	D
36.26	12.25	1.15	0.158	0.080	4705.92	D
36.26	12.25	1.39	0.191	0.105	4705.92	D
36.28	12.25	0.90	0.123	0.056	4705.92	D
36.26	12.25	1.23	0.169	0.088	4705.92	D
36.18	12.16	4.49	0.620	0.555	4712.08	C
36.14	12.16	4.79	0.663	0.608	4712.08	C
36.11	12.16	5.45	0.755	0.731	4712.08	C
36.16	12.16	4.62	0.638	0.578	4712.08	C
36.18	12.16	5.91	0.816	0.820	4712.08	C
36.20	12.20	1.10	0.152	0.075	4713.00	C
36.22	12.20	2.11	0.291	0.189	4713.00	C
36.19	12.20	1.66	0.229	0.135	4713.00	C
36.23	12.20	3.15	0.434	0.335	4713.00	C
36.24	12.20	0.91	0.125	0.057	4713.00	C
36.22	12.20	1.36	0.187	0.101	4713.00	C
36.21	12.20	2.33	0.321	0.218	4713.00	C
36.19	12.20	2.17	0.300	0.197	4713.00	C
36.25	12.20	2.61	0.359	0.256	4715.25	A
36.21	12.20	2.17	0.299	0.197	4715.25	A
36.23	12.20	2.74	0.378	0.275	4715.25	A
36.23	12.20	4.18	0.576	0.501	4715.25	A
36.18	12.20	3.28	0.453	0.355	4715.25	A
36.24	12.20	3.36	0.463	0.367	4715.25	A
36.20	12.20	4.25	0.587	0.513	4715.25	A
36.16	12.20	4.54	0.628	0.564	4715.25	A
36.17	12.20	1.81	0.250	0.152	4718.42	A
36.21	12.20	1.85	0.255	0.157	4718.42	A
36.19	12.20	1.26	0.174	0.091	4718.42	A
36.21	12.20	3.23	0.446	0.347	4718.42	A
36.18	12.20	1.47	0.203	0.113	4718.42	A
36.22	12.20	1.11	0.153	0.076	4718.42	A
36.19	12.20	1.71	0.236	0.141	4718.42	A
36.17	12.20	2.68	0.371	0.266	4718.42	A
36.22	12.20	0.77	0.106	0.045	4720.33	A
36.24	12.20	1.17	0.161	0.082	4720.33	A
36.22	12.20	3.20	0.441	0.343	4720.33	A
36.24	12.20	2.78	0.383	0.281	4720.33	A
36.19	12.20	1.10	0.152	0.075	4720.33	A
36.23	12.20	0.61	0.084	0.032	4720.33	A
36.24	12.20	0.54	0.074	0.027	4720.33	A
36.23	12.20	1.48	0.204	0.114	4720.33	A
36.25	12.20	0.93	0.128	0.059	4720.33	A
36.16	12.20	3.16	0.437	0.337	4720.33	A
36.18	12.20	2.36	0.326	0.222	4720.33	A

Champlin 369 Core Permeability Data

N2 Flow Press. (psia)	Atm Press. (psia)	Flow Rate (cc/min)	TEMCO Perm (mD)	Calc. Perm (mD)	Core Depth (ft)	Facies
36.13	12.15	2.95	0.408	0.305	4836.42	A
36.17	12.15	2.43	0.335	0.232	4836.42	A
36.19	12.15	3.29	0.454	0.356	4836.42	A
36.16	12.15	2.22	0.307	0.204	4836.42	A
36.19	12.15	1.86	0.257	0.158	4836.42	A
36.15	12.15	2.50	0.346	0.241	4836.42	A
36.17	12.15	5.13	0.708	0.671	4837.33	D
36.10	12.15	6.65	0.922	0.970	4837.33	D
36.14	12.15	10.03	1.389	1.741	4837.33	D
36.20	12.15	5.18	0.714	0.680	4837.33	D
36.20	12.15	6.92	0.954	1.027	4837.33	D
36.10	12.15	8.78	1.218	1.441	4837.33	D
36.15	12.15	8.07	1.116	1.278	4837.33	D
36.15	12.15	3.71	0.513	0.423	4837.33	D
36.24	12.23	0.61	0.083	0.032	4838.75	D
36.25	12.23	0.51	0.070	0.025	4838.75	D
36.24	12.23	0.53	0.073	0.027	4838.75	D
36.25	12.23	0.54	0.074	0.027	4838.75	D
36.23	12.23	0.74	0.101	0.043	4838.75	D
36.26	12.23	0.52	0.071	0.026	4838.75	D
36.23	12.23	2.43	0.334	0.232	4841.17	A
36.22	12.23	1.30	0.179	0.095	4841.17	A
36.20	12.23	3.16	0.435	0.337	4841.17	A
36.26	12.23	28.42	3.893	7.661	4841.17	C
36.20	12.23	11.75	1.616	2.181	4841.17	C
36.19	12.23	23.23	3.198	5.751	4841.17	C
36.27	12.23	30.97	4.245	8.658	4841.83	A
36.20	12.23	22.94	3.159	5.649	4841.83	A
36.20	12.23	41.66	5.737	13.201	4841.83	A
36.27	12.23	28.95	3.972	7.866	4841.83	A
36.24	12.23	11.99	1.647	2.244	4841.83	A
36.20	12.23	11.83	1.630	2.202	4841.83	A
36.25	12.23	8.13	1.117	1.291	4842.83	C
36.26	12.23	6.00	0.824	0.838	4842.83	C
36.21	12.23	9.45	1.301	1.600	4842.83	C
36.24	12.23	1.84	0.253	0.156	4842.83	D
36.24	12.23	1.93	0.265	0.167	4842.83	D
36.25	12.23	1.34	0.184	0.099	4842.83	D
36.18	12.23	5.76	0.795	0.791	4844.25	C
36.23	12.23	0.91	0.125	0.057	4844.25	C
36.19	12.23	13.47	1.858	2.648	4844.25	C
36.23	12.23	3.48	0.479	0.386	4846.33	C
36.23	12.23	2.21	0.304	0.202	4846.33	C
36.19	12.23	9.09	1.254	1.514	4846.33	C
36.20	12.23	3.65	0.503	0.413	4846.33	C
36.25	12.23	9.65	1.326	1.648	4847.50	D
36.25	12.23	26.30	3.615	6.861	4847.50	D
36.21	12.23	50.48	6.957	17.349	4847.50	D
36.21	12.23	1.51	0.208	0.118	4847.50	D
36.20	12.23	2.37	0.327	0.224	4847.50	D
36.24	12.23	3.19	0.439	0.341	4847.50	D
36.22	12.23	56.78	7.823	20.509	4848.17	A
36.19	12.23	37.67	5.199	11.440	4848.17	A
36.25	12.23	7.90	1.086	1.240	4848.17	A
36.24	12.23	3.34	0.460	0.364	4848.17	A
36.19	12.23	3.85	0.531	0.446	4848.17	A
36.26	12.23	34.73	4.774	10.191	4849.25	B
36.22	12.23	18.43	2.540	4.137	4849.25	B

N2 Flow Press. (psia)	Atm Press. (psia)	Flow Rate (cc/min)	TEMCO Perm (mD)	Calc. Perm (mD)	Core Depth (ft)	Facies
36.26	12.23	34.02	4.677	9.896	4849.25	B
36.22	12.23	3.78	0.521	0.434	4849.25	B
36.26	12.23	6.78	0.932	0.997	4849.25	B
36.25	12.23	6.31	0.867	0.900	4849.25	B
36.23	12.23	11.12	1.532	2.016	4854.25	C
36.25	12.23	6.24	0.859	0.886	4854.25	C
36.18	12.23	8.07	1.115	1.278	4854.25	C
36.26	12.23	3.24	0.445	0.349	4854.25	C
36.25	12.23	3.76	0.517	0.431	4854.25	C
36.27	12.23	15.91	2.186	3.356	4855.83	C
36.23	12.23	41.54	5.723	13.147	4855.83	C
36.23	12.23	43.59	6.005	14.080	4855.83	C
36.24	12.23	30.13	4.148	8.326	4855.83	C
36.19	12.23	28.87	3.987	7.835	4855.83	C
36.21	12.23	3.60	0.497	0.405	4856.67	A
36.27	12.23	0.83	0.114	0.050	4856.67	A
36.22	12.23	2.33	0.321	0.218	4856.67	A
36.25	12.23	2.76	0.380	0.278	4856.67	C
36.26	12.23	1.32	0.182	0.097	4856.67	C
36.23	12.23	2.33	0.321	0.218	4856.67	C
36.23	12.25	14.04	1.920	2.809	4857.75	C
36.27	12.25	4.01	0.548	0.472	4857.75	C
36.29	12.25	9.44	1.289	1.597	4857.75	C
36.24	12.25	11.04	1.513	1.996	4857.75	C
36.23	12.25	13.94	1.913	2.781	4857.75	C
36.29	12.25	7.22	0.988	1.091	4857.75	D
36.28	12.25	9.50	1.300	1.612	4857.75	D
36.27	12.25	4.84	0.663	0.617	4857.75	D
36.26	12.25	1.27	0.174	0.092	4859.33	B
36.26	12.25	2.63	0.361	0.259	4859.33	B
36.24	12.25	3.73	0.513	0.426	4859.33	B
36.25	12.25	4.90	0.673	0.628	4859.33	B
36.27	12.25	2.19	0.301	0.200	4861.00	A
36.24	12.25	3.04	0.418	0.319	4861.00	A
36.25	12.25	1.51	0.208	0.118	4861.00	A
36.25	12.25	79.98	10.998	33.390	4862.08	E
36.20	12.25	14.96	2.064	3.075	4862.08	E
36.23	12.25	40.11	5.524	12.508	4862.08	E
36.24	12.25	24.83	3.418	6.322	4862.08	E
36.30	12.25	6.98	0.957	1.039	4863.33	B
36.25	12.25	9.42	1.296	1.592	4863.33	B
36.26	12.25	7.90	1.086	1.240	4863.33	B
36.28	12.25	17.40	2.389	3.812	4863.33	E
36.23	12.25	18.56	2.556	4.179	4863.33	E
36.26	12.25	23.63	3.249	5.892	4863.33	E
36.24	12.25	52.68	7.253	18.434	4863.33	E
36.23	12.25	8.13	1.120	1.291	4864.67	C
36.25	12.25	12.28	1.690	2.322	4864.67	C
36.27	12.25	11.90	1.635	2.220	4864.67	C
36.23	12.25	9.01	1.241	1.495	4864.67	D
36.29	12.25	12.07	1.658	2.266	4864.67	D
36.28	12.25	11.87	1.630	2.212	4864.67	D
36.27	12.25	7.70	1.058	1.195	4864.67	D
36.23	12.25	44.80	6.172	14.639	4865.75	A
36.29	12.25	25.08	3.442	6.413	4865.75	A
36.27	12.25	16.85	2.316	3.642	4865.75	A
36.30	12.25	7.42	1.018	1.134	4865.75	A
36.27	12.25	7.66	1.053	1.186	4865.75	A
36.21	12.25	4.02	0.555	0.474	4865.75	A
36.29	12.25	14.37	1.972	2.904	4866.17	C
36.27	12.25	46.02	6.329	15.210	4866.17	C

N2 Flow Press. (psia)	Atm Press. (psia)	Flow Rate (cc/min)	TEMCO Perm (mD)	Calc. Perm (mD)	Core Depth (ft)	Facies
36.21	12.25	16.28	2.246	3.468	4866.17	C
36.23	12.25	14.54	2.003	2.953	4866.17	C
36.28	12.25	10.73	1.474	1.916	4866.17	C
36.21	12.25	61.68	8.509	23.072	4868.08	D
36.27	12.25	27.87	3.831	7.451	4868.08	D
36.29	12.25	12.63	1.734	2.417	4868.08	D
36.24	12.25	9.09	1.252	1.514	4868.08	D
36.26	12.25	11.67	1.605	2.160	4869.67	B
36.24	12.25	14.02	1.931	2.804	4869.67	B
36.27	12.25	12.06	1.658	2.263	4869.67	B
36.26	12.25	13.21	1.817	2.576	4869.67	B
36.27	12.25	8.63	1.186	1.406	4869.67	B
36.28	12.25	8.42	1.157	1.357	4869.67	B
36.25	12.25	48.33	6.652	16.307	4871.42	E
36.24	12.25	32.82	4.520	9.403	4871.42	E
36.27	12.25	48.59	6.679	16.432	4871.42	E
36.25	12.25	46.79	6.440	15.573	4871.42	E
36.30	12.25	28.09	3.854	7.535	4871.42	E
36.27	12.25	28.45	3.910	7.673	4873.92	A
36.27	12.25	27.60	3.791	7.349	4873.92	A
36.23	12.25	21.96	3.026	5.309	4873.92	A
36.27	12.25	4.59	0.631	0.573	4873.92	A
36.27	12.25	11.03	1.516	1.993	4873.92	A
36.23	12.25	68.88	9.491	26.996	4875.67	E
36.21	12.25	29.25	4.035	7.982	4875.67	E
36.29	12.25	16.52	2.268	3.541	4875.67	E
36.27	12.25	11.65	1.601	2.154	4875.67	E
36.28	12.25	20.70	2.843	4.881	4875.67	E
36.23	12.26	7.88	1.078	1.235	4876.17	B
36.30	12.26	12.72	1.735	2.441	4876.17	B
36.24	12.26	19.57	2.681	4.506	4876.17	E
36.26	12.26	36.67	5.021	11.010	4876.17	E
36.30	12.26	42.67	5.829	13.659	4876.17	E
36.28	12.26	50.28	6.881	17.251	4876.17	E
36.28	12.26	1.50	0.205	0.117	4877.92	C
36.24	12.26	1.83	0.251	0.155	4877.92	C
36.30	12.26	2.93	0.401	0.302	4877.92	C
36.29	12.26	4.45	0.609	0.548	4877.92	C
36.26	12.26	11.36	1.558	2.078	4877.92	C
36.26	12.26	11.63	1.596	2.149	4877.92	C
36.24	12.26	1.92	0.264	0.166	4878.83	E
36.25	12.26	3.16	0.434	0.337	4878.83	E
36.27	12.26	3.35	0.460	0.366	4878.83	E
36.27	12.26	5.96	0.818	0.830	4878.83	E
36.21	12.26	51.88	7.146	18.037	4880.17	A
36.28	12.26	52.08	7.143	18.136	4880.17	A
36.23	12.26	64.68	8.899	24.684	4880.17	A
36.29	12.26	1.08	0.148	0.073	4880.92	A
36.20	12.26	1.02	0.141	0.067	4880.92	A
36.25	12.26	1.47	0.202	0.113	4880.92	A
36.25	12.26	3.12	0.429	0.331	4880.92	A
36.27	12.26	2.62	0.360	0.258	4880.92	A
36.26	12.26	3.36	0.462	0.367	4880.92	A
36.24	12.26	5.86	0.806	0.810	4882.17	D
36.24	12.26	6.70	0.922	0.981	4882.17	D
36.30	12.26	6.49	0.890	0.937	4882.17	D
36.25	12.26	12.22	1.681	2.306	4882.17	D

Sidwell Core Permeability Data

N2 Flow Press. (psia)	Atm Press. (psia)	Flow Rate (cc/min)	TEMCO Perm (mD)	Calc. Perm (mD)	Core Depth (ft)	Facies
36.15	12.20	50.88	6.98	20.16	4840.50	D
36.22	12.20	27.94	3.82	8.45	4840.50	D
36.22	12.20	43.06	5.89	15.82	4840.50	D
36.23	12.20	28.20	3.86	8.56	4840.50	D
36.21	12.20	42.02	5.76	15.27	4840.50	D
36.25	12.20	21.76	2.98	5.88	4840.50	D
36.21	12.20	2.86	0.39	0.31	4841.00	B
36.21	12.20	9.04	1.24	1.64	4841.00	B
36.24	12.20	5.42	0.74	0.78	4841.00	B
36.18	12.20	1.37	0.19	0.11	4841.50	D
36.22	12.20	2.55	0.35	0.26	4841.50	D
36.24	12.20	3.94	0.54	0.49	4841.50	D
36.16	12.20	4.60	0.63	0.62	4841.67	C
36.17	12.20	5.87	0.81	0.88	4841.67	C
36.18	12.20	7.54	1.04	1.26	4841.67	C
36.39	12.34	0.64	0.09	0.04	4842.83	B
36.31	12.34	0.93	0.13	0.06	4842.83	B
36.36	12.34	1.44	0.20	0.11	4842.83	B
36.35	12.34	0.64	0.09	0.04	4842.83	B
36.32	12.34	0.61	0.08	0.03	4842.83	B
36.34	12.34	1.43	0.19	0.11	4842.83	B
36.32	12.34	15.87	2.17	3.72	4844.00	D
36.32	12.34	72.68	9.94	33.82	4844.00	D
36.33	12.34	27.67	3.78	8.33	4844.00	D
36.34	12.34	2.19	0.30	0.21	4844.50	A
36.30	12.34	4.85	0.66	0.67	4844.50	A
36.37	12.34	3.18	0.43	0.36	4844.50	A
36.31	12.34	25.48	3.49	7.39	4844.50	C
36.32	12.34	14.93	2.04	3.40	4844.50	C
36.32	12.34	3.82	0.52	0.47	4844.50	C
36.35	12.34	1.08	0.15	0.08	4844.83	B
36.34	12.34	0.95	0.13	0.06	4844.83	B
36.36	12.34	1.11	0.15	0.08	4844.83	B
36.36	12.34	25.03	3.42	7.20	4845.00	D
36.34	12.34	38.80	5.31	13.60	4845.00	D
36.34	12.34	17.04	2.33	4.12	4845.00	D
36.32	12.34	0.71	0.10	0.04	4846.42	B
36.37	12.34	0.90	0.12	0.06	4846.42	B
36.38	12.34	1.40	0.19	0.11	4846.42	B
36.33	12.34	4.24	0.58	0.55	4846.42	B
36.37	12.34	5.16	0.71	0.73	4846.42	B
36.34	12.34	4.83	0.66	0.66	4846.42	B
36.38	12.34	1.81	0.25	0.16	4846.42	C
36.31	12.34	0.96	0.13	0.06	4846.42	C
36.33	12.34	3.39	0.46	0.40	4846.42	C
36.38	12.34	0.93	0.13	0.06	4848.08	D
36.32	12.34	0.75	0.10	0.04	4848.08	D
36.36	12.34	1.46	0.20	0.12	4848.08	D
36.38	12.34	0.83	0.11	0.05	4848.42	B
36.35	12.34	0.59	0.08	0.03	4848.42	B
36.30	12.31	2.63	0.36	0.27	4848.58	A
36.31	12.31	1.75	0.24	0.15	4848.58	A
36.31	12.31	1.67	0.23	0.14	4848.58	A
36.35	12.31	4.27	0.58	0.55	4848.58	A
36.34	12.31	1.16	0.16	0.08	4848.58	A
36.27	12.31	2.28	0.31	0.22	4848.58	A
36.36	12.31	14.49	1.97	3.26	4849.00	D
36.34	12.31	13.08	1.78	2.81	4849.00	D

N2 Flow Press. (psia)	Atm Press. (psia)	Flow Rate (cc/min)	TEMCO Perm (mD)	Calc. Perm (mD)	Core Depth (ft)	Facies
36.30	12.31	19.91	2.72	5.17	4849.00	D
36.31	12.31	2.87	0.39	0.31	4849.67	B
36.34	12.31	2.53	0.35	0.26	4849.67	B
36.29	12.31	2.38	0.33	0.24	4849.67	B
36.34	12.31	74.88	10.22	35.31	4849.83	D
36.33	12.31	49.09	6.71	19.13	4849.83	D
36.32	12.31	54.38	7.43	22.20	4849.83	D
36.31	12.31	5.63	0.77	0.83	4850.50	B
36.35	12.31	3.01	0.41	0.33	4850.50	B
36.34	12.31	2.15	0.29	0.20	4850.50	B
36.33	12.31	9.68	1.32	1.81	4851.00	B
36.34	12.31	10.87	1.49	2.15	4851.00	B
36.28	12.31	9.74	1.34	1.83	4851.00	B
36.31	12.31	4.74	0.65	0.64	4851.83	B
36.33	12.31	10.32	1.41	1.99	4851.83	B
36.34	12.31	18.69	2.56	4.71	4851.83	B
36.31	12.31	9.19	1.26	1.68	4851.83	B
36.32	12.31	13.97	1.91	3.09	4851.83	B
36.34	12.31	9.79	1.34	1.84	4851.83	B
36.28	12.31	11.66	1.60	2.38	4851.83	B
36.36	12.31	9.51	1.30	1.77	4851.83	B
36.30	12.31	9.06	1.24	1.65	4851.83	B
36.30	12.31	1.91	0.26	0.17	4853.00	A
36.32	12.31	5.71	0.78	0.84	4853.00	A
36.34	12.31	6.18	0.85	0.95	4853.00	A
36.31	12.31	2.01	0.28	0.19	4854.00	B
36.29	12.31	3.62	0.50	0.44	4854.00	B
36.31	12.31	8.71	1.19	1.56	4854.00	B
36.30	12.31	1.24	0.17	0.09	4854.08	A
36.32	12.31	3.69	0.51	0.45	4854.08	A
36.31	12.31	3.95	0.54	0.49	4854.08	A
36.31	12.28	0.66	0.09	0.04	4855.00	B
36.26	12.28	2.57	0.35	0.26	4855.00	B
36.26	12.28	4.49	0.61	0.59	4855.00	B
36.30	12.28	1.02	0.14	0.07	4855.08	C
36.28	12.28	3.94	0.54	0.49	4855.08	C
36.30	12.28	0.63	0.09	0.03	4855.75	B
36.31	12.28	1.26	0.17	0.09	4855.75	B
36.31	12.28	1.16	0.16	0.08	4855.75	B
36.32	12.28	26.63	3.63	7.88	4856.50	D
36.30	12.28	47.16	6.43	18.05	4856.50	D
36.31	12.28	51.33	7.00	20.41	4856.50	D
36.29	12.28	1.42	0.19	0.11	4857.08	B
36.28	12.28	1.95	0.27	0.18	4857.08	B
36.24	12.28	2.82	0.39	0.30	4857.08	B
36.28	12.28	0.72	0.10	0.04	4858.42	A
36.29	12.28	2.10	0.29	0.20	4858.42	A
36.23	12.28	1.42	0.20	0.11	4858.42	A
36.28	12.28	20.00	2.74	5.20	4858.83	D
36.29	12.28	53.48	7.32	21.67	4858.83	D
36.27	12.28	18.77	2.57	4.74	4858.83	D
36.28	12.28	4.41	0.60	0.58	4860.00	A
36.26	12.28	16.23	2.23	3.84	4860.00	A
36.33	12.28	3.41	0.47	0.40	4860.00	A
36.33	12.28	0.76	0.10	0.05	4861.58	B
36.33	12.28	1.98	0.27	0.18	4861.58	B
36.28	12.28	2.80	0.38	0.30	4861.83	B
36.25	12.28	6.79	0.93	1.08	4861.83	B
36.27	12.29	9.56	1.30	1.78	4862.75	B
36.29	12.29	10.87	1.48	2.15	4862.75	B
36.28	12.29	9.20	1.25	1.68	4862.75	B

N2 Flow Press. (psia)	**Atm Press. (psia)**	**Flow Rate (cc/min)**	**TEMCO Perm (mD)**	**Calc. Perm (mD)**	**Core Depth (ft)**	**Facies**
36.29	12.29	1.01	0.14	0.07	4864.33	A
36.26	12.29	2.67	0.37	0.28	4864.33	A
36.33	12.29	2.33	0.32	0.23	4864.33	A
36.25	12.29	2.33	0.32	0.23	4865.50	A
36.33	12.29	4.30	0.59	0.56	4865.50	A
36.29	12.29	1.41	0.19	0.11	4865.50	A
36.29	12.29	1.02	0.14	0.07	4866.00	B
36.28	12.29	0.65	0.09	0.04	4866.00	B
36.34	12.29	0.82	0.11	0.05	4866.00	B
36.30	12.29	2.78	0.38	0.30	4866.67	C
36.27	12.29	4.23	0.58	0.55	4866.67	C
36.29	12.29	3.79	0.52	0.47	4866.67	C
36.32	12.29	4.17	0.57	0.53	4866.67	C
36.33	12.29	4.58	0.63	0.61	4867.58	A
36.29	12.29	5.18	0.71	0.73	4867.58	A
36.34	12.29	5.24	0.72	0.74	4867.58	A
36.32	12.29	0.75	0.10	0.04	4868.08	A
36.28	12.29	2.13	0.29	0.20	4868.08	A
36.26	12.29	3.73	0.51	0.45	4868.08	A
36.24	12.27	53.68	7.32	21.78	4869.08	D
36.28	12.27	37.12	5.05	12.75	4869.08	D
36.27	12.27	53.98	7.35	21.96	4869.08	D
36.26	12.27	0.58	0.08	0.03	4870.08	A
36.23	12.27	1.10	0.15	0.08	4870.08	A
36.27	12.27	1.68	0.23	0.14	4870.08	A
36.25	12.27	4.92	0.67	0.68	4870.83	B
36.27	12.27	7.21	0.99	1.18	4870.83	B
36.28	12.27	7.35	1.00	1.22	4870.83	B
36.28	12.27	51.67	7.06	20.61	4870.92	C
36.32	12.27	33.54	4.58	11.01	4870.92	C
36.31	12.27	21.10	2.88	5.62	4870.92	C
36.27	12.27	13.94	1.91	3.08	4870.92	C
36.30	12.27	0.65	0.09	0.04	4872.08	A
36.27	12.27	1.70	0.23	0.15	4872.08	A
36.26	12.27	2.56	0.35	0.26	4872.08	A
36.26	12.27	6.29	0.86	0.97	4873.00	A
36.26	12.27	1.51	0.21	0.12	4873.08	A
36.28	12.27	3.76	0.51	0.46	4873.08	A
36.25	12.27	3.15	0.43	0.36	4873.08	A
36.27	12.27	4.15	0.57	0.53	4873.83	A
36.31	12.27	5.37	0.73	0.77	4873.83	A
36.26	12.27	13.84	1.90	3.05	4874.08	D
36.27	12.27	24.82	3.40	7.11	4874.08	D
36.24	12.27	45.41	6.24	17.09	4874.08	D
36.30	12.27	1.19	0.16	0.09	4875.42	A
36.31	12.27	4.24	0.58	0.55	4875.42	A
36.26	12.27	1.79	0.25	0.16	4875.42	A
36.29	12.27	9.05	1.24	1.65	4876.58	A
36.28	12.27	8.47	1.16	1.49	4876.58	A
36.26	12.27	7.57	1.04	1.27	4876.58	A
36.27	12.27	1.41	0.19	0.11	4878.00	A
36.26	12.27	0.67	0.09	0.04	4878.00	A
36.28	12.27	3.59	0.49	0.43	4878.00	A
36.28	12.27	7.09	0.97	1.15	4879.17	B
36.31	12.27	9.74	1.33	1.83	4879.17	B
36.30	12.27	11.89	1.63	2.44	4879.17	B
36.26	12.27	3.48	0.48	0.41	4879.42	A
36.26	12.27	4.54	0.62	0.60	4879.42	A
36.31	12.27	7.74	1.06	1.31	4879.42	A
36.28	12.27	17.66	2.42	4.34	4880.08	D
36.27	12.27	41.17	5.65	14.82	4880.92	D

N2 Flow Press. (psia)	Atm Press. (psia)	Flow Rate (cc/min)	TEMCO Perm (mD)	Calc. Perm (mD)	Core Depth (ft)	Facies
36.28	12.27	12.18	1.67	2.53	4880.92	D
36.25	12.27	3.76	0.52	0.46	4882.33	A
36.26	12.27	1.06	0.15	0.07	4882.33	A
36.29	12.27	0.99	0.14	0.07	4882.33	A
36.27	12.27	1.40	0.19	0.11	4882.75	B
36.25	12.27	2.16	0.30	0.21	4882.75	B
36.27	12.27	3.62	0.50	0.44	4882.75	B
36.24	12.20	0.67	0.09	0.04	4883.92	A
36.15	12.20	1.95	0.27	0.18	4883.92	A
36.24	12.20	3.65	0.50	0.44	4883.92	A
36.23	12.20	2.92	0.40	0.32	4884.50	A
36.23	12.20	4.53	0.62	0.60	4884.50	A
36.19	12.20	2.60	0.36	0.27	4884.50	A
36.18	12.20	4.25	0.58	0.55	4885.08	A
36.23	12.20	6.25	0.86	0.96	4885.08	A
36.19	12.20	5.38	0.74	0.77	4885.08	A
36.21	12.20	18.14	2.49	4.51	4885.67	D
36.22	12.20	16.27	2.23	3.85	4885.67	D
36.24	12.20	17.68	2.42	4.35	4885.67	D
36.20	12.20	9.73	1.34	1.83	4886.08	B
36.19	12.20	8.30	1.14	1.45	4886.08	B
36.19	12.20	4.32	0.59	0.56	4886.08	B
36.22	12.20	6.30	0.87	0.97	4887.25	C
36.19	12.20	9.42	1.30	1.74	4887.25	C
36.17	12.20	11.20	1.54	2.24	4887.25	C
36.23	12.20	2.56	0.35	0.26	4887.67	C
36.20	12.20	5.73	0.79	0.85	4887.67	C
36.26	12.28	4.67	0.64	0.63	4887.67	C
36.30	12.28	5.54	0.75	0.81	4887.67	C
36.30	12.28	9.69	1.32	1.82	4887.67	C
36.28	12.28	6.43	0.88	1.00	4888.17	B
36.24	12.28	7.89	1.08	1.35	4888.17	B
36.30	12.28	8.06	1.10	1.39	4888.17	B
36.26	12.28	8.20	1.12	1.43	4888.25	A
36.32	12.28	5.20	0.71	0.74	4888.25	A
36.28	12.28	3.18	0.43	0.36	4888.25	A
36.30	12.28	3.94	0.54	0.49	4888.50	C
36.29	12.28	5.56	0.76	0.81	4888.50	C
36.28	12.28	10.58	1.45	2.06	4889.42	A
36.28	12.28	23.22	3.18	6.46	4889.42	A
36.28	12.28	9.18	1.26	1.68	4889.42	A
36.27	12.28	3.85	0.53	0.48	4890.00	A
36.28	12.28	2.72	0.37	0.29	4890.00	A
36.27	12.28	4.65	0.64	0.63	4890.00	A
36.28	12.28	2.23	0.31	0.22	4890.58	A
36.26	12.28	1.16	0.16	0.08	4890.58	A
36.30	12.28	6.61	0.91	1.04	4890.58	A
36.27	12.28	1.76	0.24	0.15	4891.08	A
36.29	12.28	2.31	0.32	0.23	4891.08	A
36.30	12.28	3.95	0.54	0.49	4891.08	A

Moser #1 Core Permeability Data

N2 Flow Press. (psia)	Atm Press. (psia)	Flow Rate (cc/min)	TEMCO Perm (mD)	Calc. Perm (mD)	Core Depth (ft)	Facies
36.23	12.20	2.98	0.410	0.310	4441.25	B
36.24	12.20	3.31	0.455	0.360	4441.25	B
36.24	12.20	2.75	0.378	0.276	4441.25	B
36.24	12.20	3.06	0.421	0.322	4441.25	B
36.23	12.20	2.13	0.293	0.192	4441.25	C
36.22	12.20	3.52	0.485	0.392	4441.25	C
36.24	12.20	2.66	0.366	0.263	4441.25	C
36.26	12.24	2.62	0.359	0.258	4442.33	D
36.25	12.24	3.08	0.423	0.325	4442.33	D
36.23	12.24	2.40	0.330	0.228	4442.33	D
36.26	12.24	2.83	0.388	0.288	4442.33	D
36.23	12.24	3.85	0.529	0.446	4442.33	D
36.23	12.24	3.17	0.434	0.338	4446.25	C
36.27	12.24	2.35	0.321	0.221	4446.25	C
36.20	12.24	1.83	0.251	0.155	4446.25	C
36.22	12.24	3.78	0.519	0.434	4446.25	C
36.24	12.24	1.98	0.272	0.173	4446.25	C
36.26	12.24	4.64	0.636	0.581	4446.25	C
36.27	12.24	1.57	0.215	0.124	4447.00	A
36.26	12.24	1.32	0.181	0.097	4447.00	A
36.23	12.24	2.64	0.363	0.261	4447.00	A
36.29	12.24	2.04	0.280	0.181	4447.00	A
36.25	12.24	2.30	0.316	0.214	4447.00	A
36.20	12.24	0.88	0.121	0.055	4447.00	A
36.21	12.24	3.11	0.429	0.329	4447.00	A
36.23	12.24	2.48	0.342	0.238	4448.00	A
36.19	12.24	2.30	0.318	0.214	4448.00	A
36.22	12.18	1.04	0.143	0.069	4448.00	A
36.18	12.18	1.53	0.211	0.120	4448.00	A
36.23	12.18	0.52	0.071	0.026	4448.00	A
36.19	12.18	0.56	0.077	0.029	4448.00	A
36.22	12.18	1.51	0.208	0.118	4448.00	A
36.23	12.18	2.49	0.342	0.240	4448.00	A
36.21	12.18	3.31	0.455	0.360	4449.08	D
36.18	12.18	1.18	0.163	0.083	4449.08	D
36.15	12.18	2.45	0.339	0.234	4449.08	D
36.21	12.18	3.71	0.511	0.423	4449.08	D
36.19	12.18	3.08	0.425	0.325	4449.08	D
36.17	12.18	5.33	0.736	0.708	4450.67	D
36.16	12.18	5.21	0.720	0.686	4450.67	D
36.20	12.18	4.50	0.620	0.557	4450.67	D
36.19	12.18	6.06	0.836	0.850	4450.67	D
36.17	12.18	6.85	0.946	1.012	4450.67	D
36.21	12.18	4.73	0.652	0.598	4450.67	D
36.19	12.18	4.73	0.653	0.598	4450.67	D
36.17	12.18	5.11	0.706	0.667	4450.67	D
36.22	12.18	3.66	0.504	0.415	4451.67	D
36.14	12.18	5.23	0.724	0.689	4451.67	D
36.18	12.18	3.68	0.508	0.418	4451.67	D
36.19	12.18	2.74	0.378	0.275	4451.67	D
36.17	12.18	2.91	0.402	0.299	4453.67	B
36.16	12.18	3.79	0.524	0.436	4453.67	B
36.20	12.18	3.06	0.422	0.322	4453.67	B
36.22	12.18	1.99	0.274	0.174	4453.67	B
36.20	12.18	1.62	0.223	0.130	4453.67	D
36.21	12.18	0.61	0.084	0.032	4453.67	D
36.13	12.18	2.26	0.313	0.209	4453.67	D
36.22	12.18	2.23	0.307	0.205	4453.67	D

N2 Flow Press. (psia)	Atm Press. (psia)	Flow Rate (cc/min)	TEMCO Perm (mD)	Calc. Perm (mD)	Core Depth (ft)	Facies
36.19	12.16	3.67	0.503	0.416	4454.67	A
36.17	12.16	2.43	0.334	0.232	4454.67	A
36.14	12.16	5.14	0.706	0.673	4454.67	C
36.19	12.16	4.47	0.613	0.551	4454.67	C
36.21	12.16	1.63	0.223	0.131	4454.67	D
36.20	12.16	2.44	0.334	0.233	4454.67	D
36.16	12.16	0.73	0.100	0.042	4457.00	A
36.15	12.16	1.01	0.139	0.066	4457.00	A
36.16	12.16	0.83	0.114	0.050	4457.00	A
36.19	12.16	1.62	0.223	0.130	4457.00	A
36.14	12.16	0.90	0.124	0.056	4457.00	A
36.15	12.16	1.27	0.175	0.092	4457.00	A
36.17	12.16	1.83	0.252	0.155	4457.00	A
36.16	12.16	1.67	0.230	0.136	4457.00	A
36.18	12.16	1.14	0.157	0.079	4460.00	A
36.18	12.16	5.80	0.800	0.799	4460.00	A
36.15	12.16	5.22	0.721	0.687	4460.00	A
36.19	12.16	4.14	0.571	0.494	4460.00	A
36.16	12.16	2.86	0.395	0.292	4460.00	A
36.16	12.16	4.60	0.635	0.574	4460.00	A
36.20	12.16	2.87	0.395	0.294	4460.00	A
36.17	12.16	2.48	0.342	0.238	4460.00	A
36.16	12.16	1.24	0.171	0.089	4462.50	A
36.18	12.16	2.56	0.353	0.249	4462.50	A
36.19	12.16	1.04	0.143	0.069	4462.50	A
36.20	12.16	0.55	0.076	0.028	4462.50	A
36.12	12.16	1.90	0.263	0.163	4462.50	A
36.16	12.16	1.02	0.141	0.067	4462.50	A
36.15	12.16	3.13	0.433	0.332	4462.50	A
36.14	12.16	4.90	0.678	0.628	4462.50	A
36.16	12.16	0.93	0.129	0.059	4462.50	A
36.15	12.16	3.18	0.439	0.340	4465.00	A
36.20	12.16	5.75	0.791	0.789	4465.00	A
36.19	12.16	2.80	0.386	0.283	4465.00	A
36.18	12.16	5.03	0.693	0.652	4465.00	A
36.10	12.16	6.75	0.935	0.991	4465.00	A
36.17	12.16	2.81	0.387	0.285	4465.00	A
36.16	12.16	2.38	0.328	0.225	4465.00	A
36.18	12.16	5.09	0.702	0.663	4465.00	A
36.21	12.16	6.69	0.921	0.979	4465.00	A
36.13	12.16	7.01	0.970	1.046	4465.00	A
36.16	12.16	3.36	0.464	0.367	4466.83	A
36.16	12.16	2.62	0.362	0.258	4466.83	A
36.17	12.16	3.16	0.436	0.337	4466.83	A
36.20	12.16	2.78	0.383	0.281	4466.83	A
36.18	12.16	1.38	0.190	0.104	4468.00	A
36.18	12.16	2.74	0.378	0.275	4468.00	A
36.15	12.16	2.76	0.382	0.278	4468.00	A
36.16	12.16	5.56	0.768	0.752	4468.00	A
36.20	12.20	1.31	0.179	0.096	4468.75	A
36.19	12.20	2.65	0.364	0.262	4468.75	A
36.22	12.20	3.50	0.480	0.389	4468.75	A
36.15	12.20	5.43	0.748	0.727	4468.75	A
36.24	12.20	0.74	0.101	0.043	4469.58	A
36.16	12.20	1.08	0.149	0.073	4469.58	A
36.21	12.20	1.50	0.206	0.117	4469.58	A
36.23	12.20	2.39	0.328	0.226	4469.58	A
36.21	12.20	1.21	0.166	0.086	4471.25	A
36.22	12.20	1.48	0.203	0.114	4471.25	A
36.22	12.20	1.18	0.162	0.083	4471.25	A
36.23	12.20	1.91	0.262	0.164	4471.25	A

N2 Flow Press. (psia)	Atm Press. (psia)	Flow Rate (cc/min)	TEMCO Perm (mD)	Calc. Perm (mD)	Core Depth (ft)	Facies
36.23	12.20	1.70	0.234	0.139	4472.08	A
36.16	12.20	1.84	0.254	0.156	4472.08	A
36.19	12.20	1.70	0.234	0.139	4472.08	A
36.20	12.20	2.02	0.278	0.178	4472.08	A
36.20	12.20	4.00	0.551	0.471	4472.92	A
36.15	12.20	10.19	1.409	1.781	4472.92	A
36.24	12.20	2.05	0.282	0.182	4472.92	A
36.19	12.20	2.74	0.378	0.275	4472.92	A
36.23	12.20	2.69	0.370	0.268	4472.92	A
36.16	12.20	4.28	0.591	0.518	4472.92	A
36.18	12.20	2.34	0.323	0.220	4472.92	A
36.18	12.20	4.76	0.657	0.603	4474.67	A
36.15	12.20	7.10	0.982	1.065	4474.67	A
36.24	12.20	12.39	1.703	2.352	4474.67	A
36.16	12.20	8.64	1.194	1.408	4474.67	A
36.24	12.20	7.78	1.070	1.213	4474.67	A
36.22	12.20	4.89	0.673	0.626	4474.67	A
36.22	12.25	0.88	0.121	0.055	4476.17	A
36.26	12.25	2.76	0.378	0.278	4476.17	A
36.28	12.25	1.67	0.228	0.136	4476.17	A
36.28	12.25	7.14	0.976	1.073	4476.92	A
36.26	12.25	10.32	1.414	1.813	4476.92	A
36.25	12.25	4.43	0.607	0.544	4476.92	A
36.28	12.25	5.62	0.769	0.764	4476.92	A
36.23	12.25	6.97	0.957	1.037	4477.17	A
36.25	12.25	10.62	1.457	1.888	4477.17	A
36.20	12.25	14.11	1.942	2.829	4477.17	A
36.22	12.25	4.16	0.572	0.498	4478.42	A
35.25	12.25	3.52	0.515	0.392	4478.42	A
35.27	12.25	2.42	0.354	0.230	4478.42	A
36.21	12.25	5.19	0.714	0.682	4478.42	D
36.21	12.25	3.32	0.457	0.361	4478.42	D
36.23	12.25	6.24	0.858	0.886	4479.33	A
36.24	12.25	6.98	0.959	1.039	4479.33	A
36.29	12.25	5.50	0.754	0.741	4479.33	A
35.25	12.25	9.92	1.451	1.714	4479.33	D
36.27	12.25	4.95	0.679	0.637	4479.33	D
36.20	12.25	2.81	0.387	0.285	4479.33	D
36.20	12.25	2.17	0.299	0.197	4479.83	A
36.25	12.25	4.74	0.651	0.599	4479.83	A
36.28	12.25	1.09	0.150	0.074	4479.83	A
36.22	12.25	4.55	0.627	0.565	4479.83	A
36.22	12.25	5.67	0.781	0.773	4479.83	A
36.24	12.25	9.69	1.333	1.658	4479.83	A
36.27	12.25	9.59	1.317	1.633	4479.83	A
36.22	12.25	8.79	1.211	1.443	4480.83	A
36.27	12.25	3.89	0.534	0.452	4480.83	A
36.23	12.25	7.16	0.986	1.078	4480.83	D
36.27	12.25	6.63	0.911	0.966	4480.83	D
36.30	12.25	2.23	0.306	0.205	4480.83	D
36.24	12.25	2.54	0.350	0.247	4481.92	A
36.25	12.25	4.45	0.612	0.548	4481.92	A
36.23	12.25	3.74	0.515	0.428	4481.92	A
36.21	12.25	13.55	1.869	2.671	4481.92	A
36.25	12.25	5.32	0.732	0.706	4481.92	A
36.20	12.25	5.07	0.700	0.660	4481.92	A
36.21	12.25	11.70	1.614	2.167	4481.92	A
36.22	12.25	7.67	1.057	1.189	4483.17	A
36.22	12.25	1.81	0.250	0.152	4483.17	A
36.20	12.25	4.27	0.589	0.517	4483.17	A
36.29	12.25	2.21	0.303	0.202	4483.17	A

N2 Flow Press. (psia)	Atm Press. (psia)	Flow Rate (cc/min)	TEMCO Perm (mD)	Calc. Perm (mD)	Core Depth (ft)	Facies
36.23	12.25	6.02	0.829	0.842	4483.17	A
36.27	12.20	0.76	0.104	0.044	4483.92	A
36.21	12.20	1.79	0.245	0.150	4483.92	A
36.22	12.20	0.95	0.130	0.061	4483.92	A
36.17	12.20	3.72	0.512	0.425	4483.92	A
36.24	12.20	4.88	0.668	0.625	4483.92	A
36.23	12.20	3.61	0.495	0.407	4483.92	A
36.18	12.20	1.52	0.209	0.119	4484.75	A
36.20	12.20	3.16	0.434	0.337	4484.75	A
36.22	12.20	1.41	0.194	0.107	4484.75	A
36.23	12.20	2.42	0.332	0.230	4484.75	A
36.16	12.20	3.33	0.459	0.363	4484.75	A
36.18	12.20	7.94	1.094	1.249	4484.75	A
36.19	12.20	2.36	0.325	0.222	4485.58	A
36.17	12.20	5.51	0.760	0.742	4485.58	A
36.17	12.20	9.24	1.274	1.549	4485.58	A
36.19	12.20	4.96	0.683	0.639	4485.58	A
36.21	12.20	2.32	0.319	0.217	4485.58	D
36.16	12.20	2.85	0.393	0.291	4486.75	A
36.21	12.20	8.63	1.188	1.406	4486.75	A
36.22	12.20	8.25	1.135	1.319	4486.75	A
36.18	12.20	6.42	0.885	0.923	4486.75	A
36.16	12.20	6.55	0.904	0.950	4487.08	A
36.18	12.20	4.75	0.655	0.601	4487.08	A
36.21	12.20	2.23	0.307	0.205	4487.08	A
36.23	12.20	3.63	0.499	0.410	4487.08	D
36.24	12.20	2.89	0.397	0.296	4488.08	A
36.17	12.20	2.34	0.323	0.220	4488.08	A
36.17	12.20	4.47	0.617	0.551	4488.08	A
36.20	12.20	3.35	0.462	0.366	4488.08	A

Appendix C

Near-wellbore Modeling and Upscaling Results

Facies Modeling

The near-wellbore facies modeling for the McHale #1 and Champlin 369 cores was done by using the four previously identified facies and compiling them into a 3-D representation of their respective cores. To start, generic facies were individually modeled to the various representations of each of the four in the cores. Multiple variations of each facies were designed and modeled to give greater flexibility in the specific modeling of each facies later. Additionally, the variations that are designed early save time when modeling specific facies in the cores as fewer variables have to be changed later. These different variations were all of the same basic design and used the same depositional processes, only minor variables within each facies were changed (e.g., increased or decreased mudrock content, higher ripple amplitude or wavelength, thickness of mudrock or sandstone laminas, etc.) In this study, these generic facies models are known as sub-models.

Once the sub-models were completed, detailed core photographs were taken and loaded into the modeling software. These photographs were taken at a foot interval with each photo only representing a one-foot section of the core. These photos were cropped and straightened so that only the core face is seen. These detailed photos were loaded into the modeling software and each was carefully depth calibrated so that it would display at the depths marked on the core. These photographs are the primary guide for determining the facies at a given depth. Core descriptions were not detailed enough to provide every facies within the core as the majority of them are at most several inches thick (appendix A). However, due to the nature of the core photos, the cores were on hand during the modeling process so direct measurements could be taken from the core (facies thickness, ripple amplitude, wavy lamina wavelengths, etc.).

Core photos were displayed along with all well-log data available for each core and each facies was hand drawn on top of them. This was used particularly with the core photos as the well-log suites have a much coarser resolution and do differentiate facies at that scale. As the boundaries for each facies were designated, each was populated with one of the sub-models created earlier. This was done incrementally, only one facies at a time. As each was populated, the facies was rendered and compared to the core photographs and the actual core. Adjustments were made and the facies was regenerated and compared again for photographs and the actual core. This process was continued until the 3-D core model matched what was observed in the core photographs and actual core. Following this, the next set of facies boundaries were created and the process was repeated throughout the entire project.

Permeability Modeling

Once the facies models were completed, permeability models were created. To generate the permeability models in NWM program, the measurements taken previously were averaged together and a mean and standard deviation were determined. The mean for the permeability data was determined using a geometric average of calibrated permeability measurements. Similarly, the standard deviation was derived from the calibrated measurements as well. The inputs for the model are done by lamina type, and for simplicity, it was assumed there was only one type of sandstone and one type of mudrock for each facies. The data was collected by lamina type and by facies making the geometric average and standard deviation simple to calculate. These were then used as inputs for permeability modeling. Each facies was populated with permeability values using the inputs. Other controls on distribution are available including variograms. However, due to the small-scale nature of the measurements and irregular spacing of the measurements, variograms could not be used. One other control on permeability values was the application of minimum and maximum values. A minimum permeability of 0.0001 mD was applied along with a maximum permeability of 15.0 mD. If any values were modeled as being outside of these values, they were rounded to the minimum or maximum values, depending on whether the value was higher or lower than each.

Permeability Upscaling and Results

Once the permeability models were created, an upscaling case was defined. The upscaling process used in this study is a flow-based algorithm that simulates flow through each facies and determines what the effective permeability is. This study chose to have an effective permeability for each facies determined, meaning that each block that is upscaled is a different size and is determined by the facies boundaries. This was preferred over the alternative, which would have been defining an upscaling block size. This option would have caused multiple facies with different permeability values to be lumped together, and the effective values generated would have no longer corresponded to a single facies. This would have made comparison of original- to effective-permeability values difficult. With the upscaling boundaries being the same as the facies boundaries, each facies is given an effective value, and a comparison of that facies' original-permeability and the resulting effective permeability could be completed.

Choosing the type of upscaling process—either single-phase or multi-phase—is important. This study uses a single-phase upscaling process. Single phase was chosen instead of a multi-phase upscaling approach because of the lack of data required for multi-phase upscaling. Multi-phase upscaling is typically done for two fluids: water and oil. To do this type of upscaling, more data is required including fluid viscosity and saturation functions for each lamina present amount others. After determining what type of upscaling will be done, determining the boundary conditions is next.

The boundary conditions that are chosen for the upscaling process can be considered one of the more important variables. This study uses what are known as periodic boundary conditions (PBC) due to its effectiveness in producing accurate results in heterogeneous reservoirs. Pickup et al. (1994) showed that PBC proved to be robust in evaluating permeabilities in the x- and y-directions. Additionally, this method was determined to be very effective at handling complex geometries, and in the context of a small-scale model like this, creating symmetric effective permeabilities (Durlofsky, 1991). Periodic boundary conditions are best applied to reservoirs that are heterogeneous and contain repeating geological structures. The Terry and Hygiene formations are heterogeneous as previously stated but also contain a pattern among the four facies with the sandstone-rich three occurring together with regular frequency and the mudrock-rich wavy laminated facies occurring with ripple laminated facies regularly as well. While this pattern isn't absolute, enough of a pattern exists to further warrant using this set of boundary conditions. Similar to these previous works, the periodic boundary conditions used in this study produces a pressure gradient, and there are no limitations to flow through any bounding surface (Fig. C.1). The results of the upscaling are presented for both the McHale #1 and Champlin 369 cores in tables C.1 and C.2.

A comparison of the original-permeability values and effective-permeability values was conducted by facies as well. Similar to the overall trend for the cores as a whole (Fig. 6.8), each individual facies shows a narrowing of the range of permeabilities, with the exception of facies D, structureless sandstone (Figures C.2, C.3, C.4, C.5). This facies was least affected by the upscaling due to its lack of mudrock. This causes the effective permeability to be almost the same as the original permeability after the upscaling is completed.

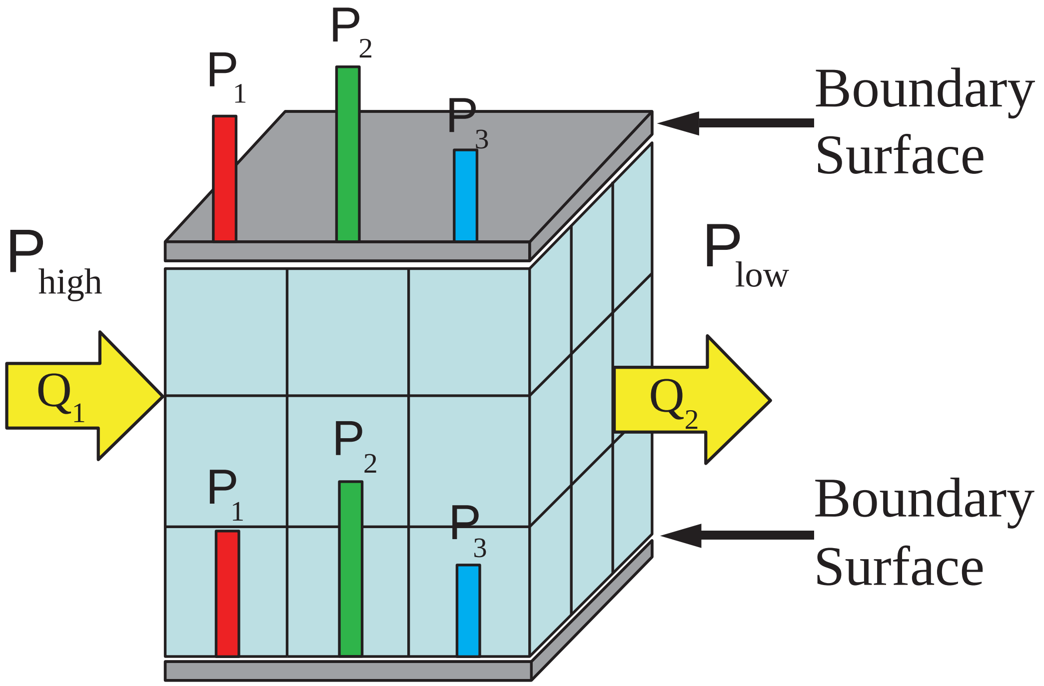

Figure C.1. Schematic of flow-based upscaling boundary conditions. No limitations in flow occur across boundary conditions. This set of boundary conditions is ideally suited for heterogeneous samples. Permeabilities using these boundary condition parameters are measured in six directions. Modified from SBED Users Manual v4.1.

Table C.1. Original- and effective-permeability values for Champlin 369 core.

Original Permeability (mD)			Effective Permeability (mD)		
Sand lamina Avg.	Sand Lamina	Mud Lamina	Geometric Avg.	Arithmetic Avg.	Standard Dev
1.500	6.170	0.004	0.235	0.283	0.162
3.080	3.926	0.004	0.206	0.527	0.599
5.290	8.259	0.004	3.548	3.559	0.260
0.730	2.271	N/A	0.341	0.374	0.224

Table C.2. Upscaled results from McHale #1 core. (N=156)

McHale #1 Upscaling Results

Facies	Effective Perm (mD)	Top (ft)	Bottom (ft)	Thickness (ft)
A	0.10	4688.00	4688.41	0.41
B	0.53	4688.41	4688.57	0.16
A	0.08	4688.57	4689.13	0.56
D	0.21	4689.13	4689.51	0.38
B	0.42	4689.51	4689.60	0.09
A	0.14	4689.60	4689.94	0.34
D	0.21	4689.94	4690.23	0.29
A	0.16	4690.23	4690.31	0.08
D	0.21	4690.31	4690.37	0.06
A	0.17	4690.37	4690.51	0.14
A	0.21	4690.51	4690.62	0.11
A	0.16	4690.62	4691.05	0.43
B	0.52	4691.05	4691.10	0.05
A	0.17	4691.10	4691.38	0.28
C	1.46	4691.38	4691.56	0.18
A	0.18	4691.56	4691.77	0.21
B	0.56	4691.77	4692.07	0.30
D	0.21	4692.07	4692.19	0.12
A	0.18	4692.19	4692.33	0.14
B	0.49	4692.33	4692.45	0.12
B	0.43	4692.45	4692.70	0.25
A	0.13	4692.70	4693.02	0.32
A	0.13	4693.02	4693.17	0.15
D	0.21	4693.17	4693.38	0.21
C	1.45	4693.38	4693.59	0.21
A	0.13	4693.59	4693.74	0.15
C	1.46	4693.74	4693.85	0.11
A	0.09	4693.85	4693.94	0.09
D	0.22	4693.94	4694.46	0.52
A	0.20	4694.46	4694.65	0.19
C	1.47	4694.65	4694.73	0.08
A	0.10	4694.73	4694.91	0.18
C	1.46	4694.91	4695.05	0.14
A	0.18	4695.05	4695.14	0.09
D	0.21	4695.14	4695.50	0.36
B	0.43	4695.50	4695.58	0.08
A	0.05	4695.58	4695.70	0.12
C	1.46	4695.70	4695.81	0.11

A	0.05	4695.81	4695.88	0.07
A	0.17	4695.88	4696.51	0.63
B	0.46	4696.51	4696.63	0.12
C	1.47	4696.63	4696.69	0.06
B	0.61	4696.69	4696.79	0.10
B	0.36	4696.79	4697.02	0.23
A	0.06	4697.02	4697.24	0.22
B	0.55	4697.24	4697.32	0.08
B	0.42	4697.32	4697.52	0.20
D	0.21	4697.52	4697.59	0.07
B	0.29	4697.59	4697.68	0.09
B	0.38	4697.68	4697.74	0.06
B	0.70	4697.74	4697.89	0.15
D	0.22	4697.89	4697.93	0.04
B	0.61	4697.93	4698.01	0.08
D	0.22	4698.01	4698.06	0.05
A	0.01	4698.06	4698.17	0.11
D	0.21	4698.17	4698.22	0.05
A	0.13	4698.22	4698.72	0.50
D	0.2137	4698.72	4698.84	0.12
A	0.07	4698.84	4698.95	0.11
D	0.21	4698.95	4699.08	0.13
B	0.43	4699.08	4699.13	0.05
A	0.10	4699.13	4699.25	0.12
B	0.60	4699.25	4699.52	0.27
A	0.03	4699.52	4699.63	0.11
C	1.46	4699.63	4699.72	0.09
A	0.00	4699.72	4699.79	0.07
C	1.47	4699.79	4699.83	0.04
A	0.02	4699.83	4700.18	0.35
D	0.20	4700.18	4700.26	0.08
B	0.16	4700.26	4700.33	0.07
D	0.17	4700.33	4700.66	0.33
A	0.02	4700.66	4700.92	0.26
B	0.50	4700.92	4701.08	0.16
A	0.14	4701.08	4701.21	0.13
D	0.21	4701.21	4701.25	0.04
A	0.06	4701.25	4701.61	0.36
D	0.21	4701.61	4701.70	0.09
A	0.08	4701.70	4701.75	0.05
B	0.58	4701.75	4701.93	0.18
B	0.25	4701.93	4702.10	0.17
A	0.01	4702.10	4702.21	0.11
D	0.21	4702.21	4702.30	0.09
A	0.14	4702.30	4702.58	0.28
D	0.21	4702.58	4702.69	0.11
B	0.31	4702.69	4702.82	0.13
A	0.04	4702.82	4702.91	0.09
D	0.21	4702.91	4702.97	0.06
A	0.02	4702.97	4703.10	0.13
A	0.11	4703.10	4703.23	0.13
D	0.21	4703.23	4703.26	0.03
A	0.12	4703.26	4703.44	0.18
B	0.38	4703.44	4703.64	0.20
B	0.59	4703.64	4703.93	0.29
B	0.45	4703.93	4704.04	0.11
B	0.31	4704.04	4704.28	0.24
A	0.00	4704.28	4704.31	0.03
D	0.20	4704.31	4704.37	0.06
B	0.30	4704.37	4704.62	0.25

B	0.30	4704.62	4704.81	0.19
A	0.19	4704.81	4705.07	0.26
A	0.12	4705.07	4705.23	0.16
B	0.60	4705.23	4705.44	0.21
B	0.47	4705.44	4705.54	0.10
B	0.51	4705.54	4705.76	0.22
A	0.04	4705.76	4705.83	0.07
C	1.47	4705.83	4705.88	0.05
A	0.01	4705.88	4705.91	0.03
C	1.47	4705.91	4705.94	0.03
A	0.06	4705.94	4706.01	0.07
B	0.11	4706.01	4706.17	0.16
C	1.47	4706.17	4706.23	0.06
A	0.07	4706.23	4706.26	0.03
D	0.22	4706.26	4706.34	0.08
B	0.68	4706.34	4706.60	0.26
D	0.21	4706.60	4707.17	0.57
B	0.68	4707.17	4707.35	0.18
A	0.08	4707.35	4708.23	0.88
B	0.55	4708.23	4708.33	0.10
D	0.21	4708.33	4708.46	0.13
B	0.61	4708.46	4708.79	0.33
A	0.07	4708.79	4709.15	0.36
D	0.21	4709.15	4709.44	0.29
A	0.12	4709.44	4709.54	0.10
A	0.05	4709.54	4709.64	0.10
B	0.57	4709.64	4709.68	0.04
C	1.47	4709.68	4709.73	0.05
A	0.17	4709.73	4709.79	0.06
C	1.46	4709.79	4709.92	0.13
A	0.03	4709.92	4710.19	0.27
B	0.29	4710.19	4710.28	0.09
D	0.21	4710.28	4710.51	0.23
B	0.32	4710.51	4710.59	0.08
D	0.21	4710.59	4710.67	0.08
A	0.03	4710.67	4710.71	0.04
D	0.21	4710.71	4710.80	0.09
B	0.51	4710.80	4710.96	0.16
B	0.63	4710.96	4711.00	0.04
B	0.60	4711.00	4711.05	0.05
B	0.51	4711.05	4711.07	0.02
A	0.04	4711.07	4711.24	0.17
D	0.21	4711.24	4711.78	0.54
A	0.08	4711.78	4712.00	0.22
A	0.10	4712.00	4712.14	0.14
A	0.06	4712.14	4712.22	0.08
A	0.18	4712.22	4712.36	0.14
A	0.04	4712.36	4712.84	0.48
D	0.21	4712.84	4713.18	0.34
A	0.10	4713.18	4713.70	0.52
A	0.17	4713.70	4713.88	0.18
B	0.43	4713.88	4714.00	0.12
A	0.10	4714.00	4714.20	0.20
A	0.11	4714.20	4714.36	0.16
A	0.17	4714.36	4714.58	0.22
A	0.05	4714.58	4714.75	0.17
A	0.10	4714.75	4714.99	0.24
D	0.21	4714.99	4715.04	0.05

Table C.3. Upscaled results from Champlin 369 core. (N=161)

Champlin 369 Upscaling Results

Facies	Effective Perm (mD)	Top (ft)	Bottom (ft)	Thickness (ft)
A	0.45	4836.25	4836.88	0.63
B	0.05	4836.88	4838.06	1.18
B	1.30	4838.06	4838.14	0.08
B	0.05	4838.14	4839.05	0.91
C	3.42	4839.05	4839.29	0.24
B	0.07	4839.29	4839.71	0.42
B	0.07	4839.71	4839.93	0.22
A	0.39	4839.93	4839.99	0.06
A	0.50	4839.99	4840.57	0.58
B	0.04	4840.57	4841.05	0.48
A	0.25	4841.05	4841.21	0.16
A	0.41	4841.21	4842.04	0.83
C	3.61	4842.04	4842.19	0.15
B	0.08	4842.19	4842.71	0.52
A	0.17	4842.71	4842.86	0.15
B	0.09	4842.86	4843.00	0.14
A	0.30	4843.00	4843.26	0.26
B	1.73	4843.26	4843.58	0.32
A	0.05	4843.58	4843.69	0.11
D	0.31	4843.69	4843.80	0.11
A	0.36	4843.80	4844.12	0.32
A	0.29	4844.12	4844.58	0.46
A	0.62	4844.58	4845.15	0.57
A	0.34	4845.15	4845.36	0.21
D	0.33	4845.36	4845.53	0.17
B	0.01	4845.53	4845.62	0.09
A	0.46	4845.62	4846.04	0.42
B	0.11	4846.04	4846.13	0.09
A	0.23	4846.13	4846.39	0.26
A	0.07	4846.39	4846.69	0.30
C	3.71	4846.69	4846.80	0.11
A	0.61	4846.80	4846.87	0.07
C	3.49	4846.87	4847.07	0.20
A	0.77	4847.07	4847.32	0.25
B	0.10	4847.32	4847.69	0.37
A	0.24	4847.69	4848.00	0.31
C	3.80	4848.00	4848.07	0.07
A	0.37	4848.07	4849.15	1.08
B	1.59	4849.15	4849.32	0.17
A	0.57	4849.32	4850.09	0.77
C	3.74	4850.09	4850.19	0.10
B	1.71	4850.19	4850.25	0.06
Core Break	0.00	4850.25	4852.00	1.75
B	1.58	4852.00	4852.46	0.46
A	0.06	4852.46	4852.61	0.15
C	3.73	4852.61	4852.71	0.10
A	0.40	4852.71	4852.89	0.18
B	0.02	4852.89	4853.12	0.23
A	0.13	4853.12	4853.23	0.11
D	0.32	4853.23	4853.47	0.24
A	0.21	4853.47	4854.24	0.77
A	0.70	4854.24	4854.60	0.36
B	0.96	4854.60	4854.71	0.11

A	0.09	4854.71	4854.87	0.16
C	3.60	4854.87	4855.02	0.15

B	0.08	4855.02	4855.48	0.46
B	0.07	4855.48	4855.67	0.19
C	3.79	4855.67	4855.74	0.07
B	0.59	4855.74	4855.92	0.18
D	0.32	4855.92	4856.31	0.39
D	1.14	4856.31	4856.45	0.14
D	0.31	4856.45	4856.69	0.24
A	0.02	4856.69	4856.79	0.10
A	0.34	4856.79	4856.94	0.15
B	0.01	4856.94	4857.07	0.13
B	0.08	4857.07	4857.46	0.39
D	0.32	4857.46	4857.70	0.24
B	0.02	4857.70	4857.83	0.13
A	0.30	4857.83	4858.38	0.55
B	0.72	4858.38	4858.48	0.10
A	0.17	4858.48	4858.78	0.30
C	3.12	4858.78	4859.20	0.42
A	0.23	4859.20	4859.41	0.21
B	0.22	4859.41	4859.52	0.11
C	3.49	4859.52	4859.73	0.21
B	0.13	4859.73	4860.33	0.60
B	0.51	4860.33	4860.73	0.40
A	0.29	4860.73	4860.92	0.19
A	0.60	4860.92	4861.12	0.20
B	1.16	4861.12	4861.20	0.08
A	0.33	4861.20	4861.50	0.30
B	0.93	4861.50	4861.71	0.21
A	0.19	4861.71	4862.11	0.40
C	2.51	4862.11	4863.31	1.20
B	0.12	4863.31	4863.36	0.05
C	3.77	4863.36	4863.45	0.09
B	0.90	4863.45	4863.91	0.46
B	1.49	4863.91	4864.61	0.70
B	0.10	4864.61	4864.73	0.12
D	0.33	4864.73	4864.88	0.15
B	0.08	4864.88	4865.09	0.21
C	3.74	4865.09	4865.18	0.09
A	0.53	4865.18	4865.25	0.07
C	3.63	4865.25	4865.39	0.14
A	0.20	4865.39	4865.68	0.29
D	0.33	4865.68	4865.80	0.12
A	0.27	4865.80	4866.04	0.24
C	3.59	4866.04	4866.20	0.16
A	0.08	4866.20	4866.50	0.30
A	0.08	4866.50	4866.66	0.16
B	1.25	4866.66	4866.97	0.31
C	3.56	4866.97	4867.14	0.17
A	0.33	4867.14	4867.38	0.24
B	1.74	4867.38	4867.52	0.14
A	0.17	4867.52	4867.56	0.04
C	3.48	4867.56	4867.77	0.21
A	0.19	4867.77	4867.85	0.08
B	0.10	4867.85	4868.46	0.61
A	0.13	4868.46	4868.78	0.32
A	0.22	4868.78	4868.96	0.18
C	3.65	4868.96	4869.09	0.13
B	1.55	4869.09	4869.14	0.05

D	0.32	4869.14	4869.35	0.21
A	0.22	4869.35	4869.47	0.12
C	3.51	4869.47	4869.66	0.19
B	0.82	4869.66	4869.80	0.14
B	0.04	4869.80	4870.07	0.27
A	0.22	4870.07	4870.30	0.23
A	0.43	4870.30	4871.03	0.73
C	3.57	4871.03	4871.20	0.17
A	0.10	4871.20	4871.33	0.13
C	3.55	4871.33	4871.50	0.17
Core Break	0.00	4871.50	4872.00	0.50
C	3.27	4872.00	4872.33	0.33
A	0.32	4872.33	4872.72	0.39
B	0.35	4872.72	4872.82	0.10
C	3.47	4872.82	4873.03	0.21
A	0.13	4873.03	4873.13	0.10
C	3.84	4873.13	4873.19	0.06
A	0.29	4873.19	4873.32	0.13
C	3.71	4873.32	4873.43	0.11
A	0.17	4873.43	4873.47	0.04
D	0.31	4873.47	4873.77	0.30
A	0.39	4873.77	4874.09	0.32
C	3.74	4874.09	4874.19	0.10
A	0.14	4874.19	4874.45	0.26
C	3.81	4874.45	4874.52	0.07
A	0.18	4874.52	4874.90	0.38
C	3.51	4874.90	4875.10	0.20
D	0.20	4875.10	4875.23	0.13
A	0.42	4875.23	4875.51	0.28
C	3.09	4875.51	4875.96	0.45
A	0.15	4875.96	4876.05	0.09
C	3.71	4876.05	4876.16	0.11
B	0.22	4876.16	4876.30	0.14
A	0.26	4876.30	4876.35	0.05
C	3.75	4876.35	4876.44	0.09
A	0.14	4876.44	4876.57	0.13
A	0.52	4876.57	4876.64	0.07
A	0.19	4876.64	4876.92	0.28
A	0.25	4876.92	4877.17	0.25
A	0.24	4877.17	4877.37	0.20
A	0.23	4877.37	4877.77	0.40
A	0.30	4877.77	4878.15	0.38
A	0.23	4878.15	4878.70	0.55
C	3.30	4878.70	4879.01	0.31
D	0.32	4879.01	4879.26	0.25
A	0.36	4879.26	4880.35	1.09
B	0.33	4880.35	4880.42	0.07
C	3.74	4880.42	4880.52	0.10
A	0.16	4880.52	4882.06	1.54
B	0.04	4882.06	4882.20	0.14
A	0.10	4882.20	4883.25	1.05

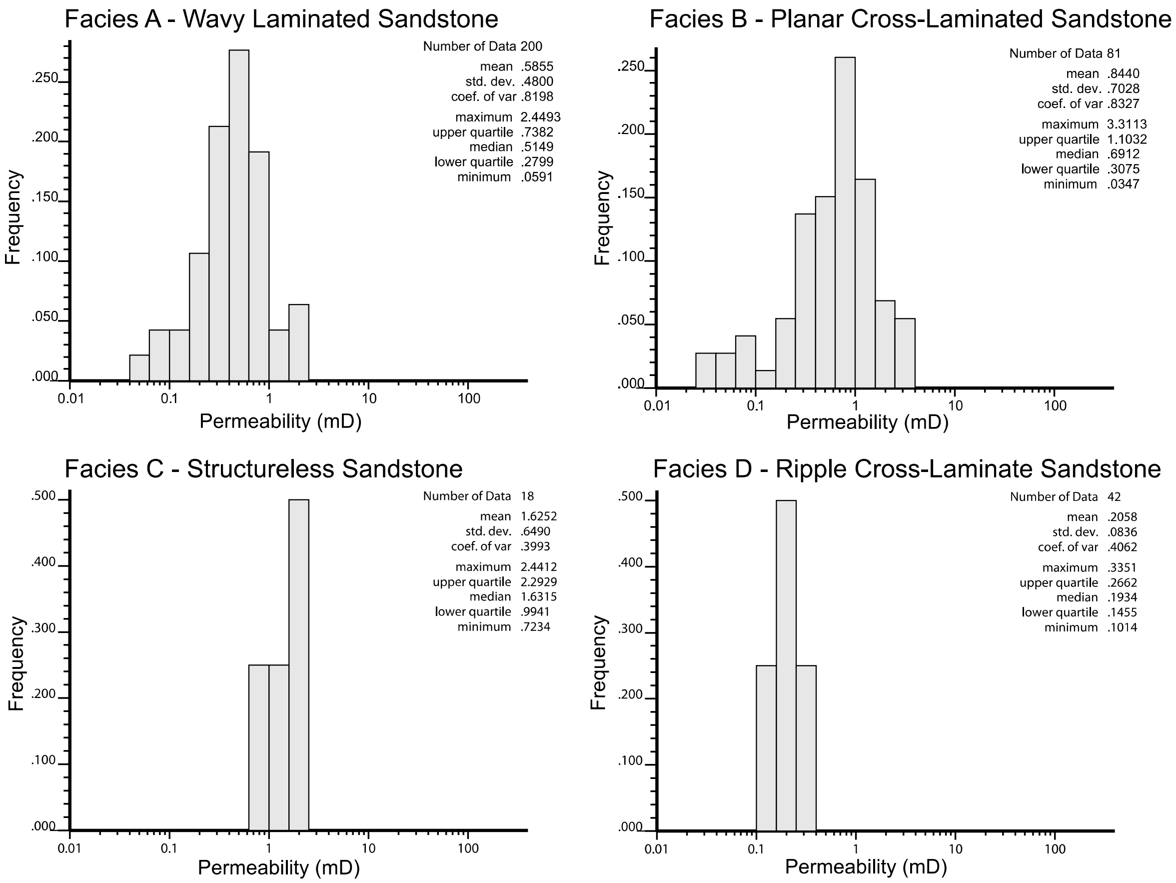

Fig. C.1. Permeabilities originally measured for the Terry Formation on the McHale #1 and Moser #1 cores. This data is used to populate 3-D original permeability models. Permeabilities are calibrated values and are determined based on core descriptions.

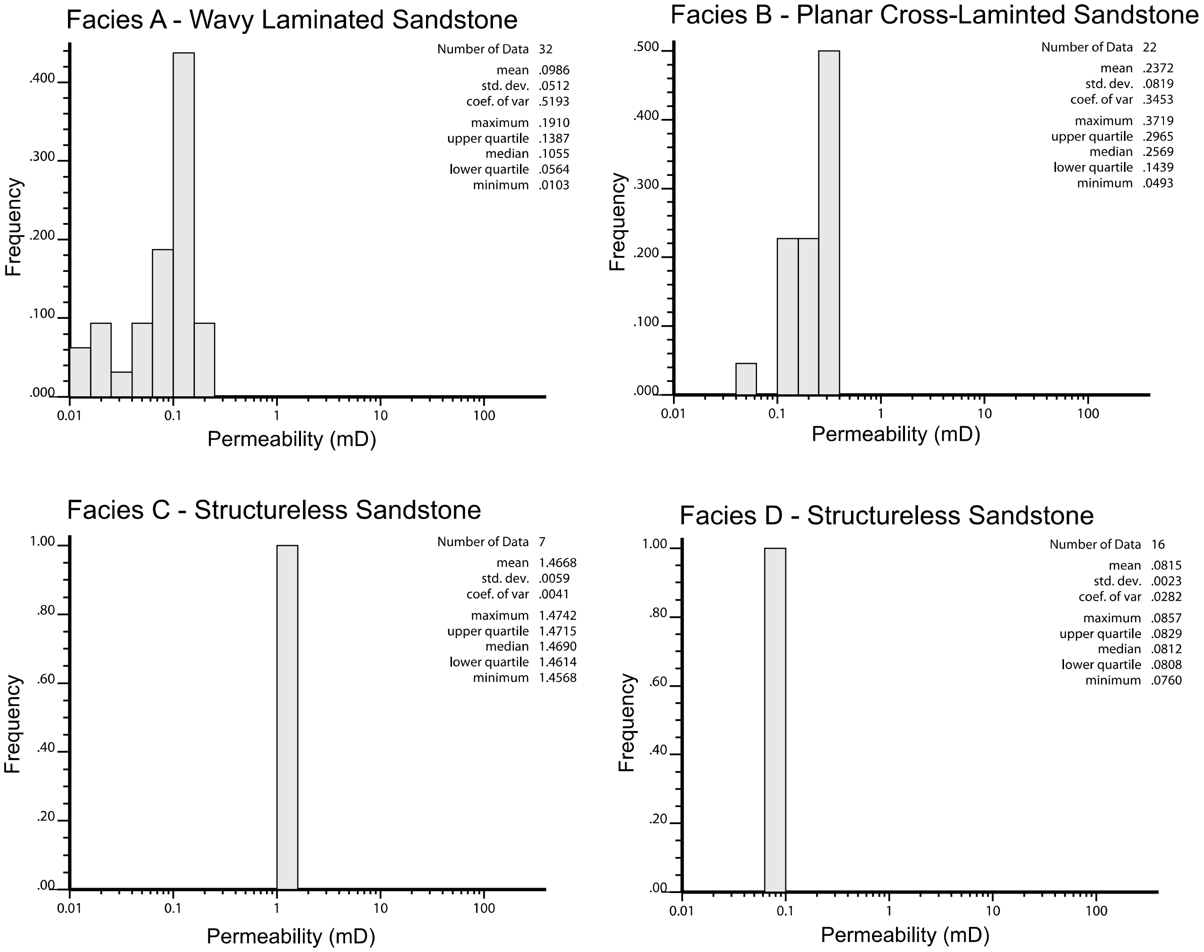
Facies A - Wavy Laminated Sandstone

Facies B - Planar Cross-Laminted Sandstone

Facies C - Structureless Sandstone

Facies D - Structureless Sandstone

Fig. C.2. Permeability values generated for the Terry Formation during the upscaling process for the McHale #1 core. Effective permeabilities show a narrowed range compared to original values and decreased mean values.

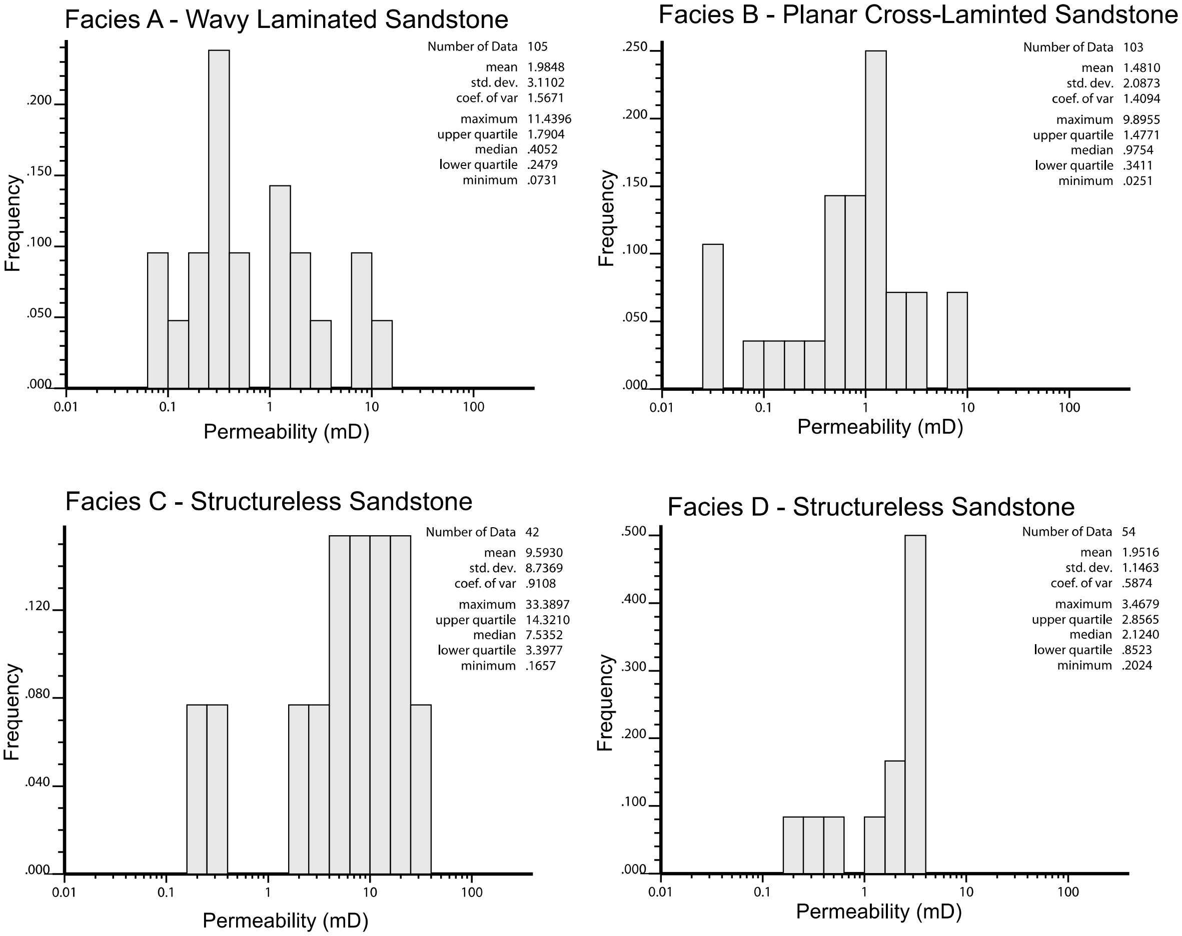
Facies A - Wavy Laminated Sandstone

Facies B - Planar Cross-Laminted Sandstone

Facies C - Structureless Sandstone

Facies D - Structureless Sandstone

Fig. C.3. Permeabilities originally measured for the Hygiene Formation on the Champlin 369 and Sidwell #1 cores. This data is used to populate 3-D original permeability models. Permeabilities are calibrated values and are determined based on core descriptions.

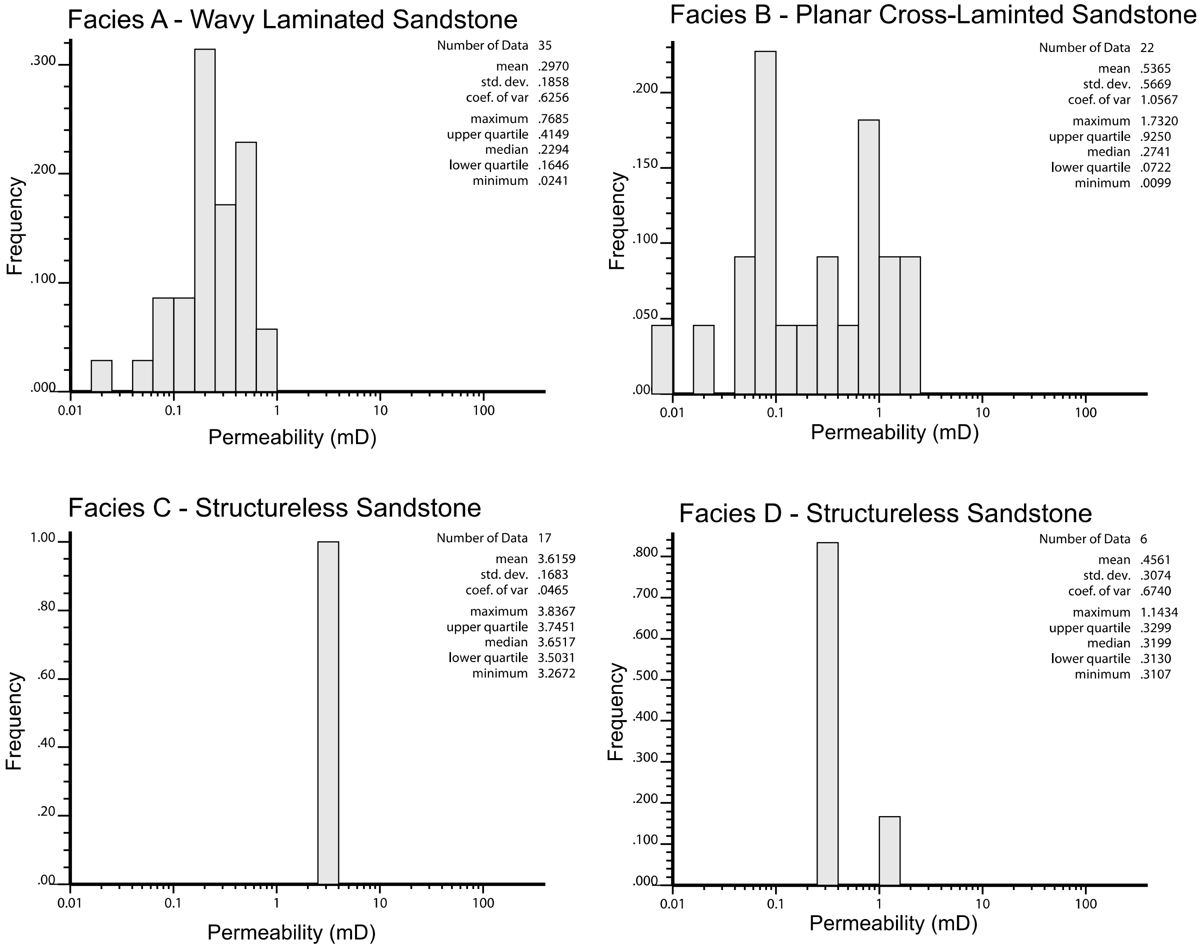
Facies A - Wavy Laminated Sandstone

Facies B - Planar Cross-Laminted Sandstone

Facies C - Structureless Sandstone

Facies D - Structureless Sandstone

Fig. C.4. Permeability values for the Hygiene Formation generated during the upscaling process for the Champlin 369 core. Effective permeabilities show a narrowed range compared to original values and decreased mean values.

Appendix D

Field-scale Modeling

Well-log Data

For the field scale modeling portion of this study, well-log data is used as the primary input data for modeling. The one exception to this is the permeability modeling in which permeability data is obtained from cores. Digital well-log data was obtained for all nine wells within the model area (Fig. 6.2). The primary well-log curves used in this study were GR, SP, RESD, and DPHI. GR, SP, and RESD logs were used in conjunction with each other to determine reservoir zonation. Additionally, SP logs were used to create a volume probability model of the property to help constrain facies distribution as it was shown to have a correlation with relative amounts of each facies within a zone. Density-porosity logs were used to create the porosity models for this study. Due to the age of the wells and the availability of data, only DPHI logs were used to create porosity models. While it is preferable to use additional porosity logs (e.g., neutron-porosity or sonic-porosity logs), only select wells had these additional porosity logs. It was determined to only use density-porosity logs in favor of combining multiple logs to create an average porosity on some wells but not others to keep the data sets equal. Finally, all well-logs used in this study were normalized to the McHale #1 cored well. Due to the nature of this study and the relationship of well logs and core-measured values, it was determined to relate all 3-D field scale models back to cored interval by normalizing the log responses to the well logs in the Terry Formation interval. The normalization process involved stretching and compressing the well log curves to the same range as a given curve. This allows for the overall shape of the log curve to remain the same with high values still being high and low values still being low relative to the original log curve. The high and low values are determined automatically from the logs for the McHale #1 core.

Model Framework

It is necessary to accurately create a stratigraphic framework for 3-D reservoir models. In this case, the study area is approximately 2828 ft by 2900 ft (length, width; 826 x 887 m; Fig. 6.2) and includes the Terry Formation which varies in thickness but averages approximately 25 ft (6.2 m) (Weimer, 1997). The cell size based on these measurements is 29.8 x 30 x 1 ft (9.08 x 9.1 x 0.3 m) for each individual cell in the model area. To create the layering within the model, five stratigraphic horizons were interpreted based on well log and core-to-log comparisons (Fig. 6.5; Table D.1).

These stratigraphic horizons define four zones within the model area that are then broken down into layers that define the cell size in the model. The number of layers within each zone was determined to give each cell an approximate 1 ft thickness (Table D.2). It is important to have each cell in the 3-D model sized appropriately for the scale of the structures that are trying to be modeled. Based on limited outcrop availability and research, the cell size of 1 ft was determined to be large enough to represent the lateral and vertical variability of the facies but also small enough as to not lump all of the permeability data collected and calculated which is on a much smaller scale.

Table D.1. Stratagraphic horizons determined for all wells used in this study. Wells denoted with astrick (*) are only used for permeability acquistion. Remaining wells used in field-scale 3-D models.

API	Well name	Terry	Terry A	Terry_B	Terry_C	Base Terry	Hygiene	Base Hygiene
05123076430000	McHale #1	4692.88	4694.46	4703.49	4710.24	4717.66	--	--
05123078320000	Hart B Unit #1	4656.04	4658.20	4668.72	4672.45	4682.84	--	--
05123089400000	Vonasek Unit C #2	4676.00	4680.09	4691.30	4699.38	4707.63	--	--
05123147970000	Weld Co. Pooling Unit #2	4690.26	4692.77	4704.95	4709.97	4719.73	5229.00	--
05123089980000	McHale #3	4688.00	4692.65	4704.27	4713.02	4722.18	--	--
05123089730000	McHale #4	4685.75	4687.67	4700.73	4708.47	4719.99	--	--
05123089590000	Champlin #1-35	4673.84	4676.12	4685.64	4694.45	4701.66	--	--
05123090960000	UPRR 42 Pan Am AF #3	4689.62	4691.40	4705.46	4710.62	4720.09	--	--
05123208600000	Newton #3-35A	4743.50	4748.68	4756.72	4761.84	4769.97	5122.00	
05123076670000	Montoya #1	4748.81	4754.81	4764.35	4769.22	4780.46	--	
05123090540000	Champlin 369 *	4463.28	--	--	--	4514.62	4834.31	4882.92
05123074700000	Moser #1 *	4431	--	--	--	--	--	--
05123079080000	Sidwell #1 *	4366	--	--	--	--	4838	--

Table D.2. Layering scheme sorted by zone within the 3-D model framework. Layers average 1 ft (0.3 m) thickness.

Zone #	Zone	Layering Scheme	Number of Layers
1	Top Terry to Terry_A (Non-reservoir)	Proportional	8
2	Terry_A to Terry _B (Reservoir)	Proportional	16
3	Terry_B to Terry_C (Non-reservoir)	Proportional	10
4	Terry_C to Base_Terry (Reservoir)	Proportional	10

SP Volume Probability and Facies Modeling

Due to the lack of facies log data, which inhibits the use of variograms for controlling lateral distribution, control of facies distribution was obtained by using a SP derived lithology probability volume model. This probability model is a 3-D model the same size as the other models used in this study in which each cell is given a probability for containing either a sandstone-rich or mudrock-rich facies. This probability was determined using the correlation between facies and SP log response (Fig. D.1). The SP logs from all 9 wells were used to create a SP model, which was then rescaled to zero to one depending on whether it was being used as a probability model for sandstone-rich or mudrock-rich facies. For the sandstone-rich facies, the more negative the SP values, the cleaner the sandstone is, which implies that the most negative SP values coincide with the structureless sandstone facies. The intermediate SP values are when the log curve is moving from zero toward the low end, that is, where the sandstone- rich facies that contain more mudrock are found (e.g., facies B and D). The B, C, and D facies could all be modeled with a single lithology probability volume model (Fig. 6.9); however, a new lithology probability volume model had to be created for the mudrock-rich facies (Fig. D.1). This model appears as the inverse of the sandstone-rich lithology probability volume model and is created in a similar way with the SP log values being closer to zero when the mudrock-rich facies is present (Fig. D.1).

With the facies modeling constraints completed, facies modeling was completed. To complete the facies modeling each facies was assigned to its respective sandstone-rich or mudrock-rich lithology probability volume model to control its lateral distribution. In the vertical direction, a traditional variogram was used to control vertical spatial distribution (Table D.3).

Table D.3 Detailed summary of maximum and minimum horizontal ranges and vertical ranges used in facies modeling as estimated from the McHale#1 facies log.

Zone	Faci-	Variogram	Maximum Range (ft)	Minimum Range (ft)	Vertical Range (ft)
1	Facies A	Spherical	500	500	1.1
	Facies B	N			
	Facies C	N			
	Facies D	Spherical	500	500	2.0
2	Facies A	Spherical	500	500	4.5
	Facies B	Spherical	500	500	8.3
	Facies C	Spherical	500	500	3.6
	Facies D	Spherical	500	500	4.9
3	Facies A	Spherical	500	500	7.7
	Facies B	Spherical	500	500	7.8
	Facies C	N			
	Facies D	Spherical	500	500	2.7
4	Facies A	Spherical	500	500	4.5
	Facies B	N			
	Facies C	Spherical	500	500	3.8
	Facies D	Spherical	500	500	3.4

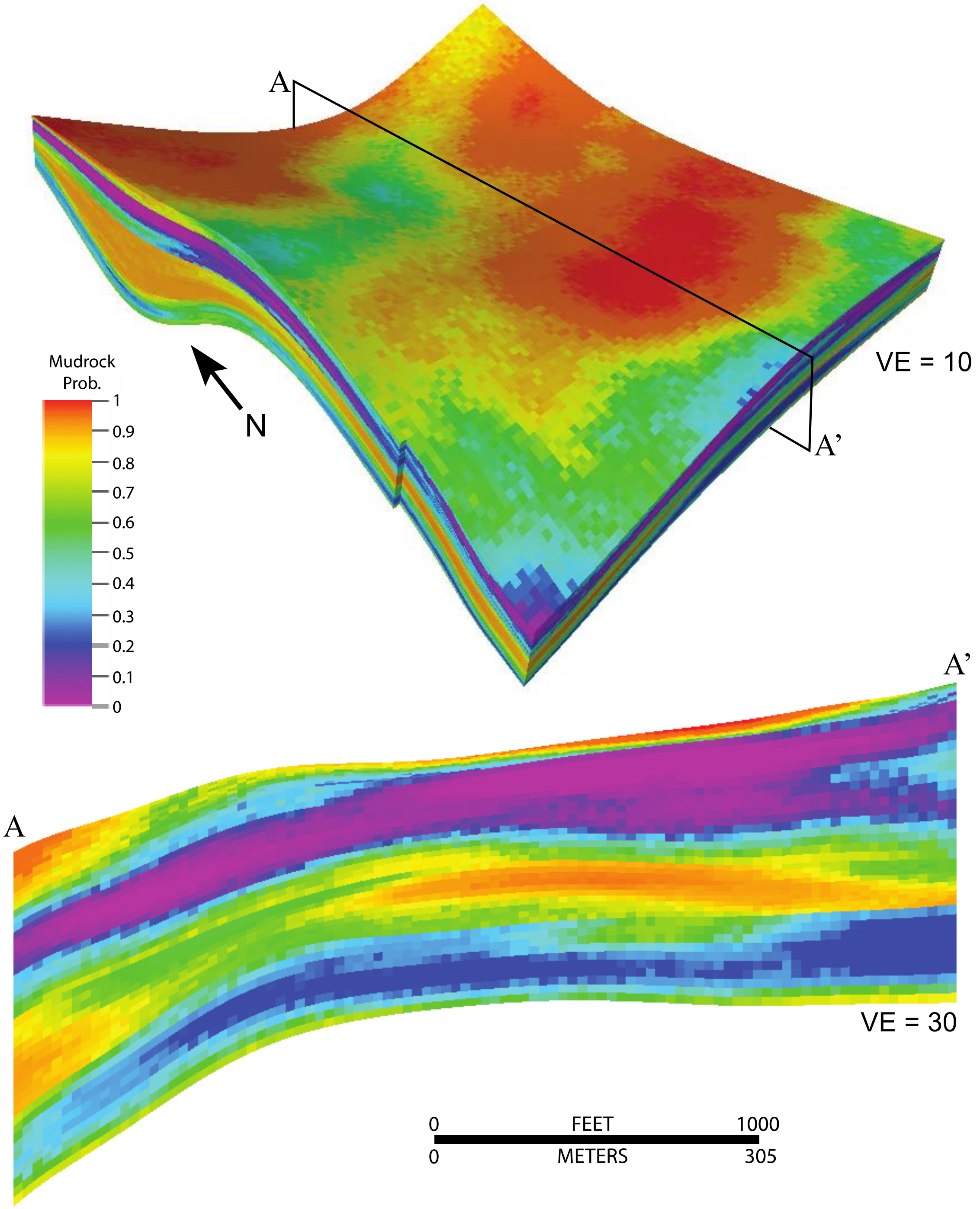

Fig. D.1. SP mud-rich facies volume probability model (SSMP) used to constrain wavy laminated sandstone facies distribution. Higher values indicate a higher probability of mud-rich facies.

Each facies variogram utilized a spherical variogram with major and minor ranges set of 500 ft (152.4 m) with no nugget. The vertical variogram was determined using the cored McHale #1 well with the vertical range set for each individual facies in each zone separately (Table D.3). All four facies were not present in each zone and are modeled accordingly.

The facies models were created using the sequential-Gaussian simulation (SGS) algorithm. This is a stochastic process based modeling technique that uses variograms and other geostatistics to spatially distribute the facies. Additionally SGS honors the original input data of facies so the percentage of facies in the entire model is the same or nearly the same as the numbers in the original McHale #1 facies log (Fig. D.2).

While variograms were used in this process, the lithology probability volume models were the primary control on the distribution. However, the variograms do affect distribution and are used to determine the level of heterogeneity within larger geobodies that are determined from the lithology probability volume models. Using this information, two types of facies models were created, a model that was derived from a single modeling attempt and a combination of thirty facies models in which thirty realizations are generated and, for a given cell, the facies that occurs most often in the thirty realizations is assigned to that cell. These are known in the study as the single facies model (SFM) and the average facies model (AFM). The AFM model was generated in an attempt at creating a modeling similar to one generated using a krigging algorithm. This particular model is preferred for this study as it generates a smoother distribution of facies throughout the model and does not appear as heterogeneous within a given facies body (Fig. 6.11). This was determined to be a more accurate model and is the only facies model used going forward. After observing what limited outcrop data that is available, the facies appear to be continuous at the scale greater than 10–30 ft (3.0–9.1 m). Outcrops were observed at Water Supply and Storage Reservoir Number 3 located 5.5 mi (8.9 km) north of Fort Collins, Colorado (Fig. D.3). Due to limited access and water levels, the upper portion of the Terry Formation was only observed from across a channel but continuous beds were visible.

Petrophysical Modeling

Porosity modeling was completed using the sequential indicator simulation (SIS) algorithm. Density-porosity logs were the primary input for the porosity modeling and are derived from eight of the nine wells in the model area. As mentioned previously, only density- porosity logs were used as there was a lack of other logs in which to substitute or combine with the density-porosity logs. The distribution of porosity in the entire model area generally matches what the original histogram of porosity values from the well logs indicates is in the model area (Fig. D.4). The same approach to facies modeling was applied to porosity modeling with respect to two different model types. A single porosity realization was generated along with an average of thirty porosity realizations. Each of these two types was biased towards the average facies model as porosity variations among reservoir zones and thus facies is observed in well-log data. Like facies modeling, variograms were also used to control the lateral and vertical variability and distribution (Table D.4) with the vertical variograms being determined from the McHale #1 well. Horizontal variograms used spherical variogram with a major and minor range of 250 ft (76 m) to help control spatial distribution.

Permeability modeling was completed after porosity modeling in a similar fashion by using the SIS algorithm. However, unlike the porosity models, only a single permeability log for the McHale #1 well exists within the model area. One solution to this problem would involve relating the permeability data to the porosity data with an equation and having porosity model control the distribution of the permeability data. However, due to the different measurement techniques (minipermeameter and well-log), the scale of investigation is dramatically different (several inches and several feet respectively) which causes no direct correlation between permeability and porosity or other well-log data (Fig. D.5). The solution to this problem used in this study is to use a bivariate transformation (cloud transformation) in order to link the permeability values to the porosity values despite the lack of correlation between the two. This method entails creating a porosity and permeability cross-plot and defining a series of bins based on the porosity values (Fig. D.6). These bins are then sampled and a cumulative frequency histogram is generated in which permeability values are linked to the porosity values. This cross-plot and bin data is then used to produce a permeability value for a cell based on the corresponding cell in the porosity model. As this study used two different permeability types (e.g., original and effective permeabilities), two cross-plots were generated (Fig. D.6). Like all previous models, for each permeability type there were two sets of model types created, a single permeability realization and an average of thirty permeability realizations. The thirty realizations tends to give a smoother distribution of permeabilities that grade into higher or lower values and are not as random. Due to the lack of data determining which distribution is correct in the permeability models, all four permeabilities models were explored for static connectivity to determine how upscaling of permeability might affect reservoir modeling.

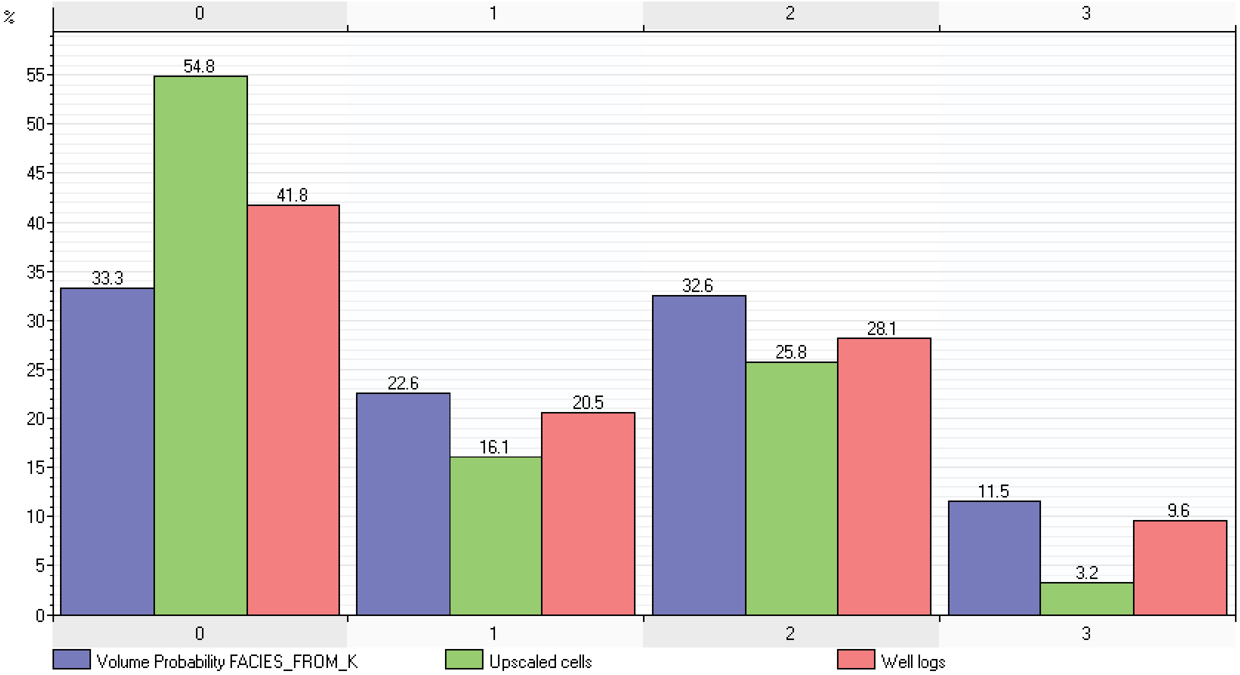

Fig. D.2. Facies histogram showing the percentage of facies from the McHale #1 core (red), upscaled model cells (green), and the entire facies model (purple). The relative percentages of each facies is approximately the same throughout the entire modeling process as the facies log on the McHale #1 well is upscaled and then modeled across the entire area.

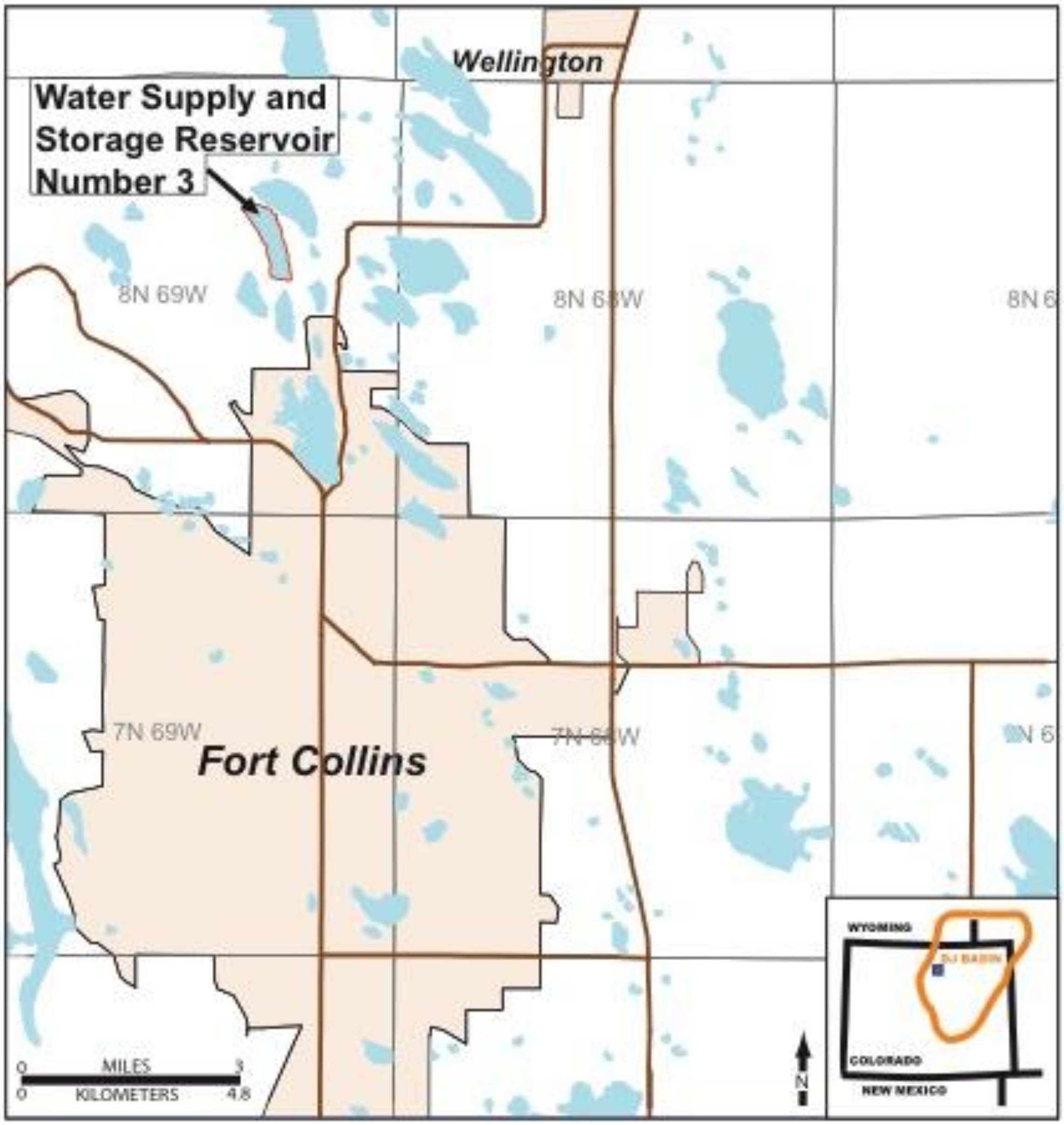

Fig. D.3. Map showing Water Supply and Storage Reservoir Number 3 (outlined in red) located 5.5 mi (8.9 km) north of Fort Collins, Colorado. Location shown on inset map. Terry outcrop is located on the northeast corner of the lake along a diversion channel.

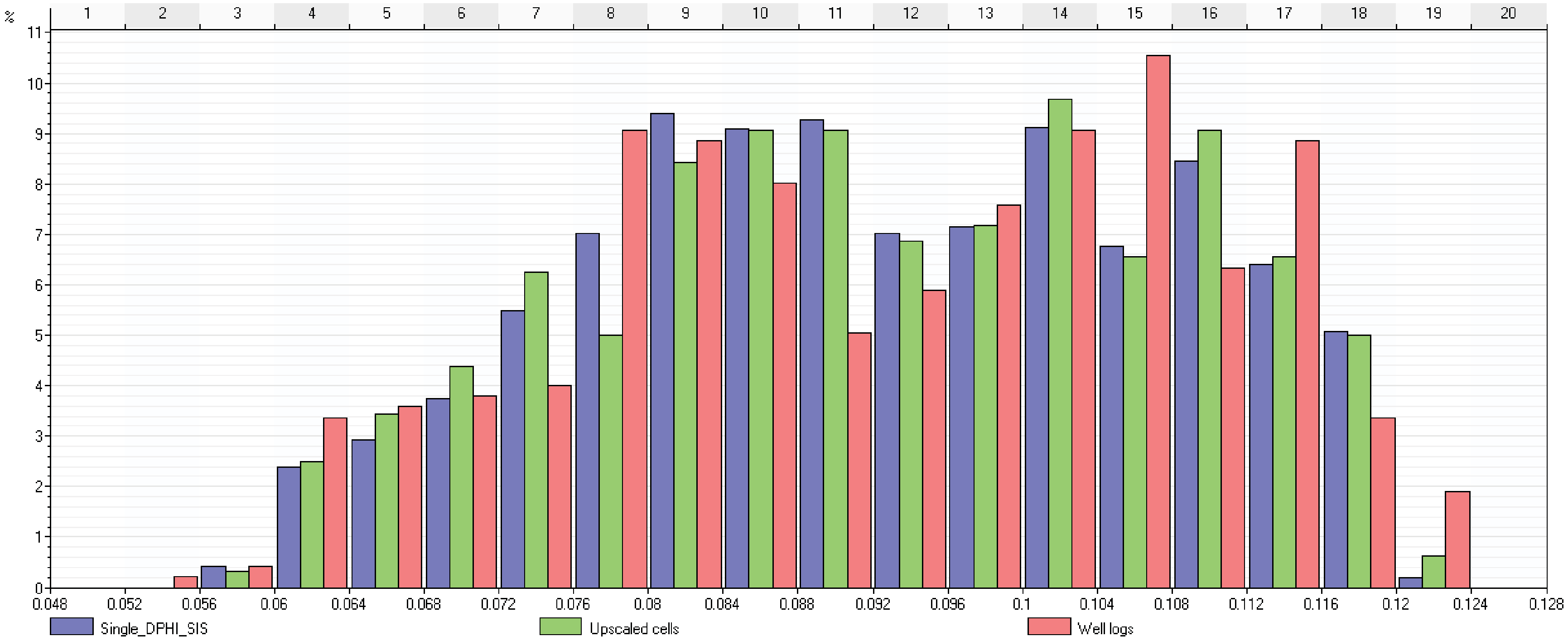

Fig. D.4. Porosity histogram showing the range of porosity values in well logs, upscaled cells (well logs), and all model cells. The distribution for all three is nearly identical with both the upscaled cells and the model cells honoring the input data. Porosity values on the x-axis are measured in decimals.

Table D.4. Detailed summary of maximum and minimum horizontal ranges and vertical ranges used in porosity modeling as estimated from density porosity logs.

Zone	**Facies**	**Variogram Model**	**Maximum Range (ft)**	**Minimum Range (ft)**	**Vertical Range (ft)**
1	Facies A	Spherical	250	250	1.3
	Facies B	N/A			
	Facies C	N/A			
	Facies D	Spherical	250	250	2.0
2	Facies A	Spherical	250	250	7.3
	Facies B	Spherical	250	250	4.8
	Facies C	Spherical	250	250	1.3
	Facies D	Spherical	250	250	4.2
3	Facies A	Spherical	250	250	7.1
	Facies B	Spherical	250	250	3.3
	Facies C	N/A			
	Facies D	Spherical	250	250	1.6
4	Facies A	Spherical	250	250	5.4
	Facies B	N/A			
	Facies C	Spherical	250	250	6.0
	Facies D	Spherical	250	250	0.6

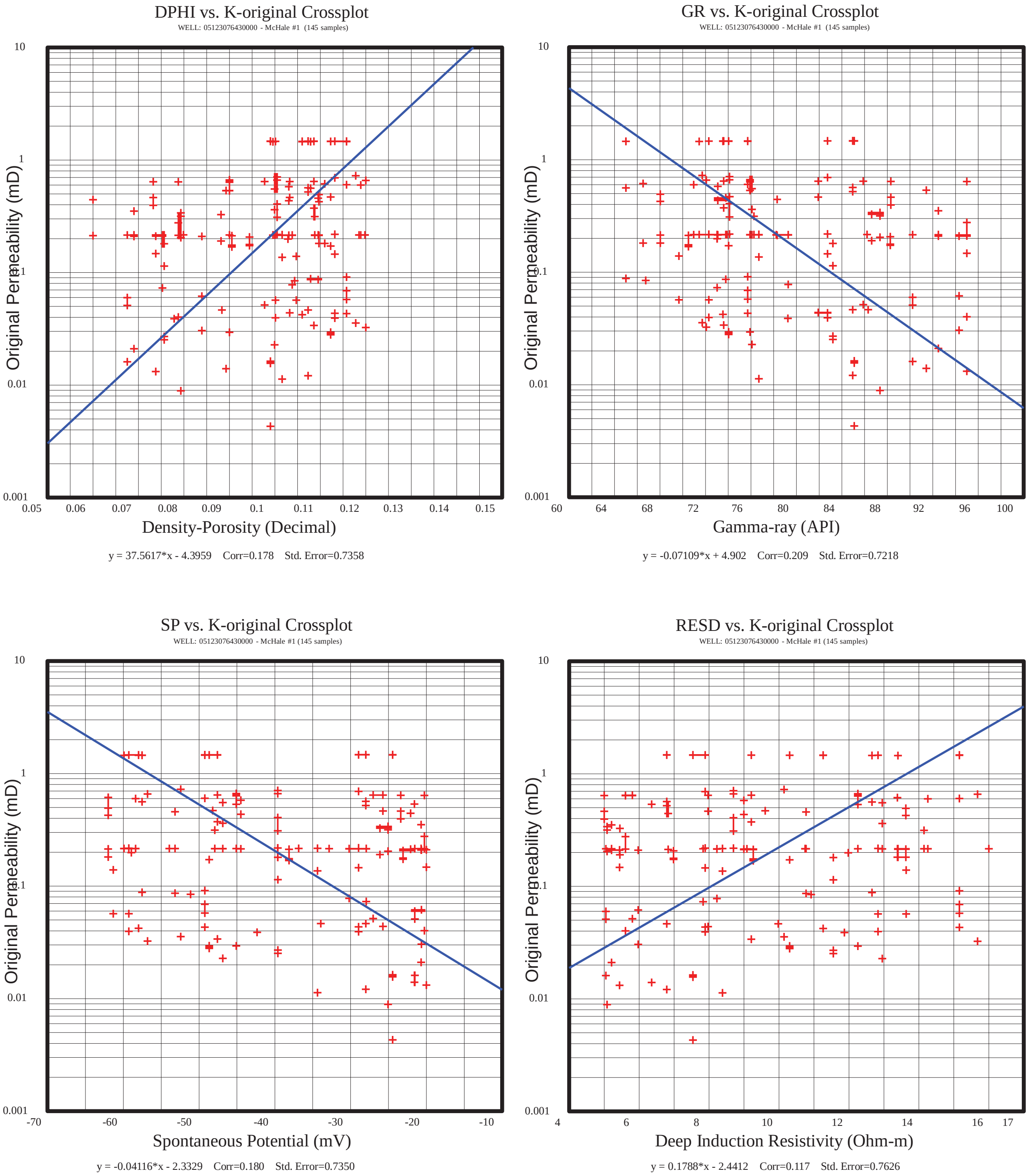

Fig. D.5. Well log crossplots showing the lack of a relationship between original permeabiilty and well log measured properties. Due to the lack of a correlation between these properties, a cloud transformation was used to create a control on permeability distribution in wells not containing measured permeabilities. Blue line=line of best fit, equation displayed below each graph.

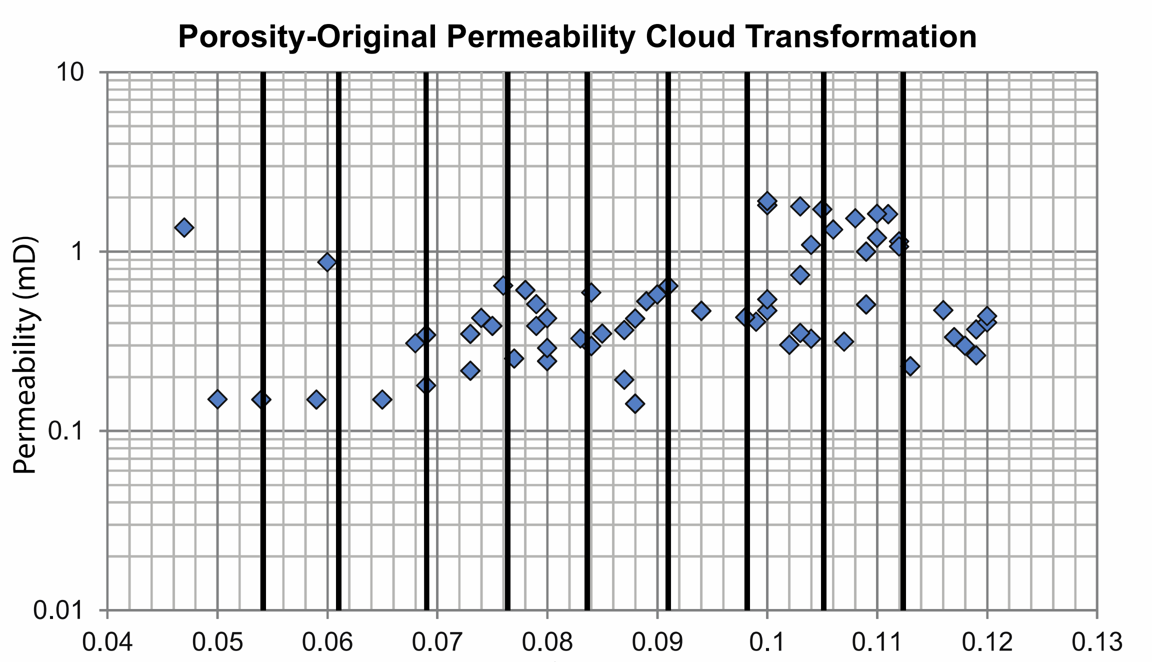

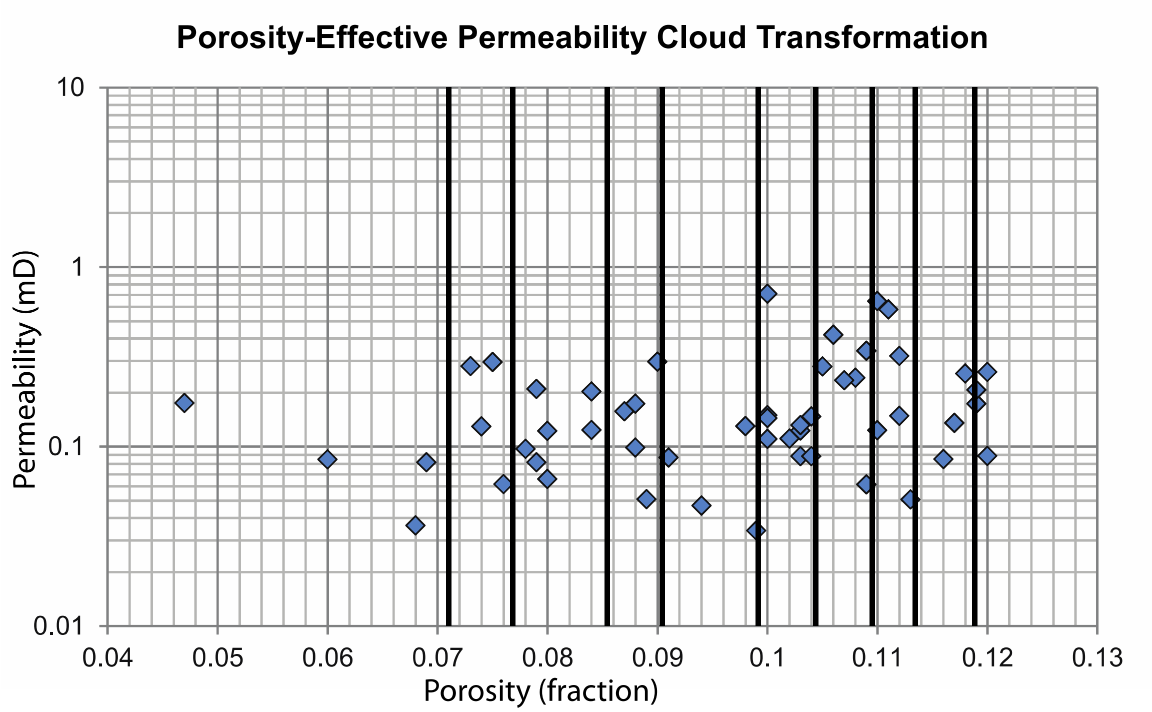

Figure D.6. Porosity-permeability crossplots used to create a cloud transformation (bivariate transformation) to link permeability models to porosity models. Dark black lines indicate bins used for transformation.

Appendix E

Static Connectivity

Static Connectivity Model Area

Static connectivity to a wellbore is used in this study to compare how reservoirs are affected by using effective-permeabilities derived from flow-based upscaling techniques and by using unaltered original-permeability measurements. To start the comparison, pseudowells were added to the model area and the model area was reduced in size (Fig. 6.2). The model size was reduced in an effort to eliminate or reduce potential errors associated with edge-effects created during the previous modeling steps for facies, porosity, and permeability. The outside area of each of these models was filtered out such that cells between the original model boundary and the static connectivity boundary are not considered for static connectivity analysis. Additionally, 20 wells were added that penetrated the entire model in a regular 5-ac (2-hectacre) space (known as pseudowells). These wells were added and used for the static connectivity analysis as there are only a few wells that penetrated the smaller area. Additionally, the regularly spaced wells offer an analogous relationship to current drilling patterns around the world in which equally spaced wells are being drilled.

Static connectivity in this study is determined by applying a porosity and permeability cutoff for a given model to determine what a reservoir cell would be. These reservoir cells are then analyzed for their spatial arrangement and a determination is made as to whether or not they are connected either directly (touching the wellbore) or indirectly (touch other cells which touch a wellbore) (Table E.1). The connectivity is reported as a bulk volume for the connected cells. This volume is then compared with the total model bulk volume and a percentage of connectivity is determined. This was done for each of the four permeability models. Each permeability model was evaluated with the corresponding porosity model that was used to create the permeability model through the cloud transformation.

Additionally, the bulk volume of reservoir cells was determined and evaluated for all the permeability models (Table E.2). This was done to determine how many of the total reservoir cells in the model are connected to a wellbore at a given permeability cutoff. At the lower cutoffs in which the permeability value is below about 1.0mD, all of the potential reservoir cells that could be connected are connected. This is likely caused by the dense well spacing of the pseudowells in the model area, which likely penetrate each dense body of reservoir cells. As each petrophysical property model is biased towards the facies model, which shows distinct groupings of reservoir facies (facies consisting mostly of sandstone with higher porosities relative to mudrock-rich facies), the cells that are likely to be defined as reservoir cells would also occur in these groupings. As the permeability cutoff value is increased however, differences do appear between the bulk reservoir cell volume and connected reservoir bulk volume (Fig. E.1). This is due to the constraints being tightened which leaves individual cells unable to be connected to a reservoir cell.

Pore volume was also evaluated in a similar way to bulk reservoir volume. A pore volume model was first created by taking the average porosity model and combining it with the bulk volume model. The resulting model had the pore volume for each cell based on the porosity that was modeled. The total pore volume was then calculated for each reservoir definition previously discussed (porosity >8.75% and a variable permeability variable). The results were then compared to the total pore volume with no restrictions by dividing the pore volume at a given reservoir definition and dividing it by the total pore volume and multiplying by 100. This is then a percentage of total model pore volume (Table E.3).

Table E.1. Static Connectivity results from all permeability models.

Effective Permeability Models

K cutoffs	**SIS Single**	**SIS Average**	**Bulk Model**	**Connectivity**	
(md)	**(ft^3)**			**(Single Φ Model)**	**(Avg. Φ Model)**
0	52248992	66518436	83615056	62.49%	79.55%
0.15	15797639	9521457	83615056	18.89%	11.39%
0.3	4164627	130404	83615056	4.98%	0.16%
0.45	38668	15275	83615056	0.05%	0.02%
0.6	11797	7552	83615056	0.01%	0.01%
0.75	502	1004	83615056	0.00%	0.00%
0.9	0	502	83615056	0.00%	0.00%
1.05	0	0	83615056	0.00%	0.00%
1.2	0	0	83615056	0.00%	0.00%
1.35	0	0	83615056	0.00%	0.00%
1.5	0	0	83615056	0.00%	0.00%
1.65	0	0	83615056	0.00%	0.00%
1.8	0	0	83615056	0.00%	0.00%
1.95	0	0	83615056	0.00%	0.00%

Original Permeability Models

K cutoffs	**SIS Single**	**SIS Average**	**Bulk Model**	**Connectivity**	
(md)	**(ft^3)**			**(Single Φ Model)**	**(Avg. Φ Model)**
0	52248992	66518436	83615056	62.49%	79.55%
0.15	52248992	66518436	83615056	62.49%	79.55%
0.3	47819652	49079060	83615056	57.19%	58.70%
0.45	28203824	27510206	83615056	33.73%	32.90%
0.6	7076063	13199585	83615056	8.46%	15.79%
0.75	3744301	7370615	83615056	4.48%	8.81%
0.9	3390688	6777145	83615056	4.06%	8.11%
1.05	2679715	6049038	83615056	3.20%	7.23%
1.2	1794726	4977874	83615056	2.15%	5.95%
1.35	1167196	4507737	83615056	1.40%	5.39%
1.5	480240	4077384	83615056	0.57%	4.88%
1.65	22458	3539519	83615056	0.03%	4.23%
1.8	3758	1163983	83615056	0.00%	1.39%
1.95	502	502	83615056	0.00%	0.00%

Table E.2. Bulk volumes for reservoir criteria in the entire model area.

Effective Permeability Models

K cutoffs	SIS Single	SIS Average	Bulk Model	Percent of Total Model	
(md)	(ft^3)			(Single Φ Model)	(Avg. Φ Model)
0	52248992	66518436	83615056	62.49%	79.55%
0.15	15797639	11146096	83615056	18.89%	13.33%
0.3	4164627	135081	83615056	4.98%	0.16%
0.45	1691031	16294	83615056	2.02%	0.02%
0.6	723675	8058	83615056	0.87%	0.01%
0.75	1004	1004	83615056	0.00%	0.00%
0.9	502	502	83615056	0.00%	0.00%
1.05	0	0	83615056	0.00%	0.00%
1.2	0	0	83615056	0.00%	0.00%
1.35	0	0	83615056	0.00%	0.00%
1.5	0	0	83615056	0.00%	0.00%
1.65	0	0	83615056	0.00%	0.00%
1.8	0	0	83615056	0.00%	0.00%
1.95	0	0	83615056	0.00%	0.00%

Original Permeability Models

K cutoffs	SIS Single	SIS Average	Bulk Model	Percent of Total Model	
(md)	(ft^3)			(Single Φ Model)	(Avg. Φ Model)
0	52248992	66518436	83615056	62.49%	79.55%
0.15	52248992	66518436	83615056	62.49%	79.55%
0.3	47819652	63010816	83615056	57.19%	75.36%
0.45	28203824	35008020	83615056	33.73%	41.87%
0.6	14249642	15109075	83615056	17.04%	18.07%
0.75	8857820	8311898	83615056	10.59%	9.94%
0.9	8362829	7629447	83615056	10.00%	9.12%
1.05	7344968	6806986	83615056	8.78%	8.14%
1.2	4746485	5614799	83615056	5.68%	6.72%
1.35	3769438	5083262	83615056	4.51%	6.08%
1.5	3018834	4606231	83615056	3.61%	5.51%
1.65	1545343	4013858	83615056	1.85%	4.80%
1.8	490346	1294235	83615056	0.59%	1.55%
1.95	502	502	83615056	0.00%	0.00%

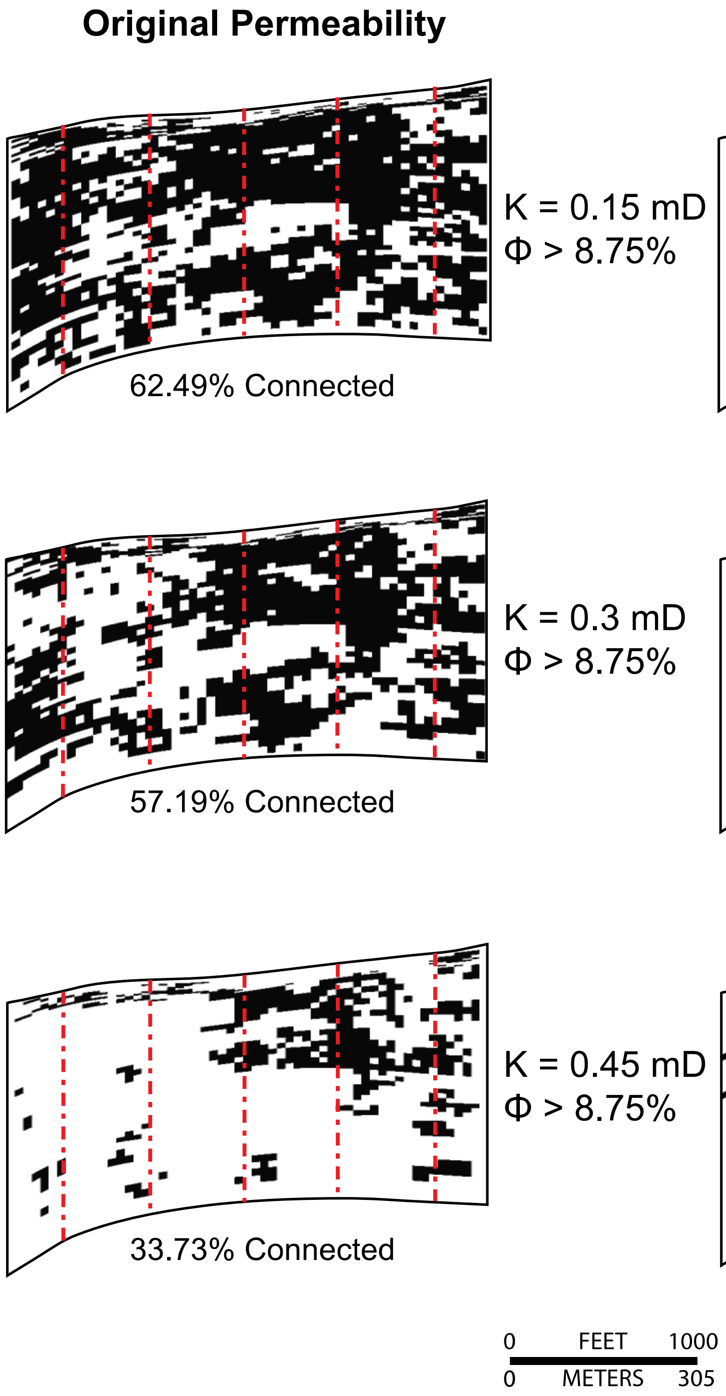

Fig. E.1. Bulk reservoir volume (expressed as percentage of bulk module volume) comparison in cross-sectional view (I=54) of single porosity referenced original- and effective-permeability models. This view shows how many cells in the given plane fit the criteria to be called a reservoir cell. Cross-sectional plane is shown in figure 6.13 and is consistent with all model cross-sections. Red lines indicate wellbores. VE = 30x

Table E.3. Pore volumes for reservoir criteria in the entire model area.

Effective Permeability Models

K cutoffs	SIS Single	SIS Average	Bulk Model	Percent of Total Model	
(md)	(ft^3)			(Single Φ Model)	(Avg. Φ Model)
0	6386043	6386043	7806366	81.81%	81.81%
0.15	6386043	6386043	7806366	81.81%	81.81%
0.3	5480185	6382369	7806366	70.20%	81.76%
0.45	5480185	5052751	7806366	70.20%	64.73%
0.6	1459267	1827075	7806366	18.69%	23.40%
0.75	846421	1631020	7806366	10.84%	20.89%
0.9	798681	912128	7806366	10.23%	11.68%
1.05	700767	256549	7806366	8.98%	3.29%
1.2	468275	58443	7806366	6.00%	0.75%
1.35	371963	18761	7806366	4.76%	0.24%
1.5	298492	4819	7806366	3.82%	0.06%
1.65	153111	1713	7806366	1.96%	0.02%
1.8	48844	311	7806366	0.63%	0.00%
1.95	50	50	7806366	0.00%	0.00%

Original Permeability Models

K cutoffs	SIS Single	SIS Average	Bulk Model	Percent of Total Model	
(md)	(ft^3)			(Single Φ Model)	(Avg. Φ Model)
0	6386043	6386043	7806366	81.81%	81.81%
0.15	1872139	1122054	7806366	23.98%	14.37%
0.3	368589	14210	7806366	4.72%	0.18%
0.45	160904	1688	7806366	2.06%	0.02%
0.6	72174	832	7806366	0.92%	0.01%
0.75	104	104	7806366	0.00%	0.00%
0.9	50	50	7806366	0.00%	0.00%
1.05	0	0	7806366	0.00%	0.00%
1.2	0	0	7806366	0.00%	0.00%
1.35	0	0	7806366	0.00%	0.00%
1.5	0	0	7806366	0.00%	0.00%
1.65	0	0	7806366	0.00%	0.00%
1.8	0	0	7806366	0.00%	0.00%
1.95	0	0	7806366	0.00%	0.00%

Task 7. Regulatory Regimes and Enforcement Structures

7.1. Goals/Objectives

The goals of this task were to evaluate the current legal framework for CO_2 storage on public lands across the western US.

7.2. Background

Based on the findings from the research conducted on pooling and unitization as a means of aggregating land to facilitate carbon capture and sequestration (CCS) projects, we were led to the ultimate conclusion that there is a strong argument that the federal government owns over 70 million acres of pore space in the West underlying lands granted under the Stock Raising Homestead Act of 1916 (SRHA). Initially, we contacted a number of "landmen," which are people who conduct title searches for all of the relevant land interests for a given oil or gas project. We learned how these landmen went about discerning every possible interest owner, for both the surface and subsurface, for every parcel that would be affected by the project. This information was supported through discussions with oil and gas specialists at the Energy, Utility & Environment Conference in February of 2011 and led us to our present conclusions about CCS transaction costs and the need for a single owner of pore space.

To cultivate our theory, we frequently used online legal databases, particularly Westlaw and LexisNexis, to research relevant case law pertaining to the SRHA and its application to subsurface resource ownership. Furthermore, we utilized Google Scholar, as well as engineering and earth science encyclopedias and textbooks, to reinforce the details of our argument. Finally, we contacted a number of Bureau of Land Management employees to better understand the intricacies of the SRHA and the ways in which the statute functions within the United States' public land scheme.

7.3. Methods/Approach

The materials used for the research include law review articles, books, textbooks, and websites pertaining to CCS and pore space ownership, as well as phone and email interviews with county clerks, landmen, employees with the BLM, and a public land expert. The materials utilized ultimately account for over 150 citations in our pore space law review article that is presently in the final stages of editing prior to submission.

7.4. Task Results

We initially considered the feasibility of using pooling and unitization as a scheme for regulatory siting for CCS. Pooling in the context of oil and gas law is the aggregation of parcels of land to achieve a predetermined number of acres on which only one well needs to be placed. Doing so reduces waste, promotes efficiency, and protects correlative rights. This issue appears to be the most significant, as a major aspect of this research focused on determining the ease and practicability of ascertaining every relevant interest for a tract of land. What we discovered is that for each parcel, there could be anywhere from one to dozens of interests, all of which must be ascertained in order to proceed with pooling every interest for a CCS site. Furthermore, determining the mineral interest for a single parcel proved to be extremely difficult and time-consuming. Thus, to aggregate every interest for a CCS site, the process would not only be incredibly protracted but inexplicably complex.

We then explored possible solutions to the issue of aggregating thousands of parcels of land. We considered the possibility of there being one owner for all of the land parcels; it follows that there would only be one owner of the pore space underlying all of these parcels, whereby circumnavigating the necessity of tracking down the owners of each parcel and committing them to the unitization scheme. We then considered the feasibility of the government owning the pore space regardless of who owned the surface of the lands above it. This turned our research to public land conveyances and the ways in which the government might have reserved to itself ownership of the pore space.

Eventually, this led us to an examination of the SRHA, which is a federal land conveyance statute that granted tracts of public land to private homesteaders while reserving to itself all of the minerals and subsurface resources underlying these tracts. Therefore, there is a strong argument that the government owns the pore space underlying lands conveyed from the SRHA, which could account for over 70 million acres in the West.

As an initial matter, we thoroughly examined the history of land grant statutes and the political climate surrounding them. We described how the evolution of homestead laws culminated with the SRHA, which uniquely reserved all the subsurface resources to the federal government, thereby breaking from the tradition of reserving only those minerals that were expressly enumerated.

Next, we turned to case law that analyzed the language of the SRHA to determine if a nexus exists between SRHA interpretations of subsurface resource ownership and pore space. The Supreme Court handed down the leading case analyzing the SRHA and subsurface ownership, Watt v. Western Nuclear, in 1983. There, the Court determined that gravel found on lands patented under the SRHA is a mineral reserved to the U.S. government. For the surface owner, the Court reasoned, the SRHA conveyed land for the purposes of stock raising and raising forage crops. Thus, Congress could not have intended to convey the right to extract gravel to the surface owner, as doing so does nothing to facilitate that purpose. Additionally, the Court employed an often-cited canon of statutory construction, which states that "land grants are construed favorably to the Government…and that if there are doubts they are resolved for the Government, not against it."

Significantly, the Supreme Court established a four-part test to determine which minerals fall within the SRHA reservation. Under the Watt test, the SRHA mineral reservation includes substances that are mineral in character (i.e., inorganic), that can be removed from the soil, that can be used for commercial purpose, and that there is no reason to suppose were intended to be included in the surface estate.

In order to determine whether pore space—specifically, the matrices that make up pore space—falls within the scope of the SRHA mineral reservation while comporting with relevant case law, we determined that the most appropriate judicial standard to employ comes from Watt. Because pore space ownership is a novel concept, federal and state jurisprudence has never specifically addressed pore space in this manner. Since the Watt test functions as the leading analysis for subsurface resources in the context of land grant statutes, it presently serves as the most suitable standard for establishing pore space ownership under the SRHA. For this reason, we analyzed pore space and the matrices that create it by applying the Watt test's four elements.

From here, we concluded that pore space, as a compilation of void and mineral with commercial value in 1916, easily meets the first and third prongs of the Watt test. The fourth prong is similarly satisfied, as Congress could not have possibly conceived of granting pore space to the surface owner when it enacted the SRHA nearly a century ago. An issue exists, however, with the second prong, as pore space is not conceptually removable from below the ground, or at least serves no commercial function for CCS should it be removed. Yet in spite of this weakness, we ultimately concluded that the arguments supporting the notion that pore space falls within the gambit of the SRHA's mineral reservation far outweigh this minor obstacle, particularly considering the fact that pore space ownership is a novel concept in United States jurisprudence.

The article ends with a discussion of the implications of our findings for the practicability of CCS—from a regulatory standpoint—in the United States. Ultimately, we determined that federal ownership of the pore space underlying SRHA land would serve to drastically reduce the transaction costs associated with a pooling and unitization scheme for CCS. We note, however, that federal ownership of pore space does not necessarily result in the effortless deployment of CCS projects, as the government tends to be risk-adverse, particularly for novel projects that are plagued with scientific and social uncertainty.

Summary and Conclusions

Task 1. Project management and planning

Management of this multi-task project was established in accordance with principles that seem to serve scientific inquiry well. The most fundamental one is to ensure that development of new theory, testing and observation is incrementally adding new insights to prior research. Each investigator, therefore, built these studies on a comprehensive background of prior published work, a fact that is reflected well in the many citations in each chapter. In addition, to ensure close communication between investigative teams and to exchange ideas and results frequently, many formal and informal workshops between the parties were conducted during the project. At least once a year, the team held a formal review attended by staff from the Pittsburgh NETL Laboratory, colleagues at the Colorado School of Mines, and invited industry participants.

The graduate students engaged in this project not only performed the majority of the real research work in the laboratory, field settings and modeling work, but they were also instrumental in organizing oral and poster technical seminars and meetings with other students, faculty and external industrial and governmental visitors. The number of people exposed to, and therefore indirectly contributing to, the project's success over these several years exceeded one hundred. Abstract booklets for the student-organized workshops are available on request.

Flow of CO_2, natural gas, oil and water in sandstone reservoirs occurs in a complex interplay of pathways from rock matrix to wellbore via connected pores as well as natural and artificially induced fractures. In subsurface reservoir rocks, the natural architecture of porosity and permeability, the structural and stratigraphic paths for fast flow alternating with seals, and the connectivity of fluid pathways from reservoir to well bore between sand bodies of different size, shape, packing and orientation all affect fluid flow rates and ultimate paths to CO_2 storage.

Because of all these complexities that control the flow of CO_2 and the associated natural gas, oil and water in reservoirs, no single technology or scientific discipline can alone guide operations related to CO_2 storage. Only an integrated workflow combining insights from geomechanics, pore scale science, geomicrobiology, and pore volume connectivity to wells can stand a chance of realistically capturing the complexity of flow in such systems. For that very reason, we assembled this broad team of researchers with experiences ranging from theory, through lab experiments and field work and practical oil and gas field applications to help develop new science principles to guide injection and long-term storage of CO_2 in the subsurface. For the CCUS industry to grow in the market place and public acceptance, it is equally important to also understand and be able to communicate the socio-economic risks, public perception and subsurface pore space ownership issues; all of which are also explicitly addressed in this report.

All research tasks explicitly included assessments of the technology status prior to commencement of new analysis, modeling and experimental work. This is normal operating procedure in most academic research, but it is taking on added significance in today's highly diverse and dispersed global research culture.

In addition to explicit review or assessment of prior technology, what has been equally important to the success of this project is the culture of open exchange of data and insights between scientists and engineers in several universities, other research organizations and consulting companies. Regular meetings of project PIs and their students during annual reviews at NETL in Pittsburgh were also of great value.

Task 2. Geomechanics of CO_2 storage reservoirs applied to saline storage

In the quest to better understand the geomechanics of CO_2 storage reservoirs, this task addressed three objectives. These were: 1) the development of a high pressure and high temperature triaxial core testing system simulating geological CO_2 sequestration at reservoir conditions, 2) the development of a model of stress-dependent wave velocity response of micro and macro-fractured porous rocks, and 3) the hydro-mechanical characterization of porous reservoir rocks at reservoir conditions.

To address these objectives, the team built a high temperature rock core testing system designed to simulate CO_2 injection in fractured porous rock samples. The goal was to use the system to study the effects of effective stress and fluid content on ultrasonic wave velocity responses of porous rock samples. The team also pursued research on the permeability of porous rock samples in the presence of two-phase fluid flow of saline water and supercritical CO_2 as well as the stress dependency of permeability of the porous rock. The third component of this research task was to develop a model for the stress-dependent elastic wave velocity response of fractured rock mass that would take into account parameters with clear physical meanings. The primary outcome of this research task was a new model for stress-dependent fracture-normal and shear stiffness. Based on the visual observation of thin sections of the Berea sandstone cores tested in this project, the microstructure of the rock mass body is idealized as an elastic matrix in which sufficiently small-scale fractures are distributed randomly. The normal stiffness of fractures dependent on effective stress is formulated as a generalized Goodman's model. The stress dependency of fracture shear stiffness is assumed to be given by a linear function.

Research in this task also included laboratory studies of CO_2 injection in specimens of fractured reservoir rocks (simulating actual storage field conditions) to provide input data to numerical models and as small-scale validation models of CO_2 injection in porous/fractured rocks under realistic geological sequestration conditions. During testing, changes in velocities of both p- and s-waves of the fractured rock samples were measured using seismic monitors installed at the ends of the sample. The aim was to determine whether changes in seismic wave velocities can be used to detect movements of CO_2 in fractured rock samples. The relative permeability of porous rocks for saline water as well as CO_2 at reservoir conditions was also determined.

One major and long-lasting benefit of this research task was the building of a new high pressure and high temperature triaxial core testing system, capable of characterizing micro- and/or macro-fractured porous rock samples in terms of permeability, relative permeability, and ultrasonic wave velocity responses. The triaxial core holder can apply up to 70 MPa of cell pressures at temperatures up to 150 ºC. The ultrasonic wave velocity measurement devices built into the system enable testing of the ultrasonic wave response change of rock samples due to changes in CO_2 saturation and effective stress.

What is arguably the most significant result of this project task on the geomechanics of CO_2 storage is the conclusion that seismic survey data can quite accurately be used for quantitative determination of concentration, distribution and movement of CO_2 in subsurface reservoirs. This is quite a step forward from the skepticism of about a decade ago, when there were serious questions about whether reflection seismic data could even detect the presence of CO_2.

Task 3. Nanometer to micrometer-scale pore network structure in fine-grained caprocks and geochemical response in high CO_2 environments

This task complements the prior one with its focus on caprocks rather than the storage reservoir itself. The research questions were related, however, because the integrity of a reservoir's seals is arguably even more critical to the deployment of a subsurface CO_2 storage industry than the properties of the reservoir itself. Therefore, the research in Task 3 focused on the geochemical and mineralogical effects on caprock integrity as a consequence of CO_2 injection and storage.

Advanced laboratory techniques including small-angle neutron scattering, electron imaging, gas adsorption and mercury porosimetry were all applied in these investigations. The analyses revealed that nanometer-scale pores contribute up to 50% of pore volume in some seal rocks. Two of the tested sets of marine shale samples demonstrated the occurrence of both mineral dissolution and precipitation in response to flooding with CO_2 brines, and this altered the pore networks. Also, the connectivity between these pores was found to decrease with total organic carbon contents of the rocks, whereas the opposite was the case for overall pore volume.

The mineralogy of the sealing rocks also plays a significant role. Specifically, this research demonstrated that silica-rich shales typically had larger initial pores and smaller pore throats and experienced decreased pore connectivity with CO_2 flooding. In contrast, the carbonate-rich shales typically had smaller initial pore size but bigger pore throats and typically increased pore connectivity with CO_2 flooding. It is important to keep in mind, however, that the changes observed in these experiments reflect the very short time scales of laboratory experiments only. Much more advanced modeling needs to be brought to bear on the problem in order to predict the geochemical and mineralogical changes that might occur in large-scale, permanent subsurface CO_2 storage sites. Much additional work needs to be done to evaluate pore network effects, and hence seal integrity, at potential future large-scale and long-term carbon sequestration sites.

Over such long time scales, the dissolution of CO_2 into pore fluids of caprock formations may create additional carbonic acid, reduce pH, and induce a state of geochemical disequilibrium. Resulting mineral dissolution and precipitation may alter the shape and size of small pores and pore throats, thus changing the structure of the pore network and impacting effective porosity, surface area, and pore size distribution. To predict long-term performance of CO_2 sequestration sites we need to not only understand the distribution and connectivity of pores in caprocks but also their geochemical response to CO_2 injection and the potential impacts on caprock integrity.

Task 4. Geomicrobiological influence on carbon storage and conversion applied to saline reservoir storage

Saline aquifers, depleted oil reservoirs, basalt aquifers as well as deep, unmineable coal seams are all considered potential targets for carbon capture, utilization, and sequestration. All these types of subsurface reservoirs also harbor diverse and active microbial communities. Therefore, understanding the potential impacts of CO_2 injection on these microbes is critical for predicting the long-term fate of the injected carbon. In addition, there is a strong economic interest in better understanding the impacts of CO_2 injection on coal bed microbial communities because of the growing production of coal-bed methane (CBM) in the United States and elsewhere. Several highly-productive basins in the continental United States are known to produce gas of biogenic origin, including the Powder River Basin (WY), the San Juan Basin (NM/CO), the Raton Basin (CO), and the Black Warrior Basin (AL). Previous studies have demonstrated the potential for either native microbes or coal samples inoculated with specialized consortia to produce methane under laboratory conditions, and a much deeper understanding of the related bio-geochemical processes is required.

To advance the understanding of these interconnected issues, the research team for this task analyzed bacterial cell membrane phospholipids, which target living microorganisms, in ground waters from two field sites where CO_2 injection had either occurred or were targeted for injection, as well as from laboratory microcosm experiments. The field sampling was designed to sample ground water wells before and after CO_2 injection in order to assess the effects on the native microbial communities. The lab experiments utilized a coal-degrading microbial consortium under varying partial pressure conditions of CO_2. A second major objective of this study was to understand the effects of changing p CO_2 on coal-metabolizing and methanogenic microbial consortia incubated in the laboratory. Thirdly, the team sought to understand what effect urea amendments might have on the methanogenic microbial community, as urea can buffer the effects of decreased pH resulting from CO_2 injections and serve as a readily available nutrient for a N-limited microbial community.

The research included in this project did find evidence for active methanogenesis even in quite acidic waters (pH ~ 3) and that acid-tolerant methanogens occur in acidic peat bogs. Yet, lower pH may inhibit H_2-consuming processes and therefore even modest changes in the partial pressure of CO_2 in a storage reservoir could have important implications for methanogenesis in coal-bearing strata.

Urea amendments may buffer the effects of decreasing pH that comes from CO_2 injections. The research conducted as part of this project was partly motivated by the thorough investigations on the effects of urea amendments on the methane flux from agricultural soils, particularly in rice paddies. There, urea amendments stimulate increased methane production. In contrast, in CO_2 storage reservoirs, this study finds that urea my stimulate biomineralization and therefore mineral trapping as a consequence of the pH increase accompanying urea hydrolysis.

Task 5. Making fossil energy more sustainable: technology pathways and conflict reduction

This task was redirected due to the departure (for family reasons) of the co-investigator that was originally assigned to examine the stratigraphy-specific CO_2 storage options in Colorado's Denver Julesburg Basin. The redirected research focused more broadly on the dual challenges of managing CO_2 emissions as well as co-produced water associated with the continued production of fossil fuels. Some aspects of CO_2 storage in the Denver Julesburg Basin were still addressed in this overall project and reported on in Task 6.

There is evidence that society is moving towards the development of more sustainable pathways for the use of fossil energy. This is demonstrated in the shift from coal to natural gas as the fuel of choice for electric power generation across the US, and the much more sustainable approach to management of both surface and groundwater. The US is currently the only major nation in the world where power-related CO_2 emissions are decreasing. In addition, over the past few years there has also been an emerging focus on reducing the emissions of methane, primarily from an aging industrial transportation and distribution infrastructure. Developing a cost-effective approach to reduce the rate of atmospheric build-up of both of these two dominant greenhouse gases requires significant advances both in storage technologies, infrastructure and energy systems management.

The management of the co-produced water is the third leg of this stool for sound technology to support a sustainable global fossil energy industry. For that reason, Task 5 of this particular report examined specifically the key issues around CO_2 emissions and release of water that is co-produced with oil and gas extraction. The important point being made is that significant advancements in geomechanics (Ch. 2), mirco- and nano-scale permeability (Ch. 3), mineralogical and organic geochemical reactions in the subsurface (Ch. 4), storage-reservoir geological properties and patterns of connectivity (Ch. 6) and the legal and economic challenges facing businesses operating in the subsurface (Ch. 7), are critical for the extraction or injection of fluids of all kinds. This long report, presenting a lot of in-depth new research on all these issues, therefore, should be seen not as a study just focused on CO_2 storage science, but as a document trying to highlight the 'foundational issues' behind the future use of the subsurface in globally sustainable energy systems.

Task 6. Assessment of scale on pore-volume and permeability estimates for geologic storage of CO_2 in saline aquifers

Reservoir "heterogeneity", that is. the spatial patterns of distribution of minerals and the open 'void' space between them, is generally predictable in a statistical sense because it reflects the depositional systems (a river channel, a delta, an offshore sand ridge, etc.) that formed in response to pretty well understood mechanisms of sediment transport and deposition. The key difficulty to be resolved, however, reflects the fact that cores from subsurface reservoirs, which contain direct permeability and porosity information, represent a volume that is many orders of magnitude smaller than the reservoir from which we are trying to extract or inject fluids during oil and gas extraction and CO_2 or water injection. In order to better quantify the 'effective' porosity and permeability, this study task focused on developing new methods for their measurements and characterization. The original permeability was measured with a mini-probe permeameter, binned according to lamina type and facies, and then 'up-scaled' to generate effective permeability values for individual reservoir rock facies. This has major impact on how one models the connectivity of the oil and gas-bearing pores to the well bore. In this study, it was found that on average, these effective permeability models typically yielded a 50% reduction in the mean permeability as compared to simple averaging procedures. This is highly significant, and we believe it is a better representation of the actual reservoir volume connected to the wells for production of oil and gas or accessible storage volume for injected CO_2.

The 'upscaling' applied to the data refers to a suite of averaging techniques that transforms a fine-scale grid of data points to a coarser grid for easier numerical handling. During the upscaling care is taken to ensure that the spatial distribution of permeability is tied to stratigraphy and lithofacies of the reservoir. For that reason, this study developed detailed 'submodels' for individual facies as a basis for constructing numerical facies successions.

With these 3D models of facies and their effective connectivity to well bores, the tools are in place to evaluate the permeability zones and patterns for the most effective flow paths for CO_2 from injector wells to permanent reservoir storage, or – in other applications – the optimal well bore patterns to optimize oil and gas production.

Task 7. Regulatory regimes and enforcement structures

Establishing a large-scale, functional CO_2 subsurface storage industry across the many sedimentary basins of the United States depends also on a series of factors that go way beyond the geoscience and engineering challenges addressed in the first 6 tasks of this study. One major, yet little discussed, issue is the complexity of ownership and operational controls of the subsurface pore space that the CO_2 would have to be stored in. The questions revolve around the fact that the economic value linked to subsurface ownership has always been thought of in the context of the minerals and water that is there, not the pore space which is something that "is not there."

Whereas there has been no specific legal testing of who owns the pore space, this analysis of the history of relevant jurisprudence over the past century leads to the conclusion that the ownership is governed by the Stock Raising Homestead Act of 1916 (SRHA). This implies that that there is a strong argument for federal government ownership of over 70 million acres of pore space in the West underlying lands granted under this act. Further, it is probable, but by no means certain, that federal ownership of the pore space underlying SRHA land could reduce the transaction costs, thereby making these lands accessible for large-scale subsurface CO_2 storage. Public acceptance of the perceived risks linked to such storage is not in any way affected by the SRHA or any other Congressional Act, however, until an actual large-scale subsurface CO_2 storage project is proposed for such lands, the issue will remain yet another uncertainty facing the CCUS industry.

References

Task 1

Romps, D.M., J.T. Seeley, D.Vollaro, and J. Molinari (2014), Projected increase in lightning strikes in the United States due to global warming, *Science*, 346, 851–854; DOE: 10.1126/science. 1259100.

Task 2

Brie A., F. Pampuri, A.F. Marsala, and O. Meazza (1995), Shear sonic interpretation in gas-bearing sands, Paper presented at the SPE Annual Technical Conference and Exhibition, Dallas, Texas, 22–25 October 1995.

Corey, A.T. (1954), The interrelation between gas and oil relative permeabilities, *ProducersMonthly*, Nov.:38–41.

Gassmann F. (1951), Über die elastizität poröser medien. *Viertel Naturforsch Ges Zürich, 96*, 1–23.

Goodman, R.E. (1974), The mechanical properties of joints, in *Proc 3rd Int Congr International Society of Rock Mechanics*, *Denver, USA*, National Academy of Sciences, pp 127–140, Washington D.C.

IPCC (2005), IPCC special report on carbon dioxide capture and storage. Prepared by Working Group III of the Intergovernmental Panel on Climate Change [Metz, B., O. Davidson, H.C. de Coninck, M. Loos, and L.A. Meyer (eds.)] Cambridge University Press, Cambridge, United Kingdon and New York, NY, USA.

Malama B, and P.H.S.W. Kulatilake (2003), Models for normal fracture deformation under compressive loading, *Int. J. Rock. Mech. MIN. 40*(6), 893–901.

Pyrak-Nolte, L.J., S. Roy, and B.L. Mullenbach (1996), Interface waves propagated along a fracture, *J. Appl. Geophys. 35*(2–3), 79–87.

Wood, A.B. (1941), *A Textbook of Sound*, Bell and Sons LTD, London.

Task 3

Al-Bazali, T.M, J. Zhang, and M.M. Sharma (2005), Measurement of the sealing capacity of shale caprocks. 2005 Annual Technical Conference and Exhibition, Dallas, Texas, October 9–12.

Anders, D. (1991), Chapter 7: Geochemical Exploration Methods, in *TR- Source and Migration Processes and Evaluation Techniques (Treatise of petroleum geology)*. American Association Of Petroleum Geologists, November 18, 1991. 213 p.

Andreani, M., P. Gouze, L. Luquot, and P. Jouanna (2008), Changes in seal capacity of fractured claystone caprocks induced by dissolved and gaseous CO_2 seepage. *Geophys. Res. Lett., 35*. L14404.

Anovitz, L.M., G.W. Lynn, D.R. Cole, G. Rother, L.F. Allard, W.A. Hamilton, L. Porcar, and M.H. Kim (2009), A new approach to quantification of metamorphism using ultra-small and small angle neutron scattering. *Geochim. Cosmochi. Acta, 73*, 7303–7324.

Baines, S., and R. Worden (2004), Geological storage of carbon dioxide, *Special Publications 2004*, *233* 1–6, Geological Society, London.

Bustin, R.M., and A.M.M. Bustin (2008), Impact of shale properties on pore structure and storage characteristics, Paper, Society of Petroleum Engineers Shale Gas Production Conference, Fort Worth, Texas, USA, 16–18 November 2008.

Bethke, C. M. (2007). *Geochemical and Biogeochemical Reaction Modeling*, 547 pp., Cambridge University Press, New York.

Carr, T.R., A. Iqbal, N. Callaaghan, H. Dana Adkins, K. Look, S. Saving, and K. Nelson (2009), A national look at carbon capture and storage—National carbon sequestration database and geographical information system (NatCarb), *Energy Procedia, 1*, 2841–2847.

Carroll, S., W. McNab, S. Torres, M. Singleton, and P. Zhao (2011), Wellbore Integrity in Carbon Sequestration Environments: 1. Experimental Study of Cement-Sandstone/Shale-Brine-CO_2, *Energy Procedia, 4*, 5186–5194.

U.S. Department of Energy (DOE) (2007), Basic research needs for geosciences: Facilitating 21st century energy systems. From the workshop sponsored by the U.S. Department of Energy, Office of Basic Energy Sciences, Bethesda, MD, February 21–23.

Ellis, B., G. Bromhal, D. McIntyre, and C. Peters (2011), Changes in caprock integrity due to vertical migration of CO_2-enriched brine, *Energy Procedia*, *4*, 5327–5334.

Farrell, R.F., S.A. Matthes, and A.J. Mackie (1980), Simple, low-cost method for the dissolution of metal and mineral samples in plastic pressure vessels, Technical Report, Bureau of Mines, Washington, D.C.

Heath, J., T.A. Dewers, B. McPherson, R. Petrusak, T. Chidsey, A. Rinehart, and P. Mozley (2011), Pore networks in continental and marine mudstones: Characteristics and controls on sealing behavior, *Geofluids, 7*, 429–454.

Hinde, A.L., (2004). PRINSAS - a Windows-based computer program for the processing and interpretation of small-angle scattering data tailored to the analysis of sedimentary rocks, *J. Appl. Crystallogr., 37*, 1020–1024.

Jin, L., G. Rother, D.R. Cole, D.F.R. Mildner, C.J. Duffy, and S.L. Brantley (2011), Characterization of deep weathering and nanoporosity development in shale - a neutron study, *Am. Mineral., 96*, 498–512.

Kaszuba, J., D. Janecky, and M. Snow (2005), Experimental evaluation of mixed fluid reactions between supercritical carbon dioxide and NaCl brine: Relevance to the integrity of a geologic carbon repository, *Chem.l Geol., 217*, 277–293.

Kohler, E., T. Parra, and O. Vidal (2009), Clayey cap-rock behavior in H_2O-CO_2 media at low pressure and temperature conditions: An experimental approach, *Clays and Clay Minerals, 57*(5), 616–637.

Labus, K., and P. Bujok (2011), CO_2 mineral sequestration mechanisms and capacity of saline aquifers of the Upper Silesian Coal Basin (Central Europe)–Modeling and experimental verification, *Energy*, *36*, 4974–4982.

Lima, V., S. Einloft, J. Ketzer, M. Jullien, O. Bildstein, O., and J. Petronin (2011), CO_2 Geological Storage in Saline Aquifers: Parana Basin Caprock and Reservoir Chemical Reactivity, *Energy Procedia*, *4*, 5377–5384.

Mildner, D.F.R., R. Erezvani, P.L. Hall, and R.L. Borst (1986), Small-angle scattering of shaly rocks with fractal pore interfaces, *Appl. Phys. Lett., 48*, 1314–1316.

Navarre-Sitchler, A., D. Cole, G. Rother, and S. Brantley (2008), Evolution of micro-porosity during weathering of basalt, *Geochim. Cosmochim. Acta*, *72*, A673–A673.

Navarre-Sitchler, A., C.I. Steefel, L. Yang, L. Tomutsa, and S.L. Brantley (2009), Evolution of porosity and diffusivity associated with chemical weathering of a basalt clast, *J. Geophys. Res. Earth Surf.*, 114(F2), F02016, doi:10.1029/2008JF001060.

Radlinski, A.P., C.J. Boreham, G.D. Wignall, and J.S. Jin (1996), Microstructural evolution of source rocks during hydrocarbon generation: A small-angle-scattering study, *Phys. Rev., B 53*, 14153.

Radlinski, A.P., (2006), Small-angle neutron scattering and the microstructure of rocks, in *Neutron Scattering in Earth Sciences,* edited by H. Wenk, pp. 363–397, Mineralogical Society of America.

Tarkowski, R., and M. Wdowin (2011), Petrophysical and mineralogical research on the influence of CO_2 injection on mesozoic reservoir and caprocks from the Polish lowlands, *Oil and Gas Science and Technology, 66*(1), 137–150.

Task 4

Balkwill, D.L., F.R. Leach, J.T. Wilson, J.F. Ncnabb, and D.C. White (1988), Equivalence of microbial biomass measures based on membrane lipid and cell wall components, adenosine triphosphate, and direct counts in subsurface aquifer sediments, *Microbial Ecol., 54*, 273–291.

Banik, A., M. Sen, and S.P. Sen (1996), Effects of inorganic fertilizers and micronutrients on methane production from wetland rice, *Biol. Fert. of Soils, 21*, 319–322.

Blotovogel, K.H., U. Fischer, M. Mocha, and S. Jannsen (1985), Methanobacterium thermoalciliphilum spec. nov., a new moderately alkaliphilic and thermophilic autotrophic methanogen, *Arch. Microbiol., 142*, 211–217.

Bodelier, P.L.E., A.P. Hahn, I.R. Arth, and P. Frenzel (2000), Effects of ammonium-based fertilisation on microbial processes involved in methane emission from soils planted with rice, *Biogeochemistry*, *51*, 225–257.

Boone, D.R., W.B. Whitman, P. Rouveire, and J.G. Ferry (1993), Diversity and taxonomy of methanogens*,* in *Methanogenesis: Ecology, Physiology, Biochemistry and Genetics*, edited by J. G. Ferry, Chapman & Hall, New York.

Bowker, K.A. and W.D. Jackson (1989), The Weber Sandstone at Rangely Field, Colorado Reservoirs in Sandstone, in Coalson, E.B., Kaplan, S.S., Keighin, C.W., Oglesby, C.A., and Robinson, J.W., eds., *Petrogenesis and Petrophysics of Selected Sandstone Reservoirs of the Rocky Mountain Region*, Denver, Rocky Mountain Association of Geologists, p. 65–80.

Bowker, K.A. and P.S. Shuler (1991), Carbon dioxide injection and resultant alteration of the Weber sandstone, Rangely field, Colorado, *AAPG Bull., 75*, 1489–1499.

Bräuer, S.L., J.B. Yavitt, and S.H. Zinder (2004), Methanogenesis in McLean Bog, an acidic peat bog in upstate New York: Stimulation by H_2/CO_2 in the presence of rifampicin, or by low concentrations of acetate, *Geomicrobio. J., 21*, 433–443.

Bronson, K.F., H.U. Neue, U. Singh, and E.B. Abao (1997), Automated chamber measurements of methane and nitrous oxide flux in a flooded rice soil. 1. Residue, nitrogen, and water management. *Soil Sci. Soc. Am. J., 61*, 981–987.

Chanton, J.P., J.E. Bauer, P.A. Glaser, D.I. Siegel, S.C. Kelley, S.C. Tyler, E.H. Romanowicz, and A. Lazrus (1995), Radiocarbon evidence for the substrates supporting methane formation within northern Minnesota peatlands, *Geochim. Cosmochim. Acta, 59*, 3663–3668.

Cicerone, R.J. and J.D. Shetter (1981), Sources of atmospheric methane: measurements in rice paddies and a discussion, *J. Geophys. Res.*, *86*, 7203–7209.

Dan, J., M. Krüger, P. Frenzel, and R. Conrad (2001), Effect of a late season urea fertilization on methane emission from a rice field in Italy. *Agr., Ecosyst. & Environ., 83*, 191–199.

Dowling, N.J.E., P.D. Nichols, and D.C. White (1988), Phospholipid fatty acid and infrared spectroscopic analysis of a sulphate-reducing consortium, *FEMS Microbio. Lett., 53*, 325–333.

Dowling, N.J.E., F. Widdle, and D.C. White (1986), Phospholipid ester-linked fatty acid biomarkers of acetate-oxidizing sulfate-reducers and other sulfide-forming bacteria, *J. of Gen. Microbiol.*, *132*, 1815–1825.

Durie, R.A., D.J. Williams, P. Mcmullan, and C.A.J. Pautlson (2001), Greenhouse Gas Technologies: Proceedings of the 5th International Conference on Greenhouse Gas Control Technologies, Csiro Publishing, Collingwood, Australia.

Ferris, F.G., V. Phoenix, Y. Fujita, and R.W. Smith (2004), Kinetics of calcite precipitation induced by ureolytic bacteria at 10 to 20°C in artificial groundwater, *Geochim. Cosmochim. Acta, 68*, 1701–1710.

Flores, R.M., C.A. Rice, G.D. Stricker, A. Warden, and M.S. Ellis (2008), Methanogenic pathways of coal-bed gas in the Powder River Basin, United States: The geologic factor, *Int. J. Coal Geol.*, *76*, 52–75.

Fukuzaki, S., N. Nishio, and S. Nagai (1990), Kinetics of the methanogenic fermentation of acetate, *Appl. Environ. Microb., 56*, 3158–3163.

Goodwin, S., R. Conrad, and J.G. Zeikus (1988), Influence of pH on microbial hydrogen metabolism in diverse sedimentary ecosystems, *Appl. Environ. Microb., 54*, 590–593.

Harris, S.H., R.L. Smith, and C.E. Barker (2008), Microbial and chemical factors influencing methane production in laboratory incubations of low-rank subsurface coals, *Int. J. Coal Geol., 76*, 46–51.

Hefner, T.A., and K.T. Barrow (1992), Rangely Field, U.S.A., Uinta/Piceance basins, Colorado, in *Structural Traps VII: AAPG Treatise of Petroleum Geology, Atlas of Oil and Gas Fields*, edited by E. A. Beaumont and N.H. Foster, American Association of Petroleum Geologists, Tulsa, OK.

Hunik, J. H., H.V.M. Hamelers, and I.W. Koster (1990), Growth-rate inhibition of acetoclastic methanogens by ammonia and pH in poultry manure digestion, *Biol. Waste, 32*, 285–297.

Jabri, E., M.B. Carr, R.P. Hausinger, and P.A. Karplus (1995), The crystal structure of urease from Klebsiella aerogenes, *Science, 268*, 998–1004.

Jones, E.J.P., M.A. Voytek, M.D. Corum, and W.H. Orem (2010), Stimulation of methane generation from nonproductive coal by addition of nutrients or a microbial consortium, *Appl. Environ. Microb., 76*, 7013–7022.

Klusman, R.W. (2003), A geochemical perspective and assessment of leakage potential for a mature carbon dioxideenhanced oil recovery project and as a prototype for carbon dioxide sequestration; Rangely field, Colorado, *AAPG Bull., 87*, 1485–1507.

Kohring, L.L., D.B. Ringelberg, R. Devereux, D.A. Stahl, M.W. Mittelman, and D.C. White (1994), Comparison of phylogenetic-relationships based on phospholipid fatty-acid profiles and ribosomal-RNA sequence similarities among dissimilatory sulfate-reducing bacteria, *FEMS Microbiol. Lett., 119*, 303–308.

Kolak, J.J. and R.C. Burruss (2006), Geochemical investigation of the potential for mobilizing non-methane hydrocarbons during carbon dioxide storage in deep coal beds, *Energ. Fuel.*, *20*, 566–574.

Kotsyurbenko, O.R., K.J. Chin, M.V. Glagolev, S. Stubner, M.V. Simankove, A.N. Nozhevnikova, and R. Conrad (2004), Acetoclastic and hydrogenotrophic methane production and methanogenic populations in an acidic West-Siberian peat bog, *Environ. Microb., 6*, 1159–1173.

Lechevalier, M.P. (1977), Lipids in bacterial taxonomy: a taxonomists view. *Crit. Rev. Microbio., 5*, 109–210.

Lin, X., D. Kennedy, A. Peacock, J. Mckinley, C.T. Resch, J. Fredrickson, and A. Konopka (2012), Distribution of Microbial Biomass and Potential for Anaerobic Respiration in Hanford Site 300 Area Subsurface Sediment, *Appl. Environ. Microb., 78*, 759–767.

Lindau, C.W. (1994), Methane emissions from Louisiana rice fields amended with nitrogen fertilizers, *Soil Biol. Biochem., 26*, 353–359.

Mathrani, I.M., D.R. Boone, R.A. Mah, G.E. Fox, and P.P. Lau (1988), Methanohalophilus zhilinae sp. nov., an Alkaliphilic, Halophilic, Methylotrophic Methanogen, *Int. J. Systematic Bacteriology, 38*, 139–142.

Mcgrail, B.P., H.T. Schaef, A.M. Ho, Y.J. Chien, J.J. Dooley, and C.L. Davidson, C.L (2006), Potential for carbon dioxide sequestration in flood basalts, *J. Geophys. Res,. 111,* B12201.

Mcgrail, B.P., F.A. Spane, E.C. Sullivan, D.H. Bacon, and G. Hund, 2011, The Wallula basalt sequestration pilot project, *Energy Procedia*, *4*, 5653–5660.

Mills, C.T., Y. Amano, G.F. Slater, R.F. Dias, T. Iwatsuki, T., and K.W. Mandernack (2010), Microbial carbon cycling in oligotrophic regional aquifers near the Tono Uranium Mine, Japan as inferred from δ13C and Δ14C values of in situ phospholipid fatty acids and carbon sources, *Geochim. Cosmochim. Acta, 74*, 3785–3805.

Mitchell, A.C., K. Dideriksen, L.H. Spangler, A.B. Cunningham, and R. Gerlach (2010), Microbially enhanced carbon capture and storage by mineral-trapping and solubility-trapping, *Environ. Sci. Technol., 44*, 5270–5276.

Nielsen, T.H., T.A. Bonde, and J. Sørensen (1998), Significance of microbial urea turnover in N cycling in three Danish agricultural soils, *FEMS Microbiol. Ecol, 25*, 147–157.

Nishihara, M., and Y. Koga (1987), Extraction and composition of polar lipids from the archaebacterium, Methanobacterium thermoautotrophicum: Effective extraction of tetraether lipids by an acidified solvent, *J. Biochem.-Tokyo*, *101*, 997–1005.

O'connell, S.P., R.M. Lehman, O. Snoeyenbos-West, V.D. Winston, D.E. Cummings, M.E. Watwood, and F.S. Colwell (2003), Detection of Euryarchaeota and Crenarchaeota in an oxic basalt aquifer, *FEMS Microbiol. Ecol., 44*, 165–173.

Olson, G.J., W.S. Dockins, G.A. Mcfeters, and W.P. Iverson (1981), Sulfate-reducing and methanogenic bacteria from deep aquifers in Montana. *Geomicrobiol. J., 2*, 327–340.

Onstott, T.C. (2005), Impact of CO_2 injections on deep subsurface microbial ecosystems and potential ramifications for the subsurface biosphere, in *Carbon Dioxide Capture and Storage in Deep Geologic Formations-Results from the CO_2 Capture Project,* edited by S.M. Benson, Elsevier Ltd., New York.

Pashin, J.C. (2007), Hydrodynamics of coalbed methane reservoirs in the Black Warrior Basin: Key to understanding reservoir performance and environmental issues, *Appl. Geochem., 22*, 2257–2272.

Renkonen, O., (1965), Individual molecular species of different phospholipid classes. Part II. A method of Analysis, *J. Am. Oil Chem. Soc., 42*, 298–304.

Rice, D.D., and R.M. Flores (1991), Controls of bacterial gas accumulations in thick Tertiary coal beds and adjacent channel sandstones, Powder River Basin, Wyoming and Montana, *AAPG Bull., 75*, 661–661.

Roedell, J. (2011), Personal Communication, Rangely, CO.

Sahl, J., R. Schmidt, E. Swanner, K.W. Mandernack, A.S. Templeton, T.L. Kieft, R.L. Smith, W.E. Sanford, R.L. Callaghan, J.B. Mitton, and J. R. Spear (2008), Subsurface microbial diversity in deep-granitic fracture water in Colorado, *Appl. Environ. Microbiol., 74*, 143–152.

Scott, A.R., W.R. Kaiser, and W.B. Ayers, Jr. (1994), Thermogenic and secondary biogenic gases, San Juan Basin, Colorado and New Mexico-Implications for coalbed gas producibility, *AAPG Bull., 78*, 1186–1209.

Shuler, P.J., E.A. Freitas, and K.A. Bowker (1989), Selection and application of barium sulfate scale inhibitors for a carbon dioxide flood, Rangely Weber Sand Unit, Rangely, Colorado Society of Petroleum Engineers Joint Rocky Mountain Regional/Low Permeability Reservoirs Symposium, SPE18973, 451–464.

Shumkov, S., S. Terekhova, and K. Laurinavichius (1999), Effect of enclosing rocks and aeration on methanogenesis from coals, *Appl. Microbio. Biot., 52*, 99–103.

Singh, S., J.S. Singh, and A.K. Kashyap (1999), Methane flux from irrigated rice fields in relation to crop growth and N-fertilization, *Soil Biol. Biochem., 31*, 1219–1228.

Sprott, G.D., and G.B. Patel (1986), Ammonia toxicity in pure cultures of methanogenic bacteria, *Syst. Appl. Microbiol., 7*, 358–363.

Stevens, T.O., and J.P. Mckinley, J.P (1995), Lithoautotrophic microbial ecosystems in deep basalt aquifers, *Science, 270,* 450–454.

Strapoc, D., M. Mastalerz, K. Dawson, J.L. Macalady, A.V. Callaghan, B. Wawrik, C. Turich, and M. Ashby (2011), Biogeochemistry of microbial coal-bed methane, *Annu. Rev. Earth Pl. Sci., 39*, 617–656.

Stumm, W. and J.J. Morgan (1996), *Aquatic Chemistry.*, John Wiley and Sons, Inc., New York.

Swensen, B. and L.R. Bakken (1998). Nitrification potential and urease activity in a mineral subsoil, *Soil Biol. Biochem., 30*, 1333–1341.

Tanner, R.S. (2006), Cultivation of bacteria and fungi, in *Manual of Environmental Microbiology,* edited by J.L. Garland, J. L., ASM Press, Washington, D.C.

Taylor, R. and R.J. Parkes (1983), The cellular fatty acids of the sulphate-reducing bacteria, Desulfobacter sp., Desulfobulbus sp., and Desulfovibrio desulfuricans, *J. Gen. Microbiol., 129*, 3303–3309.

U.S. Department of Energy, (2010), DOE/NETL carbon dioxide capture and storage RD&D Roadmap, U.S. Department of Energy, Pittsburgh, PA.

White, D.C. and D.B. Ringelberg (1998), Signature lipid biomarker analysis, in *Techniques in Microbial Ecology*, edited by R.S. Burlage, R. Atlas, D. Stahl, G. Geesey, G., and G. Sayler, G, Oxford University Press, New York.

Widdel, F. (1988), Microbiology and ecology of sulphate and sulphur reducing bacteria, in *Biology of Anaerobic Microorganisms,* edited by A.J.B. Zender, Wiley Interscience, New York, NY.

Williams, R.T., and R.L. Crawford (1985), Methanogenic bacteria, including an acid-tolerant strain, from peatlands, *Appl. Environ. Microbiol., 50*, 1542–1544.

Task 5

Alvarez, R.A., S.W. Pacala, J.J. Winebrake, Chameides, W.L, and S.P. Hamburg (2012), Greater focus needed on methane leakage from natural gas infrastructure; *Proc. Natl. Acad. Sci USA 2012, 109*(17), 6435–6440. Accessed 2014, July 27 from http://www.pnas.org/cgi/doi/10.1073/pnas.1202407109 PNAS

Clark, C.E., and J.A. Veil (2009), Produced water volumes and management practices in the United States [external site], ANL/EVS/R-09/1, prepared by the Environmental Science Division, Argonne National Laboratory for the U.S. Department of Energy, Office of Fossil Energy, National Energy Technology Laboratory, Accessed 2014, July 27 from *http://www.netl.doe.gov/technologies/pwmis/intropw.*

Hickenbottom, K.L., N.T. Hancock, N.R. Hutchings, E.W. Appleton, E.G. Beaudry, P. Xu, and T.Y. Cath (2013), Forward osmosis treatment of drilling mud and fracturing wastewater from oil and gas operations, *Desalination*, *312*, 60–66.

Logan, J., and G. Heath, J. Macknick, E. Paranhos, W.K. Boyd, and K. Carlson, (2012), Natural gas and the transformation of the U.S. energy sector: Electricity, Technical Report, NREL/TP-6A50-55538, The Joint Institute for Strategic Energy Analysis, Contract No. DE-AC36-08GO28308, Golden, CO.

McCray, J.E., and G.D. Thyne (2009), Joint sustainability of water resources and petroleum-energy production, Editorial, *Ground Water*, *47*(5), 11.

Olivier, J.G.J., G. Janssens-Maenhoot, and J.A.H.W. Peters (2012), Trends in Global CO_2 Emissions; 2012 Report, The Hague: PBL Netherlands Environmental Assessment Agency; Ispra: Joint Research Centre, DOI: 10.2788/33777

Petron, G., et al. (2012), Hydrocarbon emissions characterization in the Colorado Front Range - A pilot study, *J. Geophysic. Res., 117*, D04304, doi:10.1029/2011JD016360.

Schneider, J., and R. Snieder (2011), Putting partnership first: A dialogue model for science and risk communication, *GSA Today, 21*(1) 34–36.

Schneider, J., and A. Knaak (2013), Fractured rock, public ruptures: The debate over hydraulic fracturing and gasland, in *Technology and the Environment,* edited by P. Brey, D. Kaplan and B. Caldicott, MIT Press, in press.

U.S. Department of Energy (US DOE) (2012) U.S. energy-related carbon dioxide emissions, 2012. U.S. Energy Information Administration, Washington, D.C. (Updated yearly). Accessed 2014, July 27 from http://www.eia.gov/environment/emissions/carbon/

U.S. Environmental Protection Agency (US EPA) (2011). Investigation of ground water contamination near Pavillion, Wyoming, Draft Report, U.S. EPA Office of Research and Development, Washington, D.C.

U.S. Government Accountability Office (US GAO) (2012). ENERGY-WATER NEXUS: Information on the quantity, quality, and management of water produced during oil and gas production, Report to the Ranking Member, Committee on Science, Space, and Technology, House of Representatives, Washington, D.C., January 2012. Accessed 2014, July 27 from http://www.gao.gov/assets/650/648306.pdf

Waxman, H., Markey, E. J., and DeGette, D. (2011), Chemicals used in hydraulic fracturing, s.l, Report to the U.S. House of Representatives Committee on Energy and Commerce: Minority Staff, Accessed 2014, July 27 from http://conservationco.org/admin/wp-content/uploads/2013/02/Final-Rebuttal-Exhibits.pdf-Adobe-Acrobat-Pro.pdf

Task 6

Al-Raisi, M.H., R.M. Slatt, and M.K. Decker (1996), Structural and stratigraphic compartmentalization of the Terry Sandstone and effects on reservoir fluid distributions; Latham Bar Trend, Denver Basin; Colorado, *The Mountain Geologist*, *33*(1), 11–30.

Cant, D.J. (1992), Subsurface facies analysis, St. Johns, NL, Canada (CAN), Geological Association of Canada, St. Johns, NL.

Corbett, P.W.M., and J.L. Jensen (1993), Application of probe permeametry to the prediction of two-phase flow performance in laminated sandstones (lower Brent Group, North Sea), *Mar Petrol. Geol., 10*(4), 335–346.

de Marsily, G., F. Delay, J. Goncalves, P. Renard, V. Teles, and S. Violette (2005), Dealing with Spatial Heterogeneity, *J. Hydrol., 13*, 161–183.

Desbarats, A.J. (1987), Numerical estimation of effective permeability in sand-shale formations, *Water Resour. Res., 23*(2), 273–286.

Deutsch, C. (1989), Calculating effective absolute permeability in sandstone/shale sequences, *SPE Formation Eval.*, *4*(3), 343–348.

Dickinson, W.R., M.A. Klute, M.J. Hayes, S.U. Janecke, E.R. Lundin, M.A. McKittrick, and M.D. Olivares (1988), Paleogeographic and paleotectonic setting of Laramide sedimentary basins in the central Rocky Mountain region, *Geol. Soc. Am. Bull., 100*(7), 1023–1039.

Durlofsky, L.J. (1991), Numerical calculation of equivalent grid-block permeability tensors for heterogeneous porous media, *Water Resour. Res., 27*(5), 699–708.

Elfenbein, C., P.S. Ringrose, and M. Christie (2005), Small-scale reservoir modeling rool optimizes recovery offshore Norway, *World Oil, 226*(10), 45–50.

Goggin, D.J., R.L. Thrasher, and L.W. Lake (1988), A theoretical and experimental analysis of minipermeameter response including gas slippage and high velocity flow effects, *In Situ, 12*, (1–2), 79–116.

Haldorsen, H.H. (1986), Simulator parameter assignment and the problem of scale in reservoir engineering, in *Reservoir Characterization,* edited by L.W. Lake and H. B. Carroll, p. 293–240, Academic Press, Orlando, FL.

Helsley, R., (1985), Terry Sandstone Member of the Pierre Shale, Upper Cretaceous, Spindle Field, Denver Basin, Colorado, Master's thesis.

Higley, D.K., D.O. Cox, and R.J. Weimer (2003), Petroleum system and production characteristics of the Muddy (J) Sandstone (Lower Cretaceous) Wattenberg continuous gas field, Denver Basin, Colorado. *AAPG Bull.*, 87, 1186–1209.

Higley, D.K. (2014) Petroleum system and production characteristics of the muddy (J) sandstone (Lower Cretaceous)Wattenberg continuous gas field, Denver Basin, Colorado, *AAPG Bull.,* 87, (1), 15–37.

Hurst, A., and K.J. Rosvoll (1991), Permeability in sandstones and their relationship to sedimentary structures, in *Reservoir Characterization,* edited by L.W. Lake, H. B. Carroll and T.C Weston, p. 166–196, Academic Press, Orlando, FL.

Imam, M.B. (1989), Comparison of burial diagenesis in some deltaic to shallow marine reservoir sandstones from different basins, *J. Geolog. Soc. of India, 33*(6), 524–537.

Jackson, M.D., A.H. Muggeridge, S.Yoshida, and H.D. Johnson (2003), Upscaling Permeability Measurements Within Complex Heterolithic Tidal Sandstones, *Math. Geol., 35*(5), 499–520.

Kiteley, L.W. (1978), Hydrocarbon accumulation in Cretaceous shallow-marine sandstones of the northern Denver Basin, Geological Survey Professional Paper 1100, Washington, D.C.

Kiteley, L.W. (1975), Chart showing correlation of Upper Cretaceous rocks in the northern Denver Basin, Colorado and Wyoming, with other areas in eastern Wyoming, v. OF 75-0033.

Kiteley, L.W. (1977), Shallow marine deposits in the Upper Cretaceous Pierre Shale of the northern Denver Basin and their relation to hydrocarbon accumulation; Exploration frontiers of the central and southern Rockies, Field Conference - *Rocky Mountain Association of Geologists*, *1977,* 197–211.

Ladd, J.H. (2001), An Overview and Development History of the Wattenberg Field, in *Gas in the Rockies*, edited by Anderson, D.S., J.W. Robinson, J.E. Estes-Jackson, and E.B. Coalson, Rocky Mountain Association of Geologists.

Larese, R.E. (2008), Petrographic Analysis of Selected Sussex-Shannon Sandstone Core Plug Specimens from the Haller CR 32-11 #1 Well, Spindle Field, Weld County, Colorado, v. REL-2008-30.

Moredock, D.E., and S.J. Williams (1976), Upper Cretaceous Terry and Hygiene sandstones; Singletree, Spindle and Surrey fields; Weld County, Colorado, Professional Contributions of the Colorado School of Mines, no. 8, 264–274.

Nordahl, K., P.S. Ringrose, and R. Wen (2005), Petrophysical characterization of a heterolithic tidal reservoir interval using a process-based modelling tool, *Petrol. Geosci., 11*(1), 17–28.

Nordahl, K., and P.S. Ringrose (2008), Identifying the Representative Elementary Volume for Permeability in Heterolithic Deposits Using Numerical Rock Models, *Mathematical Geosciences, 40*(7), 753–771.

Pickup, G.E., P.S. Ringrose, J.L. Jensen, and K.S. Sorbie (1994), Permeability tensors for sedimentary structures, *Math. Geology*, *26*(2), 227–250.

Pittman, E.D. (1988), Diagenesis of Terry Sandstone (Upper Cretaceous), Spindle Field, Colorado, *Journal of Sedimentary Petrology, 58* (5), 785–800.

Pittman, E.D. (1989), Nature of the Terry Sandstone reservoir, Spindle Field, Colorado, Denver, CO, United States (USA), Rocky Mt. Assoc. Geol., Denver, CO.

Porter, K.W. (1976), Marine shelf model, Hygiene Member of the Pierre Shale, Upper Cretaceous, Denver Basin, Colorado; Studies in Colorado field geology, Professional Contributions of the Colorado School of Mines, no. 8, 251–263.

Porter, K.W., and R.J. Weimer (1982), Diagenetic sequence related to structural history and petroleum accumulation; Spindle Field, Colorado, *AAPG Bull., 66*(12), 2543–2560.

Raynolds, R.G. (2002), Upper Cretaceous and Tertiary stratigraphy of the Denver Basin, Colorado; Paleontology and stratigraphy of Laramide Strata in the Denver Basin (Part I), *Rocky Mountain Geology, 37*(2), 111–134.

Renard, P., and G. de Marsily (1997), Calculating equivalent permeability; a review, *Adv. Water Resour.*, *20*(5-6), 253–278.

Ringrose, P. S., K. Nordahl, and R. Wen (2005), Vertical permeability estimation in heterolithic tidal deltaic sandstones, *Petrol. Geosci.,11*(1), 29–36.

Ringrose, P., K. Sorbie, F. Feghi, G. Pickup, and J. Jensen (1993), Relevant reservoir characterization - recovery process, geometry, and scale, *In Situ*, 17(1), 55–82.

Rubin, D.M. (1987), Cross-bedding, bedforms, and paleocurrents, Tulsa, OK, United States (USA), *Soc. Econ. Paleontol. and Miner.*, Tulsa, OK.

Slatt, R.M., D.H. Edington, and A.A. Fursova (1997), Shoreface sequence stratigraphy of the Upper Cretaceous Terry Sandstone in Denver Basin, Colorado; AAPG Rocky Mountain Section meeting; abstracts, *AAPG Bull., 81*(7), 1234.

Sloan, J.A. (2012), Stratigraphic architecture and connectivity of a low net-to-gross fluvial system: Combining outcrop analogs and multiple-point geostatistical modeling, lower Williams Fork Formation, Piceance Basin, Colorado, M.S. thesis, University of Colorado at Boulder, United States — Colorado.

Tidwell, V.C., and J.L. Wilson (1997), Laboratory method for investigating permeability upscaling, *Water Resour. Res., 33*(7), 1607–1616.

Walker, R.G., and K.M. Bergman (1993), Shannon Sandstone in Wyoming; a shelf-ridge complex reinterpreted as lowstand shoreface deposits, *J. Sedim. Petrol., 63*(5), 839–851.

Weber, K.J. (1982), Influence of common sedimentary structures on fluid flow in reservoir models, *J. Petrol. Technol., 34*(3), 665–672.

Weimer, R.J. (1978), Influence of transcontinental arch on Cretaceous marine sedimentation; a preliminary report, *Rocky Mountain Association of Geologists, 1978*, 211–222.

Weimer, R.J., S.A. Sonnenberg, and G.B.C. Young (1986), Wattenberg Field, Denver Basin, Colorado; Geology of tight gas reservoirs, *AAPG Studies in Geology, 24*, 143–164.

Weimer, R.J., and S.A. Sonnenberg (1996), Guide to the petroleum geology and Laramide Orogeny, Denver Basin and Front Range, Colorado: Bulletin Colorado Geological Survey, Department of Natural Resources, Report #51, 127 p.

Wen, R., A.W. Martinius, A. Naess, and P. Ringrose (1998), Three-dimensional simulation of small-scale heterogeneity in tidal deposits—a process-based stochastic simulation method, in *Proceedings of the 4th annual conference of the International Association of Mathematical Geology (IAMG), Ischia*, edited by A. Buccianit, G. Nardi, and R. Potenza, p. 129–134.

Wen, R. (2008), Upscaling core plug data to reservoir modelling grid; a small-scale heterogeneity modelling approach, *Reservoir, 35*(6), 12.

Wen, X., and J.J. Gomez-Hernandez (1996), Upscaling hydraulic conductivity in heterogeneous media; an overview, *J. Hydrol., 183*(1–2), ix-xxxii.

Worthington, P.F., (1994), Effective integration of core and log data, *Mar. Petrol. Geol., 11*(4), 457–466.